Process understanding of induced seismicity during stimulation of enhanced geothermal systems

Iman Vaezi Anzeha

Ph.D. Thesis

Process understanding of induced seismicity during stimulation of enhanced geothermal systems

Author:
Iman Vaezi

Supervisor:
Dr. Víctor Vilarrasa
Tutor:
Dr. Sebastià Olivella

Department of Civil and Environmental Engineering

Universitat Politècnica de Catalunya - BarcelonaTech (UPC)

November, 2023

This thesis has received funding from the European Research Council (ERC) under the European Union's Horizon 2020 Research and Innovation Program through the Starting Grant GEoREST, under grant agreement No. 801809.

To my parents,

Fazlollah & Fereshteh

and my siblings,

Reza, Maryam, & Ahmad

Abstract

This doctoral thesis investigates the causes that induce (micro)seismicity as a result of hydraulic stimulation in fractured low-permeability rock. Understanding such phenomenon is of paramount importance to eventually forecast induced seismicity in geo-energy applications, like Enhanced Geothermal Systems (EGS). The research is driven by both scholarly and engineering considerations, addressing the intricate coupled hydro-mechanical (HM) processes that are at play and aiming to advance in the understanding of the mechanisms underlying co-seismicity during the hydraulic stimulation phase of EGS.

The thesis begins with a comprehensive review of existing modeling methodologies of coupled processes in fractured rock. This exploration highlights the significant advancements these methodologies have brought to the foundational understanding of fractures, ultimately improving predictive capabilities related to coupled processes within fractured systems.

The subsequent focus of the research involves an investigation into the flow regimes induced by constant flow rate water injection into a fracture surrounded by a low-permeability matrix. The study sheds light on the implications for hydraulic test interpretation and numerical simulations. The findings reveal that even in very low-permeability confining rock matrix, leakage is non-negligible due to the small fracture aperture, which maximizes pressure gradients across the fracture-matrix interface. The transition between flow regimes, often overlooked in field tests, has important implications for accurately estimating fracture transmissivity in injection tests in fractured media and modeling approaches.

The thesis then proposes an innovative approach for the implicit representation of fractures surrounded by low-permeability rock matrix. This approach assimilates fractures as equivalent continua, demonstrating that a relatively thick equivalent continuum layer can accurately represent a fracture and reproduce HM behavior. The proposed method is validated through the modeling of a hydraulic stimulation carried out at the Bedretto Underground Laboratory, showcasing its ability to improve the simplicity and efficacy of continuum methods in representing fractures in fractured media.

Finally, the research delves into the modeling of a highly-monitored test at the Bedretto Underground Laboratory to investigate the impact of fluid injection on permeability enhancement and induced microseismicity. Three models are examined, with the viscoplastic fracture with dilatancy and strain-weakening approach emerging as the most comprehensive in capturing the spatio-temporal coupled response of fractured rock to hydraulic stimulation. This model proves effective in estimating the extent of the stimulated fracture, permeability enhancement, and its impact on the local state of stress and pore pressure at surrounding fractures, presenting a valuable tool for the design of effective hydraulic stimulation.

In summary, this doctoral thesis contributes to the understanding of micro-seismicity induced by EGS operations, offering insights into coupled processes, flow regimes, and innovative modeling approaches, ultimately advancing the field of geothermal energy research and hydraulic stimulation design.

RESUMEN

Esta tesis doctoral investiga las causas que inducen la (micro)sismicidad como resultado de la estimulación hidráulica en rocas fracturadas de baja permeabilidad. Comprender este fenómeno es de vital importancia para prever la sismicidad inducida en aplicaciones geoenergéticas, como los sistemas geotérmicos mejorados (EGS por sus siglas en inglés). La investigación está impulsada por consideraciones tanto académicas como ingenieriles, abordando los intrincados procesos hidromecánicos (HM) acoplados que entran en juego y con el objetivo de avanzar en la comprensión de los mecanismos subyacentes a la cosismicidad durante la fase de estimulación hidráulica de los EGS.

La tesis comienza con una revisión exhaustiva de las metodologías de modelización existentes de los procesos acoplados en rocas fracturadas. Esta exploración pone de relieve los importantes avances que estas metodologías han aportado a la comprensión fundamental de las fracturas, mejorando en última instancia las capacidades de predicción relacionadas con los procesos acoplados dentro de los sistemas fracturados.

A continuación, la investigación se centra en los regímenes de flujo inducidos por la inyección de agua a caudal constante en una fractura rodeada por una matriz de baja permeabilidad. El estudio arroja luz sobre las implicaciones para la interpretación de ensayos hidráulicos y simulaciones numéricas. Los resultados revelan que, incluso en una matriz de roca confinante de muy baja permeabilidad, las fugas no son despreciables debido a la pequeña abertura de la fractura, que maximiza los gradientes de presión a través de la interfaz fractura-matriz. La transición entre regímenes de flujo, que a menudo se pasa por alto en los ensayos de campo, tiene importantes implicaciones para estimar con precisión la transmisividad de la fractura en las pruebas de inyección en medios fracturados y en los planteamientos de modelización.

A continuación, la tesis propone un enfoque innovador para la representación implícita de fracturas rodeadas por una matriz rocosa de baja permeabilidad. Este enfoque asimila las fracturas como medios continuos equivalentes, demostrando que una capa de medio continuo equivalente relativamente gruesa puede representar con precisión una fractura y reproducir el comportamiento HM. El método propuesto se valida mediante la modelización de una estimulación hidráulica llevada a cabo en el Laboratorio Subterráneo

de Bedretto, mostrando su capacidad para mejorar la simplicidad y eficacia de los métodos continuos en la representación de fracturas en medios fracturados.

Por último, la investigación profundiza en la modelización de una prueba altamente monitorizada en el Laboratorio Subterráneo de Bedretto para investigar el impacto de la inyección de fluidos en el aumento de la permeabilidad y la microsismicidad inducida. Se examinan tres modelos, y el de fractura viscoplástica con dilatancia y debilitamiento por deformación resulta ser el más completo para captar la respuesta acoplada espaciotemporal de la roca fracturada a la estimulación hidráulica. Este modelo resulta eficaz para estimar la extensión de la fractura estimulada, la mejora de la permeabilidad y su impacto en el estado local de tensión y presión de poros en las fracturas circundantes, presentando una valiosa herramienta para el diseño de una estimulación hidráulica eficaz.

En resumen, esta tesis doctoral contribuye a la comprensión de la microsismicidad inducida por las operaciones EGS, ofreciendo una visión de los procesos acoplados, los regímenes de flujo y los enfoques de modelado innovadores, avanzando en última instancia en el campo de la investigación de la energía geotérmica y el diseño de la estimulación hidráulica.

Acknowledgments

Embarking on this PhD journey has been an incredible privilege, and I am overflowing with gratitude for the remarkable individuals who have made this project not only intellectually enriching but also a joyous experience.

First and foremost, my heartfelt thanks go to my advisor, Dr. Víctor Vilarrasa. Víctor, your unwavering support has been the bedrock of this PhD adventure. Thank you for not only entrusting me with this opportunity but also for being a guiding light, imparting wisdom, and allowing me the space to grow independently. Your considerate and generous mentorship has made me feel like both a colleague and someone in the safest pair of hands. I am truly grateful for your encouragement to always push my boundaries.

A big shoutout to Francesco Parisio, Keita Yoshioka, Andrés Alcolea, Silvia De Simone, and Jesus Carrera for their invaluable contributions through insightful discussions that greatly influenced the development of this Thesis. Your collaborative spirit has been instrumental in shaping the ideas within these pages.

To my incredible peers at the GEoREST Group, Dario, Auregan, and Linus – you guys have made this journey unforgettable. From the awesome working atmosphere to the stimulating discussions (and yes, even the stressful times before deadlines), thank you for sharing both the highs and lows. Your camaraderie has been a cornerstone of this experience.

A special acknowledgment is due to my family for their unconditional love and unwavering support. To my sister, Maryam, you have been my rock through the stressful moments of these years. Thank you for being not just a sibling but also a mentor from the beginning of this adventure. And to my younger brother, Ahmad, your steadfast support has been like a mountain, and I am truly grateful.

Mil gracias!

Table of contents

1

Introduction

1.1 Background and motivation

The contemporary surge in global greenhouse gas emissions persists unabated, a concerning trend amid the urgent need for a substantial reduction (*IPCC, Climate Change*, 2023). Comprehending the origins of these emissions and how we could eliminate them stand as a crucial step towards their effective abatement. We need to find answers to questions like: which industries wield the most significant influence? How might this discernment inform the development of pragmatic solutions and proactive mitigation strategies? Figure 1.1 shows the breakdown of total greenhouse gas emissions, quantified in metric tons of carbon dioxide (CO_2) equivalents, across various sectors by 2020. Notably, the data highlights the substantial dominance of electricity and heat production as the foremost contributors to the global emission footprint, followed by diverse sectors.

The necessary shift from the existing fossil-fuel-dependent energy structure toward a sustainable paradigm, grounded primarily on renewable resources, necessitates a robust foundation of evidence-based decision-making processes (Christensen and Hain, 2017). Within the realm of renewable energy sources tackling electricity and heat production, geothermal energy stands as a promising alternative owing to its minimal environmental footprint, low greenhouse gas emissions and, unlike other renewables, non-intermittent production (Shortall et al., 2015). Geothermal energy reservoirs, ubiquitously dispersed beneath the Earth's surface, exhibit economic viability hinged upon critical factors such as depth, permeability, and temperature. These reservoirs can be broadly categorized into shallow and low-temperature formations, and deep and high-temperature formations, the

latter often exceeding 100 °C and occasionally surpassing 400 °C, particularly within volcanic regions (Tomac and Sauter, 2018). While shallow geothermal energy, situated at relatively shallow depths and lower temperatures, is typically harnessed for direct applications like heating, deep geothermal energy, with its significantly elevated temperatures, finds application primarily in electricity generation (Bayer et al., 2019; Moya et al., 2018).

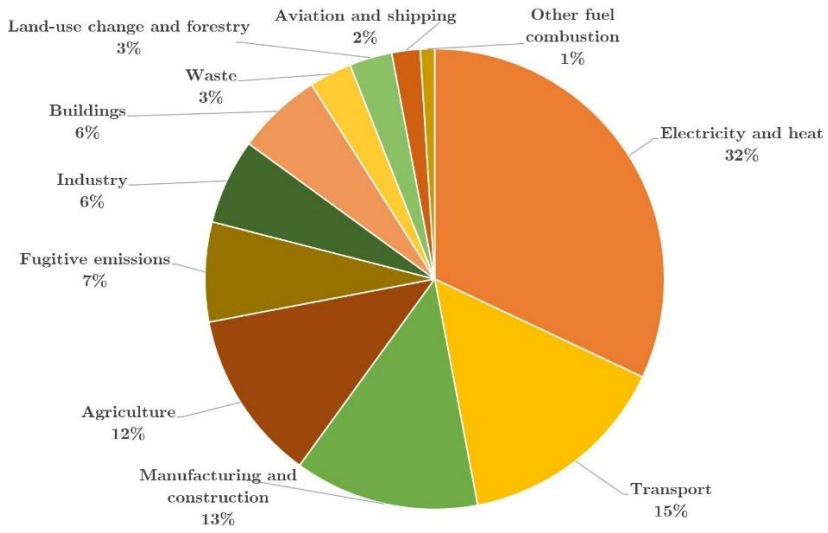

Figure 1.1 Greenhouse gas emissions by sector in the world, in 2020. Emissions are measured in carbon dioxide equivalents (CO_{2eq}). This means non-CO_2 gases are weighted by the amount of warming they cause over a 100-year timescale (ourworldindata.org). Electricity and heat production are the largest contributor to global emissions. This is followed by transport, manufacturing and construction (largely cement and similar materials), and agriculture

The viability of geothermal energy extraction from Hot Dry Rock (HDR) formations, primarily characterized by hard, low-permeable crystalline rock structures, necessitates the deployment of an Enhanced Geothermal System (EGS) capable of effectively converting geothermal energy into electricity (Olasolo et al., 2016). This involves the implementation of an intricate system of injection and production wells, engineered to stimulate fluid circulation and efficient heat extraction. Notably, hydraulic fracturing, in conjunction with hydroshearing, stands out as a key technology facilitating the establishment of stable and efficient flow paths for geothermal energy extraction (Hanano, 2004; Tangirala et al., 2023). Recent endeavors have underscored the feasibility of creating fluid-conducting fractures in both sedimentary and crystalline rock formations even at exceptionally high temperatures (>374 °C), setting the stage for the emergence of Enhanced Supercritical Geothermal Systems (Parisio et al., 2019).

However, the deployment of EGS faces challenges stemming from inadequate reservoir rock permeability and the potential for excessive induced seismicity during reservoir stimulation or operation. Subsurface fluid injection or extraction alters several crucial parameters of geological formations, including pore pressure, temperature, stress, and geochemical composition, often resulting in the destabilization of fractures and faults and subsequent seismic events. The connection between injection processes and induced seismic activity remains a subject of intense scientific inquiry, primarily due to the associated risks and uncertainties. Mismanagement of induced seismicity can yield widespread damage to surface structures, eliciting warranted criticism from regulatory bodies and the general public. Notably, induced earthquakes have led to the discontinuation of several geothermal projects, exemplified by instances such as Basel, in Switzerland, Sankt Gallen, in Switzerland, and Pohang, in Korea Republic (Grigoli et al., 2017) (Figure 1.2). Consequently, the anticipation and mitigation of potentially damaging induced seismicity, emerge as pivotal considerations in the successful execution of fluid injection projects, underscoring the necessity for an improved understanding of injection-induced fault stability and risk management strategies (Vilarrasa et al., 2017a).

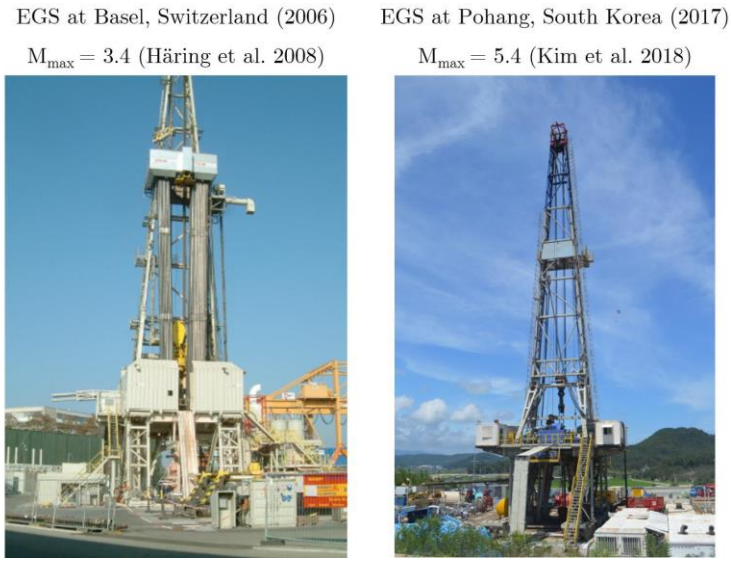

Figure 1.2 EGS may trigger unexpected induced seismic activity. If felt, induced seismicity has a negative effect on public perception and may jeopardize geoenergy infrastructure. It is necessary to reverse the damage that these incidents caused to public perception, since without geoenergy technologies, climate neutrality could be hardly reached.

Forecasting injection-induced seismic events presents a big challenge, demanding a comprehensive approach that integrates field-scale experiments and numerical simulations, thereby accounting for the pertinent physical processes. Addressing the

knowledge gap spanning laboratory and reservoir scales is achievable through the implementation of controllable meso-scale in situ experiments (Amann et al., 2018a). Several underground research infrastructures, either repurposed from existing mines and tunnels or newly excavated (e.g., Äspö HRL, Sweden; Grimsel, Switzerland; Jinping, China, Kamaishi, Japan; KURT, South Korea; Mont Terri, Switzerland; Reiche Zeche, Germany) have been established for this purpose. The exposure of the subsurface environment facilitates direct access to deep-seated rock masses, enabling sophisticated multi-disciplinary characterization, instrumentation, and experimentation at elevated spatial resolutions and controllable scales that would otherwise be unattainable from the surface or through downhole instruments. Tailored to site-specific conditions, these infrastructures offer rock volumes ranging from decameters to hectometers, catering to diverse experimental objectives and providing desired levels of heterogeneity and complexity. As part of an effort to step up the scale towards hectometer rock masses, the Bedretto Lab for Geosciences and Geoenergies (BULGG) was established in 2018. It is located inside the Bedretto tunnel in the Canton of Ticino, Switzerland (Figure 1.3). The purpose of the BULG is to host reduced scale in-situ experiments in crystalline rocks, with focus on drilling and completion, hydraulic stimulation, monitoring and seismic risk mitigation during the construction of an EGS.

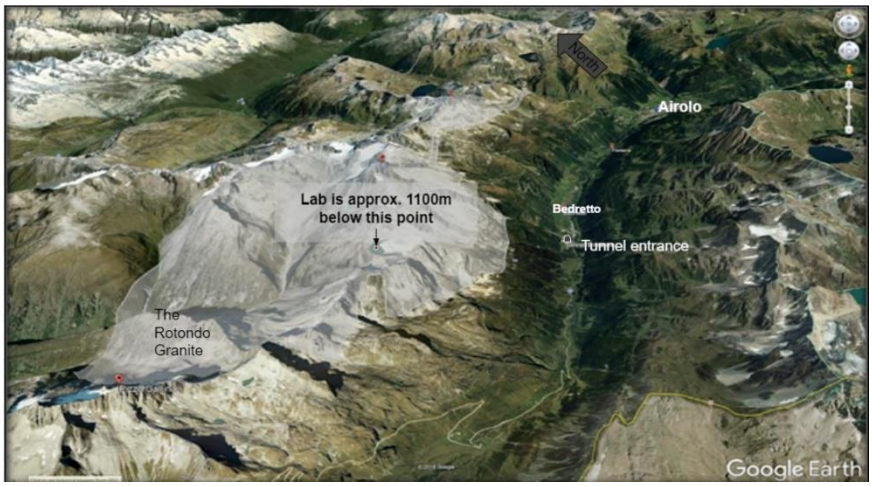

Figure 1.3 Oblique view of the Rotondo Granite in the Gotthard Massif and approximate location of BedrettoLab.

In the case of injection-induced seismicity, the prevailing triggering mechanism is conventionally ascribed to downhole overpressure, inducing a reduction in effective stresses and consequent diminution of frictional resistance (Hubbert and Rubey, 1959; Pearson, 1981; Raleigh et al., 1976). However, the intricate interplay of HM coupling

introduces a layer of complexity to this behavior. The variation in pressure instigates modifications in the stress field and deformation of the reservoir, thereby influencing the ensuing pressure response (Rutqvist and Stephansson, 2003). To unravel these intricacies, mathematical modeling and numerical simulations are imperative. The crux of the challenge lies in the necessity for a proficient numerical model that accurately captures both the rock matrix and fractures, faithfully reproducing the HM response of the system for the precise prediction of induced seismicity. On the one hand, common approaches involve utilizing continuum models, encapsulating fractures as effective properties within the rock matrix. However, fractures, being dynamic entities, not only impose static constraints influencing fluid flow but also undergo evolutionary changes that alter the stress field. On the other hand, discontinuum approaches, historically neglectful of mechanics until recent advancements, present computational challenges due to their potential costliness. Therefore, the development of a numerical model that reconciles lesser computational cost and accuracy in representing both rock matrix and evolving fractures is indispensable for understanding induced seismicity.

Incorporating fractures into numerical simulations introduces several challenges, including the representation of fractures with substantial aspect ratios, numerical difficulties arising from micrometer-scale apertures juxtaposed with fractures spanning hundreds of meters (Berkowitz, 2002; Singhal and Gupta, 2010). Furthermore, fractures exhibit distinct properties and physical processes in contrast to the surrounding rock matrix, with significantly higher permeability and a pivotal role in inducing rock deformation (Guglielmi et al., 2015a; Hubbert and Rubey, 1959). The non-linear coupled multi-physics problems inherent to fractured porous media further compound the challenges.

Due to the reasons mentioned above, developing new conceptual models and numerical schemes for fractured rocks can be a tremendous task. Despite the efforts already given to fractured rocks, the development of reliable numerical methods and simulation tools validated against field-scale experimental data for fractured rocks remains a formidable challenge. This thesis tackles parts of these challenges by considering a progressive approach. Since largest earthquakes have been induced in crystalline rocks, like in EGS, we focus on modeling fractures within a very low-permeability matrix and we try to respond to these research questions:

- What are the modeling methodologies of coupled processes in fractured rock and their respective strengths and weaknesses in terms of their modeling capabilities, computational precision and costs?
- How is the hydraulic behavior of a fracture embedded in a low-permeability matrix in response to fluid injection?
- How is elastic poromechanical behavior, considering both constant permeability and aperture-dependent variable permeability?
- What are the mechanisms that may induce microseismicity during fracture stimulation?

We define the objectives of the thesis to find answers to these questions.

1.2 Thesis objectives

The aim of this Thesis is to investigate the processes that take place during the stimulation of EGS and that may induce seismicity. We aim at deepening the understanding of the involved hydro-mechanical (HM) processes, to explain and manage co-injection seismicity. To reach this goal, it is necessary to understand the coupled behavior of fractured rock masses. Several research questions linking induced seismicity to the HM response of the pre-existing fractures remain open. Our goal is to understand the poromechanical processes that occur within the stimulated fracture and its surrounding. Shedding light on the fundamental processes will allow us to reach the following specific objectives (SO):

- SO1: To carry out an extensive literature review on modeling of coupled processes in fractured rocks with focus on the various fracture representation approaches;
- SO2: To seek an approach to model fractures following continuum approaches as in, e.g., the finite element software CODE_BRIGHT, and to find equivalent properties to overcome the limiting effect of the extreme width-to-length ratio of fractures;
- SO3: To interpret flow tests in fractures, focusing on how the transmissivity and the storage coefficient should be estimated using the theory of hydrogeology;
- SO4: To investigate hydro-shearing and permeability enhancement of fractured rock at the Bedretto Underground Laboratory, Switzerland, and interpret field-scale data.

1.3 Thesis outline

Beyond the introductory and concluding chapters, the thesis is structured into 4 distinct chapters, each corresponding to articles currently (or soon) undergoing peer review for prospective publication. Each chapter is self-contained, commencing with its own introduction and culminating with a concluding section. Thus, the subsequent sections of the thesis follow the outlined structure as delineated below:

Chapter 2 provides an overview of diverse modeling approaches concerning coupled processes in fractured rock formations. Its primary objective is to offer a comprehensive and integrated perspective on modeling methodologies, focusing on broader methodological categories rather than specific numerical techniques. The chapter highlights the strengths and weaknesses of these methods in terms of their modeling capabilities, computational precision, and associated computational costs. Additionally, it aims to enhance the reader's understanding of the various coupling schemes used in reservoir geomechanics, heat transfer, and fluid flow within fractured rock formations. The chapter contributes to give a holistic view of fundamental theoretical frameworks and modeling paradigms, while also emphasizing strategies for addressing current challenges and recent advancements in this field. Based on this extensive literature review an article titled '*A review on thermo-hydro-mechanical modeling of coupled processes in fractured rocks: A continuum to discontinuum perspective*' has been developed and will be submitted to an international scientific journal.

Chapter 3 presents the investigation of the flow regimes induced by constant flow rate water injection into a fracture surrounded by low-permeability matrix. The analysis of the pressure evolution reveals that leakage into the low-permeability rock matrix impacts fluid flow. Having analyzed the hydraulic response, implications of the leaky nature of fractures in hydraulic-test interpretation and modeling subsurface applications, the origin of the leaky nature of fractures, and the role of fracture size are discussed. This chapter resulted in an article, titled '*On the leaky nature of fractures in low-permeability rock*', which is currently under review in an international scientific journal.

Chapter 4 introduces an approach for the implicit representation of fractures surrounded by low-permeability rock matrix to accurately simulate HM coupled processes. The approach assimilates fractures as equivalent continua with a manageable scale (>>1 µm) that facilitates spatial discretization, even for large-scale models including multiple fractures. The approach has been validated through modeling a hydraulic stimulation carried out at the Bedretto Underground Laboratory in Switzerland by comparing numerical results against measured data. The contents of this chapter have been included in a manuscript, titled '*Implicit hydromechanical upscaling of fractures using a continuum approach*', and is under review in an international scientific journal.

Chapter 5 describes modeling of a highly-monitored test performed at the Bedretto Underground Laboratory to investigate the impact of fluid injection on permeability enhancement and induced microseismicity. It examines three models: (1) a homogeneous fracture whose transmissivity is manually calibrated to reproduce the observed pressure evolution at the injection borehole; (2) an elastic fracture approach, where transmissivity changes locally as a function of fracture aperture following the cubic law; and (3) a viscoplastic fracture approach with strain weakening and dilatancy that yields an additional permeability enhancement after shear reactivation. This Chapter has resulted in an article, titled '*Numerical modeling of hydraulic stimulation of fractured crystalline rock at the Bedretto Underground Laboratory for Geosciences and Geoenergies*', which is currently under review in a scientific journal.

Chapter 6 summarize the most relevant outcomes of the thesis.

2

A review on thermo-hydro-mechanical modeling of coupled processes in fractured rocks

2.1 Introduction

Fractured rock masses encompass multiple discontinuities across various length scales, ranging from pores and microfractures to joints and faults. These inherent discontinuities alter the properties of crustal rocks, making them anisotropic, inhomogeneous, and nonlinear materials (Katsuki et al., 2019; Wang et al., 2021; Zhao et al., 2021). The amalgamation of these geological features and the multitude of physical processes occurring during various engineering applications present grand challenges for modeling studies. Despite the substantial advancements in computational resources in recent years, including an explicit description of all the micro-, meso- and macro-scale features in a porous medium remains unfeasible. Thus, addressing these complexities requires simplifying assumptions in the modeling approach. A common assumption in continuum models is to consider the averaged characteristics of the microscale features without the need of representing the actual pore and micro-crack structure. The focus lies on determining the upscaled behavior of the medium, which becomes the primary quantity of interest in these modeling approaches. Nevertheless, both microscopic and macroscopic models are important and a holistic approach may consider both modeling approaches (e.g., hierarchical or multiscale modeling) to draw a more comprehensive understanding of the system.

The interplay among the processes of fluid flow, heat transfer, and stress/deformation in fractured rocks has received considerable attention in the fields of rock mechanics,

geophysics, and geological/geotechnical engineering since the early 1980s (Birkholzer et al., 2019; Jing, 2003; Tsang, 1991, 1987). This interplay is typically called coupled thermo-hydro-mechanical (THM) processes to highlight that one process influences the initiation and progression of another. THM processes are particularly complex in fractured media because of the marked heterogeneity of properties and this is central across various applications encompassing both natural and engineered systems, such as geothermal energy exploitation, groundwater management, subsurface energy and waste storage, underground construction, nuclear waste disposal, and contaminant transport analysis. Even though the relative significance of distinct physical processes may vary among these applications, they can be conceptualized as a confluence of fluid flow, heat transfer, and deformation transpiring within both the porous rock matrix and fractures. Depending on the specific application, a subset of these processes may suffice, while others might necessitate the consideration of chemical and biosphere elements as well as seismic coupling; however, we limit our focus to THM coupled models in this review.

Substantial research endeavors have been dedicated to the development of various numerical modeling approaches and techniques in response to the escalating demand for harnessing natural subsurface resources and addressing concerns pertaining to subsurface contamination (Berkowitz, 2002; Kazemi, 1969; Pruess and Narasimhan, 1985; Rutqvist et al., 2002; Tsang, 1999, 1991; Warren and Root, 1963; Wu and Pruess, 1988). Over the past few decades, several mathematical modeling approaches have been developed (see section 2.3) entailing the formulation of conceptual fracture models that incorporate geometric information of the fracture-matrix system. These approaches involve the establishment of mass and energy conservation equations for fracture-matrix domains, which are subsequently solved through discrete nonlinear algebraic equations. These numerical solutions account for the coupling of fluid flow with other relevant physical processes. However, a critical challenge encountered in simulating coupled processes in fractured rock lies in effectively addressing the complex interaction between fractures and the surrounding matrix under diverse conditions. This fracture-matrix interaction significantly distinguishes the flow through fractured porous media from that observed in homogeneous or heterogeneous single-porosity porous media.

This chapter aims at offering a comprehensive and integrated perspective on modeling methodologies of coupled processes in fractured rock, refraining from an exhaustive exposition of specific numerical techniques. Instead, it delineates broader categories of methods, elucidating their respective strengths and weaknesses in terms of their modeling

capabilities, computational precision and costs. Furthermore, this chapter seeks to furnish a thorough comprehension of the various coupling schemes employed in the context of reservoir geomechanics, heat transfer, and fluid flow within fractured rock. Particularly directed towards researchers who are newcomers to the field of modeling THM coupled processes within fractured rock, this chapter endeavors to impart fundamental theoretical frameworks and modeling paradigms, while also accentuating the strategies for addressing prevailing challenges and recent advancements within this field. We elucidate the theoretical concepts of coupled processes in Section 2.2, delving into an exploration of the multifaceted aspects of coupling mechanisms. In Section 2.3, we conduct a critical review of the conceptual models employed for representing fractured rock formations. Subsequently, Section 2.4 presents formulation foundation and governing equations for THM modeling. Lastly, the conclusions section of the chapter discerns extant research gaps and delineates prospective directions for future research endeavors.

2.2 Coupled processes in fractured rock

2.2.1 Multiphysical couplings

Both fluid pressure and temperature changes cause stress and strain variations, inducing porosity, fracture aperture and intrinsic permeability changes, which in turn impact the pressure and temperature fields. The temperature distribution and evolution depend on how fluids flow through the fractures and matrix blocks, which in turn is controlled by temperature because of the dependency of fluid density and viscosity on pressure, and especially on temperature. Figure 1.1 illustrates the couplings among mechanical, hydraulic, and thermal processes.

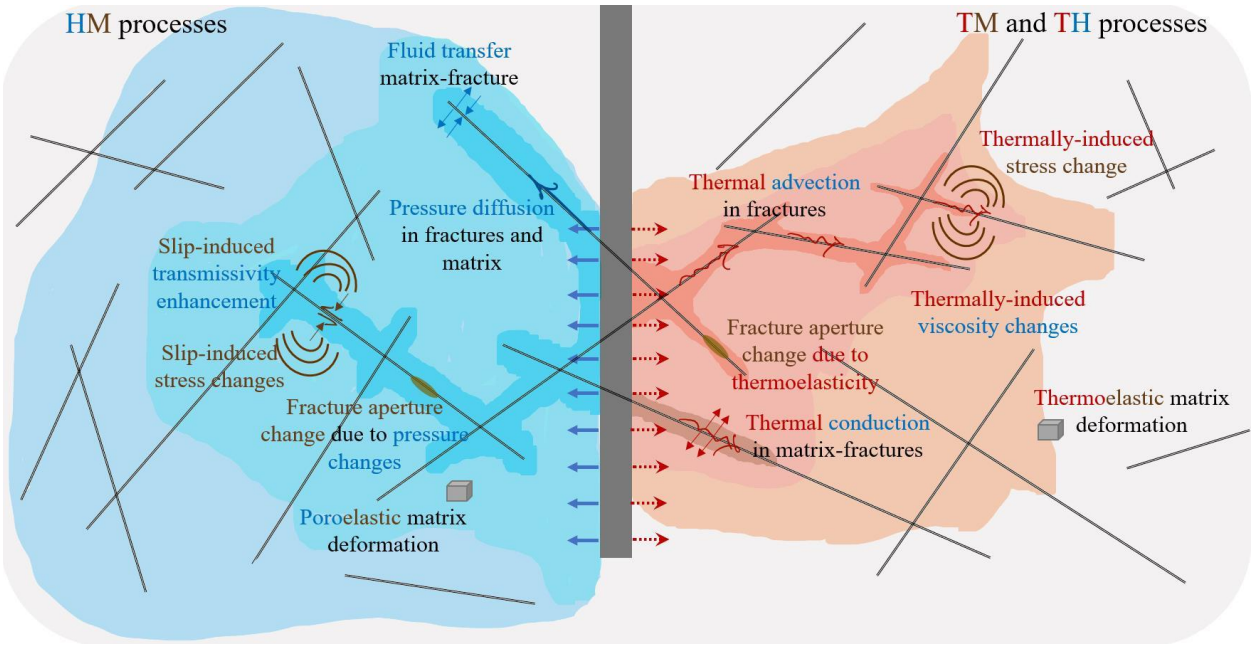

Figure 2.1 Schematic representation of coupled hydro-mechanical (HM), thermo-mechanical (TM) and thermo-hydrological (TH) processes prevailing in the stimulated zone around an injection well. For the sake of simplicity, HM and TM and TH couplings are illustrated separately on either side of the injection well and not superimposed.

2.2.1.1 Thermo-mechanical coupling

Two key mechanisms are responsible for the coupling between thermal and mechanical processes (Figure 2.1). The first mechanism is thermal expansion, which refers to the change in the volume of a material in response to a temperature change. The induced strain is proportional to the temperature change and the thermal expansion coefficient of the solid material,

$$\Delta\varepsilon^T = \alpha_s^T \Delta T, \tag{2.1}$$

where $\Delta\varepsilon^T$ is the strain change, α_s^T is the thermal expansion coefficient of the solid material and ΔT is the temperature change. This mechanism (expansion/contraction of rock) affects adjacent fractures, whose aperture could decrease/increase (McDermott et al., 2006). Temperature changes induce porosity changes, which are controlled by both the volumetric deformation and the variations in solid density (Vilarrasa et al., 2014). This change in pore volume induces pressure changes that may become significant in tight rock (Vilarrasa et al., 2021), affecting the distribution of pore pressure and, therefore, affecting the mechanical problem in terms of effective stresses. Additionally, constraints to deformations and/or differential thermal deformations generate thermal stress that may

result in the creation of new cracks and in the activation/reactivation of pre-existing fractures (Zhou et al., 2010). In particular, cooling-induced thermal stress reduction may eventually induce seismicity (Jeanne et al., 2014; Kivi et al., 2022; Parisio et al., 2019).

The second mechanism responsible for coupling between the mechanical and thermal fields only impacts the fractures, i.e., thermally-induced aperture change (Cooper and Simmons, 1977). The opening or closing of fractures will alter the volume of fluid filling them in a saturated medium, leading to variations in the heat storage capacity, which is dependent on the fluid volume filling the discontinuities. Additionally, fracture transmissivity for flow is also impacted by the variation of fracture aperture, according to the cubic law (Witherspoon et al., 1980; Zimmerman and Bodvarsson, 1996). This mechanism has minor impacts on the matrix.

2.2.1.2 Hydro-thermal coupling

Two primary mechanisms contribute to the coupling between the hydraulic and thermal fields (Figure 2.1). The first mechanism stems from the variation of the fluid viscosity and density as a result of temperature changes, which result in variations in the fluid volume (because of density changes) and transmissivity (because of both density and viscosity variations) and, thus, modify the pressure distribution in the hydraulic field. Both density and viscosity decrease with increasing temperature (Huber et al., 2009). The changes in transmissivity also modify the fluid velocity field (Darcy velocities), which in turn modify the heat transport driven by fluid movement (advection) causing alterations in the temperature distribution (Nield and Bejan, 2017). Advection primarily impacts the temperature in fractures, as they serve as preferential pathways for fluid flow, enabling heat to be transported along them at higher velocity than through the porous medium. Nonetheless, the thermal front advances much behind the pressure perturbation front as the thermal diffusivity is typically two to three orders of magnitude lower than the hydraulic diffusivity (De Simone et al., 2017).

As the second mechanism, the temperature variation affects the fluid occupying the pores or fractures, leading to volume changes proportional to its coefficient of thermal expansion α_f^T. This change in fluid volume modifies the pressure distribution in the hydraulic field and, subsequently, the effective stresses in the mechanical field. However, it is important to note that thermal expansion of fluid primarily affects the hydraulic field.

2.2.1.3 Hydro-mechanical coupling

The hydro-mechanical interaction is a well-established concept in the field of geomechanics, with seminal contributions from (Terzaghi, 1925) and (Biot, 1941) for consolidation analysis. For saturated geomaterials, the fluid occupies both the pores and discontinuities of the fractured porous medium, leading to a reciprocal influence between the pressures (hydraulic problem) and the deformations (mechanical problem). The effective stress principle captures this mutual interaction, where the pressure affects the effective stress, causing deformation of both the porous rock matrix and fractures, and this deformation (matrix porosity and fracture aperture changes), in turn, affects storativity of the matrix and fractures and intrinsic permeability of the matrix and longitudinal conductivity of fractures (Figure 2.2). These changes in the hydraulic properties of the fractured media, in turn, affect the flow and pressure fields (De Simone and Carrera, 2017; Verruijt, 1969).

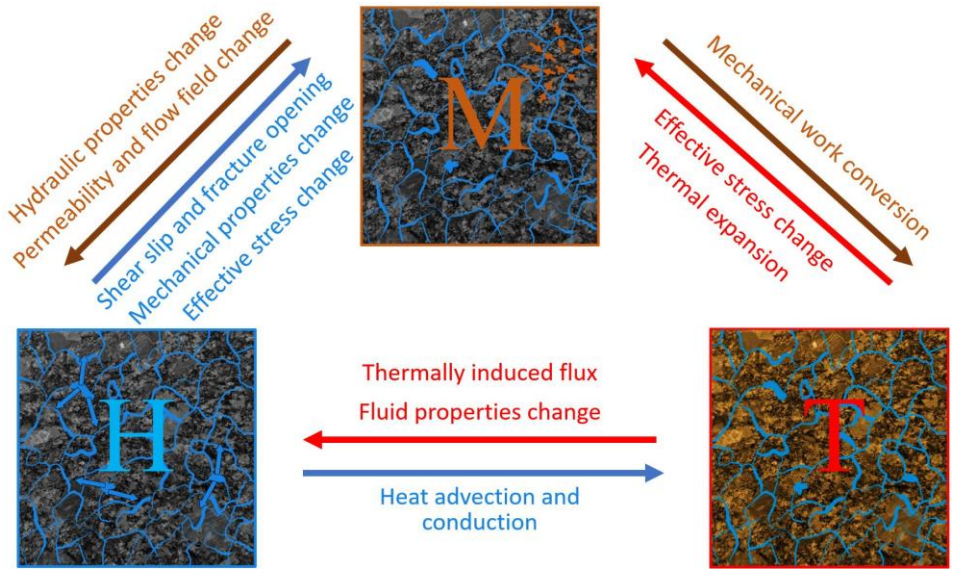

Figure 2.2 Thermo-hydro-mechanical couplings in fractured rocks.

Another marked effect is the variation of total stresses when porous deformation is restraint due to the existence of lateral constraints (e.g., inclusions, closed or compartmentalized reservoirs), or when the deformations are differential due to the existence of preferential flow paths (e.g., fault zones, high-transmissivity formations) (Rudnicki, 2011; Soltanzadeh and Hawkes, 2009). This poroelastic effect implies a non-trivial and often non-isotropic variation of the effective stress with direct consequences on deformations and failure (De Simone et al., 2017; Wu et al., 2021). In particular, the total

stress changes along the longitudinal direction of fractures as a result of pressure changes, while the total stress in the transversal direction to the fracture experiences minimal total stress changes (Zareidarmiyan et al., 2018). Overall, fractured porous media entail a number of couplings between the hydraulic, thermal and mechanical fields that should be considered in numerical models in order to reproduce the phenomena (Figure 2.2).

2.2.2 Numerical coupling techniques

2.2.2.1 Fully coupled scheme

The fully coupled approach, also called monolithic, solves all the governing equations simultaneously, i.e., the hydraulic, mechanical, and thermal equations are solved at the same time at every time step. The solution is reliable and can be used as a benchmark for other coupling approaches. This method enjoys excellent stability properties and preserves first-order convergence of non-linear iterations, but it is computationally expensive and the code development may be harder compared to other methods (Dean et al., 2006; Phillips and Wheeler, 2007; Settari and Walters, 2001). Several simulators and codes use this type of coupling: DYNAFLOW (Prevost, 1993), CODE_BRIGHT (Olivella et al., 1996), KRATOS (Dadvand et al., 2010), DuMux (Flemisch et al., 2011), COMSOL Multiphysics, UDEC/3DEC (ITASCA), MOOSE (Gaston et al., 2009), OpenGeoSys (Wang and Kolditz, 2007), Irazu (Mahabadi et al., 2016), GEOS (Castelletto et al., 2019), PorePy (Keilegavlen et al., 2021a), and ResFrac (McClure et al., 2022).

2.2.2.2 Iteratively coupled scheme

This method, also called two-way coupling, uses a sequential approach, i.e., it first solves one problem (equation), whose solution then feeds the other governing equation(s) (Figure 2.3a). The results are then sent back to the first equation. These steps may be repeated in an iterative way. Therefore, several iterations might be necessary for each time step until all the equations reach convergence and provide the same solution as that of the fully coupled approach (Almani et al., 2023, 2016; Castelletto et al., 2015; Kim et al., 2011; Preisig and Prévost, 2011). The number of iterations may be large, such that the calculation time is similar to the fully coupled method. The advantage of this staggered treatment is that it allows coupling different simulators to solve each problem with the most appropriate one (Rutqvist, 2017). In addition, diverse domains for flow and mechanics can be used, reducing the computational time due to the fact that a small domain for flow can be chosen (Tran et al., 2005). Simulators using this type of coupling include TOUGH2-FLAC3D (Rutqvist et al., 2002), Stanford's General Purpose Research

Simulator (GPRS) coupled with PyLith (Jha and Juanes, 2014), COMSOL Multiphysics, STARS (Bissell et al., 2011; CMG, 2003), VISAGE coupled iteratively with ECLIPSE (Ouellet et al., 2011; Stacey and Williams, 2017), and DYNAFLOW.

2.2.2.3 Explicitly coupled scheme

This method, also called one-way coupling, only transmits information unidirectionally within each time step, typically from the thermo-hydraulic problem to the mechanical one. This implies that pressure and temperature affect the effective stress field, causing deformation, but deformation does not change the hydraulic properties. This approach neglects to verify convergence following the solution of the ultimate equation. Accordingly, the method assumes that the outcome of the solution is accurate and proceeds to solve the next time step (Zienkiewicz et al., 1988). Examples of this type of coupling can be found in simulators like TOUGH2-FLAC3D, STARS, and DYNAFLOW, which allow selecting the coupling method. This is a straightforward technique, but the stability and the accuracy may be compromised if the time step is not adequately chosen (Preisig and Prévost, 2011).

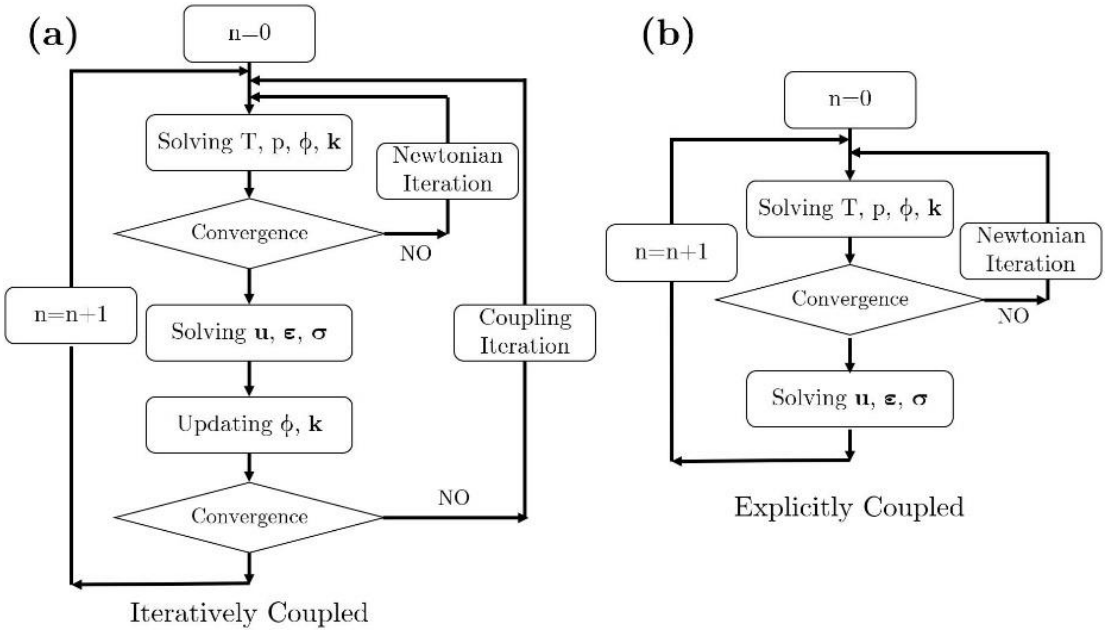

Figure 2.3 Flowcharts of (a) iteratively and (b) explicitly coupled approaches

2.2.2.4 Loosely coupled

The method is similar to the explicit coupling, but the solutions of the flow and energy equations are only transferred to the mechanical equation after a number of time steps.

The method is, therefore, computationally efficient but the intervals of coupling update have to be chosen in a reliable way (Gai et al., 2005). The VISAGE-FRONTSIM and the STOMP-ABACUS (Nguyen et al., 2016) simulators use this kind of coupling.

2.3 Representation approaches of fractured porous media

Fractures in rock formations, whether naturally occurring or induced through thermal or hydraulic means, represent separations or openings within geological structures that create discrete zones within the rock. The fundamental objective of characterizing fractures in reservoirs is to gain insight into the intricate behavior of heat, fluid flow, and transport within fractured rocks, as well as to quantitatively assess the impact of fracture-matrix interaction on the overall flow patterns. A fracture can be defined as a narrow, deformable, high-permeability (compared to the rock matrix), and heterogeneous three-dimensional zone, akin to a special porous medium sheet, surrounded by a stiff and low-permeability, yet permeable, rock matrix. Fractures typically exhibit small apertures, supported by fillings or contacts, a consequence of the considerable in situ stress exerted on the rock matrix in deep reservoir formations. Hydraulic fractures, on the other hand, necessitate the support of proppants or sands to remain open and facilitate fluid flow.

Conceptualizing fractures as a distinctive porous medium naturally leads to the application of Darcy's law to quantify flow through fractures within reservoirs. This approach has been widely utilized in the literature and practical field applications for analyzing flow behavior in fractured porous media. However, it is essential to acknowledge that flow in fractured porous media entails greater complexity than that in purely porous media. The behavior of fracture flow is contingent upon the interplay with the surrounding matrix, and it is influenced by both the flow within the matrix and the spatial distribution and geometry of fractures and matrix components within the formation. Given the inherent uncertainties concerning in situ fractures' characteristics, including geometric properties and spatial distributions, various simple or simplified conceptual models and scenarios have been proposed, developed, and employed to approximate or characterize the intricate flow behavior in fractured porous media. These models enable the calculation of fracture flow while considering the vital aspect of fracture-matrix interaction. This section presents a comprehensive overview of the commonly used conceptual models utilized for simulating coupled processes in fractured rocks.

There is not one model as a panacea and several approaches have been developed to adequately represent the mechanical, thermal, and hydraulic behavior of fractures.

Traditionally, these methods have been generally classified into three main categories: continuum, discontinuum (discrete), and hybrid methods including a system of underlying methods carrying inherent advantages and disadvantages depending on the problem of interest (Berre et al., 2019; Lei et al., 2017; National Academies of Sciences, 2015; Viswanathan et al., 2022). It should be noted that the nomenclature adopted in the literature is often confusing. For instance, the term "discrete" is sometimes used to describe a continuum model with a singular representation of a fracture, and sometimes used to distinguish models with respect to fulfilling displacement compatibility between internal elements. Here, we adopt a classification based on the fracture representation.

2.3.1 Continuum approaches

The process of converting discrete fractures into a continuum representation, commonly referred to as upscaling, plays a significant role in constructing various continuum models that are specific to the type of fracture system being investigated. The choice of the upscaling approach is contingent upon the particular characteristics of the fractured medium and may involve the use of different techniques (Berkowitz, 2002; Berre et al., 2019; Flemisch et al., 2018; Renard and Ababou, 2022; Sævik et al., 2013; Wong et al., 2020). These methods present an evident preference in scenarios in which a continuum representation offers a more suitable approximation, such as when computational efficiency is of paramount importance, the fracture network exhibits a dense topology, and quantities of interest are averaged over extended time scales (Viswanathan et al., 2022).

2.3.1.1 Equivalent porous medium (single continuum model)

In the case of a sparsely connected fracture network, this modeling approach employing a single continuum representation, namely equivalent porous medium (EPM) (or Equivalent Continuum Models (ECM)) proposed by Snow (1969), may be employed. This method considers the concept of a representative elementary volume (REV), introduced by Bear (1972) (Figure 2.4). A heterogeneous medium would be divided into several REVs, and an average set of parameters would be assigned to each of them. Therefore, there is not an explicit representation of fractures and fractures are upscaled in conjunction with the matrix (Huang et al., 2017; Jiang et al., 2013; Liu et al., 2019). The method is adequate to reproduce flow and transport along fractures, particularly in solving large-scale water-yield problems (Doolin and Mauldon, 2001; Esposito et al., 2007; Scanlon et al., 2003). However, this technique is not able to simulate the mechanical

behavior of fractures in a realistic way due to the fact that the jump in fracture displacements cannot be reproduced. The accuracy of this approach is still the topic of different investigations (Ma et al., 2023; Song et al., 2018; Zareidarmiyan et al., 2021).

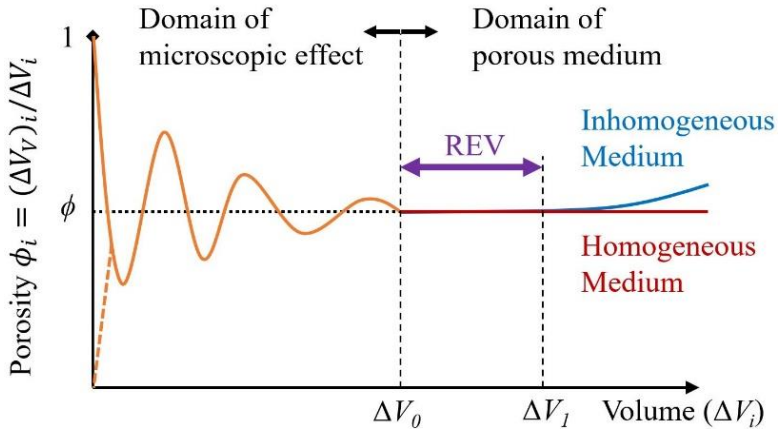

Figure 2.4 Definition of porosity and representative elementary volume, adapted from Bear (1972)

2.3.1.2 Stochastic/heterogeneous continuum medium

The term "stochastic" pertains to the utilization of probability and statistical methods to account for uncertainty associated with the properties of fractured media (Ostoja-Starzewski, 2002; Vanderborght et al., 2006). Rather than assuming a deterministic distribution of fractures, the concept of stochastic continuum medium (SCM) encompasses the consideration of variability and randomness in fracture properties (Le Guennec et al., 2014; Öhman and Niemi, 2003; Tsang et al., 1996). These properties can include fracture orientation, aperture (size), spacing, and permeability. SCM approaches, which are typically used for inverse modeling rather than forward modeling, facilitate the generation of spatially variable representations of upscaled effective properties, acknowledging stochastic characteristics originating from the underlying fracture network. Incorporating stochastic methods, such as geostatistics, Monte Carlo simulation, or random field theory, enables the creation of multiple realizations of the subsurface model that account for the statistical attributes of fractures within the matrix. These realizations capture various possible configurations of fractures, resulting in a diverse array of flow and transport scenarios. The utilization of the SCM method proves particularly advantageous in situations where pertinent information concerning specific fracture locations is limited. The adoption of the stochastic continuum approach obviates the necessity for extensive information pertaining to fracture geometry or assumptions concerning the dominant influence of individual fractures on flow and transport processes. Instead, the method

solely necessitates the delineation of a few dominant features, which can be effectively integrated into the stochastic continuum model as heterogeneous porous slabs (Ando et al., 2003; Neuman, 1988, 1987). In such cases, relying solely on a single realization of the random field may not accurately represent the intricacies of a particular field site. However, despite this limitation, the SCM method offers valuable insights by providing information regarding the anticipated ranges of bounding behavior.

2.3.1.3 Multi-continuum medium

2.3.1.3.1 Two-domain model (Dual-continuum model)

This concept encompasses two categories assuming either one (i.e., mobile–immobile model or double-porosity model) or two flow domains (i.e., mobile–mobile model or dual-permeability) (Figure 2.5). Reviews on two-domain models are given by (Gerke, 2006; Šimůnek et al., 2003). The idea of the double-porosity model (also known as mobile–immobile model (MIM)), introduced by (Barenblatt et al., 1960) and (Warren and Root, 1963), is based on the concept of dividing the porous medium into two distinct continua: a mobile region characterized by a high degree of connectivity between the pores and an immobile region characterized by a low degree of connectivity (Geiger et al., 2013; Yan et al., 2016; Zimmerman et al., 1993). Two distinct values of porosity are given for each system and flow is supposed to occur only through the fracture system while the matrix provides the storage capacity (Abushaikha and Gosselin, 2008; Chen and Teufel, 1997; Hosking et al., 2018; Xue et al., 2020; Zhao and Chen, 2006). This model treats matrix blocks as spatially distributed sinks or sources to the fracture system without accounting for global matrix–matrix flow. The interaction between both regions (fluid or heat exchange) is governed by the difference in pressures between the two systems in a "quasi-steady" manner (Gelet et al., 2012; Hosking et al., 2020). Building upon the double-porosity concept, some works have been carried out to explore the behavior of THM coupled processes in fractured media. Notably, (Bai and Roegiers, 1994) developed an early coupled THM constitutive model for double-porosity media, while (Masters et al., 2000) proposed a model assuming a single representative thermodynamics continuum encompassing heat conduction and convection. Conversely, (Zhang and Cui, 2011) devised a THM model that disregards the thermal impact on the hydraulic field. In contrast, (Khalili and Selvadurai, 2003) introduced a comprehensive, fully coupled THM constitutive model crafted systematically at a macroscopic scale. While predominantly grounded in the mechanics framework, some studies like (Gelet et al., 2012; K. Wang et al., 2023) contributed to a thermodynamics-based THM model.

Contrary to the double-porosity method, in dual-permeability models (mobile–mobile model), flow occurs not only in the fracture system but also within the matrix blocks and between them (Barenblatt et al., 1960; Dykhuizen, 1987; Moinfar et al., 2011; Šimůnek et al., 2003; Vogel et al., 2000). This modeling approach postulates the representation of the system as a composite of two overlapping interacting domains (Figure 2.5). One domain depicts an inter-aggregate fractured or meso-porous media, while the other domain represents an intra-aggregate meso-micro pore subsystem. The equations are solved simultaneously for both permeable and less permeable subsystems like porous media continuum models (Aguilar-López et al., 2020; Leij et al., 2012).

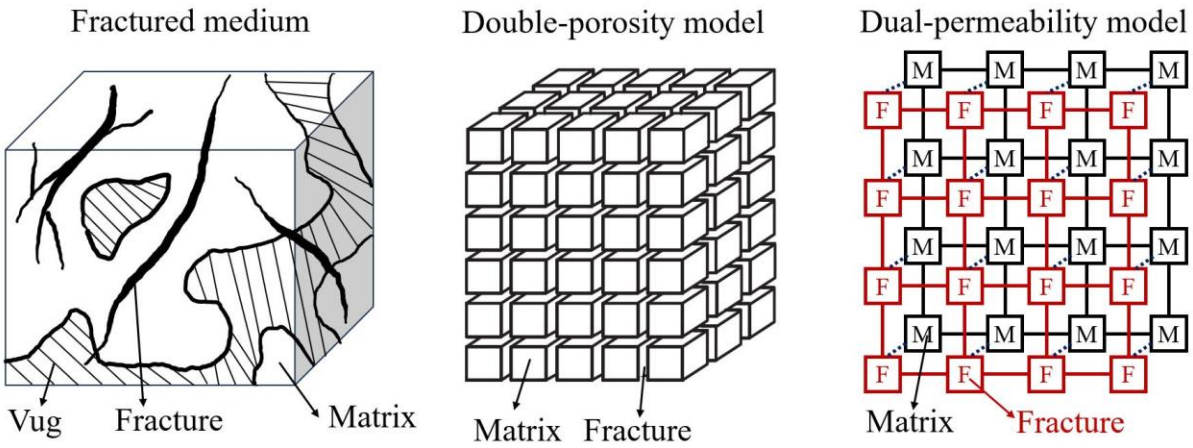

Figure 2.5 Schematic of dual-continuum models. In the double-porosity model, the flow domain of a naturally fractured medium is composed of low-permeability matrix blocks, embedded in a network of interconnected fractures. However, in the dual-permeability model, fractures and matrix are represented by separate grid blocks that are also connected to each other locally.

2.3.1.3.2 Triple-continuum model

In the dual-continuum approach, both the fracture and matrix systems are treated as locally uniform and homogeneous. An extension of the dual-continuum approach has been developed, known as the triple-continuum approach, to account for the influence of heterogeneity present in fractures or the rock matrix on flow within fractured porous media (Wang, 2005; Wu, 2016; Wu et al., 2004). This extended model encompasses rock matrix heterogeneity, the effect of small fractures, and fractured vuggy media (Abdassah and Ershaghi, 1986; Bai et al., 1993; Youssef and Alnuaim, 2017; Zhang et al., 2015). The utilization of triple-continuum models aims to address varying levels and scales of heterogeneity in the rock matrix or fractures. This is achieved by subdividing the rock matrix or fractures into two or more subdomains or continua, each characterized by distinct properties to represent the diverse flow behaviors within the fractured medium.

In the triple-continuum model, the fracture-matrix system is conceptualized as consisting of a single porous-medium rock matrix and two types of fractures: large globally connected fractures, and small fractures that are locally connected to both the large fractures and the rock matrix. In essence, the triple-continuum method extends the dual-permeability approach by introducing an additional connection through the small fractures, which further interacts with the large fractures and the matrix blocks.

2.3.1.3.3 Multiple INteracting Continua (MINC)

The Multiple INteracting Continua (MINC) is a generalization of the dual-continuum model in order to handle non-isothermal and multi-phase flow. MINC is rigorous for handling transient flow between fractures and the matrix. In this method, each matrix block is discretized in a nested way in order to be able to reproduce the gradients (pressures, temperatures, capillary forces, or concentrations) in the matrix (Figure 2.6). Moving from the boundary to the center of the matrix block, different matrix regions are crossed, which are functions of the distance from the fractures and allow for a transient exchange between fractures and matrix. This transient regime enables the simulation of multi-phase and non-isothermal flow, coupling between fluid and heat flow, and variable compressibility (Bedoya-Gonzalez et al., 2023; Tatomir et al., 2011; Wang et al., 2017, 2014). The method was initially introduced by Pruess (Pruess, 1983; Pruess and Narasimhan, 1985; Wu and Pruess, 1988) for cubic matrix blocks but can be extended to irregular grids. Although the suitability of this technique has to be analyzed case-by-case, it has become a popular method and it is used by several simulators like STARS, TOUGH2 (Pruess, 1992) or Dumu^{x} (Flemisch et al., 2011).

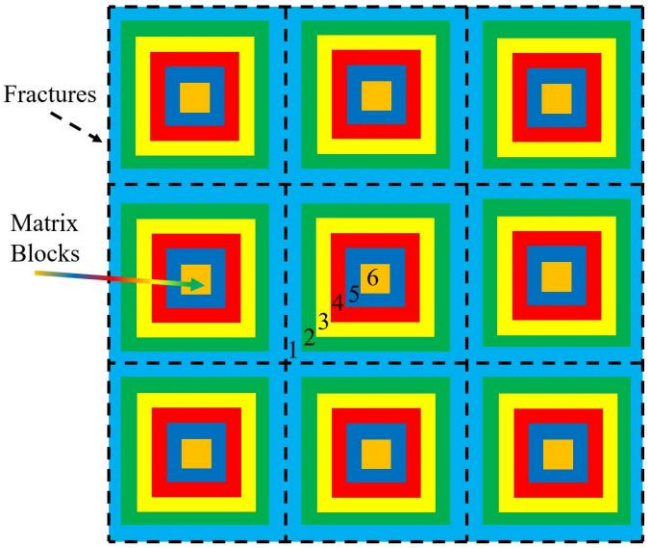

Figure 2.6 Computational mesh in the MINC approach

2.3.2 Discrete approaches

The explicit or discrete-fracture modeling approach is characterized by the inclusion of every individual fracture within the model domain, explicitly describing the flow through each fracture. This modeling approach represents a rigorous method in contrast to continuum approaches. However, its practical application in field-scale modeling studies presents significant challenges, stemming from demanding data requirements and computational intensity. The large number of fractures typically encountered in field simulations makes their comprehensive inclusion impractical. Additionally, this approach necessitates a detailed understanding of the geometric properties of fractures and the matrix, as well as their spatial distributions, which are rarely available for natural fractures at field sites. The complexity of the explicit modeling approach escalates when addressing multi-phase flow and thermal processes within intricate fracture-matrix systems observed in actual reservoirs. Consequently, the explicit-fracture modeling approach had limited utility in field-scale studies until approximately a decade ago. Nevertheless, recent advances have led to the increasing popularity and extensive adoption of the discrete-fracture model in various geo-engineering applications.

2.3.2.1 Channel/pipe network (C/PN)

This model explicates the fact that fracture distribution and aperture heterogeneity give rise to preferential pathways (Larsson et al., 2012; Tsang and Neretnieks, 1998; Tsang and Tsang, 1987), creating a network of interconnected channels or pipe elements, where

each channel or pipe represents an individual fracture or a set of fractures (Gylling et al., 1999; Khademi et al., 1999; Moreno and Neretnieks, 1993). These channels or pipes characterized by their hydraulic and mechanical properties are connected by nodes, which correspond to the intersections or junctions of fractures within the system (Tsang et al., 1988). It is conventionally assumed that these channels or pipes have a constant cross-sectional area and are often approximated as circular or rectangular in shape. While fluid flow and heat transfer equations are solved within these channels or pipes, the deformation and fracture propagation are modeled in the surrounding rock mass using continuum mechanics. To simulate fluid flow through a fractured medium using a channel/pipe network approach, the network is discretized into a set of equations describing the flow through each channel or pipe, as well as the flow through the connecting nodes. Subsequently, this system of equations is numerically solved to obtain the pressure and flow rate at each point in the network (Y. Chen et al., 2018; Fernández-Pato and García-Navarro, 2014). The flow equations in the C/PN model are locally one-dimensional and can be analytically solved in the Laplace domain, and in some cases, even in the time domain (Moreno and Neretnieks, 1993; Sharma et al., 2023). Additionally, transport in the channels (in-fracture advective transport) is modeled via particle tracking methods, while the interaction with the rock matrix (diffusion, absorption, etc.) can be included in the particle tracking formulation in the form of analytical solutions (Liu et al., 2018; Mahmoudzadeh et al., 2013; Neretnieks, 2006; Shahkarami et al., 2016), which obviates the need for numerical discretization of the domain and allows for a more direct focus on the network structure and connectivity to reproduce field data (Dessirier et al., 2018; Li et al., 2014). Some C/PN frameworks utilize full lattices of channels and stereological arguments to infer lattice spacing and flow-wetted surfaces from observations along borehole sections. These derived parameters are then employed to calculate flow and transport through the system. C/PN models have the advantage of being computationally efficient due to a significant reduction in the number of degrees of freedom in the solution matrix. They are relatively simple to set up and can handle large and complex fracture networks. They are also flexible, allowing for the inclusion of additional processes such as two-phase flow or geomechanical deformation (Dessirier et al., 2023; Junqi et al., 2022; Shahkarami et al., 2019). However, they are limited by their assumption of steady-state flow and their inability to capture spatial variations in permeability or other properties of the fractures. Diverse adaptations of C/PN models have garnered considerable attention for the representation of deep crystalline rock systems characterized by low overall hydraulic conductivity. Among these adaptations is the sparse channel network, featuring sparsely populated lattice networks. This configuration comprises a limited number of

elongated channels, which are notably spaced far apart, yet retaining the ability to interact at their intersections (Black et al., 2017; Black and Barker, 2018; Dessirier et al., 2018). Notably, it is pertinent to highlight that the conventional regular lattice arrangement is not a prerequisite for the utilization of the underlying analytical solutions governing channel flow and transport. For an in-depth review of the applications of sparse channel network models, interested readers are directed to the work by (Figueiredo et al., 2016).

2.3.2.2 Discrete fracture network (DFN)

The Discrete Fracture Network (DFN) is a method suitable for the modeling of flow and transport processes through a connected large-scale fracture network (Baisch et al., 2010; Bruel, 2007; Li et al., 2020; McClure and Horne, 2011). In this approach, the reservoir is treated as a combination of distinct, individual fractures and an impermeable rock matrix, and all fluid is assumed to reside within the fracture network (Figure 2.7). DFN models are especially suitable for porous media where the complete porosity and permeability can be attributed to fractures that can be explicitly represented. The model is also commonly employed as a means to model fractures in low-permeable porous media in a generalized context.

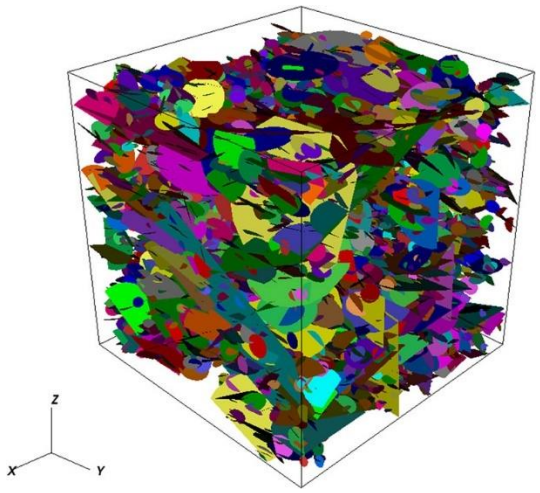

Figure 2.7 Stochastically generated Discrete Fracture Network (DFN) with 5033 fractures in a 109 m^3 domain. Each fracture is shown in a distinct color. DFN parameters represent the natural repository site Forsmark, Sweden (Makedonska et al., 2015).

DFN models exhibit an advantageous capability of effectively capturing the distinct effects of fractures, albeit at the cost of higher computational intensity compared to continuum models. Notably, this approach encounters challenges due to the inherent heterogeneous structure of fractured rock (de Dreuzy et al., 2012; Li et al., 2021),

particularly when dealing with the leaky nature of fractures in high-pressure injections and temporal scales that demand consideration of matrix diffusion. Moreover, the presence of fractures of varying sizes, locations, and orientations necessitates the explicit representation of a significant number of fractures, which inevitably impacts the computational efficiency of the model. Additionally, due to practical limitations, it becomes unfeasible to include all contributing fractures to the flow within the model, further introducing complexities and uncertainties (Fadakar Alghalandis, 2017; Jing and Stephansson, 2007a).

The main characteristics of DFN are the geometry of the fracture system and the transmissivity of the fractures. Nevertheless, these features are generally unknown, because of the lack of information. Hence, to overcome these problems, the fracture geometry is often stochastically generated based on the statistical distributions of fracture parameters which are assumed or inferred from borehole and outcrop observations (Afshari Moein et al., 2018; Bour et al., 2002; Darcel et al., 2003; Hyman et al., 2015; Lei and Wang, 2016; Ringel et al., 2022, 2019; Somogyvári et al., 2017; Xu and Dowd, 2010). Similar to CP/N models, advective transport through the system of connected fractures is usually solved via particle tracking, while diffusive exchange between the fluid in the fractures and the rock matrix is solved analytically (Cvetkovic et al., 1999; De Simone et al., 2023a; Hyman et al., 2019). Besides flow and transport, many conventional DFN models do not incorporate mechanical processes, because they mostly occur in the rock matrix which is not represented. Simplified formulations including the semi-analytical estimation of thermal rock deformation and consequent fracture aperture variation have been recently proposed, e.g., (De Simone et al., 2021). Some recent advances have been made to consider the effects of matrix in THM processes. For exmaple, DFN modeling has been employed to provide a hydro-mechanical characterization of anisotropic fractured rock masses (Davy et al., 2018; De Simone et al., 2023b; Gottron and Henk, 2021) and to simulate THMC properties/responses of fractured porous media (Lei et al., 2021, 2020; Lei and Gao, 2018), making this method to be not only applicable for densely but also sparsely fractured scenarios. Recently, (Hadgu et al., 2017) carried out a comparative study of DFN and ECM models for simulating flow and transport and their results showed that both methods can be used to model the far field of a nuclear waste repository in crystalline rock.

In contrast to the CP/N method, DFN models necessitate substantial computational resources to adequately discretize each fracture plane within the entire network system,

considering the potential incorporation of variable aperture and transmissivity across these fracture planes. It is important to highlight that contemporary advances in DFN modeling have sought to streamline complex fracture networks into configurations resembling channel networks through the application of graph theory and topological analysis (Berrone et al., 2020; Doolaeghe et al., 2020; Hyman et al., 2018; Osthus et al., 2020). (Lei et al., 2017) presented a discussion of the state-of-the-art on the use of DFN for modeling geometrical characteristics, geomechanical evolution, and hydromechanical behavior of fractured rocks.

2.3.2.3 Discrete fracture-matrix (DFM)

The Discrete Fracture-Matrix (DFM) method aims to resolve the trade-off between reduced precision resulting from upscaling of fractures and increased geometric complexity from representing fractures explicitly (Bogdanov et al., 2003; Matthäi et al., 2007; Matthäi and Belayneh, 2004; Monteagudo and Firoozabadi, 2004; Mourzenko et al., 2004; Noorishad and Mehran, 1982; Painter et al., 2002). By localizing the fluid within explicitly represented fractures and the interstitial porous matrix, this approach allows for the assimilation of fractures with lengths significantly smaller than the domain size into the matrix domain, thereby contributing to secondary permeability without being explicitly characterized by the fracture network (Wang and Lei, 2021). Consequently, the DFM technique effectively handles fractures in permeable media that necessitate explicit representation due to their significant and dominant influence on processes. While the fundamental framework of DFM models for flow dates back several decades (first introduced by (Baca et al., 1984; Noorishad and Mehran, 1982)), their development for at-scale applications is relatively recent compared to other computational models discussed in the literature (Jiang and Younis, 2017; Nick and Matthäi, 2011).

DFM models allow for a thorough investigation of processes occurring at the interface between fractures and the rock, such as capillary pressures in two-phase flow (Aghili et al., 2019) and the hydro-mechanical interaction between flow and the host medium (Garipov et al., 2016). The resolution of this interface in DFM models offers a detailed representation of these processes. However, this formulation poses numerous challenges concerning computational geometry and mesh generation, as well as numerical schemes for THM processes. Multi-dimensional computational meshes (3D volumes and 2D fracture planes) are inherent to DFM models, necessitating the development of novel numerical methods and ensuring the preservation of conservation laws. Existing DFM models can be broadly categorized into two classes based on how they address the first

issue, which subsequently dictates their approach to the second issue. DFM models either employ a mesh representation of the matrix that aligns or coincides with the mesh of the fracture network, referred to as the conforming mesh method (Ahmed et al., 2017; Karimi-Fard et al., 2004), or they do not, known as the non-conforming mesh method (Berrone et al., 2017; Boon et al., 2018; Flemisch et al., 2016; Schwenck et al., 2015). Presently, most DFM models for THM coupled processes in fractured media are either 2D, quasi-2D, or limited to relatively simple 3D geometries, owing to the method's relative infancy and computational constraints (Aghili et al., 2019; Hægland et al., 2009; Jiang and Younis, 2015; Sandve et al., 2012). However, for flow modeling, recent studies have considered rather complex 3D geometries (Hyman et al., 2022; Keilegavlen et al., 2021b; Stefansson et al., 2021; Wang et al., 2022). (Berre et al., 2021) and (Flemisch et al., 2018) have presented benchmark cases and various numerical schemes currently in use for DFM models and investigated the capabilities of DFM methods in handling complexities common to fracture networks. A detailed review on DFM methods can be found in (Berre et al., 2019).

2.3.3 Hybrid approaches

In practice, the combination of continuum methods and discrete methods is being increasingly employed to represent fractured porous media. These methods, known as hybrid methods, involve various combinations of continuum and DFM approaches (Wong et al., 2020). Theoretically, all fractures within the whole system could be integrated into the fracture domain. However, due to computational complexity, the explicit representation of all fractures is not practical. This issue can be overcome by the combination of DFM models with continuum methods, which provides computational efficiency (Figure 2.8). Hybrid methods offer a flexible and effective approach for modeling flow and transport in permeable rocks, accommodating the advantages of both continuum and DFM methods.

The more complex the hybrid model is, the higher the accuracy as well as the computational cost. Thus, a trade-off between accuracy and computational time should be reached. In cases where fracture network properties exhibit heterogeneity across different zones, it may be necessary to apply distinct hybrid models in each zone to optimize computational efficiency. This shift towards hybrid models has been motivated by the observation that fractured reservoirs exhibit multiple length scales, leading to potential errors in upscaling on a grid cell basis. A full representation of the fracture network via DFM methods would ideally overcome such errors. However, due to

computational limitations, continuum methods must often be employed in conjunction with DFM methods.

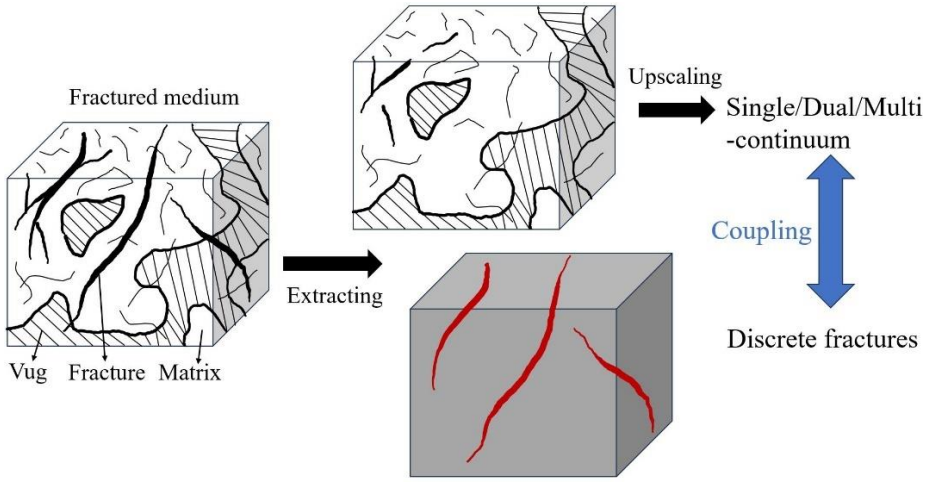

Figure 2.8 Schematic illustration of the hybrid modeling approach where large-scale fractures are modeled by a DFM model and a continuum approach is used to capture the dense small-scale fractures and vugs.

2.3.3.1 Single-porosity hybrid model

This model utilizes a single continuum to represent the matrix and small-scale fractures, known as the pseudo-matrix, while explicitly accounting for larger fractures (Arbogast, 1992; Lee et al., 2001; Li and Lee, 2008; Rogers et al., 2007; Siripatrachai et al., 2016). Consequently, it can be viewed as a streamlined version of the more complex DFM model, offering a reduction in model complexity without compromising the accuracy. Within the larger framework of hybrid models, the single-porosity hybrid model is recognized as the most straightforward hybrid model available.

The advantages of this method include its ability to capture the effects of both advection and diffusion in the porous medium, and its ability to accurately predict transport behavior for a wide range of flow and transport conditions. Additionally, the model is relatively easy to implement and computationally efficient. One major limitation is that it assumes a constant immobile porosity, which may not be accurate in all cases. Additionally, the model does not account for the effects of spatial heterogeneity, which can significantly impact transport behavior in porous media. Finally, the model may not accurately capture transport behavior in cases where the immobile phase plays a significant role in transport, such as in some multi-phase flow systems.

2.3.3.2 Challenges in hybrid models

The emergence of hybrid methods represents a promising development in the field of geomechanics, flow, and transport modeling in fractured media. However, their implementation raises several questions regarding their construction. Notably, the issue of which fractures should be upscaled and which should be explicitly modeled is a significant concern. Furthermore, determining how many continua should be used to represent upscaled fractures and which continuum each fracture should belong to presents an additional challenge. The resolution of these questions may be zone-dependent, considering the possibility of spatial variations in fracture network properties within a reservoir. The determination of optimal hybrid method construction and implementation strategies represents a critical area for future research.

The process of determining which fractures to allocate to the fracture domain or matrix domain lacks a well-established methodology. Typically, the selection is made based on fracture lengths (Lee et al., 2001; Liu et al., 2021; Wang and Lei, 2021; Wong et al., 2020; Zhang et al., 2020). However, more advanced and application-specific selection criteria may be employed, such as fracture connectivity and the volume of host material, where fractures represent the main conduit for the global flow field. The method of upscaling representation may also be tailored to suit the specific application; while the traditional approach has been a single-continuum method, as detailed by (Karimi-Fard et al., 2004), multi-continuum approaches have also been applied, as demonstrated by (Jiang and Younis, 2017).

2.4 Theoretical formulations for modeling THM processes

2.4.1 Balance laws in the rock matrix

THM coupling models have been formulated based on two fundamental partial-coupling mechanisms firmly established in the framework of continuum mechanics. The first mechanism is the thermo-elasticity of solids describing the interaction between the stress/strain and temperature fields through thermal stress and thermal expansion. The second is poroelasticity theory accounting for the interplay between pore fluid effects and macroscopic deformation in porous media. These mechanisms are grounded in classical physical laws such as Hooke's law of elasticity, Darcy's law of flow in porous media, and Fourier's law of heat conduction. The derivation of the equations of poroelasticity and thermoelasticity couplings is given by (Coussy, 2004; Noorishad and Tsang, 1996;

Stephansson et al., 1997; Tsang, 1999; Zimmerman, 2000). These equations are closely analogous to one another and within the framework of this analogy, the temperature and the pore pressure play similar roles. The THM coupling effects are expressed as three interrelated partial differential equations (PDEs) to conserve mass, energy, and momentum, which describe the interactions among fluid flow, heat transfer, and solid deformation processes. The fluid balance equation describes the conservation of mass and the flow of fluids through the fractured media, including the interconnections between fractures and the surrounding matrix. The momentum balance equation governs the forces that influence fluid flow, including pressure gradients, fluid viscosity, and mechanical deformation. The energy balance equation describes the exchange of heat between the fluid and the surrounding rock matrix, which affects the temperature and pressure of the subsurface system. Here, we adopt geomechanics sign convection in which compression is positive.

2.4.1.1 Fluid mass balance

The mass balance of fluid in a porous medium accounting for Darcy's law and the advection provoked by solid motion can be expressed by the continuity equation (Bear, 1972) as

$$\rho_f \alpha_B \frac{\partial \varepsilon_v}{\partial t} + \rho_f S \frac{\partial p}{\partial t} + \phi \alpha_T \frac{\partial T}{\partial t} + \nabla.\left(\rho_f \mathbf{q}\right) = f_w, \tag{2.2}$$

$$\mathbf{q} = -\frac{k}{\mu}(\nabla p + \rho_f g \nabla z), \tag{2.3}$$

$$S = \frac{\phi}{K_f} + (\alpha_B - \phi)\frac{1 - \alpha_B}{K_d}, \tag{2.4}$$

where ρ_f and μ are the fluid density and dynamic viscosity, respectively, which are functions of pressure and temperature, a_B is the the Biot–Willis coefficient, ε_v is the rock matrix volumetric strain, t is time, S is the storage coefficient, p is fluid pressure, ϕ [-] is the porosity, a_T is the linear thermal expansion coefficient, T is temperature, q is the Darcy velocity, f_w is the source/sink term of fluid (representing fluid influx or outflux from the rock element), k is the intrinsic permeability, g is the acceleration of gravity, z is the elevation from a reference plane, K_f is fluid bulk modulus, and K_d is the drained bulk modulus of the rock. The first three terms on the left side of Eq. (2.2) describe the changes in rock matrix volume due to strain, pressure, and temperature, and the last term gives the liquid flow due to pressure gradient and gravity according to Darcy's Law.

2.4.1.2 Momentum balance

Neglecting the inertial term, that is, under a quasi-static condition, the momentum balance reduces to the equilibrium equation of stresses (Biot, 1956; McTigue, 1986)

$$\nabla.\boldsymbol{\sigma} + \mathbf{b} = \mathbf{0}, \tag{2.5}$$

where $\boldsymbol{\sigma}$ is the total stress tensor and b is the vector of body forces. The relationship between stress tensor $\boldsymbol{\sigma}$, strain tensor ε, and fluid pressure p is

$$\boldsymbol{\sigma} = \mathbf{C}(\varepsilon - \varepsilon_T) - \alpha_B p\mathbf{I}, \tag{2.6}$$

$$\varepsilon_T = \alpha_T(T - T_0), \tag{2.7}$$

where C is the constitutive matrix, ε_T is the thermal strain, I is the identity matrix, and T_0 is the reference temperature. According to Biot's theory (Biot, 1962), the fluid pore pressure is proportional to the dilation of the porous matrix and the variation of fluid content (ξ_v)

$$p = B(\xi_v - \alpha_B\varepsilon_v), \tag{2.8}$$

where B is the Biot modulus, which is the inverse of the storage coefficient.

2.4.1.3 Energy balance

Energy balance is given by the convection–diffusion equation (Nield and Bejan, 2017), which reads

$$(\rho H)_{eff}\frac{\partial T}{\partial t} + \rho_f H_f \mathbf{q}.\nabla T - \nabla.(\kappa_{eff}\nabla T) = f_h, \tag{2.9}$$

$$(\rho H)_{eff} = (1-\phi)\rho_r H_r + \phi\rho_f H_f, \tag{2.10}$$

$$\kappa_{eff} = (1-\phi)\kappa_r + \phi\kappa_f, \tag{2.11}$$

where H is the specific heat capacity, κ is the thermal conductivity (Huber et al., 2012), and f_h is an external/internal supply of energy. The subscripts "f", "r", and "eff" represent fluid, rock matrix, and effective value, respectively. Note that the thermodynamic properties are volumetrically averaged (weighted arithmetic mean) to account for solid matrix and pore fluid as the effective values (Eqs. 2.10 and 2.11). The first term on the left-hand side of Eq. (2.9) is the change in energy, the second term describes the convective

energy due to heat carried by the moving liquid, and the third term represents the temperature conduction in the liquid-filled rock matrix.

2.4.2 Balance laws of fractures

Within the framework of continuum mechanics, rock fractures can be characterized by a dual set of surfaces, accommodating both normal and shear displacements. The fluid dynamics occurring within these fractures are expounded through the integration of the continuity equation and a tangential adaptation of Darcy's law, specifically tailored to the distinctive attributes of fracture elements

$$\rho_f S_{fr} b_{fr} \frac{\partial p}{\partial t} - \nabla_{fr}.(\rho_f \mathbf{q}_{fr}) = b_{fr} f_w, \tag{2.12}$$

$$\mathbf{q}_{fr} = -\frac{k_{fr}}{\mu} b_{fr}(\nabla_{fr} p + \rho_{fr} g \nabla_{fr} z), \tag{2.13}$$

where S_{fr} is the storage coefficient of fractures, k_{fr} is the fracture element's permeability, b_{fr} is the aperture of the fracture element, $\mathbf{q}_{fr}$ is the flow velocity in the fracture (the volumetric flow rate per unit length in the fracture element), and ∇_{fr} denotes the gradient operator restricted to the fracture element's tangential plane. When void fluid-filled fractures are assumed, it is widely accepted that the storage term (first term of Eq. (2.12)) is equal to the temporal variation of the fracture aperture and that k_{fr} is proportional to the square of the fracture aperture according to the cubic law. In doing these assumptions, the distinction between hydraulic aperture and true (mechanical) aperture is ignored (Renshaw, 1995). Similarly, heat transfer in fracture elements can be expressed as

$$b_{fr}(\rho H)_{eff} \frac{\partial T}{\partial t} + b_{fr} \rho_f H_f \mathbf{q}_{fr}.\nabla_{fr} T - \nabla_{fr}.(b_{fr} k_{eff} \nabla_{fr} T) = b_{fr} f_h, \tag{2.14}$$

2.4.3 Fractured media constitutive models

The present work does not strive to provide an exhaustive review of all the available rock and joint constitutive models. Interested readers are advised to refer to (Barton et al., 1985; Jaeger et al., 2009; Jing and Stephansson, 2007b; Lei and Barton, 2022; Yan et al., 2020). Instead, we briefly introduce the main categories of various constitutive models.

The classical constitutive models are predominantly grounded in the principles of elasticity and plasticity. Linear thermoporoelasticity has emerged as the prevalent assumption to model the behavior of rocks. When adopting the CHILE (Continuous,

Homogeneous, Isotropic, Linear Elastic) hypothesis, the constitutive law can be expressed through two distinct material properties (Jing, 2003). These can either be represented by the widely recognized Young's modulus and Poisson's ratio, or by Lame's two parameters, signifying their independence. Consequently, changes in stresses are a function of changes in strain, pressure, and temperature (Biot, 1956; McTigue, 1986) and Eq. (2.6) turns to

$$\Delta\boldsymbol{\sigma} = K\varepsilon_v\mathbf{I} + 2G\left(\Delta\boldsymbol{\varepsilon} - \frac{\varepsilon_v}{3}\mathbf{I} + \frac{\alpha_b}{2G}\Delta p\mathbf{I} + \frac{3K}{2G}\alpha_T\Delta T\mathbf{I}\right). \tag{2.15}$$

Conversely, elastic strain tensor $\boldsymbol{\varepsilon}$ can be expressed with the total stress, pressure, and temperature as

$$\boldsymbol{\varepsilon} = \frac{1+\nu}{E}\boldsymbol{\sigma} - \frac{3\nu}{E}\sigma_m\mathbf{I} - \frac{1-2\nu}{E}(\alpha\Delta p\mathbf{I}) - \Delta T\alpha_T\mathbf{I}, \tag{2.15}$$

where $\sigma_m = \frac{tr(\boldsymbol{\sigma})}{3}$ is the mean total stress, $K = \frac{E}{3(1-2\nu)}$ is the bulk modulus, $G = \frac{E}{2(1+\nu)}$ is the shear modulus, E is Young's modulus, ν is the Poisson ratio. The effective stress tensor is $\boldsymbol{\sigma}' = \boldsymbol{\sigma} - \alpha_B p\mathbf{I}$.

More complex anisotropic elastic models can be formulated through closed-form derivations by exploring alternative elastic symmetry conditions for intact rocks (Dutler et al., 2018; Noorian Bidgoli and Jing, 2014; Yang et al., 2014). This includes transversely isotropic elasticity, as well as models for a continuum of fractured rocks intersected orthogonally by either infinitely large or finite-sized fractures. Such approaches enable the development of equivalent or effective elastic properties for fractured media, leading to more sophisticated constitutive models of anisotropic elasticity (Murakami and Hegemier, 1989; Singh, 2000; Wu and Wang, 2001).

Plastic and elastoplastic models have been developed and extensively employed for fractured rocks since the 1970s, established primarily on the foundations of the classical theory of plasticity, with Mohr-Coulomb (linear) and Hoek-Brown (non-linear) failure criteria serving as common yield functions and plastic potentials in typical models (Hoek, 1983; Hoek and Brown, 1997; Rafiei Renani and Cai, 2022). Moreover, two fundamental features of the plastic behavior of fractured rock are strain-softening and strain-hardening, with the former being more frequently observed in the context of uniaxial compression testing (Desai and Salami, 1987; Du et al., 2015; Read and Hegemier, 1984; Shen et al., 2019; Zhang et al., 2021; Zienkiewicz and Mroz, 1984). Strain localization closely linked to the constitutive models is another deformational phenomenon in fractured rocks and

has been the subject of study through the use of plasticity and damage mechanics models (Agard et al., 2011; Fossen et al., 2007; Gardner et al., 2017; Pardoen et al., 2015; Rattez et al., 2018; Zhang et al., 2013).

Incorporating failure criteria is an integral aspect of the constitutive modeling of rocks, as they serve as yield surfaces or plastic potential functions in plasticity models. While the Mohr-Coulomb and Hoek-Brown criteria are widely used, various failure criteria have been suggested for rock masses over the years (Bahrami et al., 2017; Das and Basudhar, 2009; González Nicieza et al., 2006; Jaiswal and Shrivastva, 2012; Labuz et al., 2018; Lee et al., 2012).

The effect of viscosity has been considered in constitutive modeling in combination with other basic deformation mechanisms (elasticity and plasticity) leading to constitutive models with visco- prefixes. Two mechanisms account for the effect of viscosity: creep and relaxation. Creep pertains to the phenomenon of increasing deformation (strain) under constant loading (stress), while relaxation pertains to decreasing loading (stress) while the deformation (strain) remains constant (Borja et al., 2020; de Borst and Duretz, 2020; Farhat et al., 2017; Fossum and Brannon, 2006; Maranini and Yamaguchi, 2001; Souley et al., 2011; H. Zhou et al., 2008).

Constitutive models for rocks have been also developed utilizing continuum damage mechanics principles (Kachanov, 1958). These models incorporate either isotropic damage, which uses a scalar representation (Oliver, 2000; Saksala et al., 2015), or anisotropic damage, using a tensor representation (Fernández and Ayala, 2004; Olsen-Kettle and Sarout, 2022) of the void formation, micro-cracking, or embedded fracture phenomena that occur in the rock under loading. This theory has a close relationship with both continuum mechanics and fracture mechanics, providing a bridge between these two. The formulation of the damage mechanics models exhibits certain parallels with plasticity models, such as the use of damage evolution laws instead of flow rules. However, unlike plasticity theory, damage mechanics principles are not subject to the restriction of the normality rule. Additionally, damage mechanics theory has distinct advantages in simulating strain-localization factors using continuum approaches and in studying the brittle-ductile deformation model transitions that are observed during rock sample testing (Chen and Qiao, 2018; de Borst, 2002; Liu and Yuan, 2015; Liu and Zhang, 2015; Liu et al., 2015; Oliver et al., 2002; Xie et al., 2020a, 2020b). Generally, the utilization of a damage mechanics model is deemed more pertinent for materials exhibiting brittle or semi-brittle characteristics, while the employment of a plasticity model is perceived as more

appropriate for the analysis of ductile materials. Nevertheless, it should be noted that the incorporation of softening within the plasticity framework can, to some extent, accommodate the representation of brittle behavior (Wang and Lei, 2023).

2.4.4 Fracture constitutive models

Fracture constitutive models have been formulated either through empirical or theoretical approaches. In general, within the matrix, displacement, pressure, and temperature are recognized as the primary variables, while, for fractures, the primary variables predominantly consist of contact tractions (including both normal and shear components), pressure, and temperature, whereas fluxes and displacements assume roles as variables along the interfaces that bridge the fracture and matrix. When implementing fracture constitutive models into continuum numerical methods (via interface elements), numerical instabilities may arise due to the zero-thickness of interface elements. In contrast, the implementation of these models into discontinuum methods is generally simpler due to the use of contact mechanics principles. However, inter-penetration of solid blocks must be prevented through the use of techniques like penalty function, Lagrangian multipliers techniques, or regularization scheme (Abedi and Clarke, 2019; Hou et al., 2023; Jones and Papadopoulos, 2000; Lei et al., 2016; Salimzadeh et al., 2018; Stefansson et al., 2021).

2.4.4.1 Quasi-static constitutive models

A number of constitutive models have been developed to characterize the mechanical behavior of rock fractures under quasi-static loadings through empirical approaches. Among them, Goodman's model stands out for its treatment of nonlinear fracture deformation characteristics (Goodman et al., 1968), while the Barton-Bandis model is renowned for its ability to capture the coupled hydro-mechanical response and to consider non-linear normal/shear behavior of fractures examined against extensive experimental data (Bandis et al., 1983; Barton et al., 1985; Lei and Barton, 2022). These empirical models offer valuable insights into fracture behavior and are frequently used in rock engineering practice due to their typically simpler mathematical forms and reduced number of parameters required, particularly in cases where simple loading mechanisms are anticipated. Yet, their potential violation of the second law of thermodynamics in complex stress-displacement scenarios raises concerns. Furthermore, their applicability outside of their original databases remains uncertain, necessitating the development of robust validation techniques and the incorporation of a thermodynamic framework.

Improved attention to these factors will bolster the reliability and wider applicability of these models in practical rock engineering contexts (Asadollahi and Tonon, 2010; Babanouri and Fattahi, 2018; Chen et al., 2023, 2020; Grasselli and Egger, 2003; Jing and Stephansson, 2007c; Lei et al., 2016; Lei and Barton, 2022; Lin et al., 2019).

The development of theoretical models for rock fractures is typically grounded in the principles of solid mechanics, specifically in plasticity or contact mechanics. In contrast to empirical models, theoretical models must adhere strictly to thermodynamic principles, thus establishing a more rigorous foundation in rock mechanics. However, this theoretical correctness comes at the cost of typically more complex mathematical forms and an increased number of parameters (like (Amadei and Saeb, 1990; Souley et al., 1995)), which in turn requires additional considerations and costs for parameterization when implementing such models. The most common constitutive models for rock fractures developed via the theoretical approach are formulated using principles of plasticity theory. These models leverage the similarity between the plastic hardening-softening deformation of solids and the shear stress (traction)-shear displacement components of rock fractures (Desai and Fishman, 1991; Lee and Cho, 2002; Nguyen and Selvadurai, 1998; Oliveira and Lourenço, 2004; Plesha, 1987; Xie et al., 2022a, 2022b).

2.4.4.2 Dynamic constitutive models

To properly replicate the transient slip resulting from shear failure of pre-existing fractures, it is imperative to employ a suitable dynamic constitutive law, in addition to representing the fracture as a discontinuity plane. The determination of shear resistance in pre-existing fractures can be approached through the application of static friction coefficient (μ_s) in accordance with the Mohr-Coulomb theory. Additionally, in scenarios where the deformation of fractures is influenced by frictional resistance, it becomes necessary to define a dynamic friction coefficient (μ_d). Empirical evidence from experiments has motivated the development of four common friction models for fracture surfaces (Daub and Carlson, 2010):

- Stress-weakening/strengthening model
  This model operates by instantaneously reducing the coefficient of friction to a new dynamic value (μ_d) when the shear stress of a fracture surpasses the Mohr-Coulomb failure criterion determined by the static friction coefficient (μ_s). This model is also referred to as the velocity-weakening model due to the decrease in shear strength with increased slip velocity. It provides a simplistic representation of the failure

behavior of fracture surfaces subjected to a sudden increase in slip velocity (Dieterich, 1979). Notably, this friction model is classified as "inherently discrete" since the strength of the failing elements experiences a discontinuous drop during the slip (Ben-Zion and Rice, 1993; Rice, 1993). While the model lacks convergence properties, it has been observed to yield qualitatively acceptable results (McClure and Horne, 2011).

- Slip-weakening/strengthening model
  In slip-weakening models, the frictional resistance between two surfaces decreases as the slip or relative displacement between the two surfaces increases. This implies that the fracture becomes weaker as it slips. Slip-weakening is commonly associated with dynamic rupture processes during seismic events, where the fault initially experiences high frictional resistance but gradually weakens as slip occurs, allowing the fault to slide more easily (e.g., (Boyet et al., 2023)). In the slip-weakening model, the friction of fracture surfaces diminishes from a static value (μ_s) to a dynamic value (μ_d) as slip progresses over a critical distance (d_c) (Andrews, 2005, 1985; Bizzarri, 2012; Borja and Foster, 2007; Ikari et al., 2013). Slip-strengthening, on the other hand, refers to the phenomenon where the frictional resistance between two surfaces increases as the slip or relative displacement between them increases. Slip-strengthening can be associated with certain geological conditions where the fault becomes more resistant to sliding as it slips, potentially leading to more significant stress accumulation and higher levels of ground shaking during a seismic event (Suzuki and Yamashita, 2008, 2007; Ujiie et al., 2009; Yuan and Prakash, 2012).
- Time-weakening model
  It is similar to the slip-weakening friction model with the only difference of a required threshold, the critical time t_c, for friction to decrease from a static to a dynamic value (Andrews, 2004; Hatano, 2009; Hu et al., 2017).
- Rate- and state-dependent friction model
  This model arose from observing the results of some experiments (Dieterich, 1979, 1978; Ruina, 1983), where variations in the value of friction coefficient were noticed. It enables the simulation of fault slip, while also reproducing fast and inertially limited slip (Segall, 2010), a characteristic of earthquakes. Based on the evolution of the slip rate (or velocity) and the state variable, which induces changes in the friction coefficient value, rate and state friction models offer an effective means of modeling this phenomenon. In contrast to the previous friction models, this friction

model can capture the healing (strengthening mechanisms) of friction after a high-velocity slip, which is essential for earthquake modeling if both seismic and aseismic slip should be captured (Scholz, 1998). This constitutive law, which does not suffer from convergence issues, has become very popular due to its capacity of reproducing seismic slip and it is widely used to this end (Cueto-Felgueroso et al., 2017; Jha and Juanes, 2014; McClure and Horne, 2011).

2.4.5 Permeability evolution

Porous media encompass both solid (V_s) and pores (V_p). The summation of these constituent volumes coalesces to define the overall bulk volume of the composite system ($V = V_s + V_p$). Therefore, the evolution of the porosity can be described as

$$d\phi = d\left(\frac{V_p}{V}\right) = (1-\phi)\frac{dV}{V} - (1-\phi)\frac{dV_s}{V_s}, \tag{2.17}$$

where $\varepsilon_v = \frac{dV}{V}$ is the volumetric strain of the porous medium, and $\frac{dV_s}{V_s}$ is the volumetric strain of the solid matrix as

$$\frac{dV_s}{V_s} = -\frac{1}{K_s}dp + \alpha_T dT. \tag{2.18}$$

Subsequently, Eq. (2.17) yields

$$\phi = 1 - (1-\phi_0)\exp\left[\frac{-(p-p_0)}{K_s + \alpha_T(T-T_0) - (\varepsilon_v - \varepsilon_{v0})}\right], \tag{2.19}$$

where the subscript 0 indicates the reference value of the variable.

Initially, if fractures are closed, fluid flows through the matrix. Changes in matrix permeability can be estimated with Kozeny's model based on the evolving porosity change as

$$k_m = k_{m0}\frac{\phi^3}{(1-\phi)^2}\frac{(1-\phi_0)^2}{\phi_0^3}, \tag{2.20}$$

where k_m is matrix intrinsic permeability and k_{m0} is the reference matrix intrinsic permeability. Lab measurements in tight rock have revealed that the exponent should be much larger (Kim and Makhnenko, 2020). However, once pore pressure starts to increase, the normal effective stress acting on the fracture is reduced, causing its opening. Since

fracture transmissivity obeys the cubic law, fluid will preferentially flow through open fractures because of their higher transmissivity (Dippenaar and Van Rooy, 2016; Oron and Berkowitz, 1998; Witherspoon et al., 1980). Based on the parallel plate model (Huitt, 1956; Snow, 1965), the Navier-Stokes equations can be simplified to the so-called cubic law (Brush and Thomson, 2003; Zimmerman and Yeo, 2000) in which fracture transmissivity becomes

$$T_{fr} = \frac{\rho g}{\mu} k_{fr} b_{fr} = \frac{\rho g}{\mu} \frac{b_{fr}^3}{12}. \tag{2.21}$$

Here, fracture permeability is assumed to be isotropic and given by $k=k_{fr}(I-M)$, where M is the tensor of the fracture plane ($M_{ij}=m_i m_j$, where m is the unit vector perpendicular to the fracture), and

$$k_{fr} = \frac{b_{fr}^2}{12}. \tag{2.22}$$

The dependence of transmissivity on b_{fr}^3 is the essence of the cubic law expressing that fracture transmissivity is extremely sensitive to small variations in aperture, which implies a strong coupling of fluid flow and geomechanical response of fractured rocks.

Fracture permeability can vary over several orders of magnitude as a result of fracture aperture changes. An increase in the normal loading closes fractures, reducing their permeability, while shear slip opens fractures due to dilation under low normal stresses (Rinaldi and Rutqvist, 2019; Wang, 2017), significantly increasing their permeability (Agheshlui et al., 2018; Barton et al., 1985; Min et al., 2004; Rutqvist and Stephansson, 2003; Tao et al., 2011). Notably, the permeability of sheared fractures increases more perpendicular to the direction of shear slip, thereby enhancing flow and transport connectivity in the direction orthogonal to the slip direction (Mallikamas and Rajaram, 2005; Vilarrasa et al., 2011; Yeo et al., 1998).

To account for fracture permeability enhancement as a result of changes in the effective stresses, three main approaches can be followed, where fracture permeability varies as a function of (1) strain (Lee et al., 2015; Olivella and Alonso, 2008), (2) effective stress (Min et al., 2004; Su et al., 2022; Zhou et al., 2019), or (3) pore pressure (Walsh, 1981; Zhang et al., 2017). The first approach is more physically-based because it directly relates deformation with fracture aperture changes and consequently permeability changes as (Olivella and Alonso, 2008)

$$k_{fr} = k'_{fm} + \frac{(b_0 + a\Delta\varepsilon)^3}{12a}, \tag{2.23}$$

Where k'_{fm} is the intrinsic permeability of the matrix within the fracture zone, a is the spacing between the fractures within the fracture zone, b_0 is the initial fracture aperture, $\Delta\varepsilon$ is the volumetric strain change $\Delta\varepsilon = \varepsilon - \varepsilon_0$, and ε_0 is a threshold strain.

In the second approach, to reduce model complexity, an alternative is to use a continuum model and assume that fractures are oriented according to a certain direction. Then, the changes in the effective stress in the direction normal to the fractures are used to compute aperture changes, and from the aperture, using the cubic law, to determine fracture permeability changes (Rutqvist, 2015). It is assumed that the fracture aperture equals the residual fracture aperture for normal effective stress above a certain threshold. Below this threshold, the fracture opens up following an exponential law (Liu and Rutqvist, 2013; A. P. Rinaldi et al., 2014). Additionally, the effect of dilatancy on permeability enhancement can be included by changing the stress-dependent permeability once shear failure conditions are reached (Vilarrasa et al., 2017b).

The third category relating pore pressure with permeability is usually derived from field or laboratory measurements and thus, are case dependent and difficult to be generalized. The relationship can be made directly with pore pressure or indirectly, through another variable, like a porosity function that depends on the mean effective stress (Antonio P. Rinaldi et al., 2014; Trautwein, 2002).

2.4.6 Fracture nucleation/initiation

The phenomenon of fracture nucleation is a multifaceted process that is influenced by a variety of factors such as pore pressure, coefficient of internal friction, cohesion, elastic properties, fracture toughness, and anisotropy, among others. The nucleation of fractures can be traced to microscopic manifestations such as frictional sliding and tensile cracks along grain boundaries (Brace et al., 1966). These early indications may eventually coalesce to form a shear plane (Lockner et al., 1991). Three main modes of fracture nucleation/initiation can be differentiated: (1) Mode I, or Opening Mode; (2) Mode II, or Sliding Mode; and (3) Mode III, or Tearing Mode (Figure 2.9). The nucleation of cracks through previously intact rock can be attributed to any of these modes. In order to accurately simulate these processes through numerical methods, it is necessary to implement a constitutive model that describes the behavior of the material both before and after failure, as well as a failure criterion to determine when the material reaches its

strength limit. Furthermore, a means of representing the movements associated with failure must also be incorporated, as failure results in a significant jump in the displacement field across the fracture.

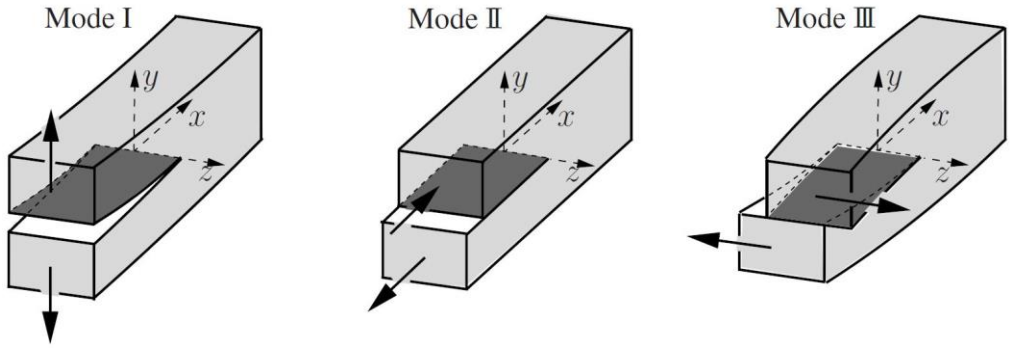

Figure 2.9 Different modes of fracture initiations, (Gross and Seelig, 2017); Mode I denotes a fracture aperture symmetrically manifesting across the x, z-plane. Conversely, Mode II is distinguished by an asymmetrical disjunction of the fracture interfaces, brought about by disparate translations along the x-direction, perpendicular to the fracture forefront. Lastly, the designation of mode III encapsulates a separation due to relative displacement in z-direction, tangential to the fracture Forefront.

Tensile failure occurs in rocks when the tensile forces exceed the rock tensile strength, which is typically low (Lockner, 1995). In-situ stresses at depth are generally compressive, and therefore, tensile failure in the subsurface typically occurs when the pore pressure surpasses the least principal stress by the tensile strength. This phenomenon is the basis of hydraulic fracturing, which significantly increases the system's permeability. The occurrence of tensile failure implies a separation of the fracture edges, leading to an increase of the fracture aperture, which strongly enhances permeability. Conversely, pore pressure reduction causes the fracture to close, causing a decrease in permeability. The shear (mode II) dilation process increases the fracture aperture and, therefore, permeability due to dilation, which causes irreversible fracture opening and channeling, especially in the direction perpendicular to shear (Vilarrasa et al., 2011). All three modes should be combined to effectively stimulate reservoirs (Qin et al., 2023).

Transitional failure behavior is observable in rocks (Byerlee, 1968; Evans et al., 1990), in which a transitional failure behavior from brittle- to ductile-dominated deformation occurs with increasing effective confining stress (Walton, 2021; Wang et al., 2020; Winhausen et al., 2022; Zheng et al., 2023). This means that at low stresses, the rock breaks by forming multiple shear fractures, while at high stresses, the rock deforms by

intergranular sliding and bending of grains. For a detailed review refer to (Wong and Baud, 2012).

2.4.7 Fracture propagation

Fractures, once initiated, can propagate into the surrounding rock in mode I (opening mode), mode II (sliding mode), or mixed mode (Schultz, 2000). The growth of fractures due to tensile failure is of particular importance in hydraulic fracturing operations, where the fluid pressure is deliberately increased above the least principal stress to induce fracture propagation (Bredehoeft et al., 1976). Subsequently, the fractures are filled with sand or proppant to prevent their closure and enhance the system permeability (Valkó and Economides, 1995). See a review on the initiation and propagation of fractures in intact rock in (Hoek and Martin, 2014) and a review of hydraulic fracturing simulation in (Chen et al., 2022).

Heterogeneity of the medium, like the presence of microcracks, and the local stresses affect the orientation of fracture propagation, but the key parameter that controls fracture propagation is the excess of pore pressure above the least principal stress, which strongly depends on the crack opening displacement (Yoshioka et al., 2020). The fracture toughness is only relevant in the creation of the fracture and in its initial growth (Carrier and Granet, 2012). Another important factor that controls fracture propagation is the stress interaction between fractures as they propagate (Desroches et al., 1994). Since the stress field is altered around the fractures, the propagation of adjacent hydraulic fractures may be hampered by one fast-growing fracture when multiple hydraulic fractures are formed at the same time (Lecampion et al., 2015; Lecampion and Desroches, 2015; Salimzadeh et al., 2018). Hydraulic fracture propagation has commonly been modeled considering that the fractured rock is impervious and thus, the fracturing fluid does not penetrate into the rock (Chen et al., 2022; Detournay, 2004). However, considering the actual permeability of rocks leads to a slower fracture propagation as a result of fluid leak-off (Carrier and Granet, 2012; Detournay, 2016; Salimzadeh et al., 2017).

A fracture propagation criterion is employed to determine the fracture propagation and the choice of fracture criterion largely depends on the adopted numerical scheme. In the context of discrete fracture approaches, Linear Elastic Fracture Mechanics (LEFM) and cohesive zone model are often employed. The LEFM criteria can be categorized into stress-based criteria (Irwin, 1957) or energy-based criteria (Griffith, 1921). However, for pure loading mode (e.g., mode I, or II), either stress- or energy-based criteria are identical.

LEFM expresses the criteria for propagation in terms of stress intensity factors (SIF) 376. Stress-based criteria proposes that a fracture propagates when a combination of stress intensity factors at the crack tip exceeds fracture toughness. The maximum principal stress criterion (Erdogan and Sih, 1963), maximum tensile stress criterion (Rahman et al., 2000), and the maximum principal strain criterion fall under this category. Although this method is relatively easy to apply, it is highly dependent on the mesh refinement at the tips. In contrast, energy-based criteria do not require extensive refinement at the tips. In accordance with Griffith's theory (Griffith, 1921), these criteria propose that a fracture propagates when the energy release at the fracture tip exceeds a critical threshold, which is a material property (Gc, a measure of material resistance against fracturing). G-criterion (Maximum Strain Energy Release Rate Criterion) (Irwin, 1957), S-criterion (Minimum Strain Energy Density Criterion) (Sih, 1974), and F-criterion (Shen and Stephansson, 1994) are such methods. Additionally, they can be further divided according to the method utilized to numerically calculate the SIF.

The Griffith criterion (Griffith, 1921) states that a fracture line propagates when the energy release rate (J, which is the released potential energy with respect to fracture growth) reaches the critical energy release rate (Gc). The energy release rate can be calculated from the stress intensity factors in all modes of loading as

$$J = \frac{K_I^2 + K_{II}^2}{E'} + \frac{K_{III}^2}{2G}, \tag{2.24}$$

where K_I, K_{II}, and K_{III} are stress intensity factors for opening (Mode I), shear (Mode II) and tearing (Mode III) loadings, respectively, and $E'=E/(1-\nu^2)$ for plane strain and $E'=E$ for plane stress.

Alternatively, cohesive zone methods, first developed by (Barenblatt, 1962; Dugdale, 1960), which are commonly used to account for non-linear mechanics effects, employ a potential to establish the relationship between cohesive tractions and the separation or slip of the fracture edges (Sarris and Papanastasiou, 2011). Therefore, fracture propagation is a gradual process that permits overcoming the stress singularities at the fracture tips calculated by LEFM (Figure 2.10). In the process zone, a traction-separation law is introduced to define the relationship between fracture width and cohesive traction. That law can take different forms, yet, in the simplest case, the fracture surfaces initiate the separation when the cohesive strength σ_c (i.e., tensile strength) is reached, and when the separation reaches a critical value δ_c (satisfying $G_c=\sigma_c\delta_c/2$), the traction decreases

linearly to zero and failure occurs (Nguyen et al., 2017; Sarris and Papanastasiou, 2011; Secchi and Schrefler, 2012). Similarly, the variational approach used in fracture propagation modifies Griffith's criterion by aiming to sequentially minimize energy (Bourdin et al., 2012; Yoshioka and Bourdin, 2016).

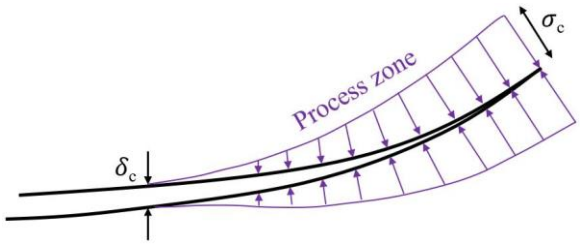

Figure 2.10 Schematic representation of cohesive zone model

Additionally, subcritical crack growth and the development of microcracks at the crack tip are two important phenomena, which cannot be explained by linear elastic principles of fracture mechanics (Anders et al., 2014). Subcritical crack growth manifests when fractures extend under stress intensity factors below the critical threshold (Atkinson, 1984; Ko and Kemeny, 2013, 2011; Nara et al., 2013; Orlecka-Sikora and Cielesta, 2020). As visually depicted in Figure 2.11, microcracks initially manifest in close proximity to the crack tips and progressively evolve into predominant meso- and macro-scale discrete cracks (Tejchman and Bobiński, 2012). The region immediately preceding the crack tip, denoted as the Fracture Process Zone (FPZ), represents the locus of microcrack initiation and coalescence (Vermilye and Scholz, 1998). A comprehensive investigation into the FPZ was conducted by (Brooks, 2013). This region, which plays a dual role in the fracture process, serves to ameliorate the impact of the applied load by inducing softening in the adjacent rock material and concurrently diminishes the resistance to fracture (Ortiz, 1988).

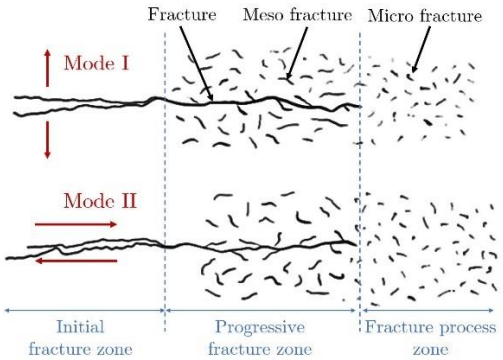

Figure 2.11 Schematic representation of fracture process zones in front of a fracture tip

2.5 Computational methods

Despite dedicated research efforts, modeling of coupled THM processes continues to present formidable challenges owing to its intricate nature. In light of the advancements in computational geomechanics, numerical techniques have emerged as robust tools, progressively employed for the investigation of fractured rock systems. However, while certain methods have been devised, not all possess the requisite capacity for effectively capturing the intricacies of the coupled processes. Simultaneously, the rapid advancements in computational capabilities have furnished a propitious environment for addressing computationally intensive challenges, thereby facilitating the development and refinement of these numerical methodologies. Consequently, the current landscape encompasses a diverse array of methods, primarily classified into two distinct categories: continuum and discontinuum-based numerical approaches. Figure 2.12 illustrates the main methods in each category. Contingent upon the continuum-based approach, the domain is discretized into constituent elements, treating the overall domain as an integrated, continuous entity. This methodological framework involves a systematic mathematical formulation incorporating a constitutive law, balance principles, as well as boundary and initial conditions. In contrast, the discontinuum-based methodologies, while relatively recent, conceptualize the domain as an assembly of discrete bodies, each capable of dynamic movement, rotation, and interactive behaviors. Consequently, their mathematical framework encompasses the interplay between individual particles and relevant balance principles. However, certain complex scenarios necessitate the amalgamation of the strengths inherent in both of these main methodologies, leading to the development of hybrid methods, coupled methods, and multi-scale coupled methods. Given the intricate and multifaceted nature of this subject, we refrain from delving into the specifics of these methodologies and instead direct the attention of interested readers to other comprehensive review articles that meticulously expound upon this particular domain (Jalali and Dusseault, 2012; Jing, 2003; Jing and Hudson, 2002; Lei et al., 2017; Mohammadnejad et al., 2021; Nikolić et al., 2016; Zhao et al., 2011).

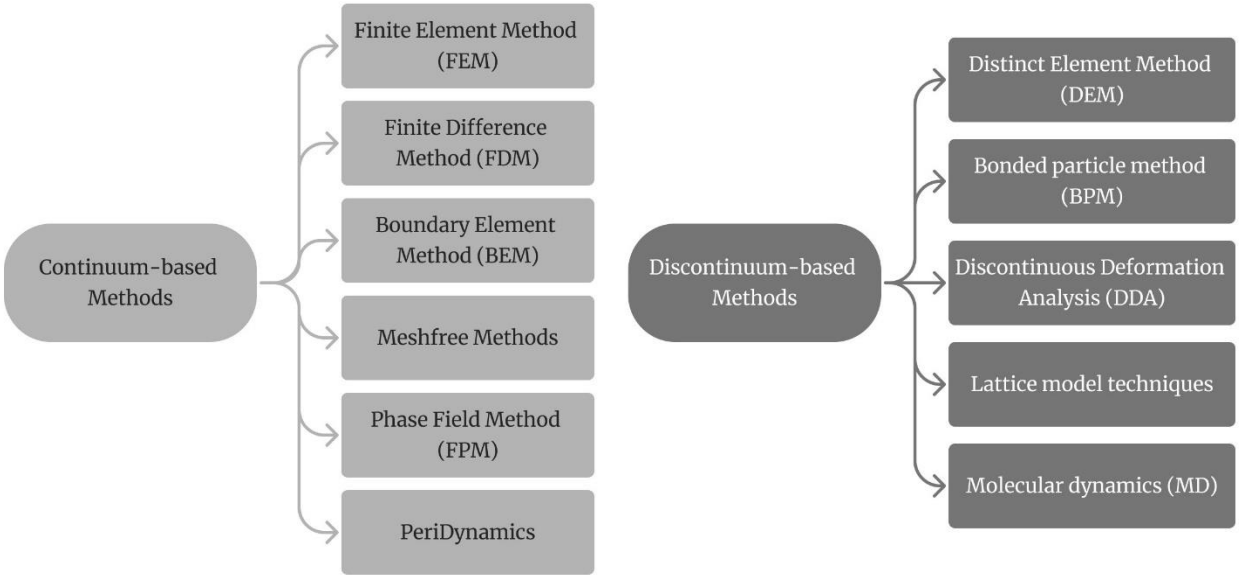

Figure 2.12 Main numerical techniques in continuum and discontinuum-based categories to solve coupled THM problems.

2.6 Research gaps, challenges and future research directions

Since the 1960s, considerable strides have been achieved in comprehending and modeling flow and transport phenomena in deformable fractured rock. Notwithstanding these notable advancements, the endeavor to model the coupled processes of fluid flow, heat transfer, and mechanical deformation in a fractured porous medium presents a formidable conceptual and mathematical challenge. This challenge arises primarily due to three key factors:

1. Inherent heterogeneity and uncertainties: One of the principal impediments lies in the inherent heterogeneity and uncertainties associated with characterizing a fracture-matrix system for field-scale problems. The complex nature of these systems necessitates dealing with a wide range of variables and parameters, making accurate characterization and prediction a daunting task.
2. Complicated coupling processes: The complexities involved in conceptualizing, understanding, and describing flow, deformation and transport processes within intricate formation systems further contribute to the challenge.
3. Limitations in field fracture properties and computational intensity: Additionally, limitations stemming from measurements of field fractures (and their intersections) properties pose challenges in developing realistic three-dimensional (3D) mathematical models. The incorporation of such an intricate 3D field of fractures

demands significant computational intensity, leading to practical limitations in model development and implementation.

Addressing these challenges in modeling coupled THM processes in fractured porous media is of paramount importance to further our understanding of these systems and enhance the accuracy of predictions in real-world scenarios. The contemporary landscape of computational technologies has exerted a profound influence on the trajectory of scientific inquiry in coupled THM processes, underscoring the escalating significance of numerical modeling. However, it is vital not to solely rely on computer simulations and visualization. Attention must be paid to the fundamental theories and principles established through past experimental evidence and practical experience as well. To ensure that THM simulations are genuinely beneficial in understanding and predicting the behavior of fractured rocks within the tangible world, computational researchers should implement simulation tools realistically. This means integrating existing knowledge and empirical data from the last few decades. An additional, and often overlooked in modeling studies, imperative pertains to the setting and calibration of model parameters, which should be based on typical ranges reported in the literature. It is paramount to invoke the adage "All models are wrong, but some are useful" to highlight the value of THM models in geo-engineering and geo-resources research. However, realizing these potential calls for a methodical conceptualization, implementation, and, where feasible, calibration to foster simulation outcomes that intricately reflect the nuanced complexities of geological phenomena. Future research efforts should focus on innovative approaches to tackle these hurdles and advance the state-of-the-art in this critical field of study.

3

On the leaky nature of fractures in low-permeability rocks

3.1 Introduction

Fractures are ubiquitous in the subsurface, which provide permeable pathways for energy and mass transport and present both opportunities and potential issues for geo-engineering applications (Adler et al., 2013). For instance, in crystalline rock, fracture permeability is sought to be increased in Enhanced Geothermal Systems (EGS) (Goto et al., 2021; McClure and Horne, 2014; Olasolo et al., 2016; Parisio and Yoshioka, 2020), but it should remain as low as possible in nuclear waste disposal (Amann et al., 2018b; Parisio et al., 2018; Xu et al., 2020) or in the caprocks for geologic carbon storage (Vilarrasa et al., 2013a) and underground hydrogen storage (Krevor et al., 2023; Xue et al., 2020). To sustainably develop and exploit geo-resources, an improved understanding of fluid flow through fractured porous media is crucial (Viswanathan et al., 2022; Zareidarmiyan et al., 2018).

Despite the small volume fraction of fractures compared to the rock volume, fluid flow and transport is controlled by fractures because they are several orders of magnitude more permeable than the surrounding rock matrix (Neuzil and Tracy, 1981). This fact commonly leads to the assumption that the rock surrounding fractures is impermeable (Koudina et al., 1998; Long et al., 1982). For instance, in most Discrete Fracture Networks (DFN) methods, the matrix is considered impervious and any flow in fractures not presented in the model is ignored (Hyman et al., 2016; Trimmer et al., 1980). Such methods are usually employed when the host rock is several orders of magnitude less permeable than fractures, such as in low-permeability limestone, shales, or granite

(Fumagalli et al., 2019). However, this assumption generally leads to inaccurate predictions of the pressure changes in hydraulic tests performed in fractured media (Lin and Yeh, 2021).

In geo-resources applications, hydraulic testing is one of the few means to characterize hydrogeological properties which are essential for resource management (Illman et al., 2009; Klaas et al., 2019). In particular, hydraulic tests in fractured media are discussed in compendiums of aquifer test analysis (Beauheim et al., 2004; Cheng and Morohunfola, 1993; Kruseman and De Ridder, 1994; Nielsen, 2007; Walton, 2006). Through the interpretation of fracture hydraulic tests, accounting for the flux between fractures and rock matrix improves the predictions (Lin and Yeh, 2021). Yet, the specific contribution of leakage to pressure evolution is not fully characterized (Lee et al., 1995; Oda, 1985; Shahbazi et al., 2020; Snow, 1969; C. B. Zhou et al., 2008; Zoorabadi et al., 2022).

To interpret hydraulic tests, analytical solutions, as opposed to numerical models, are typically employed in subsurface flow and transport applications because of their practical convenience and computational efficiency (Zhou et al., 2017; Zoorabadi et al., 2022). Analytical methods are also valuable in computationally inexpensive sensitivity studies or uncertainty quantifications. They are particularly apt when dealing with a large number of injection and leaky wells, while numerical simulations would require local mesh refinement around each well to assure accurate results (Celia et al., 2011).

Even though fractures in rock masses are often interconnected, the behavior of the flow through a single fracture should be understood in detail before more complicated field-scale fracture networks can be addressed (Brown et al., 1998; Cao et al., 2019; Konzuk and Kueper, 2004; Pyrak-Nolte et al., 1988; Xiong et al., 2011; Zhang and Nemcik, 2013; Zhong et al., 2022; Zimmerman and Yeo, 2000). To tackle the challenge of representing fractures in numerical models, we propose a method to accurately simulate fluid flow in fractures represented as an equivalent continuum at a numerically tractable scale ($>>$10-6 m). This method differs from conventional equivalent medium models where the fracture and matrix properties are homogenized within a physically larger equivalent medium. Instead, we replace a fracture, which physically occupies a negligible space, with a physically bigger element with computationally equivalent fracture properties without homogenizing it with the surrounding rock matrix. In Appendix A, we introduce the calculation of the equivalent properties for a fracture numerically represented as a layer several orders of magnitude thicker than the real aperture. And then we verify our proposed approach against a model with the real aperture, i.e., explicit

representation of the fracture, in a case of fluid injection into a fracture surrounded by low-permeability rock matrix.

The aim of this chapter is to understand the hydraulic response of water injection into a single fracture surrounded by low-permeability rock and the implications for the interpretation of field tests. The chapter is structured as follows: first, we analyze the injection pressure evolution by comparing numerical results with analytical solutions while investigating the role of rock matrix permeability. Next, we discuss the implications of our findings for the interpretation of field-scale injection tests in fractured rock masses. Our results show that the pressure evolution in a semi-log plot corresponds to the one of a leaky fracture since early times of injection, which implies that leakage into the low-permeability rock matrix controls pressure diffusion.

3.2 Methodology

3.2.1 Equivalent fracture layer

To model fractures, instead of explicitly representing them in a numerical model, a popular approach, namely continuum or implicit method, is to represent the fracture network as equivalent porous media. The transformation from discrete fractures to a continuum representation entails a procedure known as upscaling. Given the fracture system type, various continuum models may be employed via diverse approaches (Berkowitz, 2002; Berre et al., 2019; Flemisch et al., 2018; Wong et al., 2020). Considering a single fracture embedded in a low-permeability matrix, we use a method in which just the fracture itself is upscaled as a separate continuum than the matrix, whose properties are not modified. Upscaling follows analytical-based methods to calculate the equivalent properties related to the equivalent fracture layer (Figure 3.1).

Consider fluid injection into a saturated fracture surrounded by low-permeability rock matrix: transient flow through a confined layer is governed by the flow equation (Bear, 1972)

$$\nabla \cdot (T \nabla s) = S \frac{\partial s}{\partial t} + f_w, \tag{3.1}$$

where S is the storage coefficient, $s = p/\gamma_w + z$ is the hydraulic head, t is time, and f_w is a sink/source term. The left-hand side of Eq. (3.1) corresponds to flux, which is controlled by the transmissivity, and the first term in the right-hand side to storage, which depends

on the storage coefficient. To obtain identical solutions of Eq. (3.1) between a fracture with its actual aperture and an equivalent fracture layer with upscaled thickness (Figure 3.1), the same transmissivity and storage coefficient have to be applied in the two problems.

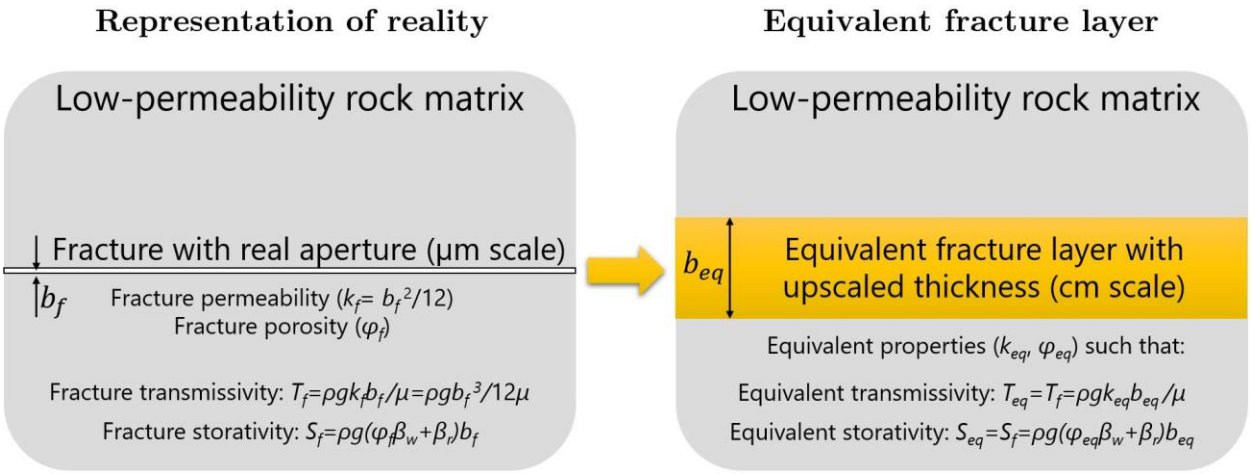

Figure 3.1 Conceptualization of the equivalent fracture layer with upscaled thickness and how to obtain its equivalent properties from the actual fracture ones

The transmissivity of a layer is calculated as

$$T = Kh = \frac{\rho g}{\mu} kh, \tag{3.2}$$

where K is the hydraulic conductivity, h is the thickness of the layer, ρ is the fluid density, g is gravity, μ is the fluid viscosity and k is the intrinsic permeability. If flow through a fracture is regarded as the parallel plate model (Huitt, 1956; Snow, 1965), we can simplify the flow rate from the Navier-Stokes equations to the so-called cubic law (Brush and Thomson, 2003; Witherspoon et al., 1980; Zimmerman and Yeo, 2000; Zou et al., 2015), in which fracture transmissivity, T_f, becomes

$$T_f = \frac{\rho g}{\mu} k_f b_f = \frac{\rho g}{\mu} \frac{b_f^3}{12}\ , \tag{3.3}$$

where b_f is fracture aperture and the fracture permeability, k_f, equals

$$k_f = \frac{b_f^2}{12}. \tag{3.4}$$

The storage coefficient of a fracture, S_f, is defined as

$$S_f = S_S b_f = \gamma_w(\varphi_f \beta_w + \beta_r) b_f \tag{3.5}$$

where S_S is the specific storage coefficient, φ_f is the fracture porosity, β_w is the water compressibility and β_r is the bulk compressibility of the fracture. Fracture porosity equals 1 for open clean fractures, but can take lower values if the fracture has gouge or asperities.

The equivalent permeability, k_{eq}, of the equivalent fracture layer can be calculated by equating Eqs. (3.2) and (3.3), resulting in

$$k_{eq} = \xi k_f, \tag{3.6}$$

where

$$\xi = \frac{b_f}{b_{eq}}, \tag{3.7}$$

and b_{eq} represents the thickness of the equivalent continuum fracture layer (Figure 3.1).

Similarly, the equivalent porosity can be derived from Eq. (3.5) as

$$\varphi_{eq} = \xi \varphi_f, \tag{3.8}$$

where the equivalent parameter ξ is the same as for permeability (Eq. (3.7)).

For fluid injection into a fracture, the injected volumetric flow rate, Q, must be maintained in order to obtain the same solution when upscaling fracture thickness with the equivalent fracture layer approach. Given that the flux injected into a layer through a fully penetrating well equals Q/A, where A is the area where fluid is injected, i.e., $2\pi r_w h$, r_w being the radius of the well, the equivalent injection flux into the equivalent fracture layer, q_{eq}, should be

$$q_{eq} = \xi q_f, \tag{3.9}$$

where $q_f = Q/(2\pi r_w b)$ is the injection flux for the actual fracture.

3.2.2 Analytical solutions of pressure evolution

Since 1930s, many works have been carried out to characterize the transient flow of pumping/injection tests performed in naturally or artificially fractured aquifers (Barker, 1988; De Smedt et al., 2018; Delay et al., 2007; Dewandel et al., 2014; Hamm and Bidaux,

1996; Jourde et al., 2002; Moench, 1984; Muskat, 1938; Russell and Truitt, 1964; Tiab, 2005; Warren and Root, 1963). As a result, several analytical solutions have been developed to reproduce the flow behavior induced by a well intersecting and pumping/injecting a vertical, horizontal or inclined permeable layer (Cheng and Morohunfola, 1993; Cinco Ley et al., 1978; Gringarten et al., 1974; Hantush, 1960; Hantush and Jacob, 1955; Moench, 1985; Neuman and Witherspoon, 1969; Ramakrishnan and Kuchuk, 1993; Theis, 1935). More recent solutions improve earlier works considering less restrictive assumptions on flow conditions in the aquitard, representing more realistic aquitards, and obtaining more accurate model prediction (Cihan et al., 2011; De Smedt, 2022, 2011; Dewandel et al., 2018; Zhou et al., 2009).

The problem of fluid injection into a planar fracture surrounded by low-permeability rock matrix is analogous to problems of hydrogeology of fluid flow into thick aquifers which have analytical solutions. If the confining layers can be considered impermeable, the Theis solution (Theis, 1935) applies; but if leakage into the surrounding low-permeability rock matrix is non-negligible, then the solution of Hantush for leaky aquifers should be used (Hantush, 1960). Given the low-permeability of the rock matrix (particularly in crystalline and shaly rocks), it is commonly assumed that the rock matrix is impermeable, as in DFN approaches.

For the former situation, i.e., impermeable confining layers, considering injection at a constant flow rate through a fully penetrating well into a confined saturated aquifer and assuming homogeneity and infinite lateral extent, the hydraulic response to water injection can be computed analytically as (Theis, 1935):

$$s = \frac{Q}{4\pi T}\int_{u}^{\infty}\frac{e^{-y}}{y}dy = \frac{Q}{4\pi T}W(u), \qquad u = \frac{Sr^2}{4Tt} \tag{3.10}$$

where Q is the injected volumetric flow rate, T is the transmissivity, p is the fluid pressure, γ_w is the specific weight of the fluid, z is the elevation from an arbitrary plane, r is the radial distance from the well, and $W(u)$ is the so-called well function.

Based on the Theis solution, several methods have been developed to estimate transmissivity and the storage coefficient from the pressure evolution (Chow, 1952; De Smedt, 2022, 2011; Jacob, 1947, 1940; Jacob and Lohman, 1952). The most used approximation is the one proposed by (Cooper Jr and Jacob, 1946):

$$s = \frac{2.3Q}{4\pi T}\log\left(\frac{2.25Tt}{Sr^2}\right). \tag{3.11}$$

If we plot drawdown against radial distance (r) and time (t), the curves cross distance/time axes in certain points (at s=0). Defining those points as the radius of influence, R, and the response time, t_0

$$R = \sqrt{\frac{2.25Tt}{S}}, \qquad t_0 = \frac{Sr^2}{2.25T}, \tag{3.12}$$

the solution becomes

$$s = \frac{2.3Q}{2\pi T} log\left(\frac{R}{r}\right) = \frac{2.3Q}{4\pi T} log\left(\frac{t}{t_0}\right), \tag{3.13}$$

where R represents the pressurization front when no leakage occurs to the confining layers and scales with the square root of time.

Eq. (3.13) shows two important properties of the aquifer response to injection. The first one is that pressure buildup follows a linear log distribution of distance from the well: injection causes a cone-shaped pressure profile along the radial direction. The size of the cone grows in a self-similar manner with time. The cone is centered at the well and its external radius evolves with the radius of influence R (Eq. (3.12)). The second one is that when pressure changes are plotted against log t, they follow a straight line whose slope (m) is inversely proportional to the transmissivity and intercepts the time axis at t_0. Consequently, the transmissivity and the storage coefficient can be estimated as

$$T = \frac{2.3Q}{4\pi m} = 0.183\frac{Q}{m}, \qquad S = \frac{2.25Tt_0}{r^2}. \tag{3.14}$$

The linear relationship of pressure changes against log(t) under radial flow conditions prompted researchers to use the derivative of pressure changes with respect to log time as an interpretation method (Bourdet et al., 1989, 1983). The joint representation of the pressure changes and its log-derivative, known as diagnostic plots (Renard et al., 2009), can be highly informative. The flow dimension, d, can be calculated from the slope n of the log-derivative as a function of time in a log-log plot as (Niemi et al., 2017):

$$d = 2(1 - \mathrm{n}). \tag{3.15}$$

Considering the leaky nature of the system, the drawdown in the fracture shows typical characteristics inherent in double-porosity behavior in which the matrix is considered as a primary porous system with low hydraulic conductivity and high storage capacity and the fractures as a secondary porous system with high hydraulic conductivity and low storage capacity (Hamm and Bidaux, 1996). In the double-porosity concept, the initial drawdown is due to the fracture storage as if the rock matrix were non-existing (first stage); leakage gradually gains weight and the matrix storage becomes dominant (second stage); and eventually the whole medium acts as a homogeneous system with the storage capacity of the fractures and matrix combined (third stage) (De Smedt, 2022). For situations in which fracture spacing is large, in the dm scale, and the permeability of the rock matrix is several orders of magnitude lower than that of fractures, the first stage disappears immediately and it requires a long time to reach the third stage (homogeneous system). As a result, only the first and second stages and the transition between them are relevant. Such situations are our focus in this chapter.

Early analytical solutions to the leaky aquifer problem neglected the storage of the confining layers (Hantush, 1956; Hantush and Jacob, 1955), while a generalized expression that accounts for storage of the confining layers was later proposed by (Hantush, 1960), which reads

$$s = \frac{Q}{4\pi T}\int_u^\infty \frac{e^{-y}}{y} erfc\left(\beta\sqrt{u}/\sqrt{y(y-u)}\right) dy = \frac{Q}{4\pi T} H(u,\beta), \tag{3.16}$$

where

$$\beta = \frac{r\lambda}{4}, \qquad \lambda = \sqrt{\frac{K'/b'}{T}\frac{S'}{S}} + \sqrt{\frac{K''/b''}{T}\frac{S''}{S}}, \tag{3.17}$$

and K is the hydraulic conductivity, b is the thickness of the layer, H is the Hantush well function, and superscripts $'$ and $''$ denote the properties associated to the upper and lower confining layers, respectively. We compute the Hantush well function by numerical integration. The solution is valid for time lower than both $b'S'/10K'$ and $b''S''/10K''$: at these times, the pressure perturbation reaches the upper and lower boundaries. (Veling and Maas, 2010) reviewed several representations of the Hantush well function and introduced a practical and fast approximation. The Hantush well function can be approximated by (Hantush, 1960)

$$H(u,\beta) \approx W(u) - \frac{4\beta}{\sqrt{\pi u}}\left(0.2577 + 0.6931e^{-u/2}\right) \tag{3.18}$$

for early time or $u \geq 10^4\beta^2$, and by

$$H(u,\beta) \approx \frac{1}{2}\ln\left(\frac{0.044}{\beta^2 u}\right) \tag{3.19}$$

for $u \leq 10^5/\beta^2$ and $u \leq 10^{-4}\beta^2$. The transition between these approximations happens in $u = \beta^2$ and based on that, we can define the transition time as

$$t_t = \frac{S_s b^2}{K'}, \tag{3.20}$$

where S_S is the specific storage coefficient. The radius of influence for leaky aquifers can be obtained by numerical integration of the Hantush solution or more simply using the approximation in Eq. (3.19). The radius in which the approximation for the Hantush well function reaches zero is

$$R = \sqrt[4]{\frac{0.704T^2b't}{K'S'}}. \tag{3.21}$$

I generalize the problem using the following dimensionless variables

$$t_D = \frac{t}{t_c};\ s_D = \frac{s}{s_c}; r_D = \frac{r}{L_c}; \phi_D = \frac{\phi}{\phi_c} \text{ and } k_D = \frac{k}{k_c}, \tag{3.22}$$

where ϕ is the porosity, k is the intrinsic permeability, L is length, and the subscripts D and c denote dimensionless and characteristic variables, respectively. Based on the hydraulic boundary condition, i.e., a constant flow rate, the characteristic hydraulic head can be defined as

$$s_c = \frac{Q\mu}{2\pi b\rho g k_c}, \tag{3.23}$$

where ρ is the fluid density, g is gravity, and μ is the fluid viscosity. The characteristic length, porosity, and permeability are chosen as the well radius and porosity and permeability of the fracture, respectively (i.e., $L_c = r_w$, $\phi_c = \phi_f$, and $k_c = k_f$). The characteristic time can be defined from the flow equation, yielding the characteristic time of diffusion

$$t_c = \frac{L_c^2 S_s \mu}{\rho g k_c}. \tag{3.24}$$

3.2.3 Numerical modeling

We numerically model a fracture both explicitly and implicitly using an equivalent fracture layer. We use an axisymmetric model to represent a single circular fracture in which water is injected in the center through a well with a radius of 0.1 m, i.e., L_c=0.1 m (Figure 3.2). The fracture is horizontal, confined, and with uniform thickness. The model represents a fracture with a radius of L_D=10^4 embedded between two thick layers of low-permeability rock (b_{mD}=*100*) at a depth of z_D=10^4. Each continuum, i.e., the fracture continuum and the matrix continuum, is assumed to have homogeneous and isotropic hydraulic properties. The radial extent of the fracture is such that the nature of the outer boundary, i.e., constant pressure or no flow, does not affect results during the duration of injection, i.e., the radius of influence (Eq. (3.21)) is smaller than the radial extent of the model. A linear hydrostatic pressure gradient is applied to the model as the initial condition. The injection is at a constant rate ($q = 50$ kg/s/m^2) and the flow in the fracture is described by the classical groundwater flow equation (Barenblatt et al., 1960; Bear, 1972; Moench, 1984; Warren and Root, 1963).

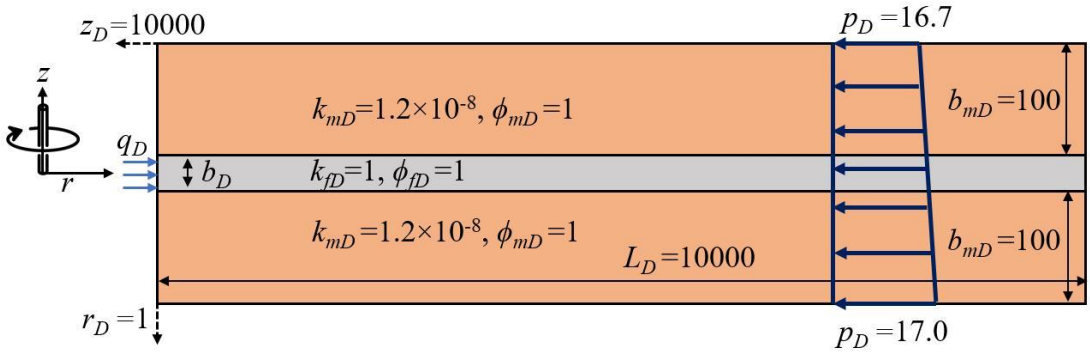

Figure 3.2 Schematic representation of the axisymmetric model geometry and initial conditions; a flux q_D is injected in the center of a L_D=10,000 radius fracture with aperture b_{eqD}. The properties of the confining rock matrix are denoted by subscript 'm'.

The reference model explicitly represents the fracture by discretizing the actual fracture aperture of 10^{-5} m. The fracture permeability is calculated using the cubic law (Eq. (3.4)), resulting in $8.33 \cdot 10^{-12}$ m^2. The fracture porosity is set to 0.1. The permeability and porosity of the confining layers are 10^{-19} m^2 and 0.1, respectively. The reference solution is the one given by a model that represents the actual aperture, i.e., explicit

representation of the fracture. We build several additional models with increasing thickness of the equivalent fracture layer and apply the equivalent properties, i.e., permeability, porosity, and injection flux rate, to each model using the relationships given in Equations (3.6)-(3.9) (Table 3.1). Equivalent properties are set to impose a constant fracture transmissivity ($8.33 \cdot 10^{-10}$ m^2/s), storage coefficient ($4.41 \cdot 10^{-12}$), and flow rate ($3.14 \cdot 10^{-4}$ kg/s).

Neglecting the solid phase compressibility, the same storage coefficient is assumed for the matrix. The model simulates water injection at a constant rate for 300 hours and we analyze the pressure evolution at the injection well and the pressure profile along the fracture at the end of injection. (Birkholzer et al., 2009) demonstrated the influence of leakage on lowering pressure buildup (pressure bleed-off) in the aquifer for aquitard permeability as low as 10^{-18} m^2. To investigate lower permeability, we carry out a sensitivity analysis to assess the effect of the rock matrix permeability on pressure evolution by taking values in the range from 10^{-18} to 10^{-24} m^2 for 100 hours of injection using an equivalent fracture layer with an upscaled thickness of 1 cm.

Table 3.1 Input parameters for the fracture and equivalent fracture layer models

Ratio of the equivalent fracture layer b_{eq} to the fracture aperture b ($1/\xi$)	**Permeability k_{eqD}**	**Porosity φ_{eqD}**	**Injection flux q_{eqD}**
1	1	1	1
10^3	10^{-3}	10^{-3}	10^{-3}
10^4	10^{-4}	10^{-4}	10^{-4}
$2.5 \cdot 10^4$	$4 \cdot 10^{-5}$	$4 \cdot 10^{-5}$	$4 \cdot 10^{-5}$
$5 \cdot 10^4$	$2 \cdot 10^{-5}$	$2 \cdot 10^{-5}$	$2 \cdot 10^{-5}$
10^5	10^{-5}	10^{-5}	10^{-5}

We employ the Finite Element Method (FEM) numerical program CODE_BRIGHT (Olivella et al., 1996). We use structured mesh including 12,322 quadrilateral elements. The mesh configuration is the same for all models in which the fracture has 10 vertical elements and the matrix slabs have 30 elements in the vertical direction. The elements in the matrix are concentrated toward the fracture-matrix interfaces to accurately capture leakage effects. The horizontal distribution of the elements has refinement toward the

well. We have performed a mesh sensitivity analysis to ensure that further refinement does not affect the results.

3.3 Results

Equivalent fracture layer models can simulate pressure evolution accurately (figure 3.3). Even the models with large upscaled thicknesses reproduce the results of the actual aperture model after a short time. At early time (dimensionless time lower than 1), simulation results from large upscaled thickness deviate from the benchmark solution (real fracture) because the flow within the equivalent fracture layer is not 1D radial and the pressure diffusion normal to the layer plays a role in the pressure evolution. The equivalent approach to model a fracture will work if the porous layer can be considered thin enough to assume 1D flow within the element. The equivalent fracture layer reproduces the pressure evolution well after

$$t_D > C\frac{b_{eqD}^2}{D_{vD}} \tag{3.25}$$

where D_v is the vertical pressure diffusivity and C is a coefficient that depends on the equivalent fracture thickness. For $b_{eqD} > 10^{-2}$, $C = 13.2 \cdot b_{eqD}^2 + 191.5 \cdot b_{eqD} - 130.4$, while for values of $b_{eqD} < 10^{-2}$, the equivalent fracture layer yields the same results as the actual fracture in less than milliseconds.

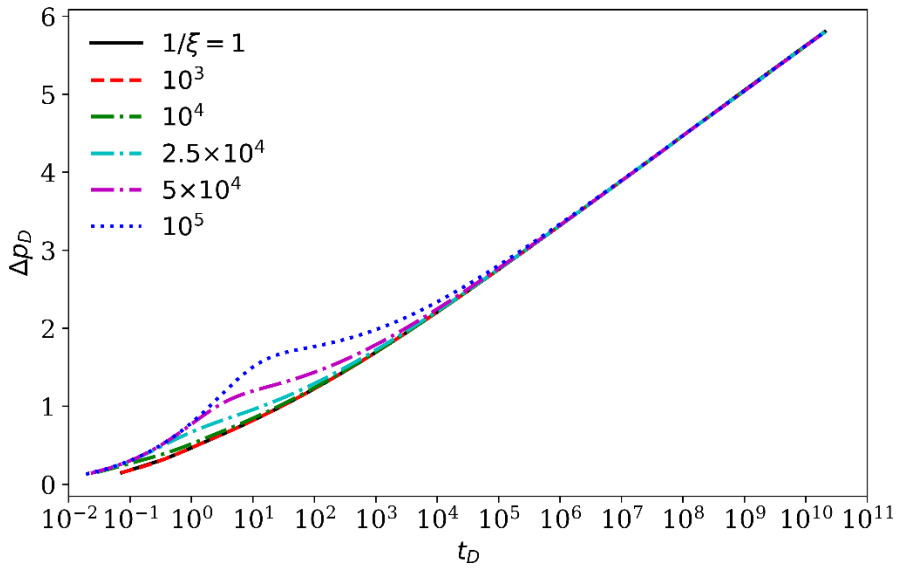

Figure 3.3. Dimensionless pressure evolution at the injection well for equivalent fracture layer models with increasing ratio of the equivalent fracture layer thickness to the fracture aperture ($1/\xi$=b_{eq}/ b_f) during

constant flow rate injection. The solid black line is the response of the real fracture aperture and other colors are associated to models with upscaled thickness using equivalent parameters

Equivalent fracture models are accurate during the whole injection time when the ratio of the equivalent fracture layer to the actual fracture aperture, i.e., $1/\xi$, is lower than or equal to 10^3. The pressure evolutions shown in Figure 3.3 include solo-fracture stage as well as fracture-matrix stage with leakage, but not the final stage in which the fracture and matrix act as a single medium. These curves display the typical pressure evolution with constant slope in a semi-log plot, from which the transmissivity and storage coefficient can be derived. Also, all models yield an identical pressure distribution along the middle of the fracture aperture or the upscaled thickness at the end of the injection phase (Figure 3.4). The pressure perturbation extends up to r_D=1000, which is much smaller than the radius of influence in a confined fracture within impervious layers (Eq. (3.12)), and corresponds to the radius of influence when leakage dominates (Eq. (3.21)).

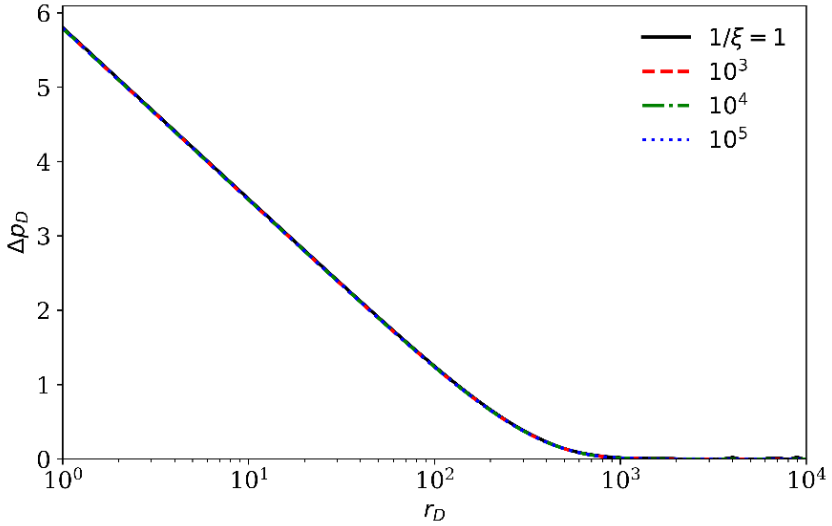

Figure 3.4 Dimensionless pressure profile along the dimensionless radial coordinate measured at the middle of the fracture aperture or the equivalent fracture layer at the end of the injection for the reference model with the actual fracture aperture and equivalent fracture layer models with different thickness. All models give identical results

Simulation results show that the thickest equivalent fracture layers yield identical results to the actual aperture model after a short period, which defines the limit of applicability of the method. For different equivalent apertures, the results are eligible after a certain time, given by Eq. (3.25). On the one hand, one can use thick equivalent fracture layers for applications in which the pressure evolution and distribution in early times are

not relevant, like for long-term geothermal energy production. On the other hand, thinner equivalent fracture layers should be used when early times are of importance, like in interpretation of injection tests. To achieve accurate results during the whole injection time, it is sufficient to represent fractures with a thickness of 10 cm ($1/\xi = b_{eq}/b = 10^4$). Such thickness permits multiple fractures in models, although the treatment of fractures intersection may pose additional challenges, which will be a topic of future research

Fracture transmissivity and storage coefficient can be obtained based on the pressure evolution measurements from the slope and intercept of the curve (Renard et al., 2009). A simulation result with $k_{mD} = 1.2 \times 10^{-8}$ shows an initial transition phase dominated by the storage effect, which is followed by a straight line in a semi-log plot (Figure 3.5). The Theis solution can be fitted with a transmissivity that is twice the actual fracture transmissivity, and 5 times the real storage coefficient. This storage coefficient would correspond to a fracture with an aperture of $b'_{eqD} = 5 \times 10^{-4}$. The Theis solution can be reproduced if we neglect the matrix permeability and porosity in the numerical model (see the solid and dashed blue lines in Figure 3.5). This demonstrates that the neglecting the rock permeability can lead to huge errors in curve-fitting interpretation with the Theis solution.

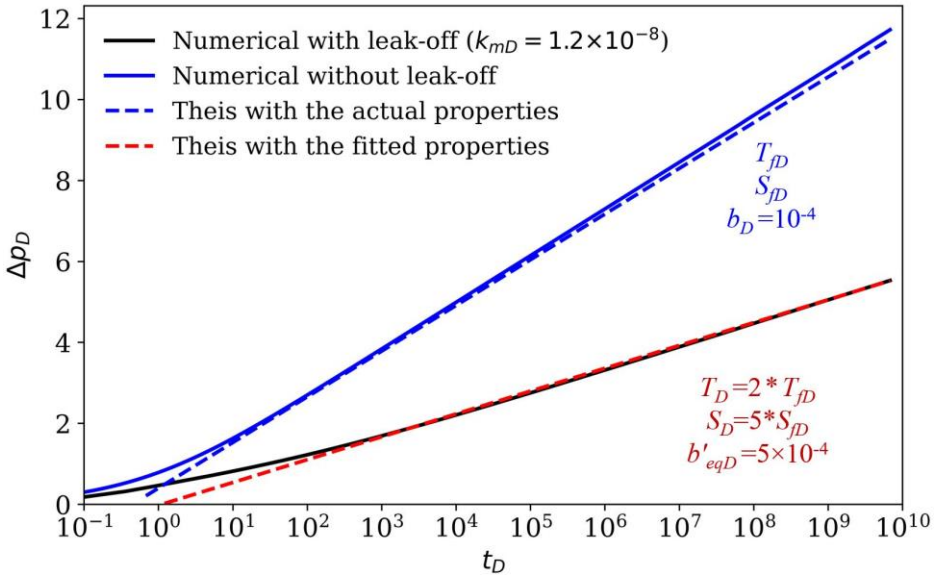

Figure 3.5 Dimensionless pressure evolution response to injection into a fracture surrounded by low-permeability rock resulting from numerical and Theis solutions. The solid black line is the pressure produced by the numerical model, the dashed black line is the Theis solution considering the real fracture properties and the dashed red line is the fitted straight line to estimate transmissivity and the storage

coefficient, resulting in a transmissivity that is twice that of the fracture and a storage coefficient five times larger, which would imply a fracture aperture b'_{eqD} of $5{\cdot}10^{-4}$, 5 times larger than the actual one

Next, we perform a sensitivity analysis to dimensionless rock matrix permeability ranging from 1.2×10^{-7} to 1.2×10^{-13} (Figure 3.6). The slope that would correspond to twice the actual fracture transmissivity appears immediately after injection in the cases with the rock matrix permeability up to 1.2×10^{-9}. For the cases with a lower permeability, the enhanced transmissivity slope does not immediately appear. Instead, the pressures first follow a steeper slope that corresponds to the slope of the actual fracture transmissivity, and then the slope that corresponds to a hither transmissivity. The lower the rock matrix permeability is, the longer the transition time between the two slopes becomes. The transition time (shorter than a few seconds in all cases) is proportional to the rock matrix permeability, i.e., one order of magnitude smaller rock matrix permeability implies a one order of magnitude longer transition time.

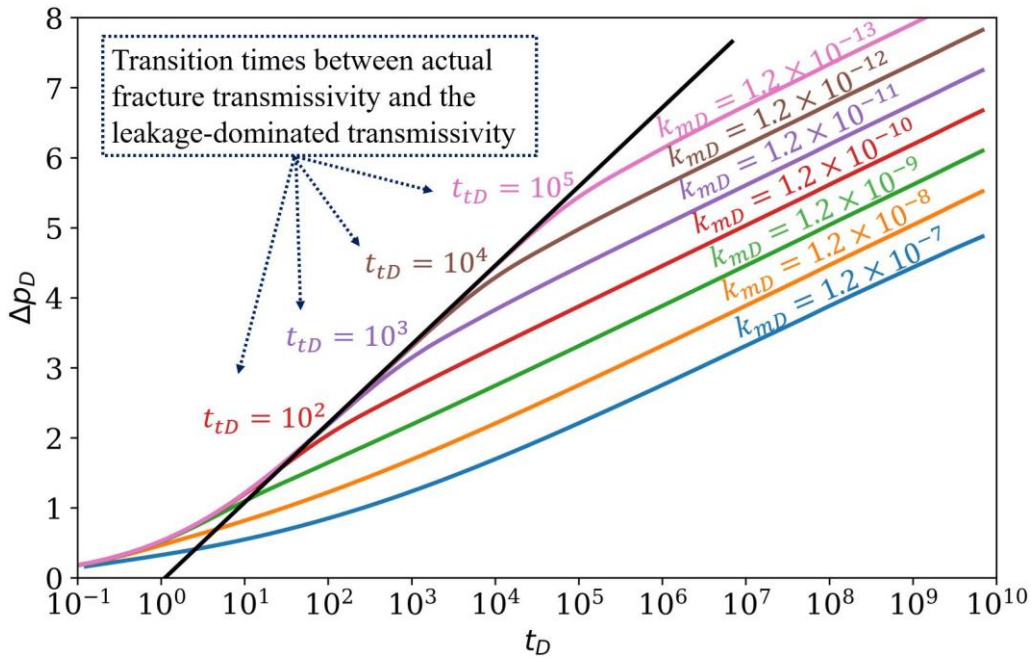

Figure 3.6 Dimensionless pressure evolution response to a wide range of dimensionless rock matrix permeability and the corresponding dimensionless transition time, t_{tD}, for each case. The solid black line indicates the fitted Theis solution (same transmissivity as the real fracture transmissivity, but modified storage)

We analyze the slopes and transition time for the case of rock matrix permeability of $k_{mD} = 1.2 \times 10^{-12}$ (Figure 3.7). The first slope that arises only for the lowest matrix permeabilities corresponds to that of the real fracture transmissivity (indicated by the

solid black line in Figure 3.6 as well as phase I in Figure 3.7). Nonetheless, the interpreted storage coefficient (from the Theis solution) is 2.5 times the actual fracture one, which would be equivalent to a fracture aperture of $b'_{eqD} = 2.5 \times 10^{-4}$. After a transition, the slope turns into twice the actual fracture transmissivity and a storage coefficient that is $4{\cdot}10^{-4}$ times that of the actual fracture (phase II in Figure 3.7). The transition time between these two phases can be estimated from the intersection of the fitted straight lines of each phase, giving a value of $t_{tD} = 10^4$.

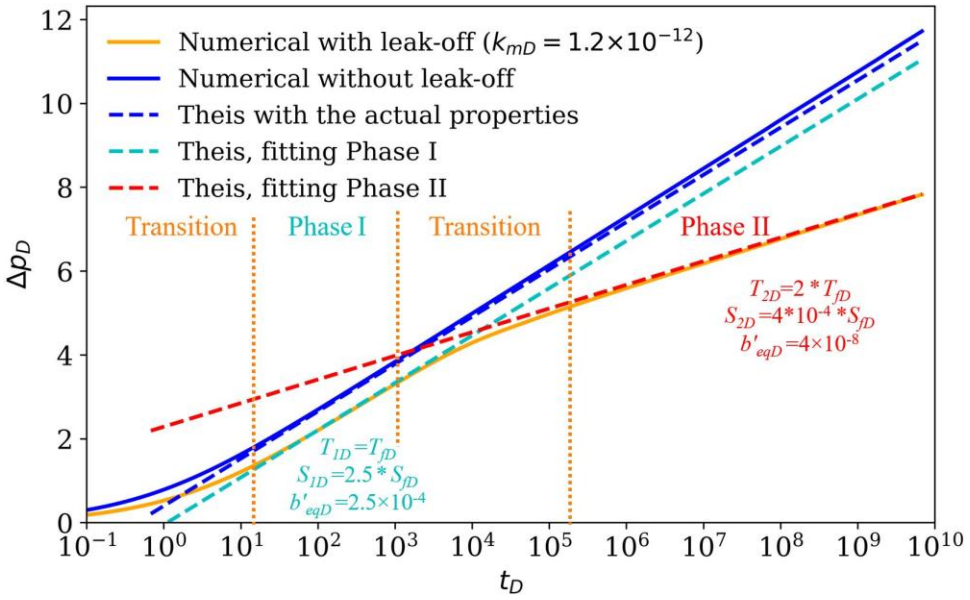

Figure 3.7 Phases of the pressure evolution and fitting of transmissivity and storage coefficient for each phase (using Theis solution) for a dimensionless rock matrix permeability of 1.2×10^{-12}. The solid orange line is the pressure from the numerical simulation with leakage, the solid dark blue line is from numerical simulation neglecting any transfer between the fracture and the matrix, the dashed cyan and red lines are the fittings for each phase, and the dashed blue line is the expected pressure evolution when applying the analytical solution of Theis for this problem.

To explore the contribution of leakage on the pressure evolution, we compare simulation results with the Hantush (1960) solution (Eq. (3.8)) (Figure 3.8). At early times, i.e., during phase I in Figure 3.7, which lasts for a short period (in the order of milliseconds to seconds), numerical results deviate from the Hantush solution. In phase I, the slope of the pressure evolution in a semilog plot presents the actual fracture transmissivity (the same as in the Theis solution), but with more storage, provided by the matrix. In other words, the extra storage provided by the matrix becomes effective sooner in the numerical model compared to the Hantush solution. In fact, both storage and transmissivity of the matrix activate together in Hantush's solution (based on the

assumptions of a thick aquifer), but storage of the matrix starts to play a role sooner than the transmissivity of the matrix in the numerical solutions (Figure 3.8) (See Figure 3.9 for more details). In addition, the analytical solution may also introduce some errors at early times because it relies on the quasi-steady-state assumption for continuum flow, which is not satisfied during the early rapid transient flow. Therefore, the numerical solution is more accurate for early time behavior. After the transition time, simulation results fit the Hantush solution for the double-transmissivity slope, i.e., when there is leakage into the low-permeability matrix (phase II in Figure 3.7). This fitting confirms that fractures surrounded by low-permeability rocks have a leaky nature.

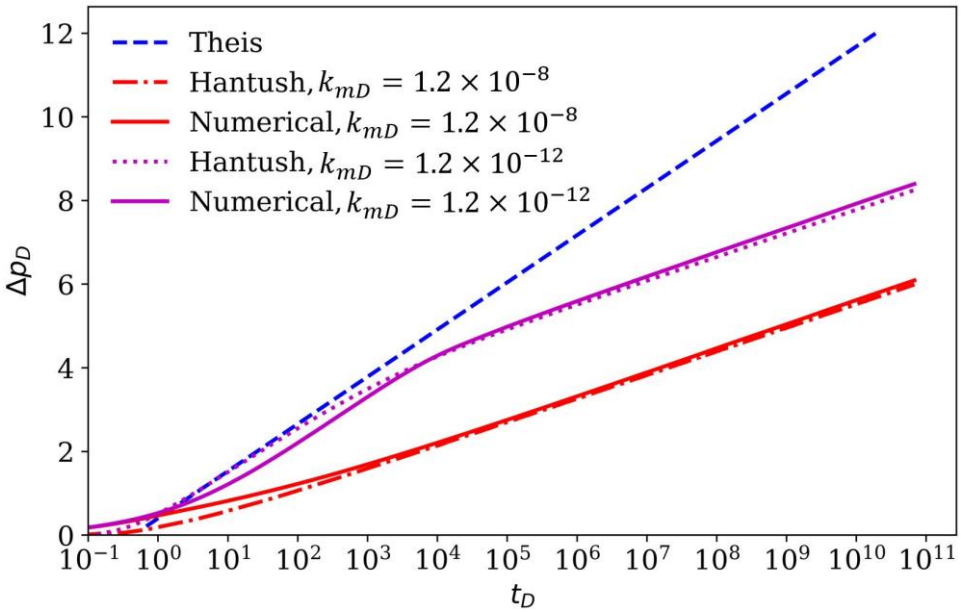

Figure 3.8 Dimensionless pressure evolution as a result of injection into a fracture calculated with numerical and the Hantush (1960) solutions for two different permeability of the confining rock matrix. The Theis (1935) solution is also included for comparison purposes. Deviation from the Theis solution, which assumes impermeable rock matrix, occurs in less than a second when the rock matrix permeability is 12 orders of magnitude smaller than the fracture permeability

In our analysis, the porosity of the matrix is ϕ_{mD}=1, causing a difference in the early-time response between numerical and Hantush's solution (Figures 3.8 & 3.12). A detailed look at the pressure evolutions during Phase I (defined in Figure 3.7) in Figure 3.9 reveals that in the numerical model, the storage of the matrix starts to play a role sooner than the transmissivity of the matrix compared to the analytical solution in which both transmissivity and storativity act simultaneously. However, in the case of the lower matrix porosity (ϕ_{mD}=0.1), i.e., negligible matrix storage, there is no difference between numerical result and both analytical solutions during phase I, showing that the rock matrix behaves

as completely impermeable. Thus, the difference between the numerical and Theis solution in our base case (red line in Figure 3.9) is due to storage of the matrix. Matrix storage has also an effect on the long-term pressure evolution: the larger the storage, the lower the pressure build-up at a given time (compare the colored continuous (high matrix storage) and colored dashed lines (low matrix storage) in Figure 3.9). Despite the vertical shift in the pressure evolution curves by decreasing the matrix porosity, transition time to Phase II remains the same.

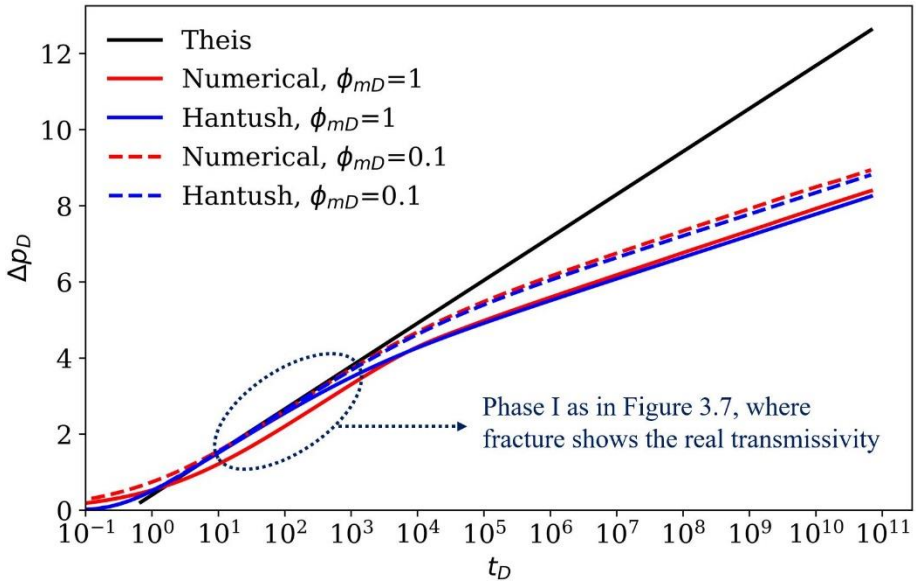

Figure 3.9 Dimensionless pressure evolution as a result of injection into a fracture from numerical and the Hantush (1960) solutions for two different porosities of the confining rock matrix (i.e., 0.1 and 0.01; dimensionless matrix permeability of 1 and 0.1, respectively) (dimensionless permeability of the matrix is 1.2×10-12). The Theis (1935) solution is also included for comparison purposes (it is independent from the matrix porosity).

As the leaky nature of fractures depicts the twice higher fracture transmissivity on the semi-log plot, one may try to double the fracture transmissivity in numerical models with impermeable rock matrix to obtain accurate results. Such a manipulation would result in a reasonable pressure evolution at the well (Figure 3.10). However, the pressure distribution along the fracture would be significantly different from what it should be because of the pressure front propagation speed (compare the radius of influence when neglecting and considering leakage (Eqs. (3.12) and (3.21), respectively)). While the simulated pressure distribution with leakage agrees well with that of Hantush (Figure 3.10), the distribution differs by more than two orders of magnitude from Hantush's solution if the rock matrix permeability is neglected (Figure 3.10).

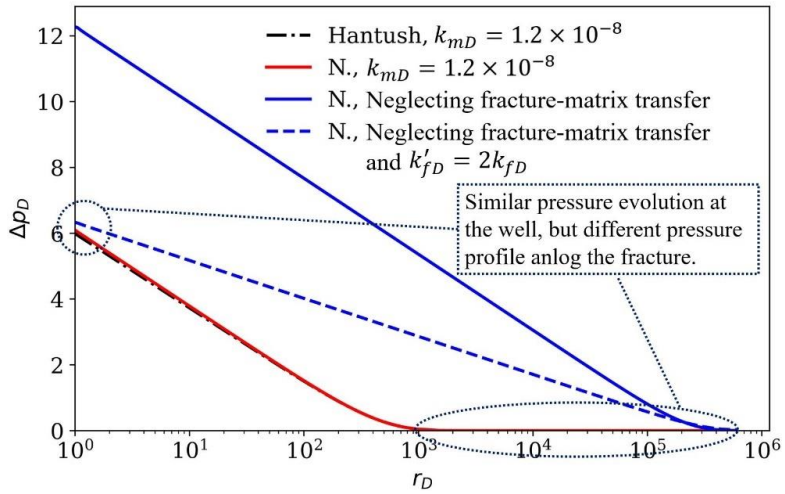

Figure 3.10 Dimensionless pressure profiles along the fracture at the end of the injection, predicted by the numerical (red line) and the Hantush (1960) solutions for a dimensionless permeability of the rock matrix of 1.2×10^{-8}. Two blue lines are the results of numerical simulations where fracture-matrix transfer is neglected (Note that the dashed line model employs double permeability for the fracture)

We investigate what causes different pressure evolutions between numerical and analytical (Hantush, 1960) solutions using diagnostic plots for the case of dimensionless rock matrix permeability equal to $k_{mD} = 1.2 \times 10^{-12}$ (Figures 3.11 and 3.12). Diagnostic plots help identifying the flow regime during fluid injection by simultaneously plotting the pressure and the logarithmic derivative of the pressure in semi-log and log-log plots. The logarithmic derivative magnifies subtle variations in the pressure evolution and allows us to detect behaviors often overlooked on the pressure evolution curve alone. The straight black lines in Figure 3.11 unveil the flow regimes from their slopes (Renard et al., 2009). At the beginning of injection, the log-derivative of pressure in a log-log plot presents a slope of 1/4, which corresponds to a flow dimension of 1.5 (Eq. (3.15)), i.e., between linear and radial. The Hantush (1960) solution has an initial slope of 1, which corresponds to a flow dimension equal to 0 (Eq. (3.15)). This discrepancy brings the numerically simulated curve downward during phase I (Figures 3.8 & 3.9). In phase I, the flow regime turns into radial, as shown by the constant pressure derivative. In this initial phase, flow is confined within the fracture and the surrounding rock matrix acts as an impermeable boundary, as shown by the slope of the pressure evolution corresponding to that of the actual fracture transmissivity (Figure 3.7). This radial flow regime lasts for a limited time and turns into a slope of -1/4 in the log-log derivative plot, i.e., a flow dimension of 2.5 (Eq. (3.15)), which is between radial and spherical (Figure 3.11). This flow regime indicates the onset of leakage from the fracture into the rock matrix. When compared with the diagnostic plots of the Hantush (1960) solution, the flow dimension of this transient stage is 2.15,

which is closer to radial (Figure 3.12). The lower flow dimension in the second transient stage in Hantush (1960) leads to slight differences in the pressure evolution with respect to the numerical solution. Finally, the flow becomes radial again, but with a value of the pressure derivative that is half of the first radial flow, i.e., the effective transmissivity of the system becomes twice higher than the fracture transmissivity (phase II in Figure 3.7). The latter radial flow implies not only flow along the fracture, but also into the low-permeability rock matrix.

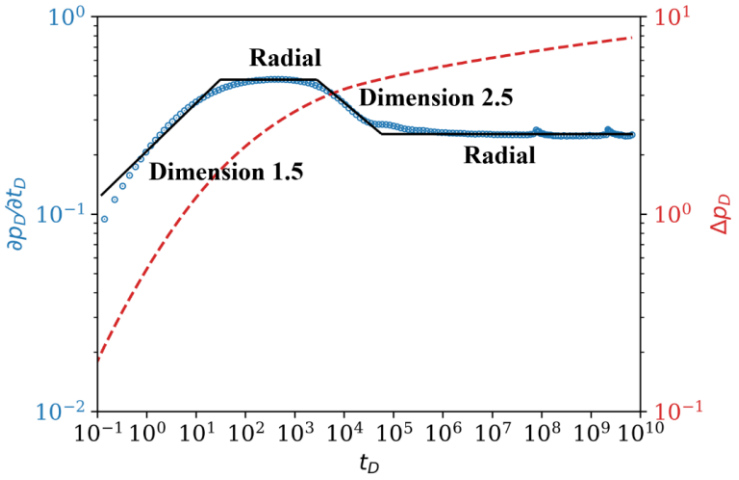

Figure 3.11 Diagnostic plot for the case with dimensionless rock matrix permeability of 1.2×10^{-12}. The blue dots are the pressure derivative, the red dashed line is pressure evolution, and the solid black line is the flow regime trend based on the pressure derivative.

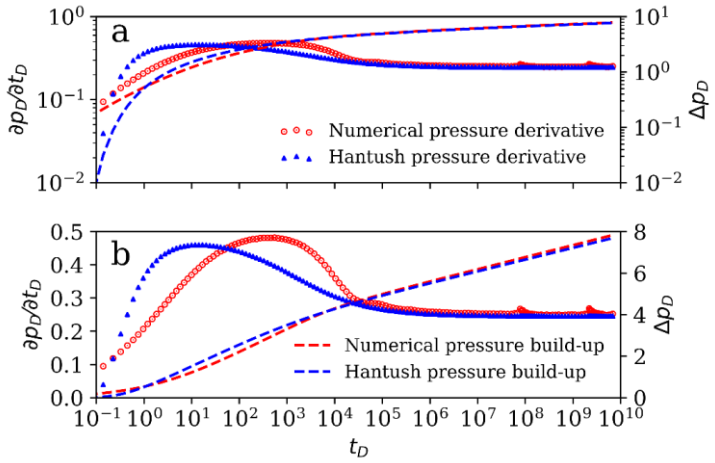

Figure 3.12 Diagnostic plots of the numerical and the Hantush (1960) solutions for the case with dimensionless rock matrix permeability of 1.2×10^{-12} in (a) log-log and (b) semi-log diagrams. Derivative of dimensionless pressure evolutions (scatter curves) correspond to the first y-axis (on the left) and dimensionless pressure evolutions (dashed lines) to the second y-axis (on the right).

3.4 Discussions

3.4.1 Implications of the leaky nature of fractures in hydraulic-test interpretation

We have analyzed the pressure evolution during fluid injection into a single fracture surrounded by low-permeability rock matrix and found that leakage into the matrix occurs from early times (milliseconds to seconds), reducing the slope of the pressure evolution in a semilog plot by a factor of two, which corresponds to a twice higher fracture permeability in the Theis solution. For interpretation of hydraulic tests in fractures, it is important not to neglect leakage even in low-permeability rock matrix (Figure 3.6). In practice, it is challenging to record pressures with higher frequencies than every few second and pressure measurements during the first few seconds of injection may be noisy or masked by wellbore effects. If measurements at early times are missed, the pressure evolution would depict a straight line with log t, which could be misinterpreted as the pressure evolution with no leakage into the low-permeability matrix (e.g., Figure 3.5). Thus, using conventional methods for interpreting field tests (e.g., Cooper & Jacob, 1946), one may erroneously interpret the fracture permeability twice higher than the actual permeability. If this double permeability were used in analytical or numerical models to estimate the pore pressure propagation into the fractured rock, the pressure at the injection well would be accurately estimated, but the pressure propagation into the fracture would be overestimated by a few orders of magnitude (Figure 3.10).

This factor of 2 arises from the difference in the slopes of the pressure change as a function of log t given by the solutions of Theis (1935) (for a layer confined by impermeable boundaries) and Hantush (1960) (for a leaky layer). Their slopes are given by the time derivative of Eqs. (3.10) and (3.16), respectively. The functions $W(u)$ and $H(u,\beta)$ do not have an analytical expression of their time derivative, but we can use their approximations. The slope becomes $Q/(4\pi T)$ for the case of impermeable confining layers and $Q/(8\pi T)$ for the case of leaky confining layers. Leakage actually occurs when injecting into fractures surrounded by very low-permeability rock, giving rise to a slope that is half of the one of Theis (1935). Thus, neglecting leak-off in the interpretation of field tests overestimates fracture transmissivity, which may give rise to erroneous predictions in numerical models.

The typical pressure response to fluid injection into a fractured aquifer is as follows (Cinco-Ley and Meng, 1988; De Smedt, 2011). In a semi-log graph (Figure 3.13), the

pressure curve shows two parallel straight lines representing the fracture dominated flow (Phase I) and the total system (fracture-matrix) dominated flow (Phase III). There is a transition period between these parallel lines (Phase II) called stabilization period in which the pressure curve, for the transient matrix flow, is represented by a straight line whose slope is half the slope of the parallel lines. The pressure evolution initially follows the Theis solution as storage and leakage into the matrix are negligible (dark blue line in Figure 3.13). Subsequently, the injected fluid starts to leak into the rock matrix, reducing the slope of the pressure as a function of the logarithm of time by a factor of two, as reproduced by the Hantush solution (red line in Figure 3.13). Pressure diffusion into the rock matrix eventually leads to pressure equilibration between the pressure in the fracture and the pressure within the rock matrix blocks (Zareidarmiyan et al., 2021). After equilibration, the pressure gradient between the fracture and the rock matrix becomes negligible, hindering fluid flow from the fracture to the matrix, and the whole system is controlled again by the fracture permeability, recovering the initial slope (light blue line in Figure 3.13). In a fractured aquifer, the rock matrix permeability is orders of magnitude higher than in tight rocks (such as in low-permeability shales or granite) as assumed in this study. As a result, we do not observe phase III because, for the time scale of our analysis, i.e., a few hundreds of hours, pressure diffusion does not propagate into the rock matrix. Additionally, Phase I only lasts for less than a few seconds, depending on the rock matrix permeability (Figure 3.6). Hence, in a field test, which typically lasts for a few hours, one may miss the first few seconds of pressure measurements and only observe the second phase. For this reason, bearing in mind the leaky nature of fractures is essential to interpret tests and derive the proper fracture properties.

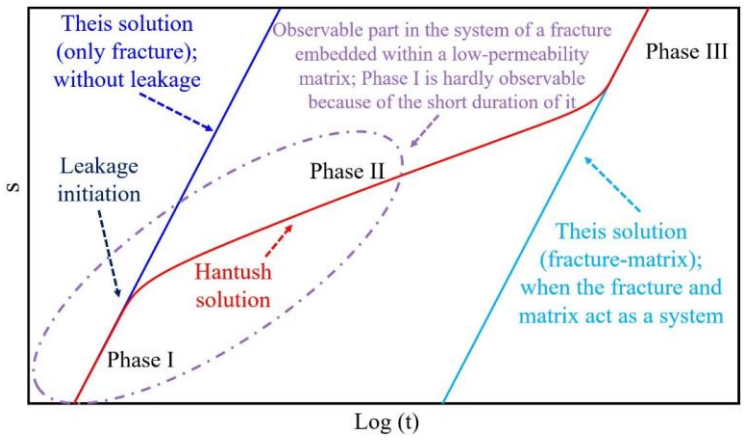

Figure 3.13 Typical drawdown versus log-time curves for a pumping/injection test in a fractured aquifer, the dark blue line is the fracture Theis solution (upper bound). The light blue line is the fracture-matrix Theis solution (when both fracture and matrix act as a single system).

3.4.2 Implications of the leaky nature of fractures in modeling subsurface applications

The transition time at which leakage becomes non-negligible depends on the subsurface application. This transition time affects the ability to characterize and model these systems. To assess the role of leakage into the surrounding low-permeable rock, we estimate the transition time at which the slope of the pressure evolution curve is reduced by a factor of 2 for several geo-energy, geo-engineering, and water resources applications (Table 3.2). Isolines of the transition time are parallel straight lines when plotted as a function of the thickness of the injection layer and the permeability ratio between the low-permeable rock and the injection layer (Figure 3.14). Two groups of applications can be distinguished. On the one hand, transition times are short for the applications in which fluids are injected into or produced from fractured tight rock, like Enhanced Geothermal Systems (EGS), hydraulic fracturing (HF) and groundwater pumping from fractured aquifers (GWFM), indicating that leakage dominates almost from the beginning of injection. On the other hand, longer transition times are expected for the applications in which fluids are injected in or produced from thick permeable layers, like waste water disposal (WWD), Carbon Capture and Storage (CCS), compressed air energy storage (CAES), hydrogen storage, and groundwater production from aquifers (GWA). In some occasions transition times may be longer than the duration of the operation and, hence, the effect of leakage may be ignored. However, to obtain reliable long-term estimates, leakage must be considered from the beginning, both in well-test interpretation and in numerical simulations, in applications in which fluids are injected into or produced from fractures surrounded by low-permeability rock (applications placed in the left-hand side of Figure 3.14), regardless of how low is the permeability of the rock matrix

Table 3.2 Dimensionless transition time at which leakage becomes non-negligible for several geo-energy, geo-engineering, and water resources applications

Application		**Enhanced Geothermal Systems (EGS)**	**Hydraulic fracturing (HF)**	**Carbon Capture and Storage (CCS)**	**Waste water disposal (WWD)**	**Compressed Air Energy Storage (CAES)**	**Hydrogen storage**	**Groundwater from aquifers (GWA)**	**Groundwater from fractured media (GWFM)**
Dimensionless transition time	Max	10^{7}	10^{8}	9×10^{14}	6×10^{14}	3×10^{13}	10^{14}	10^{14}	10^{21}
	Min	10^{-7}	10^{-8}	10^{7}	2×10^{9}	10^{5}	10^{7}	10^{7}	10^{15}

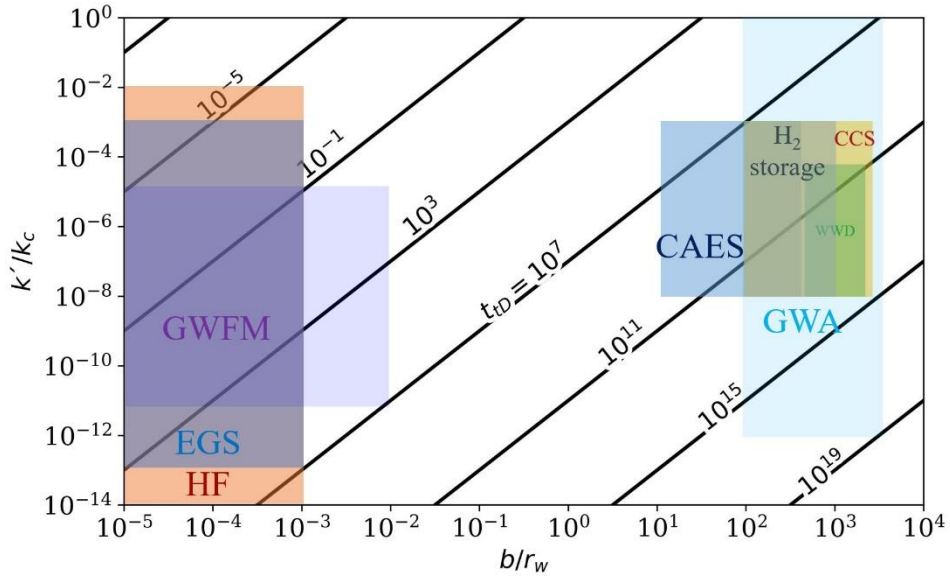

Figure 3.14 Dimensionless transition time at which leakage becomes non-negligible as a function of the ratio between matrix and injection layer permeability, and the ratio of the injection layer thickness and the well radius (characteristic time is the same as Eq. (9)). The range of transition time is indicated for several geo-energy and geo-engineering applications (EGS: Enhanced Geothermal Systems; HF: Hydraulic fracturing; CCS: Carbon capture and storage; WWD: Waste water disposal; CAES: Compressed air energy storage; H2 storage: Hydrogen storage; GWA: Groundwater from aquifers; and GWFM: Groundwater from fractured media).

In approaches like DFN, discrete element method (DEM) and stochastic fracture models, when dealing with low-permeability media, impervious matrix is commonly assumed which reduces the fracture network to hydraulically connected pathways (Baghbanan and Jing, 2008; Long et al., 1982; Min et al., 2004; Rutqvist et al., 2013). However, doing so leads to inaccurate predictions of the pressure propagation through the fracture network (Lang et al., 2014; Taylor et al., 1999) as illustrated in Figure 3.10. Our results highlight further that even in extremely low-permeability rock matrix, leakage cannot be neglected and it starts to dominate since the early stages of injection (Figure 3.6). Therefore, the rock matrix permeability should be included in numerical models to reproduce leakage into the matrix and properly simulate the pressure diffusion through the fracture network in the subsurface applications in which leakage is non-negligible.

3.4.3 The origin of the leaky nature of fractures

The extremely low thickness of fractures plays a dominant role on the onset of leakage into the rock matrix after a short injection time, even for extremely low-permeability matrix. The assumption of impermeable confining layers of the Theis solution does not

apply to fractures. The reason is that for a given layer with fixed permeability and porosity, but variable thickness, the transmissivity decreases with the layer thickness. Assuming a prescribed injection flow rate, pressure increases as the layer becomes thinner because pressure is inversely proportional to transmissivity, inducing a higher pressure gradient perpendicular to the interface between the injection and the confining layers (Figure 3.15a). Increasing the pressure gradient results in an enhanced leakage relative to the injection flow rate. Comparing a hectometer-thick aquifer with a micrometer-thick fracture, fracture transmissivity is 8 orders of magnitude smaller than that of the aquifer. Consequently, pressure buildup and, thus, the pressure gradient from the injection layer into the confining layer, is 8 orders of magnitude larger in the fracture than in the aquifer. This difference explains why the assumption of impervious confining layers applies for aquifers, but not for fractures.

To highlight the leaky nature of fractures even further, let us assume a prescribed injection pressure instead of a flow rate to impose the same vertical pressure gradient at the interface with the confining layers, and thus the leakage regardless of the layer thickness (Figure 3.15b). Let us consider two cases: a 100 m-thick aquifer and a fracture with an aperture of 10 μm. To induce the same pressure build-up in both cases, the ratio of the flow rate to the transmissivity has to be maintained. Since the thicknesses differ by 7 orders of magnitude in the two cases, the injection flow rate into the fracture is 10^7 times smaller than the injection flow rate in the thick aquifer. Given that the leakage flow rate is identical in both cases, the ratio between the leakage flow rate and the injected flow rate is 10^7 times lager for the fracture than for the thick aquifer. Consequently, leakage becomes non-negligible in fluid flow in fractured media.

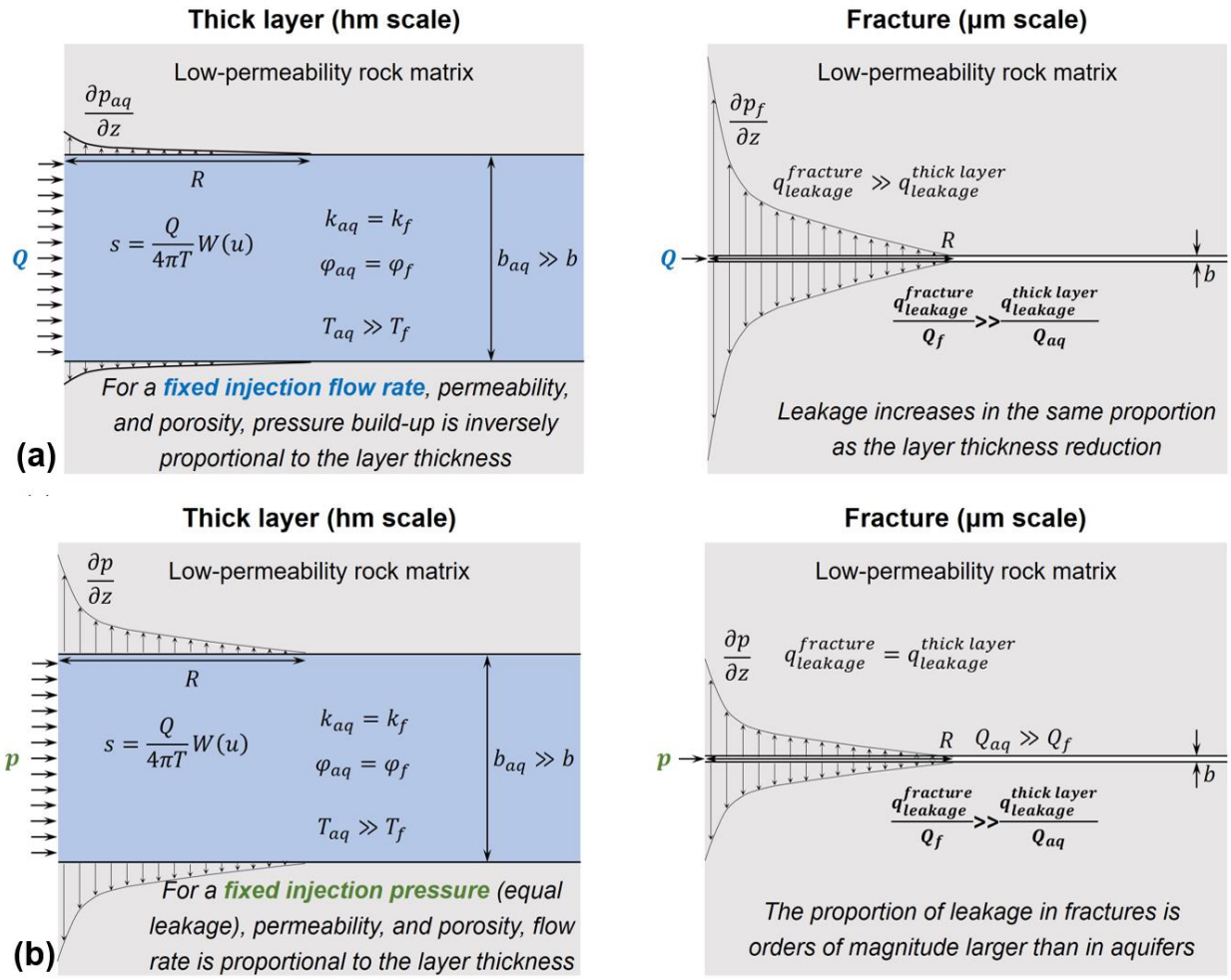

Figure 3.15. Schematic representation of the different response to fluid injection of a thick layer (thickness in the 10^2 m scale) and a fracture (thickness in the 10^{-6} m scale) with the same permeability and porosity when (a) imposing the same injection flow rate and (b) prescribing the same injection pressure. In both cases, the ratio between the leakage into the low-permeability rock matrix and the injection flow rate is orders of magnitude larger for the fracture.

3.4.4 The role of fracture size

We have assumed an infinitely acting fracture, i.e., the pressure perturbation front does not reach the end of the fracture during injection. In real applications, it is likely that the length of fractures is finite and, thus, the tip is reached or that the fracture intersects other fractures, which would also affect the pressure evolution. For this reason, we analyze the pressure evolution in finite size fractures in which the tip is reached during injection (Figure 3.16). The early-time hydraulic behavior is the same for both finite and infinite fractures embedded in a low-permeability rock matrix. The pressure evolution is governed by leakage and the transition time between the two radial flow regimes (see

Figure 3.11) is a function of the rock matrix permeability. However, when the pressure front reaches the fracture tip, the pressure build-up exhibits a steeper increase due to limited diffusivity and the pressurization changes from linear in log-scale to linear with time (Mathias et al., 2011; Q. Zhou et al., 2008). Noticeably, the shorter the fracture, the earlier the deviation occurs. The deviation time for the linear evolution of pressure as a function of the logarithm of time can provide information on the fracture length or the intersection with other fractures (Eq. (3.21)). Accounting for the proper pressure propagation evolution has implications, for instance, for induced seismicity forecasting, or for the design of hydraulic stimulation (a shorter duration than necessary may be chosen).

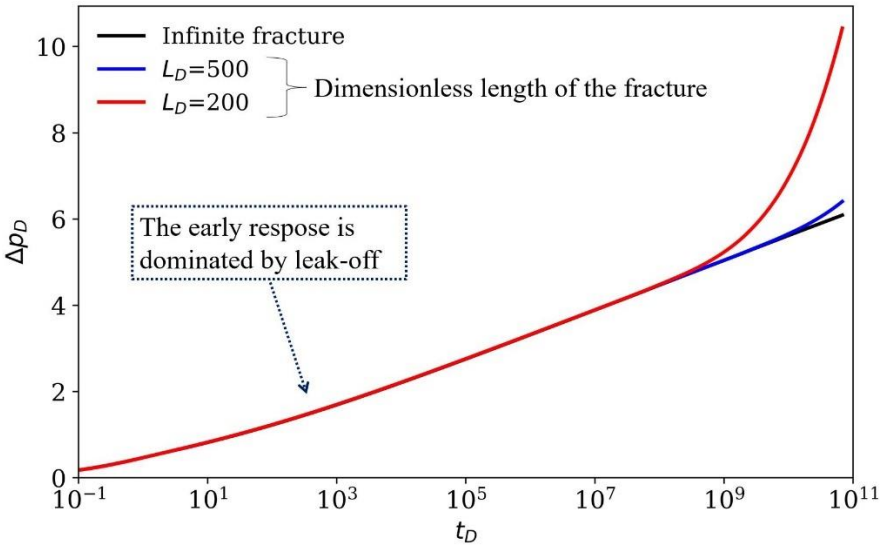

Figure 3.16 Dimensionless pressure evolution response to injection into a fracture surrounded by low-permeability rock for an infinitely acting fracture (the black line) and two finite fractures (blue and red lines for dimensionless length of 500 and 200 respectively); Note that leakage occurs since very early time, and when the pressure perturbation front reaches the fracture tip, the pressure build-up increases dramatically.

3.5 Conclusion

We have investigated the hydraulic response of water injection into a fracture surrounded by low-permeability rock. The analysis of the pressure evolution reveals that leakage into the low-permeability rock matrix impacts fluid flow. The pressure evolution follows a straight line as a function of the logarithm of time whose slope corresponds to a transmissivity that is twice the actual one when injecting into a single fracture surrounded by low-permeability rock. This slope is reached within a few seconds after the start of injection. As a result, fractures should be considered as leaky rather than being surrounded

by impermeable layers, even for very low-permeability rock matrix. The short transition time to leakage-dominated flow implies that field measurements may not show the initial transition prior to the stage in which leakage dominates. Furthermore, this leakage-dominated regime can last for a long time (several days) in low permeable formations, which may lead to wrong interpretations of the pressure evolution if leakage is neglected. Overall, our findings reveal the leaky nature of fractures and have important implications for the interpretation of injection tests and modeling of fractured media because neglecting leakage overestimates fracture transmissivity and the pressure perturbation front.

4

Implicit hydro-mechanical representation of fractures using continuum approach

4.1 Introduction

Fractures are abundant in crystalline media. Either natural or engineered, fractures provide conductive pathways for mass and energy transport, supplying opportunities for exploitation of georesources, but also potential challenges for geo-engineering applications (Adler et al., 2013). For example, in Enhanced Geothermal Systems (EGS) or water resource exploration in fractured geological media (Berkowitz, 2002), fractures are the principal pathways for productivity (Goto et al., 2021; Olasolo et al., 2016; Parisio and Yoshioka, 2020). In contrast, permeability of fractures (if present) should be as low as possible in host rocks for nuclear waste disposal (Amann et al., 2018b; Xu et al., 2020) or cap rocks for geologic carbon storage (March et al., 2018; Vilarrasa et al., 2014, 2013b, 2013a). In geo-engineering applications, fractured porous media behave under complex and fully coupled (thermo-)hydromechanical processes. For instance, fractures intersected by or in the vicinity of the injection well may open as a result of pore pressure build-up causing permeability to increase, thus attenuating pressure build-up. Quantifying the dependence of fracture transmissivity on its aperture was the subject of some debate until Tsang (Tsang, 1992) settled it by distinguishing between hydraulic (cubic law, approximately the geometric mean aperture), mass balance (mean aperture) and viscous dissipation apertures as the equivalent apertures of a parallel plate fracture with the same flow, transport, and energy dissipation as the actual fracture with spatially variable aperture. The distinction is adequate for coupled problem and support using the cubic

law, which has proven adequate for hard rocks (Dippenaar and Van Rooy, 2016; Guimerà and Carrera, 2000; Konzuk and Kueper, 2004; Witherspoon et al., 1980). This law implies a strong coupling of fluid flow and geomechanical response of the fractured media to fluid injection/production. The coupling may be further complicated by thermal effects caused by, e.g., the injection of cold water into a hot system, which not only contracts the rock but also modifies the density and viscosity of the fluid, and therefore, e. g., hydraulic conductivity (De Simone et al., 2013). The meaningful modeling of strongly coupled processes demands a cost-effective simplified yet accurate representation of the fractured medium.

The highly heterogeneous nature of fractured media, including complex networks of heterogeneous fractures (Meier et al., 2020), poses challenges to modeling approaches (Jin and Zoback, 2017) and calls for adequate representations of both matrix and fractures. One of the main challenges is to define and measure model parameters that allow the continuum scale modeling of scenarios in which fractures are either treated explicitly or considered implicitly within the porous medium itself. Explicit modeling comprises, amongst others (McLennan et al., 2010), techniques such as (1) Discrete Fracture Matrix (DFM), attempting to strike a balance between loss of accuracy by upscaling and geometric complexity (Alcolea et al., 2016; Flemisch et al., 2018; Jiang and Younis, 2017; Karimi-Fard et al., 2004; Martinez-Landa and Carrera, 2006), (2) Discrete Fracture Network (DFN), in which all fluid is assumed to be contained within the fracture network and the matrix is considered impermeable (Berrone et al., 2013; Fumagalli et al., 2019; Hyman et al., 2014; Li and Lee, 2008), and (3) Conduits (channels) Networks (CN) that represent fractured media as a network of 1D connected pipe-like elements forming a series of channels for fluid flow (Black and Barker, 2018; Cacas et al., 1990; Tsang et al., 1988). In a porous medium, the secondary permeability offered by a conductive fracture may yield an overall effective permeability much greater than the primary permeability provided by the connected pores (Neuzil and Tracy, 1981). As a result, flow occurs mainly along fractures and commonly leads to the assumption that the rock surrounding fractures is impermeable (Koudina et al., 1998; Long et al., 1982). However, this assumption generally may lead to inaccurate predictions of pressure changes. Instead, accounting for the flux between fractures and rock matrix (so-called leak-off (Geertsma and Haafkens, 1979)) improves the predictions (Lin and Yeh, 2021).

Both explicit and implicit approaches present advantages and disadvantages. Explicit approaches are simple and render enhanced accuracy in the representation of fractures.

However, they entail complex geometries and high computational costs (Pandey et al., 2017; Salimzadeh et al., 2018; Watanabe et al., 2012). The conventional implicit approach, called the continuum method, includes both fractures and matrix in an equivalent porous medium. Transforming discrete fractures into continuum representations requires upscaling (Bonnet et al., 2001; Farmer, 2002; Gerritsen and Durlofsky, 2005; Lee et al., 2001; Renard and Ababou, 2022). Upscaling can be performed analytically or numerically. Analytical approaches (Liu et al., 2016; Oda, 1985) are generally based on geometry and/or flow features. Geometry-based upscaling approaches superimpose a grid onto the fracture network in which the corresponding fracture hydraulic conductivity (actually, any given property) is mapped on the grid formed by the intersections between fractures and the boundaries of the grid cells (Roubinet et al., 2010; Svensson, 2001). In flow-based upscaling, local steady-state solutions to the Laplace problem are usually employed to back-calculate effective permeabilities using Darcy's law (Durlofsky, 1991; Jackson et al., 2000; Oda, 1985; Sánchez-Vila et al., 1995). In numerical-based methods, representative sub-grid scale DFN simulations can be used to obtain upscaled relationships including elements of the permeability tensor (Bogdanov et al., 2003; T. Chen et al., 2018; Karimi-Fard and Durlofsky, 2016; Romano et al., 2020).

The most common implicit numerical approaches include Equivalent Porous Medium (EPM, also known as the single-continuum approach), Stochastic Continuum (SC), and Dual Continuum Medium (DCM). If fractures are not well connected, the EPM method may be employed to define grid block-scale effective properties describing the behavior of the entire fractured rock mass (Botros et al., 2008; Jackson et al., 2000; Sweeney et al., 2020). There are several flow-based upscaling procedures such as the numerical upscaling proposed by (Durlofsky, 1991) where equivalent grid-block permeabilities are computed by solving the fine scale pressure diffusion equation using effective medium theory representing fractures as thin ellipsoids embedded in a matrix (Sævik et al., 2014, 2013), and aggregation-based method (Hui et al., 2018). However, there is no separation of the characteristic lengths in the fractures and in the matrix. Hence, upscaling to the average characteristics often leads to low model accuracy, even from the conceptual standpoint. For example, the secondary permeability provided by conductive fractures often yields an average effective permeability several orders of magnitude larger than the primary permeability of connected pores in the matrix, which leads to a different and generally more clustered pore pressure distribution through the equivalent porous medium than the expected one (Zareidarmiyan et al., 2021). Therefore, EPM approaches fail to deliver

reliable solutions whenever fracture spacing is in the order of the reservoir characteristic length (Zareidarmiyan et al., 2021).

SC approaches aim to develop equally-likely heterogeneous continua with stochastic representations of effective properties based on actual properties of the underlying fracture network (Neuman, 2005). The double or multi-continuum medium (DCM) approach is a preferable option among implicit approaches due to the more accurate representation of the embedding matrix. However, unconnected fractures can still communicate via the matrix (whose permeability is considered), making it difficult to identify hydraulic backbones (the dominating high transmissive structures) (Matthäi and Belayneh, 2004). In the presence of considerable matrix permeability, dual-permeability and dual-porosity models are advantageous as they represent fractures and matrix as separate continua that interact with each other through transfer functions. Dual-permeability models permit flow between matrix blocks, while dual-porosity models consider no communication between matrix blocks (Aguilar-López et al., 2020; Lemonnier and Bourbiaux, 2010; Warren and Root, 1963). Figure 4.1 shows a schematic of aforementioned methods and their relatively approximate accuracy versus each other and against the "true" fractured porous medium that is not possible to be fully characterized at all length scales (Neuman, 1990).

We introduce another implicit approach treating fractures as continuum layers, adjacent to the porous matrix, which are upscaled individually. This approach, termed Equivalent Fracture Layer (EFL), has the advantages of implicit (moderate computational cost), while displaying an accuracy similar to that of explicit methods (Figure 4.1). However, the question of how to choose the assigned properties of the continuum-equivalent individual fracture models to reproduce the behavior of discrete fractures remains open. Property assignment is a non-trivial problem aggravated by the large differences between fracture aperture (usually μm to mm) and reservoir characteristic length (generally m to hm) (Andrés et al., 2021; Zareidarmiyan et al., 2020), which leads to a negligible fracture volume compared with the volume of the surrounding medium (Faybishenko et al., 2015). In fact, the lower-dimensional nature of fractures with an extreme area-aperture ratio poses a great challenge to numerical simulations (Lei et al., 2017; Thomas et al., 2020; Yoshioka et al., 2019) using either implicit or explicit representations of fractures (Berre et al., 2019; Lepillier et al., 2020).

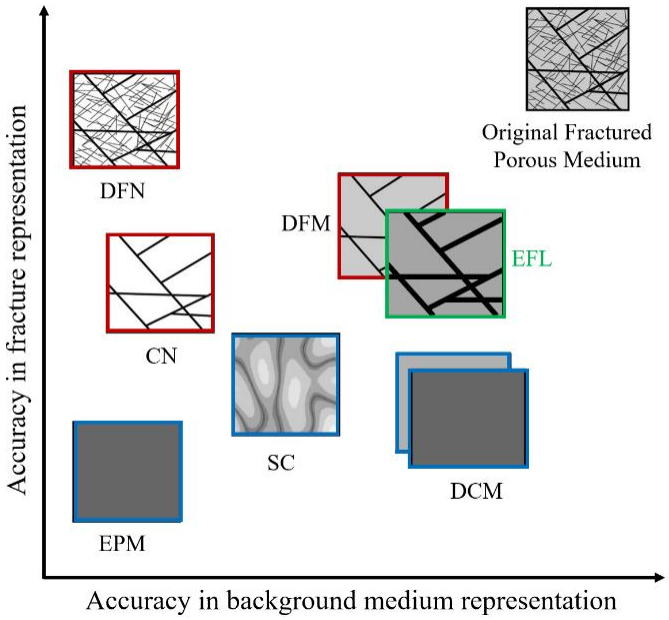

Figure 4.1 Sketch comparing the accuracy of fractures and matrix modelling of different representation approaches. The suggested approach, EFL, (green frame) has the advantages of implicit approaches (blue) while generally yielding more accurate results like explicit approaches (red). Adapted from (Berre et al., 2019; Viswanathan et al., 2022)

Continuum methods are increasingly being combined with discrete fracture and matrix methods (DFM) (Ji et al., 2012; Joyce et al., 2014; Lee et al., 2001). Such approaches, familiarly known as hybrid methods, can incorporate diverse implicit-explicit method combinations. Several complex models coupling DFM and multi-continuum approaches have been developed, e.g., a dual-permeability hybrid model combining DFM and the dual-permeability model (Jiang and Younis, 2016). While complex hybrid models have demonstrated the capability of producing accurate results, the issue of expensive computational resources remains. Therefore, simpler hybrid models are preferred whenever they are applicable. The simplest hybrid model known as the single-porosity hybrid model can be considered a simplified DFM model with reduced complexity. This model explicitly represents large fractures in a fractured medium and represents small-scale fractures and the matrix using a single continuum known as a pseudo-matrix (Lee et al., 2001; Li and Lee, 2008; Rogers et al., 2007). To make this model a step simpler, the proposed method (EFL approach) can be used to upscale the explicitly represented fractures to an equivalent-continuum layer.

In this chapter, we propose a new EFL approach to accurately model not only fluid flow, but also the geomechanical response in fractures with arbitrary orientation,

represented as equivalent continua at a numerically tractable scale (>>μm). For illustration purposes, we focus on a single fracture embedded in low-permeability rock matrix, resulting in distinctive flow time scales. The manuscript presents first the methodology for calculating the equivalent hydromechanical properties of a fracture, analytically upscaled as a layer with a thickness much larger than the actual aperture. Second, we verify the procedure by considering fluid injection into a fracture embedded in a low-permeability rock matrix by comparing results of a finite element model including the real aperture (reference model) with those of models including the upscaled thicknesses of the equivalent fracture layer. Next, we validate the approach by comparing numerical results against field data acquired during a hydraulic stimulation at the Bedretto Underground Laboratory for Geosciences and Geoenergies in Switzerland. Finally, we discuss the implications of our findings to introduce another simple, yet, practical upscaling approach for fractured media.

4.2 Methodology

4.2.1 Governing equations

Transient fluid flow within a saturated fracture confined by a low-permeability rock matrix is governed by the flow equation (Bear, 1972)

$$\nabla \cdot (T \nabla h) = S \frac{\partial h}{\partial t} + r_s \tag{4.1}$$

where T [L^2T^{-1}] is transmissivity, $h = p/\gamma_w + z$ [L] is hydraulic head, p is fluid pressure [$ML^{-1}T^{-2}$], γ_w [$ML^{-2}T^{-2}$] is the specific weight of the fluid, z [L] is elevation from an arbitrary plane, S [-] is the storage coefficient, t [T] is time and r_s [$ML^{-3}T$] is a sink/source term, including from/to the matrix, which can be important during transient periods even for low permeability matrix (See (Carrera and Martinez-Landa, 2000) for details). The mechanical process is solved by satisfying momentum balance that, neglecting inertial terms, reduces to the equilibrium of stresses

$$\nabla \cdot \boldsymbol{\sigma} + \mathbf{b} = \mathbf{0}, \tag{4.2}$$

where σ [$ML^{-1}T^{-2}$] is the total stress tensor and b [$ML^{-2}T^{-2}$] is the vector of body forces.

The relation between stress, strain, and pore pressure for isotropic materials within the linear elasticity theory for continuous media is given by Hooke's law

$$\Delta\boldsymbol{\sigma} = K\varepsilon_v\mathbf{I} + 2G\left(\boldsymbol{\varepsilon} - \frac{\varepsilon_v}{3}\mathbf{I} + \frac{\alpha}{2G}\Delta p\mathbf{I}\right), \tag{4.3}$$

where ε_v [-] is the volumetric strain, $\boldsymbol{\varepsilon}$ [-] is the strain tensor, $K = E/\big(3(1-2\nu)\big)$ [$ML^{-1}T^{-2}$] is the bulk modulus, $G = E/\big(2(1+\nu)\big)$ [$ML^{-1}T^{-2}$] is the shear modulus, E [$ML^{-1}T^{-2}$] is Young's modulus, ν [-] is the Poisson ratio, and α [-] is the Biot effective stress coefficient. In this work, we assume α =1, which leads to the strongest hydromechanical coupling (Zimmerman, 2000).

Equation (4.3) can be coupled with the flow equation through fluid pressure. Acknowledging that external loading and compressibility of the solid phase may affect water storage in the fracture, fluid mass conservation can be written as

$$\frac{\phi}{K_f}\frac{\partial p_f}{\partial t} + \frac{d}{d\,t}(\nabla\cdot\mathbf{u}) + \nabla\cdot\mathbf{q} = r_s, \tag{4.4}$$

where ϕ [-] is porosity, K_f [$ML^{-1}T^{-2}$] is the fluid bulk modulus, u [L] is the displacement vector and q [L^3T^{-1}] is the fluid flux, given by Darcy's law. Note that Equations (4.3) and (4.4) can also be coupled through the volumetric strain, which can be expressed as the divergence of the displacement vector.

4.2.2 The embedded model

Consider an open fracture with hydraulic aperture b_f [L]. Fracture permeability is assumed to be isotropic and given by $\mathbf{k} = k_f(\mathbf{I} - \mathbf{M})$ [L^2], where $\mathbf{I}$ [-] is the identity matrix, $\mathbf{M}$ is the tensor of the fracture plane ($M_{ij} = m_i m_j$, where $\mathbf{m}$ is the unit vector perpendicular to the fracture), and

$$k_f = \frac{b_f^3}{12a} \tag{4.5}$$

where a [L] denotes a somewhat arbitrary width for each fracture (strictly speaking the cubic law expresses the fracture permeability as $k_f = b_f^2/12$). When dealing with sets of parallel fractures, a is usually taken as the mean distance between fractures. Here, we seek an equivalent medium, so we take $a = b_f$ (Olsson and Barton, 2001). Equation (4.5) highlights the strong nonlinear relationship between fracture aperture and flow (Adler et al., 2013). Acknowledging the strain dependence of intrinsic permeability is needed for coupled modeling in fractured media (Olivella and Gens, 2005). Variable fracture

permeability can be computed by taking into account that aperture changes are a function of volumetric strain as (Olivella and Alonso, 2008)

$$b_f = b_0 + (\varepsilon - \varepsilon_0)a \leq b_{max}, \tag{4.6}$$

$$k_f = k'_m + \frac{(b_0 + a\Delta\varepsilon)^3}{12a}, \tag{4.7}$$

where k'_m [L^2] is the intrinsic permeability of the matrix within the fracture layer, b_0 [L] and b_{max} [L] are the initial and maximum fracture aperture, $\Delta\varepsilon$ [-] is the volumetric strain change ($\Delta\varepsilon = \varepsilon - \varepsilon_0$), and ε_0 [-] is a threshold strain.

4.2.3 Equivalent hydromechanical properties of a fracture

Three entities play a role in the equations governing HM problems: flux, storage, and displacement. These which are controlled by transmissivity, storage coefficient, and stiffness, respectively. The adopted upscaled parameters of the equivalent fracture layer must represent the actual behavior of the real fracture (Figure 4.2). In other words, both the actual fracture and the equivalent fracture layer should have the same transmissivity, storativity, and stiffness, both initially and along its time evolution.

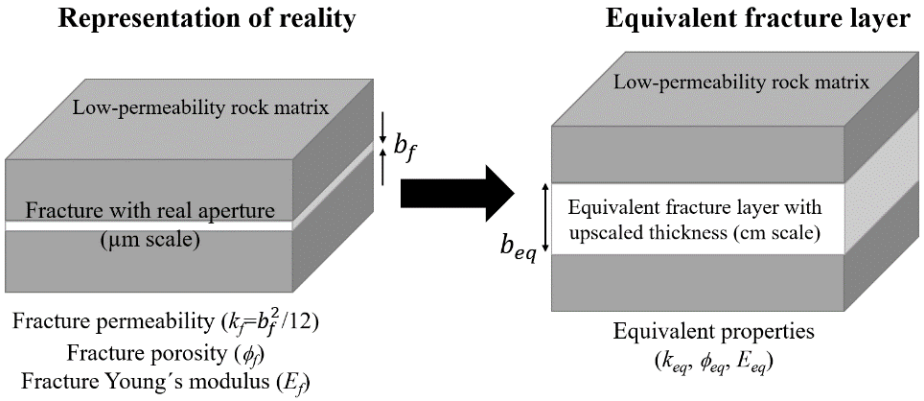

Figure 4.2 Concept of the equivalent fracture layer representing a real fracture

The transmissivity of a fracture is given by the product of hydraulic conductivity and aperture

$$T_f = \frac{\rho g}{\mu} k_f b_f = \frac{\rho g}{\mu} \frac{b_f^3}{12}, \tag{4.8}$$

where ρ [ML^{-3}] is fluid density, g [LT^{-2}] is gravity, and μ [$ML^{-1}T^{-1}$] is fluid viscosity. The dependence of transmissivity on b_f^3 is the essence of the well-known cubic law (Brush and Thomson, 2003; Witherspoon et al., 1980; Zimmerman and Yeo, 2000) and expresses that fracture transmissivity is extremely sensitive to small changes in aperture. The Equivalent fracture layer with thickness of b_{eq} should carry the same flow rate as the actual fracture:

$$T_{eq} = T_f \rightarrow k_{eq} b_{eq} = k_f b_f, \tag{4.9}$$

where k_{eq} [L^2] is the intrinsic permeability of the equivalent fracture layer. When equating the actual and upscaled fracture properties to represent the actual fracture aperture (b_f) by an equivalent continuum layer with a thickness b_{eq}, the upscaled equivalent hydromechanical fracture transmissivity, stiffness, and storativity become a function of the equivalency coefficient

$$\xi = \frac{b_f}{b_{eq}}. \tag{4.10}$$

To have the same transmissivity, equivalent parameters can be derived from equations (4.7) and (4.9) as

$$k'_{meq} = \xi k'_{mf}, \qquad b_{0eq} = b_{0f}, \qquad b_{max.eq} = b_{max.f}, \qquad a_{eq} = \frac{a_f}{\xi}, \qquad \varepsilon_{eq} = \xi \varepsilon_f, \tag{4.11}$$

where the subscript f and eq denote the properties of the fracture with its actual aperture and equivalent fracture layer, respectively.

The mechanical behavior of fractures can be characterized by normal and shear stiffnesses (Puig Damians et al., 2022; Yu et al., 2015)

$$\sigma_n = \lambda_n u_n, \qquad \tau_s = \lambda_s u_s \tag{4.12}$$

where σ_n [$ML^{-1}T^{-2}$] and τ_s [$ML^{-1}T^{-2}$] are normal and shear stresses, λ [$ML^{-2}T^{-2}$] is stiffness, and u [L] is displacement. The superscripts n and s denote normal and shear components, respectively. In general, one may expect λ_s to be itself a tensor, especially if the fracture is shear origin. In such case, irregularities tend to align with shear direction (orthogonal to the open channels), so that λ_s will be initially smaller in this direction. For the sake of simplicity and assuming that the impact of the initial irregularities diminishes as the fracture opens, we will assume scalar λ_s. Normal and shear stiffnesses of an arbitrary-oriented fracture can be obtained as

$$\lambda_n = \frac{E_{of}}{b_f}, \qquad \lambda_s = \frac{G}{b_f}, \tag{4.13}$$

where E_{of} is an apparent oedometric modulus of the fracture. If the deformation out of the fracture plane is constrained, the modulus E_o is defined as

$$E_{of} = \frac{1-\nu}{(1+\nu)(1-2\nu)} E_f. \tag{4.14}$$

From equations (13) and (14), fracture stiffnesses can be determined as

$$\lambda_n = \frac{1-\nu}{(1+\nu)(1-2\nu)} \frac{E_f}{b_f}, \qquad \lambda_s = \frac{E_f}{2b_f(1+\nu)}. \tag{4.15}$$

where E_f and ν are the apparent Young's modulus and Poisson ration of the fracture. Maintaining normal and shear stiffnesses, the equivalent Young's modulus and Poisson's ratio of the equivalent fracture layer can be obtained by

$$E_{eq} = \frac{3\lambda_n - 4\lambda_s}{\lambda_n - \lambda_s} k_s b_{eq}, \qquad \nu_{eq} = \frac{\lambda_n - 2\lambda_s}{2(\lambda_n - \lambda_s)}, \qquad with\ \lambda_n > 2\lambda_s. \tag{4.16}$$

In principle, the aperture and stiffness of the real fracture can be estimated (or measured) and, from them, the equivalent properties of the upscaled fracture can be easily calculated.

Finally, both layers should have same storativity as

$$S_{eq} = S_f \rightarrow S_{seq} b_{eq} = S_{sf} b_f, \tag{4.17}$$

where S_s [L^{-1}] is the specific storage (i.e., $\rho g(\phi\beta_w + \beta_x)$), β_w [$M^{-1}LT^2$] is the compressibility of the fluid, and $\beta_x = 3(1\text{-}2\nu_x)/E_x$ [$M^{-1}LT^2$] is the bulk compressibility of the layer x (either fracture (β_f) or equivalent layer (β_{eq})). Expanding the equation, we can calculate equivalent porosity as $\phi_{eq} = \xi\phi_f$.

4.3 Model verification and validation

4.3.1 A single fracture embedded in a low-permeability matrix

4.3.1.1 Model setup

We numerically modeled a single circular fracture in which water is injected into its center through a well with radius r=0.1 m (Figure 4.3). As reference, we modeled the fracture with actual properties and compared results with implicitly upscaled models. The axisymmetric model represents a 100-m radius horizontal circular fracture with uniform thickness (10 µm as real aperture) embedded between two 10-m thick layers of low-permeability rock at a depth of 1 km. The large radial extent of the fracture is such that the nature of the outer boundary, i.e., prescribed hydrostatic pressure or no flow, does not affect results during the injection. Both fracture and rock matrix continua have homogeneous and isotropic properties. Boundary conditions include zero horizontal displacement at both inner and outer lateral boundaries and zero vertical displacement at the bottom boundary. A constant flow rate q=50 kg/s/m^2 is injected at the fracture segment of the inner boundary. A constant initial stress field (σ_x=15 MPa, σ_y=25 MPa, σ_z=15 MPa) and a linear hydrostatic pressure gradient (10 and 10.2 MPa at model top and bottom, respectively) were applied to the model. The fracture is assumed to be clean, i.e., actual porosity is set to 1, and its initial intrinsic permeability is calculated using equation (5) and assuming a=b_f, which results in k_f = $8.33 \cdot 10^{-12}$ m^2. Input parameters for the matrix, fracture, and equivalent fracture layers are listed in Figure 4.3 and Table 4.1.

We built three additional models with increasing thickness of the equivalent fracture layer and applied the equivalent properties, i.e., permeability, porosity, and Young's modulus (Poisson's ratio is independent of the equivalent layer thickness) using the relationships derived in the section 2.3. A common structured finite element mesh consisting of 12,322 quadrilateral elements is used as spatial discretization for all models. The fracture consists of 5 rows of elements, whereas the matrix slabs contain 30 rows of elements in the vertical direction. The elements in the matrix are concentrated toward the fracture-matrix interfaces to capture the leak-off more accurately. Also, for the sake of accuracy, finite elements are concentrated towards the well to properly captured fluxes caused by injection and corresponding pressure variations in both fracture and matrix. We performed a mesh sensitivity analysis to ensure that further refinement does not affect the results, not displayed here for the sake of brevity. The models simulate water injection at a constant rate for 30 hours and are run twice, considering both constant and variable

fracture permeability depending on deformation. We analyzed the pressure evolution at the injection well (r=0.1 m) and the hydromechanical response along the fracture at the end of the injection. The fully coupled hydromechanical numerical models were implemented using the finite element software Code Bright (Olivella et al., 1996, 1994).

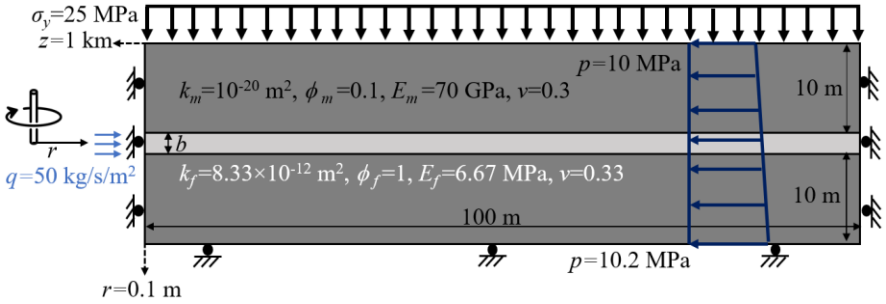

Figure 4.3 Sketch of the axisymmetric model used for verification purposes: geometry, boundary, and initial conditions. Input parameters are indicated in the insets, where subscripts m and f denote matrix and fracture respectively (see also Table 4.1)

The injected volumetric flow rate into a fracture, Q [L^{3}T^{-1}], must be conserved when upscaling fracture thickness with the equivalent fracture layer approach. Given that the flux injected into a layer through a fully penetrating well equals $q = Q/A$, where A [L^2] is the cross-sectional area to flow, i.e., $2\pi r_w w$, r_w [L] being the radius of the well and w [L] the thickness through which fluid is injected, the equivalent injection flux into the equivalent fracture layer, is $q_{eq} = \xi q_f$ where $q_f = Q/(2\pi r_w b_f)$ is the injection flux for the actual fracture.

Table 4.1 Input parameters for the fracture and equivalent fracture layer models used for verification purposes

Fracture aperture (m)	$\xi = \frac{b_f}{b_{eq}}$	***Fracture Permeability (m^2)***	***Porosity***	***Injection flux (kg/s)***	***Young´s modulus (MPa)***
Original fracture					
10^{-5}	1	$8.33\cdot10^{-12}$	1	50	6.67
equivalent fracture layer models					
0.001	10^{-2}	$8.33\cdot10^{-14}$	10^{-2}	0.5	667
0.01	10^{-3}	$8.33\cdot10^{-15}$	10^{-3}	0.05	6670
0.1	10^{-4}	$8.33\cdot10^{-16}$	10^{-4}	0.005	66700

4.3.1.2 Numerical results

Both the pore pressure evolution at the injection well and the radial pressure distribution were reproduced accurately by the models with equivalent fracture layers compared to the reference model with explicit fracture representation (Figure 4.4). The pressure evolution curves (in Figure 4.4a) follow the typical Hantush leaky solution (Hantush, 1960, 1956). At beginning, after a short transition, it follows Theis solution (Theis, 1935) as storage in and leakage into the matrix are neglected, then during a transition period leak-off starts to play a role and decreases the pressure build-up. For the time scale of our analysis, i.e., 30 h, the low-permeability of the rock matrix does not allow the pressure evolution curve to reach to the fracture-matrix Theis solution (where both fracture and matrix act as a single system with steady state leakage and combined storage). Considering variable permeability decreases pressure build-up due to permeability enhancement since early times (less than a second) when volumetric strain starts to accumulate (Figure 4.4a, blue curves). Constant injection in the fracture forms a conical pressure profile versus radial distance (Figure 4.4b).

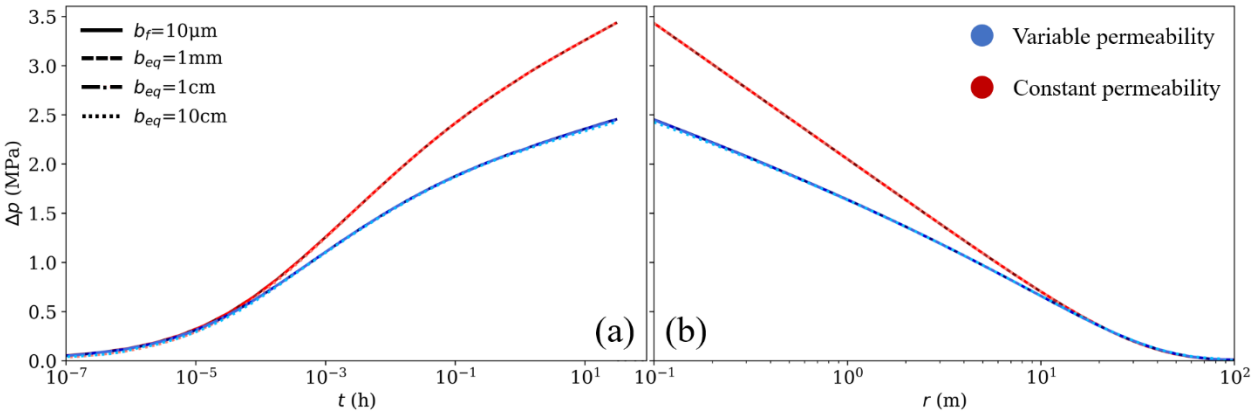

Figure 4.4 a) Pressure evolution at the injection well for reference models (actual fracture aperture; solid lines) and models with equivalent fracture layer for both constant (red lines) and variable (blue lines) permeability during constant flow injection; line styles correspond to different fracture apertures. b) Radial pressure profile along the horizontal mid-line of the fracture at the end of the injection (30 h)

Pressure build-up in the variable permeability model with b_{eq}=10 cm (blue dotted line in Figure 4.4a) starts to slightly deviate from the reference curve after ca. 2 hours of injection. This deviation is caused by more permeability enhancement ratio in that model compared to other models, which means transmissivity is no longer maintained constant for the upscaled model (Figure 4.5). In other words, the smaller is the equivalent aperture, the closer the model reproduces the reference case, as expected. This deviation could limit

the upper bound of the upscaled aperture for an equivalent fracture layer since the coupled hydromechanical response not any more reflect the reference solution. However, models with 1 cm and 1 mm equivalent apertures yield well fitted results.

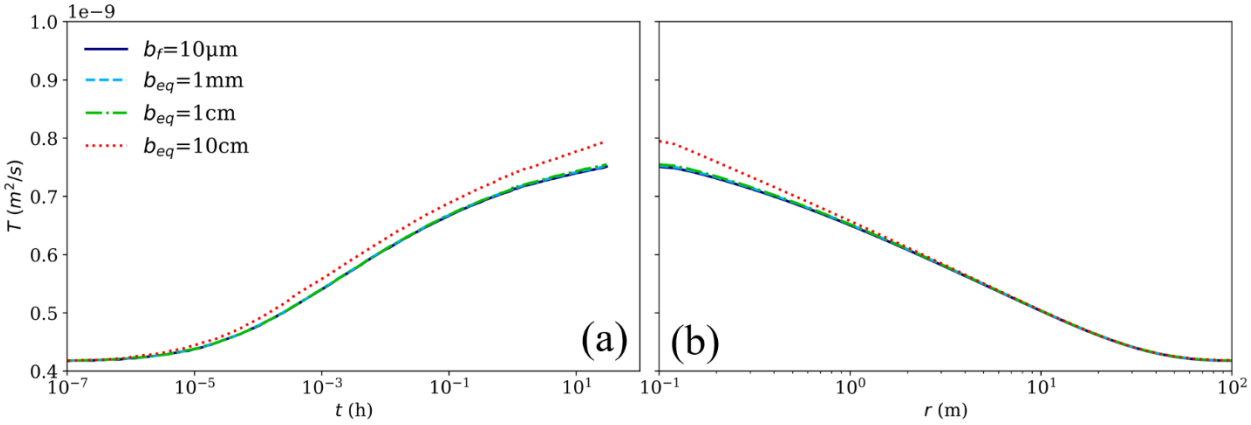

Figure 4.5 Transmissivity enhancement (a) and profile along the horizontal mid-line of the fracture at the end of the injection (30 h) (b) caused by accumulated deformation in the reference model (solid lines) and models with equivalent fracture layers (variable permeability cases). The magnitude orders of permeability are defined during upscaling, yet, the enhancement rates are similar in all models except b_{eq}=10 cm model which shows more enhancement

The embedded model employed here to account for variable permeability is a function of volumetric strain and discrepancy in models with larger equivalent aperture (i.e., 10 cm) stems from a different mechanical response of the fracture. Figure 4.6 shows stress profiles along the horizontal mid-line of the fracture, where lower compressive stresses are mobilized around the injection well at the end of the injection (30 h) for the thickest equivalent fracture layer. It is worth mentioning that the differences between the mechanical responses of the b_{eq}=10cm models against the reference model are smaller in the variable permeability model because of the lower pressure build-up compared to the constant permeability models (Fogure 4.4a).

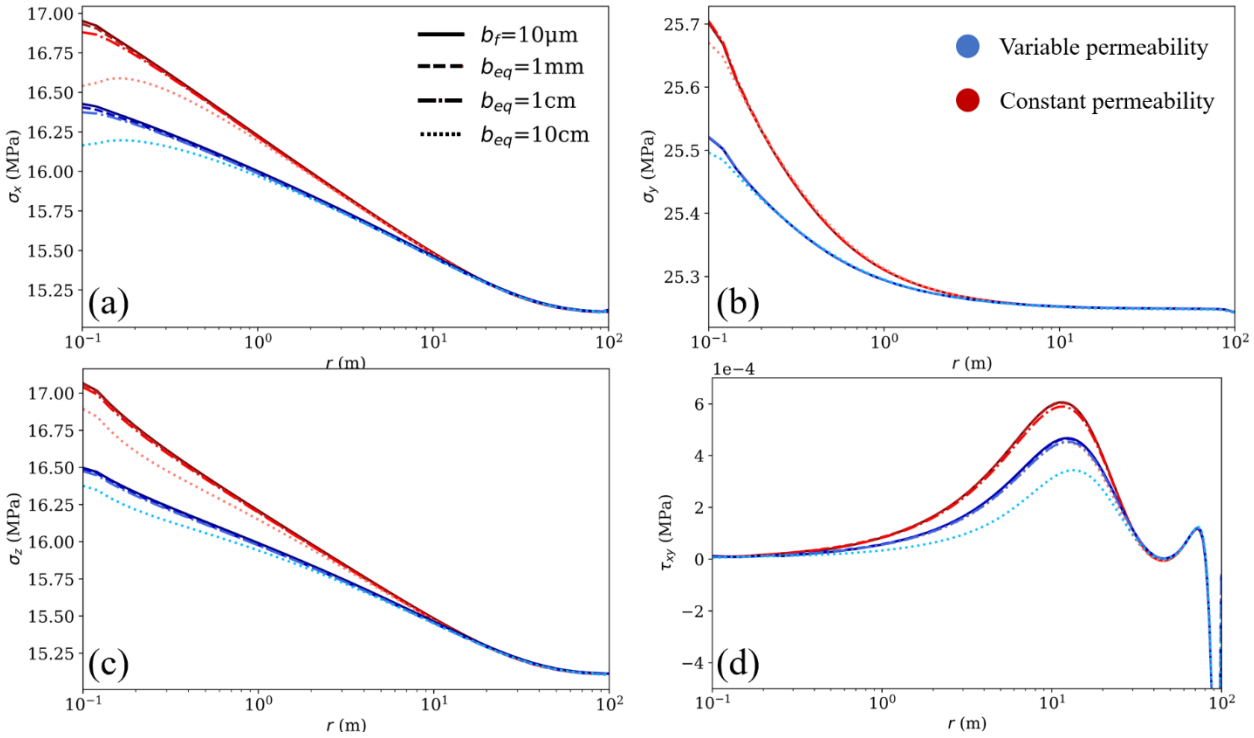

Figure 4.6 Profiles of stress components along the horizontal mid-line of the actual fracture and equivalent layers for both constant (red) and variable (blue) permeability models

Lower pressure build-up leads to smaller fracture opening in variable permeability models. Fracture layer apertures open around 3 and 2.2 μm for constant and variable permeability models, respectively (Figure 4.7; opening is calculated based on displacement difference of top and bottom of the fracture). Although b_{eq}=10 cm model reproduces the pressure evolution better in the constant permeability model in comparison to the variable permeability model (Figure 4.4a), it is less accurate in reproducing aperture enhancement in the constant permeability model. Note that the variable permeability models represent the actual fracture behavior more realistically than constant permeability models because fractures open in response to injection-induced overpressure, yielding significant permeability enhancement as a result of the cubic law (equation 4.5).

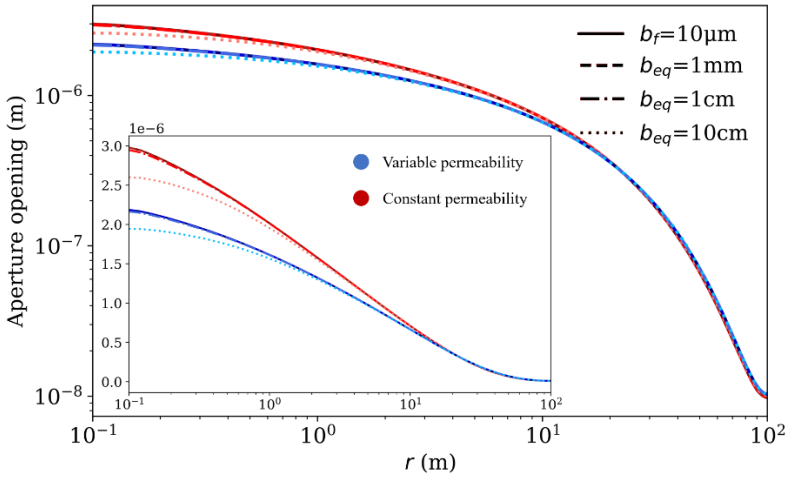

Figure 4.7 Fracture aperture change along the horizontal mid-line of the actual fracture (solid) for both constant (red) and variable (blue) permeability upscaled models in log-log and semi-log scales at the end of the injection (30 h). Aperture changes are calculated by displacement difference between top and bottom of the fractures

Vertical displacement at the top of the overlying rock layer in response to fluid injection presents a constant value until a radius of around 3 m and it follows a typical bell shape further away (Figure 4.8). The displacement in variable permeability models is lower due to the smaller pressure build-up (Figure 4.4b). The discrepancy of the b_{eq}=10 cm model compared with the reference solution is around 14% and it is related to differences in the fracture aperture changes (Figure 4.7).

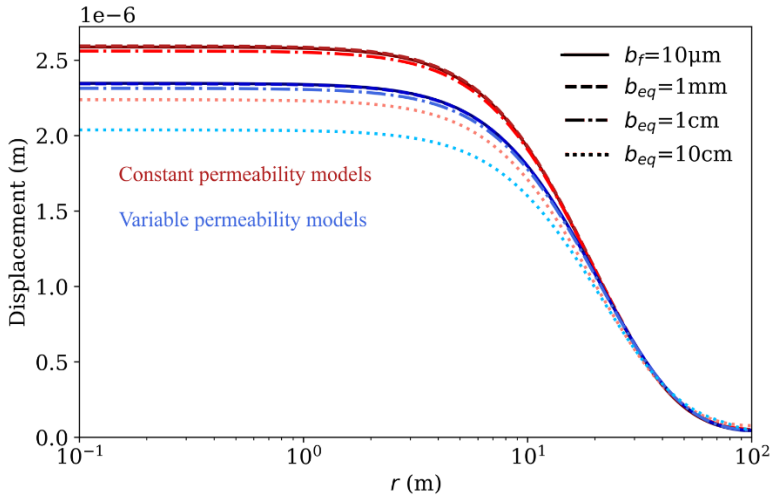

Figure 4.8 Vertical displacement at the top boundary of the model versus radial distance at the end of the injection (30 h)

4.3.2 Bedretto experiment

4.3.2.1 Model setup

We validated our upscaling approach of implicitly representing fractures with an equivalent fracture layer by comparing numerical results with field data acquired during the hydraulic stimulation of a fracture at the Bedretto Underground Laboratory for Geosciences and Geoenergies (BULGG; see more detailed information in http://www.bedrettolab.ethz.ch). BULGG enables medium- to large-scale in-situ experiments with a focus on hydraulic stimulation and fault reactivation (Figure 4.9). The overburden directly above the laboratory is approximately 1500 m, providing conditions that start to resemble realistic EGS systems (scale 1:3 approximately) (Meier et al., 2020, 2022). To characterize the rock mass, several boreholes were drilled perpendicular to the tunnel axis with lengths ranging from 100 m to 400 m MD (Measured Depth; Figure 4.9c). A large number of hydraulic stimulation tests have been and are being performed at BULGG to stimulate the intersected fractures (Meier et al., 2022). Based on stress measurements (Bröker and Ma, 2022), BULGG is in a normal faulting and/or strike-slip stress regime, and the rock mass is close to be critically stressed (David et al., 2020; Gischig et al., 2020; Ma et al., 2019).

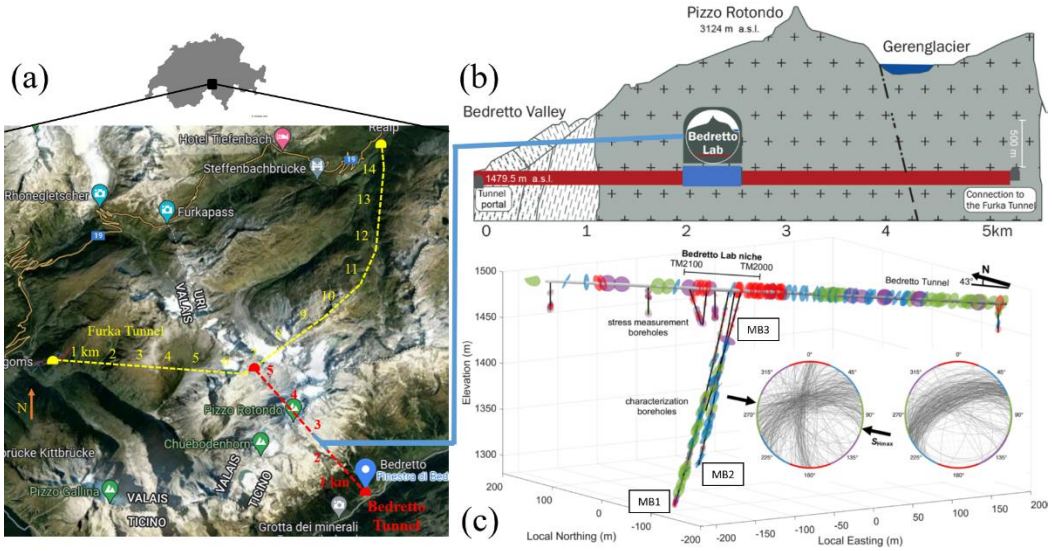

Figure 4.9 a) Location and trace of the Bedretto gallery excavated in Rotondo granite in Switzerland. b) Cross-sectional view of the Bedretto lab through the tunnel (Ma et al., 2022; Shakas et al., 2020). c) Configuration of the MB1, MB2 and MB3 boreholes with respect to the Bedretto Tunnel. Fractures and fault zones, mapped along the tunnel and intersected by the boreholes, are colored according to fracture strike

We developed a 2D plane-strain numerical model to simulate the hydraulic stimulation in Bedretto. It comprises an inclined plane dipping (on average) 42º downwards following the trajectory of the boreholes and has a large extension covering around 75 km^2 of the site (Figure 4.10a). The Bedretto gallery is located at the center of the upper boundary of the model (Figure 4.10b) and the bottom boundary is at a true vertical depth of 5000 m (-7472.4 m in the inclined model). The model comprises the main characterization boreholes (MB1 to MB4) and the two main stimulation boreholes (ST1 and ST2) as well as the major fracture and shear zones identified through borehole logging and geological structural analysis (Ma et al., 2022; Meier et al., 2020). We used an unstructured mesh that consists of 27,248 quadrilateral elements and 27,420 nodes and is highly refined at the closest vicinity of the modeled fracture/shear zones and the boreholes. Both sides and the bottom of the model are fixed against lateral and vertical displacements, respectively. A linear distributed fluid pressure and initial stresses are applied to the model from top to bottom (Figure 4.10a).

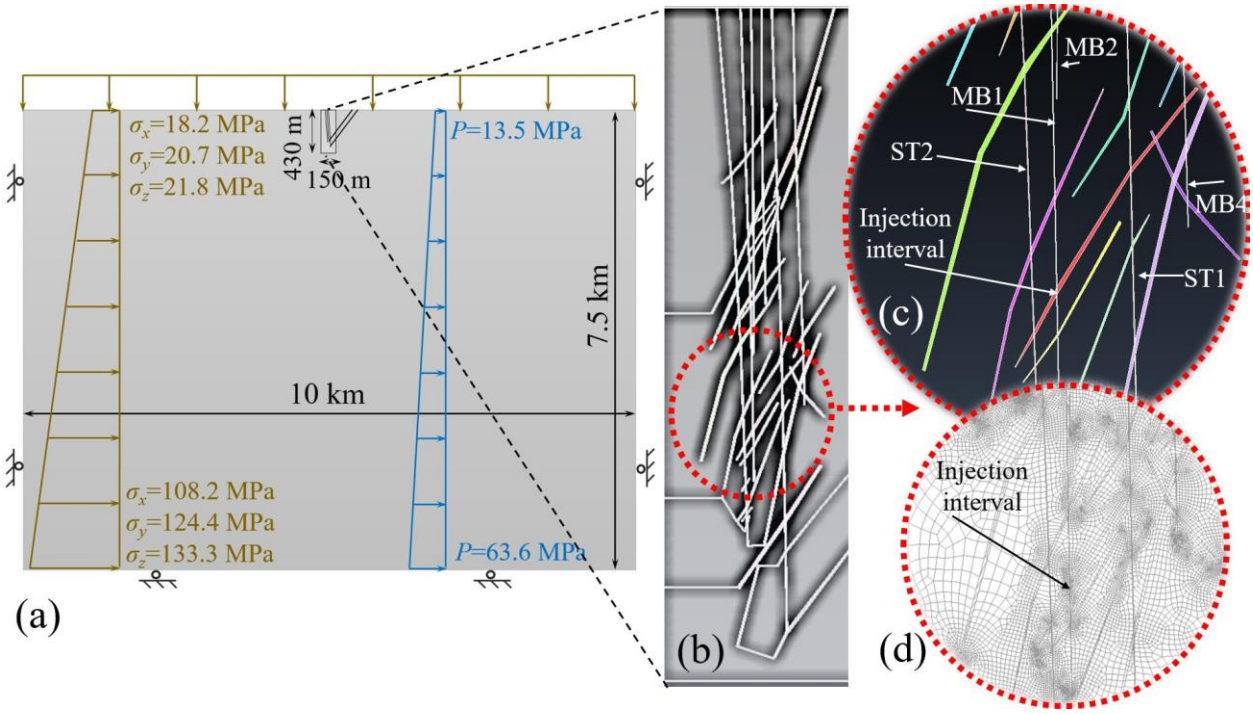

Figure 4.10 a) Model geometry, boundary and initial conditions, and state of stress at top and bottom boundaries. b) Configuration of wellbores and the identified fracture/shear zones within the model. c) Detailed view around the stimulated fracture (in red). d) Mesh configuration of the same detailed view

Fractures are modeled as an elastic continuum medium with homogeneous hydromechanical properties. We used the embedded model to compute fracture

permeability changes according to Equation (4.7). As a result, fracture permeability varies with distance from the injection well, being largest near the well and approaching the initial value further away from the pressurization front, where the fracture has not undergone overpressure-induced opening. Table 4.2 lists the equivalent parameters of the stimulated fracture and rock matrix properties used in the numerical simulation. The modeling sequence includes the tunnel drainage effect on pore pressure during and after excavation and the subsequent consolidation covering 40 years (since the end of the tunnel excavation). The injection interval is within borehole MB1 (Figure 4.10c), in which water is injected through an isolated section into the fracture at a measured depth of 267 m (true vertical depth 188.8 m)

Table 4.2 Input parameters for rock matrix and equivalent fracture layer

	E (GPa)	ν	ϕ	k (m^2)			
				k_m (m^2)	b_0 (m)	a (m)	b_{max} (m)
Fracture (equivalent)	23	0.37	0.005	5×10^{-17}	2.25×10^{-6}	0.01	1.34×10^{-4}
Rock matrix	46	0.37	0.005	2.5×10^{-18}			

4.3.2.2 Simulation of the field injection experiment

The numerical simulation covers the first 40 minutes of the field experiment, which overall lasted 8 hours). Figure 4.11 compares the temporal evolution of the generated overpressure at the injection interval predicted by the numerical model against the experimental data. The model accurately reproduces field measurements, with a small discrepancy at the beginning of each injection steps, which attribute to non-modelled equipment compliance effects. Despite these small deviations, (1) simulated and measured trends are very similar, and (2) simulated injection pressure fits well the field data from the mid-times of each injection step.

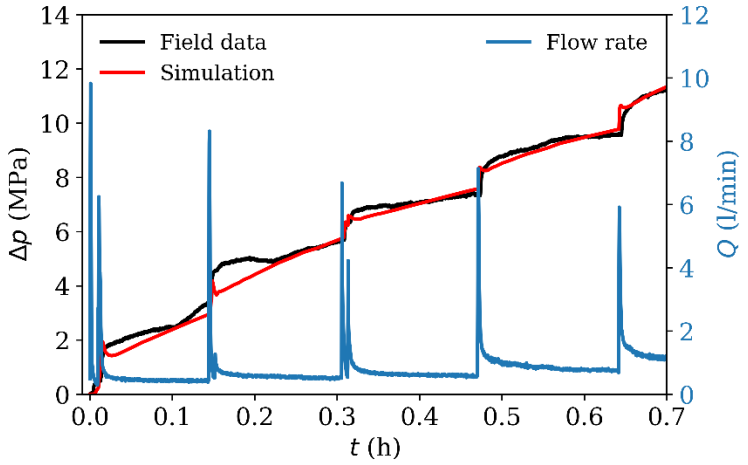

Figure 4.11 Pressure evolution at the injection interval reproduced by the numerical model (red line) against injection pressure measured at the field (black line) as well as fluid injection rate (blue line)

The embedded model used in this simulation enhances permeability of the fracture in the vicinity of the injection interval (around 6 m) after 40 min of injection (Figure 4.12). Note that the behavior of the fracture is assumed to be elastic and the permeability enhancement in the embedded model is based on elastic strains only. Permeability linearly increased around 7% at a point near the injection interval after 40 min of injection which was not enough to reach the jacking pressure. Notably in the vicinity of ST2 well the permeability of the fracture has a spike governed by the permeability of the well.

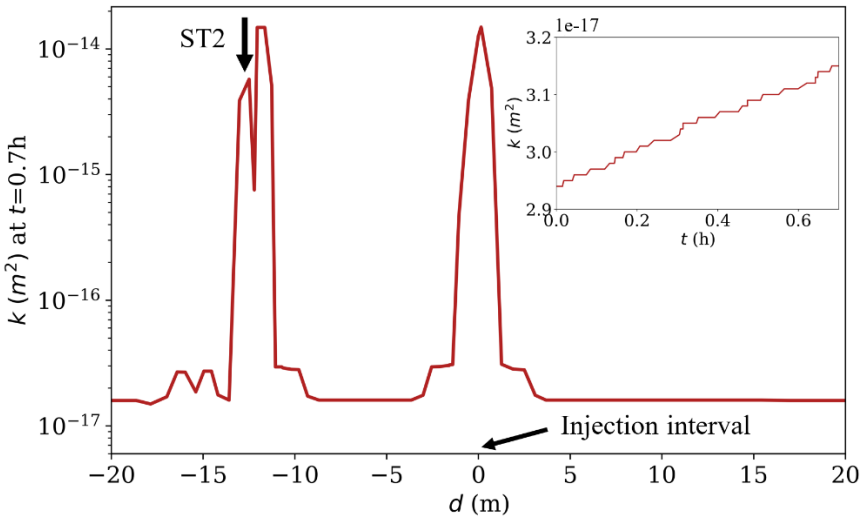

Figure 4.12 Permeability profile in the middle of the fracture (d is the distance along the middle of the fracture) at the end of the injection period (t=0.7 h) in both sides of the injection interval (located at d=0); In the inset: permeability evolution at a point near the injection interval.

4.4 Discussion

Numerical modeling of fractured media faces the major challenge of very different spatial scales of fractures and matrix, which lead to very different flow characteristic times. In a kilometer-scale reservoir problem, it is difficult to express the micrometer aperture of actual fractures using a 1:1-scale element. We show that a viable approach is to upscale the fracture thickness while maintaining fracture transmissivity, storage coefficient and stiffness to preserve flow and deformation. The equivalent properties through an adequate upscaling for representing fractures (section 4.2.3) provide an approach to employ a layer with a thickness several orders of magnitude larger than the actual fracture aperture, thus alleviating discretization issues whilst reproducing the behavior of the actual fracture with accuracy.

Simulation results show that there is an upper bound for the validity of the suggested upscaling approach. Although the model with b_{eq}=10 cm yields accurate results for hydraulic analysis (Figure 4.4), the hydromechanical response is not as accurate as models with thinner apertures (Figures 4.5-4.7). It is worth mentioning that, during upscaling of Young´s modulus, we have noticed that when E_{eq} exceeds Young´s modulus of rock matrix (E_m), the results become unreliable. For instance, the upscaled equivalent modulus is E_{eq}=66 GPa (for b_{eq}=10 cm model) and we had to set E_m=70 GPa to have a reliable result. This is another limiting upper bound factor for the proposed approach. However, using b_{eq}=1 cm provides the required accuracy as well as a convenient discretization process.

Suffice to say that the closer is the equivalent aperture to the actual one, the better is the accuracy as expected, especially in the mechanical response. However, differentiating between b_{eq}=1 cm and b_{eq}=1 mm models is difficult and the results are almost the same. This reinforces the applicability of the methodology, since we get what we expected. Furthermore, the method can be applied to any geometry of the fracture and with multiple fractures, as we have applied to a complex fracture network like Bedretto experiment.

Preferably, fully-explicit fracture network representation employing DFM methods would circumvent any error arising from upscaling procedures (Garipov and Hui, 2019). However, limitations on computational resources entail the use of continuum methods in conjunction with DFM methods. For a porous medium in which the properties of fracture networks vary between zones, different models might be employed in each zone to diminish the total required computational expenses. Our proposed approach validated by

reproducing the field experiment result at Bedretto presents a simple, yet, effective method to utilize in the modeling of fractured media.

4.5 Conclusion

We have derived equivalent hydromechanical properties for an equivalent-continuum layer that is several orders of magnitude thicker than the represented fracture. We have obtained identical simulation results for equivalent fracture layers represented with cm-scale thickness as the actual fracture aperture (which is in the μm scale). Employing this method, the discretization of fractures is much more tractable while the accuracy is maintained. Much remains to be done such as applying the method to complex fracture networks, still, we have validated the upscaling approach by reproducing a field experiment of water injection into a fracture at Bedretto. Thus, the equivalent fracture layer approach represents a useful method to model geo-energy and geo-engineering applications in fractured media involving scales differing several orders of magnitude to handle discretization problem.

5

Numerical modeling of hydraulic stimulation of fractured crystalline rock at the Bedretto underground laboratory

5.1 Introduction

A global trend towards CO_2 and nuclear-free technologies has promoted interest in deep geothermal energy as an alternative renewable source, free from seasonal fluctuations and, thus, with a potential for continuous energy output (Pruess, 2006; Randolph and Saar, 2011). Geothermal energy production has been successful in locations with favorable geological conditions such as volcanic fields, hydrothermally active areas, or sedimentary basins with deep-seated permeable rock formations. Enhanced (or Engineered) Geothermal Systems (EGS), previously referred to as Hot Dry Rock or Petrothermal Systems, are envisioned as a way to tap heat from any place in the territory (Brown et al., 2012; Olasolo et al., 2016).

The goal of EGS is the exploitation of regions with relatively high geothermal gradients through the creation (hydrofracturing) or reactivation (hydroshearing) of a fracture network of sufficient permeability to enable fluid circulation (Baria et al., 1999; Breede et al., 2013; Gan and Elsworth, 2014; Pine and Batchelor, 1984). The temperature necessary to produce electricity, i.e., >150 ^{o}C, is found at depths greater than 4-6 km, which is typically within the crystalline basement. The crystalline basement is assumed to be critically stressed (Townend and Zoback, 2000). Therefore, fluid injection concerns not only rock mass permeability, but also crustal strength and deformability, and

ultimately fault instability and induced seismicity (Achtziger-Zupančič et al., 2017; Ingebritsen and Manning, 2010; Manga et al., 2012).

To enhance permeability, injection-induced shear slip and dilation of preexisting fractures have been recognized as the most promising approach for extracting geothermal energy from hot ultralow-permeability rocks at depth (Riahi and Damjanac, 2013; Ye and Ghassemi, 2018). Shear reactivation of fractures/faults caused by pressurized fluid injection is of utmost importance in many subsurface engineering problems and reservoir stimulation (Rutqvist et al., 2007; Safari and Ghassemi, 2015; Vilarrasa et al., 2021), particularly with regard to induced microseismicity (Ellsworth, 2013; Evans et al., 2005; Guglielmi et al., 2015a; Kim, 2013; Majer et al., 2007; Safari and Ghassemi, 2016; Vilarrasa et al., 2019). It is referred to as shear stimulation or hydroshearing in EGS in which, contrary to the hydrofracturing process (which involves short-duration high-pressure injection and proppant usage), the injection pressure aims at causing shear slip and dilation of existing rough fractures (Mallikamas and Rajaram, 2005; Vilarrasa et al., 2011). This fracture self-propping by asperities is considered an effective means of permanently enhancing permeability (Kc and Ghazanfari, 2021; Meng et al., 2022). Furthermore, new cracks can be created because shear slip increases the stress intensity at the tips of preexisting fractures, potentially leading to fracture propagation and/or generating fracture networks (Bunger et al., 2013; Evans et al., 2005; Rahman et al., 2002; Willis-Richards et al., 1996). The main challenge is to develop adequate permeability in the reservoir while retaining sufficient heat transfer area and keeping the magnitude of induced seismicity as low as possible during reservoir stimulation (Grigoli et al., 2017; Kraft et al., 2009; Majer et al., 2007). Understanding the governing processes is of utmost importance to improve, and ultimately standardize, the applicability of EGS shear stimulation (Kumari and Ranjith, 2019).

Although the process of shear stimulation is theoretically well understood and routinely modelled, fundamental investigations through laboratory tests and field measurements have been limited. Laboratory-scale experiments can provide an understanding of coupled processes pertinent to the shear stimulation but suffer from test conditions as well as scalability that might lead to oversimplistic fracture flow that is not representative of a heterogeneous rock mass. (Guglielmi et al., 2015a, 2015b) completed two mesoscale reactivation tests by injecting high-pressure fluid into carbonate and shale faults. One of the insights achieved from these in situ reactivation tests is that aseismic/seismic shear slip by fluid injection enhanced the conductivity of the faults.

Another intermediate-scale hydro-shearing experiment was executed in the naturally fractured and faulted crystalline rock mass at the Grimsel Test Site (Switzerland) in 2017 (Amann et al., 2018a; David et al., 2018a, 2018b). One of the key findings of this experiment is that initially low-transmissivity structures were stimulated more productively compared with structures of higher initial transmissivity. However, these field tests were conducted on faults and fractured zones at a relatively shallow depth (<600 m), i.e., in rocks with relatively low confinement and low enthalpy potential.

Considering the necessity of an experiment with a more similar condition to intermediate and high enthalpy geothermal systems, the Bedretto Underground Laboratory for Geosciences and Geoenergies (BULGG) hosts medium to large-scale in-situ experiments with a focus on hydraulic stimulation and fault reactivation and associated induced seismicity (Figure 5.1). These experiments aim at developing effective and safe hydraulic stimulation protocols to enhance permeability at a controlled risk of induced seismicity for creating an EGS. The overburden directly above the laboratory is approximately 1500 m, providing conditions that start to resemble realistic EGS systems (scale 1:3 approximately) (Meier et al., 2020, 2022). To characterize the rock mass, several boreholes were drilled perpendicular to the tunnel axis with lengths ranging from 100 m to 400 m MD (Measured Depth). An additional set of short 30-40 m-long vertical boreholes were drilled, for conducting mini-frac tests aimed at quantifying the local state of stress (Bröker and Ma, 2022). A suite of hydraulic stimulation tests has been performed at the BULGG to stimulate the fractures intersected by the long boreholes MB1, ST1 and ST2 (Figure 5.1). Stress measurements by hydraulic fracturing technique indicate that the BULGG is in a normal faulting - strike-slip stress regime and that the rock mass is close to critically-stressed (Bröker and Ma, 2022; David et al., 2020; Gischig et al., 2020; Ma et al., 2022, 2019).

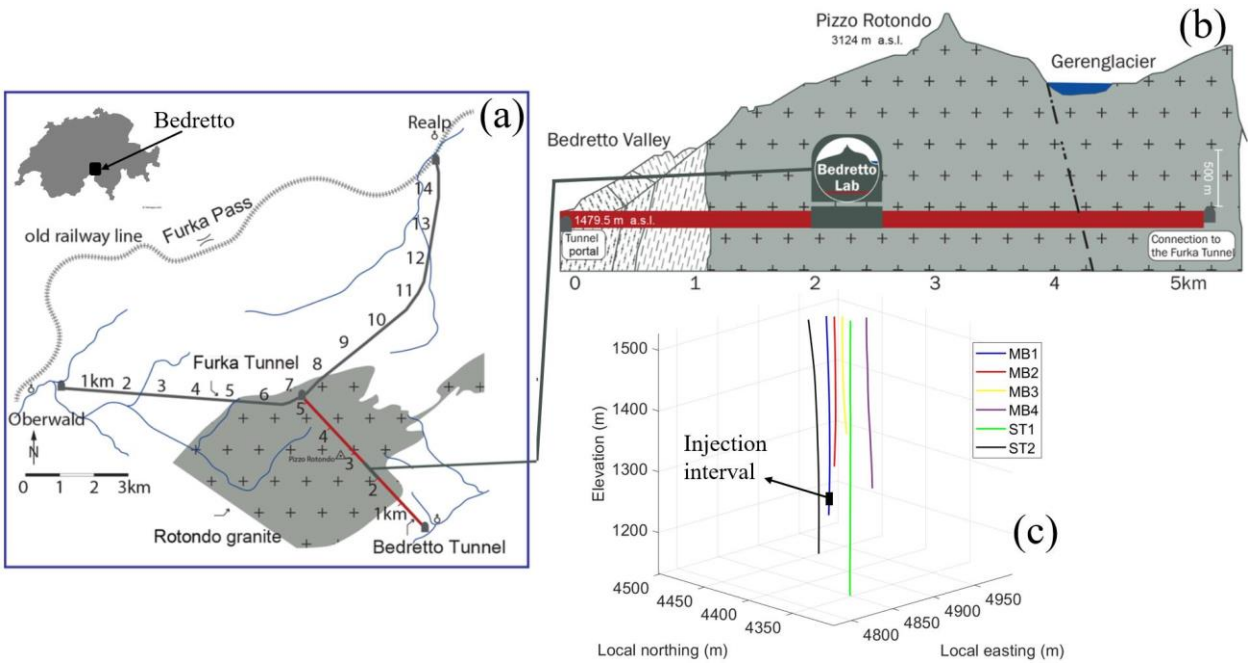

Figure 5.1 a) Top view of the Bedretto gallery and the hosting Rotondo granite; b) SE to NW cross-sectional view of the Bedretto lab; c) 3D view of the longest boreholes. Adapted from (Ma et al., 2022; Shakas et al., 2020).

This chapter aims at numerically modeling and analyzing the hydraulic stimulation performed in borehole MB1 (in blue in Figure 5.1c) at the BULGG in February 2020. Numerical simulation is an essential method to investigate coupled hydromechanical processes and to better understand the fundamental mechanisms and feedbacks that occur in geothermal reservoirs. This understanding is particularly important due to the coupling of permeability and fracture aperture (Taron and Elsworth, 2009). I present three numerical models with increasing complexity (in terms of material constitutive law and coupling of permeability and fracture aperture), which we find to get progressively closer to the conceptual model representing the behavior of the system. Then, I compare numerical results with field experiment data and discuss the implications. Based on the best model, I extend our analysis to poromechanical processes occurring during the stimulation and discuss our findings. Simulation results reveal the extent of the stimulated fracture and permanent permeability enhancement and show that hydroshearing in the stimulated fracture has a non-negligible impact on the stability of adjacent joints due to stress redistribution, which may affect their subsequent stimulation.

5.2 Methodology

5.2.1 Numerical models

The numerical model is a 2D plane-strain inclined plane that contains the boreholes that, on average, dip 42° downwards to the southwest (Figure 5.1). The model is refined at its center, which represents the BULGG and its vicinity, and grows to a large extension (75 km^2; Figure 5.2), beyond the whole Bedretto gallery (top center of the model) to avoid spurious boundary effects. For similar reasons, the bottom boundary is at a true vertical depth of 5000 m (y=-7472.4 m in the inclined plane). Both sides and the bottom of the model are fixed against lateral and vertical displacements, respectively. A linear distributed fluid pressure and initial stresses are applied to the model from top to bottom (Figure 5.2a). The major fractures and shear zones identified through borehole logging and geological structural analysis are included in the model (Ma et al., 2022; Meier et al., 2020). The fractures have been modeled as upscaled elastic continuum media with different hydromechanical properties but homogeneous in their space. The mesh also includes the main boreholes (MB1 to MB4, ST1, and ST2 with 20 cm thickness) and is highly refined at the closest vicinity of the modeled fractures and the boreholes. Overall, the mesh consists of 27,248 quadrilateral elements with corresponding 27,420 nodes (Figure 5.2d).

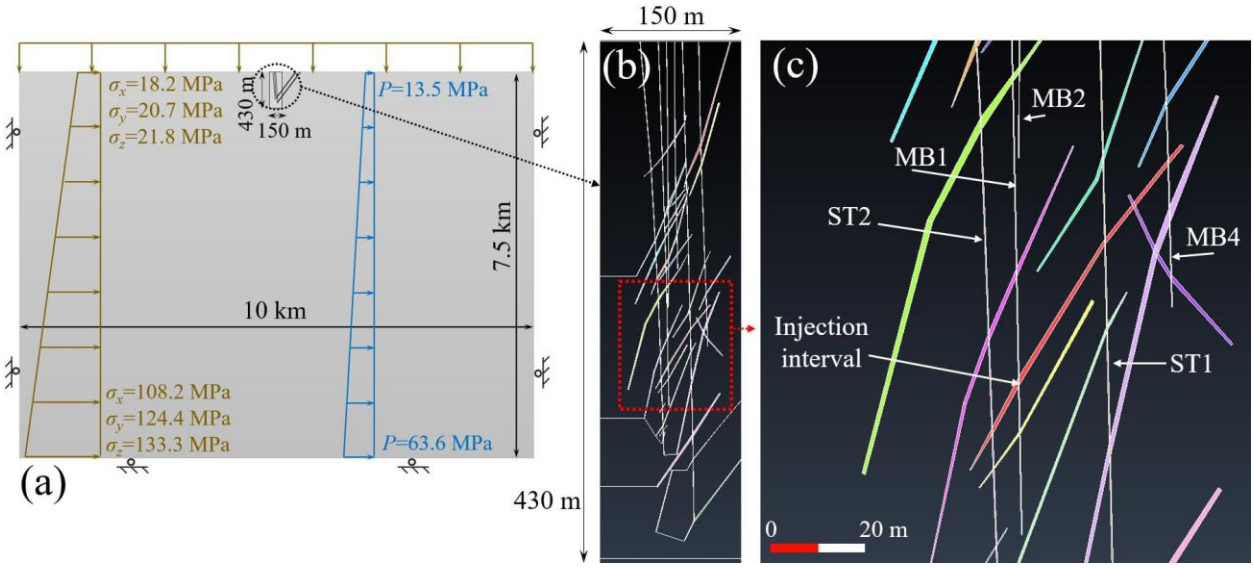

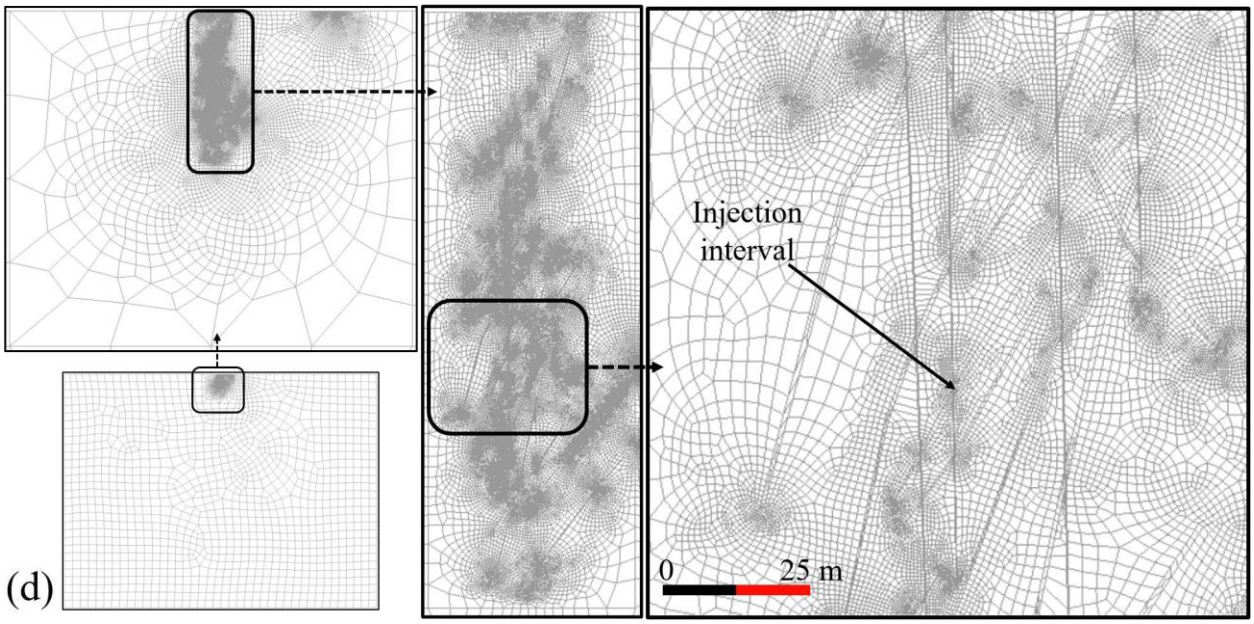

Figure 5.2 a) Model geometry and boundary conditions; b) Configuration of boreholes, identified fractures and fault zones; c) Detailed view around the stimulated fracture (in red); d) Mesh configuration from global to detailed view around the stimulated fracture zone.

Three models were built on this setting. In the first model (termed here model EP, for "Elastic Prescribed transmissivity") the permeability of the main fracture crossing the injection interval (in red in Figure 5.2c) has been assigned (homogeneous all along the fracture, but variable in time) to achieve a reasonable fit of the measured pressure evolution at the injection interval. However, changes in fracture aperture occur mainly in the vicinity of the injection interval as a result of injection-induced overpressures. Hence, the second model (model EE, "Elastic Embedded") incorporates the "embedded model", in which permeability is a function of volumetric strain described in section 5.2.4. In this second model, fracture permeability varies with distance from the injection interval and remains constant and equal to the initial value far away from it, where pressurization has not dilated the fracture. While this approach allows obtaining a good reproduction of the measured injection pressure at early stages, it fails to provide a good fit once the fracture reactivates and inelastic strains occur. Thus, to account for permeability enhancement induced by dilatancy due to the shear slip of the fracture, the third model (model VE) incorporates a viscoplastic constitutive law that includes dilatancy and strength softening. Table 5.1 summarizes the main input values for these models and the host rock. Notably, each fracture has different hydraulic and mechanical properties inferred from well logging and hydraulic tests. However, variable permeability is considered only in the stimulated fracture because the main impact at the surrounding fractures is mainly poroelastic but

not hydraulic. The hydraulic and mechanical parameters of the surrounding fractures are not relevant to system changes induced by injection, which are mainly local and driven by the parameters of the stimulated fracture and surrounding matrix. The fully coupled hydromechanical numerical models are implemented using the software CODE_BRIGHT (Olivella et al., 1996, 1994).

Table 5.1 Hydromechanical properties of the rock matrix (granite) and the stimulated fracture for different tested models

	Granite	Stimulated fracture		
		EP	**EE**	**VE**
Mechanical constitutive behavior	Elastic	**E**lastic		**V**iscoplastic
Permeability (k)	2.5×10^{-18} m^2	**P**rescribed	**E**mbedded model	
Young´s modulus (E)	46 GPa	23 GPa		
Poisson ratio (ν)	0.37	0.37		
Porosity (ϕ)	0.005	0.005		
Viscosity (μ)	-	-	-	2.5 GPa·s
Peak friction angle (φ_{peak})	-	-	-	23º
Residual friction angle (φ_{res})				20º
Cohesion (c)	-	-	-	0.01 MPa
Dilatancy angle (ψ)	-	-	-	20º
Critical value of the softening parameter (η^*)	-	-	-	0.001

The models are initialized by simulating the drainage effect of the tunnel on porewater pressure by imposing atmospheric pressure at the top boundary, and the subsequent consolidation, which tends to close fractures. The drainage period spans from the end of the excavation in 1976 until now. As such, the initial decompression of the system caused by excavation is not considered because its transient effects are small, as shown in a prior sensitivity analysis. In the same line of arguments, the drilling of boreholes is not modelled explicitly. Subsequently, the stimulation test (the first one in a series of many at the BULGG) is modeled by injecting water through an isolated section of borehole MB1, at a measured depth of 267 m (true vertical depth 188.8 m), into the fracture (in red in Figure 5.2c). Isolation was achieved by a double packer, also included in the model as a very stiff and low-permeability section of the borehole (E=4600 GPa, k=2.5×10^{-18} m^2, after inflation). The permeability of the boreholes, also modelled explicitly, is 2.5×10^{-14} m^2. The numerical simulations cover the first 3.4 hours of the field experiment, during

which we compare the outcomes of the three models with the experimental results. Results of model VE are extended in time up to the first 8 hours of the experiment.

5.2.2 Governing equations

The mechanical problem is solved by satisfying the momentum balance. Neglecting inertial terms, the momentum balance reduces to the equilibrium of stresses,

$$\nabla \cdot \boldsymbol{\sigma} + \boldsymbol{b} = \mathbf{0} \tag{5.1}$$

where σ [$ML^{-1}T^{-2}$] is the total stress tensor and b [$ML^{-2}T^{-2}$] is the vector of body forces.

In linear elasticity theory for continuous media, the relationship between stress, strain, and fluid pressure for isotropic materials is given by Hooke's law,

$$\Delta\boldsymbol{\sigma} = K\varepsilon_v \boldsymbol{I} + 2G\left(\boldsymbol{\varepsilon} - \frac{\varepsilon_v}{3}\boldsymbol{I} + \frac{\alpha}{2G}\Delta p_f \boldsymbol{I}\right), \tag{5.2}$$

where ε_v [-] is volumetric strain, $\mathbf{I}$ [-] is the identity matrix, $\boldsymbol{\varepsilon}$ [-] is the strain tensor, $K = E/\big(3(1-2\nu)\big)$ [$ML^{-1}T^{-2}$] is the bulk modulus, $G = E/\big(2(1+\nu)\big)$ [$ML^{-1}T^{-2}$] is the shear modulus, E [$ML^{-1}T^{-2}$] is Young's modulus, ν [-] is the Poisson ratio, p_f [$ML^{-1}T^{-2}$] is fluid pressure, and α [-] is the Biot effective stress coefficient. In this work, I assume $\alpha = 1$, which leads to the strongest hydromechanical coupling (Zimmerman, 2000).

Equation (5.2) is coupled with the flow equation through fluid pressure. Assuming that there is no external loading and neglecting the compressibility of the solid phase, fluid mass conservation can be written as

$$\frac{\Phi}{K_f}\frac{\partial p_f}{\partial t} + \frac{d}{d\,t}(\nabla \cdot \boldsymbol{u}) + \nabla \cdot \boldsymbol{q} = 0, \tag{5.3}$$

where Φ [-] is porosity, K_f [$ML^{-1}T^{-2}$] is water bulk modulus, t [T] is time, u [L] is the displacement vector, q [L^3T^{-1}] is the water flux, given by Darcy's law, and $\mathrm{d}/\mathrm{d}t$ denotes material derivative. Note that the flow (Eq. (5.3)) and mechanical (Eq. (5.2)) equations can be also coupled through the volumetric strain (second term in the left-hand side of Eq. (5.3)), which can be expressed as the divergence of the displacement vector.

5.2.3 Fracture constitutive model

Fracture reactivation is modeled by a viscoplastic constitutive law in which fracture failure is given by the Mohr-Coulomb criterion and includes dilatancy and strain softening. The yield function (F) and the flow rule (G) are defined as

$$F = p \cdot \sin\varphi(\eta) + \left[\cos\theta - \frac{1}{\sqrt{3}}\sin\theta \,.\, \sin\varphi(\eta)\right] \cdot \sqrt{J_2} - c(\eta) \cdot \cos\varphi(\eta)\,, \tag{5.4}$$

$$G = \xi \cdot p \cdot \sin\psi + \left(\cos\theta - \frac{1}{\sqrt{3}}\sin\theta \cdot \sin\psi\right) \cdot \sqrt{J_2} - c(\eta) \cdot \cos\varphi(\eta)\,, \tag{5.5}$$

where p [ML^{-1}T^{-2}] is the mean stress, J_2 [ML^{-1}T^{-2}] is the second invariant of the deviatoric stress tensor, η [-] is the softening parameter, ξ [-] is a parameter for the plastic potential, φ [°] is the friction angle, c [ML^{-1}T^{-2}] is cohesion, and ψ [°] is the dilatancy angle. The invariant θ [°] (Lode's angle) is defined as

$$\theta = \frac{1}{3}\sin^{-1}\left(-\frac{3\sqrt{3}}{2}\frac{J_3}{J_2^{3/2}}\right), \quad -30^{\circ} \le \theta \le 30^{\circ}, \tag{5.6}$$

where J_3 [ML^{-1}T^{-2}] is the third invariant of the deviatoric stress tensor. The stress function $T(F)$ is

$$T(F) = F^m \quad for\ F \ge 0,\ \ T(F) = 0 \quad for\ F < 0, \tag{5.7}$$

where m [-] is a constant power, chosen equal to 3 here (Vilarrasa et al., 2010). Both the cohesion and the friction angle can depend on the softening parameter (η) as

$$\lambda(\eta) = \begin{cases} \lambda^{peak} & \eta \le 0 \\ \lambda^{peak} + \left(\dfrac{\lambda^{res} - \lambda^{peak}}{\eta^*}\right) \cdot \eta & 0 \le \eta \le \eta^*\,, \\ \lambda^{res} & \eta^* \le \eta \end{cases} \tag{5.8}$$

where λ represents either cohesion (c) or friction angle (φ), and λ^{peak} and λ^{res} are user defined peak and residual values, respectively (see Table 5.1). As shown in Table 5.1, cohesion is low and we assume a constant value equal to 0.01 MPa. η^* is the value of the softening parameter controlling the transition between the softening and residual stages. The softening parameter depends on plastic strain as

$$\eta = \sqrt{\frac{3}{2} \cdot \left[\left(\varepsilon_x^p - \varepsilon_m^p\right)^2 + \left(\varepsilon_y^p - \varepsilon_m^p\right)^2 + \left(\varepsilon_z^p - \varepsilon_m^p\right)^2 + \left(\frac{1}{2}\gamma_{xy}^p\right)^2 + \left(\frac{1}{2}\gamma_{yz}^p\right)^2 + \left(\frac{1}{2}\gamma_{zx}^p\right)^2 \right]}, \quad (5.9)$$

where $\varepsilon_m^p = \frac{1}{3}(\varepsilon_x^p + \varepsilon_y^p + \varepsilon_z^p)$ [-] is the mean plastic strain, and ε and γ are the diagonal and off-diagonal terms of the plastic strain tensor.

The quantification of shear slip tendency and proximity to shear failure conditions can be calculated with the mobilized friction angle. Shear failure occurs when the mobilized friction angle equals the actual friction angle. An alternative means of representing mobilized friction resistance, without implying a specific spatial orientation, involves expressing it in terms of invariants of the effective stress tensor. Considering the mean effective stress p' and deviatoric stress q, the mobilized friction angle can be expressed as

$$\varphi_{mob} = \sin^{-1}\left(\frac{3M}{6+M}\right), \quad (5.10)$$

where $M = \frac{q}{p'}$ is the slope of the stress path curve in the p'-q diagram.

5.2.4 The embedded model

The modelled fracture was identified in the lithological and image logs and in cores retrieved during the drilling of borehole MB1. This zone is a composite of several smaller fractures embedded in a matrix material. The permeability of the stimulated fractured zone is computed using the cubic law (Witherspoon et al., 1980), which makes fracture transmissivity proportional to b^3 (b being the aperture). Since CODE_BRIGHT adopts a small displacements approach, the geometrical grid aperture is fixed. Therefore, actual aperture changes, which are proportional to volumetric strain, are modeled by changing permeability as

$$k = k_m + \frac{(b_0 + a\Delta\varepsilon)^3}{12a}, \quad (5.11)$$

where k_m [L^2] is the intrinsic permeability of the matrix within the fracture zone (in red in Figure 5.2c), a [L] is the spacing between the fractures within the fracture zone, b_0 [L] is the initial fracture aperture, $\Delta\varepsilon$ [-] is the volumetric strain change ($\Delta\varepsilon = \varepsilon - \varepsilon_0$), and ε_0 [-] is a threshold value. For the stimulated fracture zone, the following parameters are considered: $k_m = 5 \cdot 10^{-17}$ m^2, i.e., 20 times larger than that of surrounding granite, $b_0 =$

$2.25 \cdot 10^{-6}$ m , $a = 0.01$ m, and $b_{max} = 1.34 \cdot 10^{-4}$ m, which is the maximum aperture (upper bound of aperture), above which fracture permeability stops increasing.

5.3 Results

5.3.1 Reproduction of measured injection pressures

In the EP model, the temporal evolution of the permeability of the stimulated fracture is manually adjusted as constant during each injection interval so as to reproduce the observed injection pressure each interval. Although the overall model fit is good up to 2.5 h of injection (green dotted line in Figure 5.3a), it fails to reproduce the shape of the pressure curve in each injection step, in which pressure sharply increases at the beginning and the subsequent pressure build-up diminishes smoothly with time under constant flow rate (note that the first steps, until t~1.3h were intended to be constant pressure head tests). In short, the EP model fits well the beginning and end pressures for each step, but not the intermediate evolution. As discussed below, this discrepancy reflects that permeability changes are imposed for the whole fracture and not just for the actually stimulated region, which results in an unrealistic rapid pressure propagation along the whole fracture (Figure 5.4a).

The EE model (Eq. 5.10) accounts for both the spatial and temporal evolutions of fracture transmissivity in response to deformation. The brown curve in Figure 5.3a depicts the temporal evolution of generated overpressure at the injection interval predicted by the model with variable permeability as a function of fracture aperture (EE model). This model can accurately reproduce the field test results until 0.7 h. We attribute subsequent discrepancies to fracture dilatancy caused by shear slip, which leads to an additional, and irreversible, permeability enhancement. The elastic nature of this model cannot reflect this irreversible hydromechanical response. Consequently, the generated strain is smaller than the actual one, and the embedded model EE yields less permeability enhancement than the actual one. As a result, the calculated overpressure is higher than the measured one at late times, when shear slip has become significant. This limitation is overcome by the VE model.

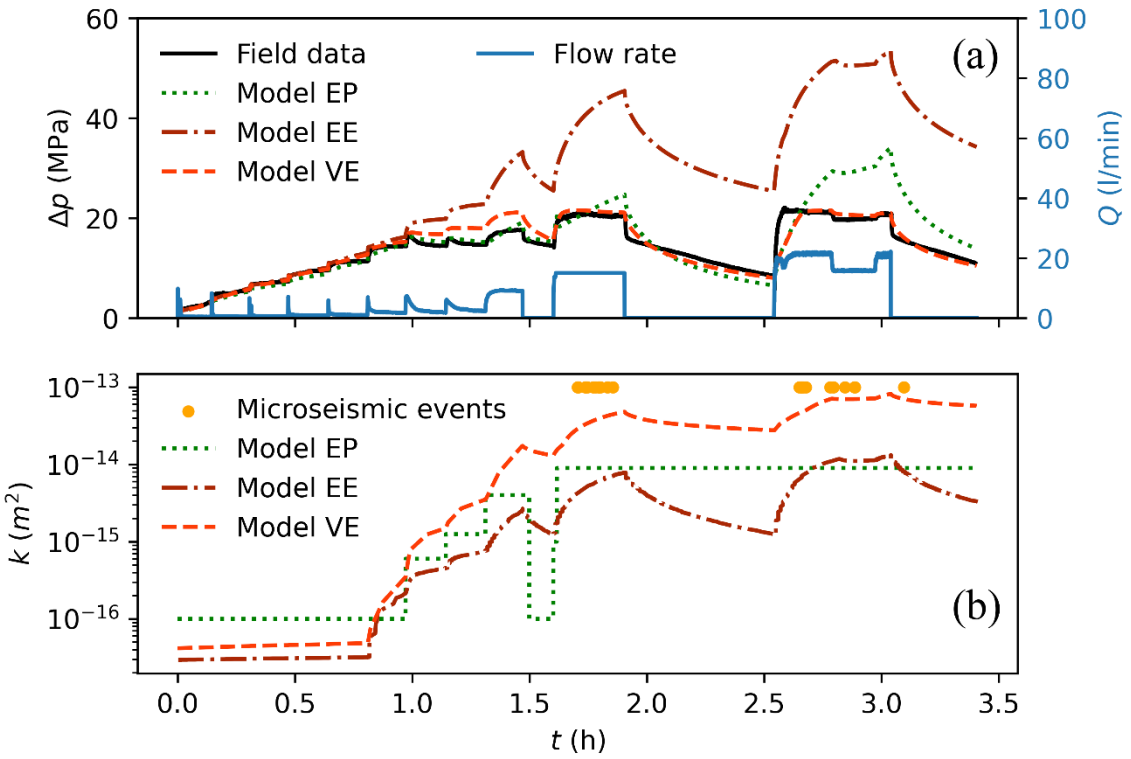

Figure 5.3 a) Temporal evolution of calculated and measured overpressure (i.e., above formation pressure) at the injection borehole; b) Temporal evolution of fracture permeability in models with prescribed and variable permeability near the injection interval (point 1 in Figure 5.6c) and timestamps of observed induced microseismic events.

Figure 5.3b displays the temporal evolution of permeability prescribed (model EP) or calculated (models EE and VE). As observed in Figure 5.3a, all models render more or less a good fit with the generated overpressure until around 0.7 h, when the jacking pressure is achieved and the initially tight fracture gets opened, which leads to (1) the first sudden pressure drop under constant flow rate (Figure 5.3a), and (2) the corresponding sudden permeability increase (Figure 5.3b). The sudden increases in storage capacity and permeability hindered the control of pressure, which tended to drop. Therefore, the injection protocol was changed to constant flow rate injection at 1.3 h. A first shut-in at t=1.5 h led to a sudden drop of fracture permeability. Notably, the permeability drop required by the EP model to still reproduce the measured injection pressure is way larger than those calculated by the EE and VE models, what confirms the need to accommodate spatial variability in permeability enhancement. During the two additional shut-in episodes until t=3.4 h, the EE model shows a severe permeability

reduction compared to the VE model, which reveals the need to accommodate permanent enhancement of fracture permeability.

The VE model reproduces the temporal evolution of injection overpressure better than previous models, especially during the last injection phase ($t > 2.5$ h). The VE model allows to simulate fracture reactivation and yields an additional and permanent permeability enhancement when compared with the elastic models EP and EE. In this case, permeability enhancement is given by both elastic and plastic strains as shear slip accumulates. Plastic strain further enhances fracture permeability, leading to smaller pressure build-ups and thus, to a better approximation of field data. Permeability enhancement is one order of magnitude larger for the viscoplastic model than for the elastic model. Obviously, permeability decreases during shut-in periods (associated to closure of the elastic portion of strain), but a significant fraction of the permeability enhancement is permanent, thus contributing to improved borehole injectivity. This behavior has been observed, e.g., in Basel, by comparing data acquired during the stimulation carried out in 2006 with that of hydrotests carried out years later (Häring et al., 2008; Ladner and Häring, 2009). Note that the timestamps of located microseismic events (Figure 5.3b) correspond approximately to the times of maximum permeability enhancement. This observation will be further discussed later.

The main limitation of the EP model, beyond the arbitrariness in manually modifying permeability, is that fracture permeability is homogeneous at any given time (Figure 5.4b). Using an embedded model (in which permeability is a function of volumetric strain) shows that permeability increases locally near the injection borehole and that the enhancement is lower away from the well. The longitudinal profile of fracture permeability displays an increase (around 3 orders of magnitude at maximum, Figure 5.4b) in fracture permeability due to the increase in fracture aperture (Figure 5.4c). Note that permeability enhancement occurs within the pressurized region of the fracture (Figure 5.4a). However, the permeability enhancement is moderate, with permeability remaining below 10^{-14} m^2 in EP and EE models, and thus, the predicted pressure build-up becomes excessively high compared to field measurements at late times (Figure 5.3). Considering shear failure and dilatancy yields an additional increase in fracture permeability of one order of magnitude that permits reproducing the measured pore pressure evolution at the injection borehole.

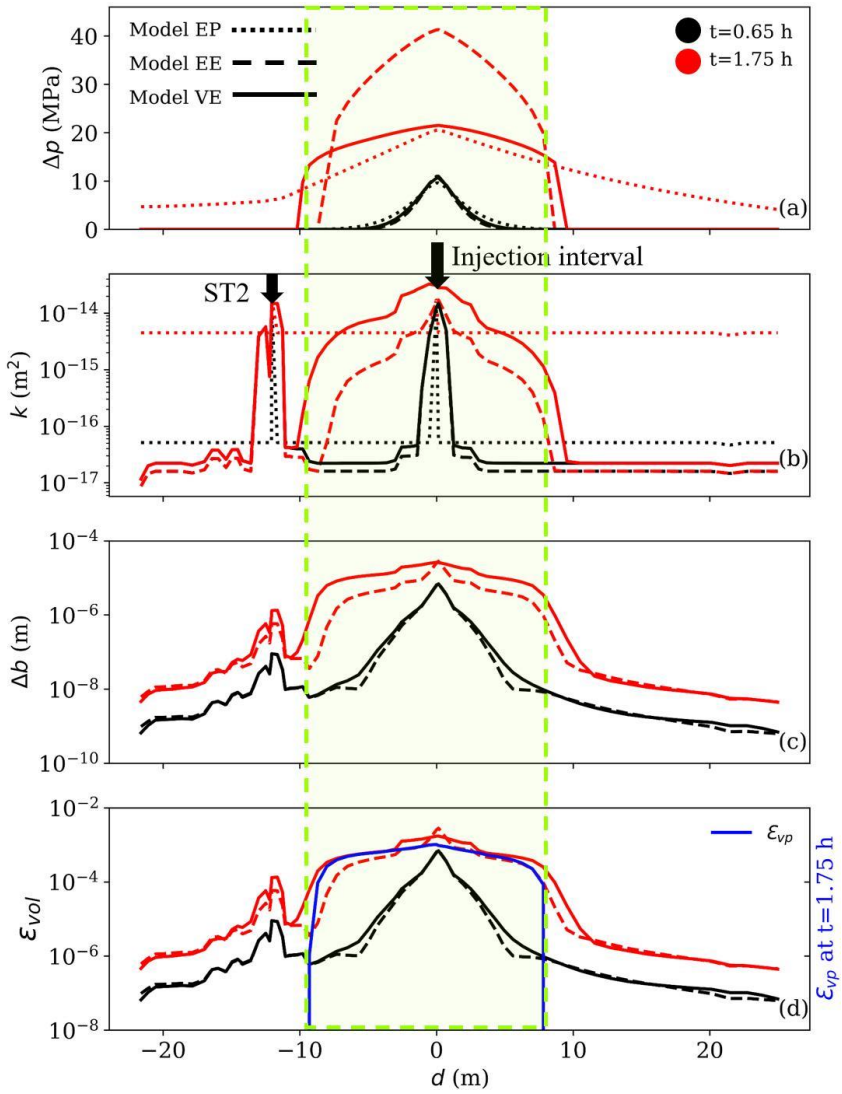

Figure 5.4 Profiles along the stimulated fracture of a) pressure build-up, b) fracture permeability, c) fracture aperture change ($b_0 = 2.25 \cdot 10^{-6}\, m$), and d) volumetric strain (and volumetric plastic strain (ε_{vp}) at t=1.75 h for model VE). Results are displayed at two moments for all models. The injection interval is located at d=0 and is positive upwards. Note the intersection with well ST2 around d=-12 m (Figure 5.2c).

The pore pressure build-up along the stimulated fracture (Figure 5.4a) mainly occurs within the reactivated region with irreversible strain (highlighted in green; Figure 5.4d). Figure 5.4a displays the fact that even though the EP model can reproduce measured pressures as good as the VE model at the injection borehole, pressure profiles along the fracture are significantly different. The EP model underestimates the pressure buildup within the reactivated region and overestimates it away the reactivated region. Until 1.75 h of injection, fracture aperture has already dilated and opened around 10 µm in the

reactivated fracture patch (VE model, solid red line in Figure 5.4c). Model VE gives insights of the actual pore pressure distribution within the fracture.

5.3.2 Fracture reactivation

The contour plots of pore pressure at several stages of the stimulation (Figure 5.5) reveal that adjacent fractures and wellbores start to be pressurized after 2.6 h of stimulation. The pressurization becomes significant outside the stimulated fracture during the last phase of stimulation (t=3 h in Figure 5.5), when shearing has become relevant. This overpressure includes the low-permeability rock matrix and becomes marked after shearing, which indicates that it is largely driven by poroelastic effects (analytical solutions are available to gain insight into these effects (De Simone and Carrera, 2017)). These effects overlap with hydraulic connectivity (pressure diffusion) along fractures, apparent from the reduced pressure gradient along fractures in Figure 5.5. Hydraulic connection causes a non-negligible leak-off, which may be responsible for water back-flow into the injection wellbore outside the isolated interval. Bypass (back-flow to the section above the upper packer) was measured in the field during most stimulation experiments in BULGG. Leak-off can also be detected in the diagnostic plots of such stimulations by observing the derivative of injection pressure with respect to log-time as a function of time, which correlates well with the flow dimension n (Bourdet et al., 1983; Ramos et al., 2017). The flow dimensions are, in most cases, initially linear to bilinear (n=1 to 1.5), followed by an infinite acting radial flow period (n~2) during which flow occurs mainly along the fracture, and finally by a spherical flow period (n=2 to 3), which reveals the pressurization of the surrounding area and flow the overall medium via nearby fractures and boreholes.

Realism of the VE model is further supported by the anti-symmetric changes in pressure at the edges of the shearing region. Extension occurs away from the shearing tip at the side displacing towards the injection point (left side of the fractur at the top and right at the bottom in Figure 5.5a). (Vilarrasa et al., 2022, 2021) argue that this effect is one of the causes of delayed seismicity (aftershocks occurring some time after the main event). These extension zones would tend to fail, but become temporarily stabilized by the pressure drop. This mechanism may contribute to enhanced stimulation beyond the initial fracture and to broad block connectivity. Pressure increases on the other side of the fracture near the tip, thus yielding an antisymmetric poroelastic effect.

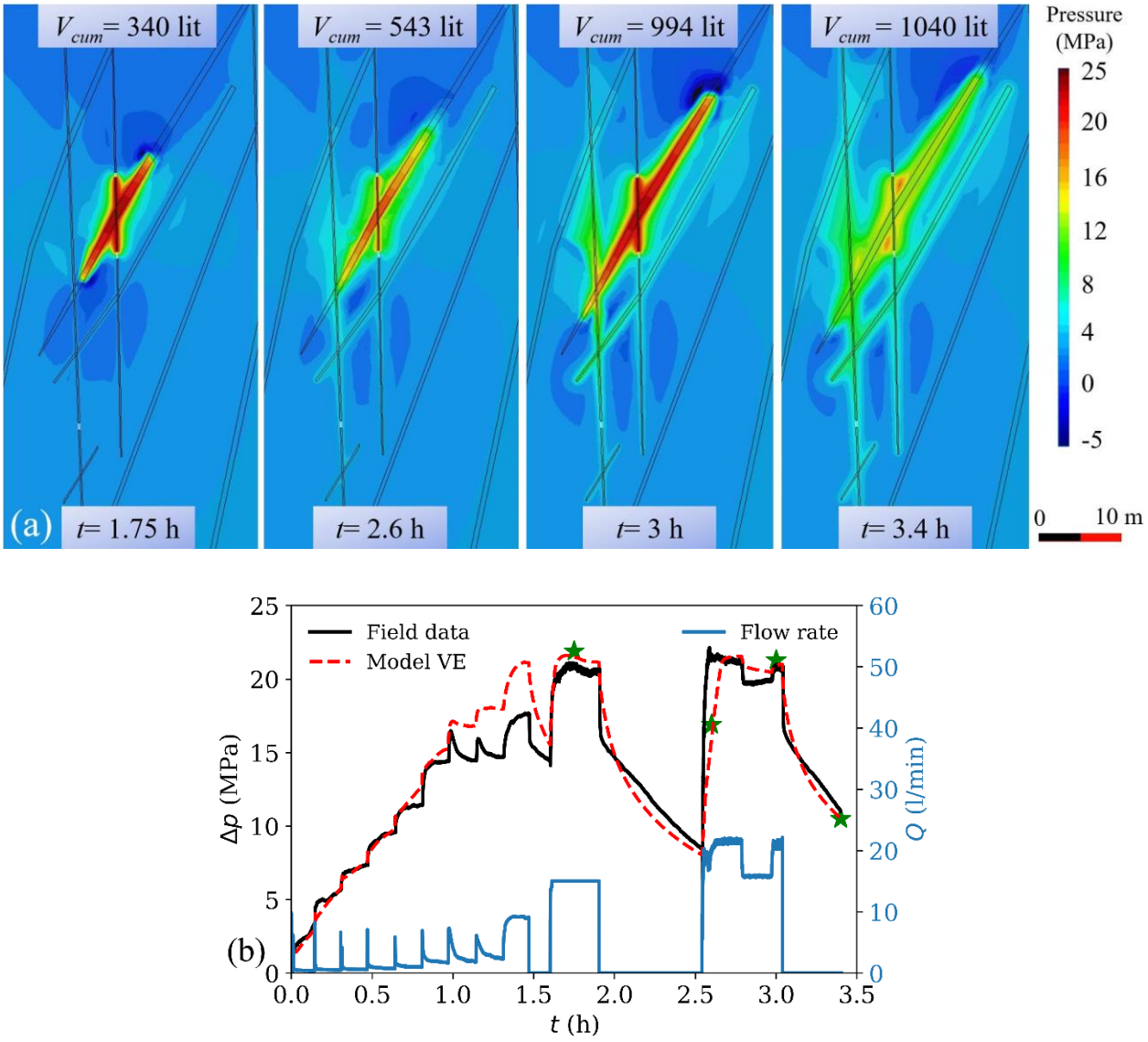

Figure 5.5 a) Contour plots of pore pressure at four stages of the stimulation (indicated with green stars in b) with the corresponding cumulative injected fluid volume V_{cum} using the VE model. b) Observed and simulated pressure evolution and injection flow rate at the injection borehole.

Further insight into the microseismicity mechanisms can be gained from the evolution of the deviatoric plastic strain during injection (shown for five fracture points in Figure 5.6c). The strain sharply rises after failure, coinciding with jacking of the fracture at that location, in all points (Figure 5.6a). Once jacking occurs, irreversible strain accumulates at a very low rate. The reactivation front, which coincides with the sharp increase in plastic strain, progressively advances away from the injection borehole. Plastic strain propagates by the end of the simulation (t=3.4h) along 45 m of the fracture, i.e., some 20 m away to each side of the injection borehole. Fracture reactivation propagates further

upwards than downwards (Figure 5.6b). Even though it is common that seismic clouds develop predominantly upwards (Xie and Min, 2016), in this case, downwards propagation is limited by the presence of borehole ST2, which causes a local reduction in pore pressure because of its high permeability and inhibits further reactivation.

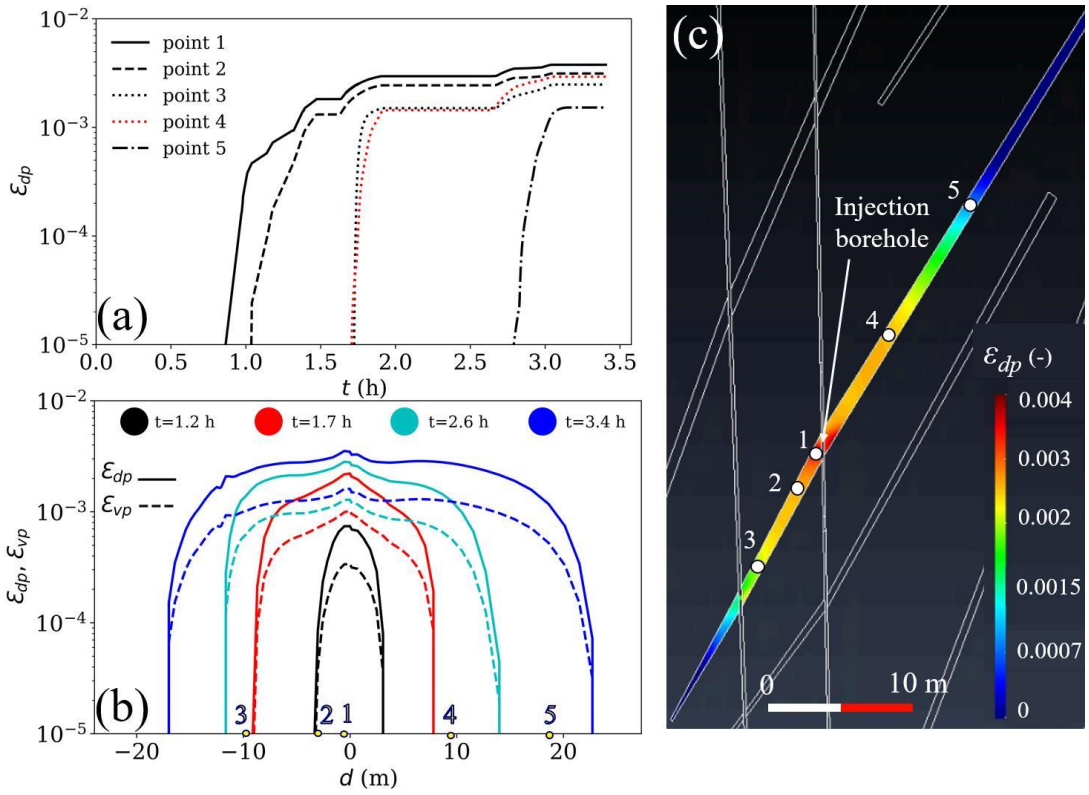

Figure 5.6 a) Temporal evolution of the deviatoric plastic strain at five points in the fracture (indicated in panel c); b) Profiles of deviatoric and volumetric plastic strains (ε_{dp} and ε_{vp} respectively) along the fracture at four times of the simulation (color coded with respect to time), the location of the monitoring points are indicated on the x axis; c) Contour plot of deviatoric plastic strain in the stimulated fracture at t=3.4 h. The five observation points are indicated on the x axis in panel b.

The stress paths of points 1-3 (location shown in Figure 5.6c) in the q-p' plane, i.e., deviatoric versus mean effective stress, display trajectories that move towards the failure surface until failure conditions are reached and then, the stress paths move along the failure surface (Figure 5.7). Note that the initial stress state is stable in all cases because the drainage of the tunnel increases the effective mean stress. Close to the injection borehole (point 1), the effective mean stress is reduced as liquid pressure increases with a progressive deviatoric stress increase. Further away (points 2 and 3), the deviatoric stress increases more pronouncedly at the beginning of injection because of stress transfer caused by slip of the portion of the fracture located closer to the injection borehole and because

the further away a point is located from the injection borehole, the longer it takes to the pressure front to reach that point. Failure occurs under compression in all cases ($p' > 0$). A detailed look on the stress path at point 1 reveals a relation between timestamps of the stress path direction and those of measured induced microseismic events (Figure 5.3b). After the activation, the first time when stress path goes downward left, $t_{1\text{-}1}$=1.64 h, corresponds approximately to the timestamp of the first recorded microseismic event (t=1.704 h). Note that not all recorded microseismic events are plotted in Figure 5.3, but only the ones that could be located, i.e., some smaller magnitude events, below the magnitude of completeness of the seismic monitoring work, may have occurred before. Going downward-left lasts until $t_{1\text{-}2}$=1.89h, which approximately corresponds to the arrest of microseismicity (t=1.875 h). The second one starts at $t_{2\text{-}1}$=2.63 h and lasts until $t_{2\text{-}2}$=3.04 h. The second onset of microseismicity (t=2.625 h) happens when stress path is near the Mohr-Coulomb failure line. The last located event (t=3.093 h) occurs slightly after $t_{2\text{-}2}$, during the shut-in phase. Similar qualitative conclusions are attained by observing the stress path of point 2, located 4.2 m away from the injection interval. In a nutshell, microseismicity develops since the stress path approaches the failure surface until it starts to go away from it. In the field, located seismic events aligned well with the simulated fracture fingerprint and developed (subject to the accuracy of the monitoring network) some 10 m downwards and 40 m upwards. The detailed spatio-temporal correlation between stress paths and timestamps of the located microseismic events is out of the scope of this work.

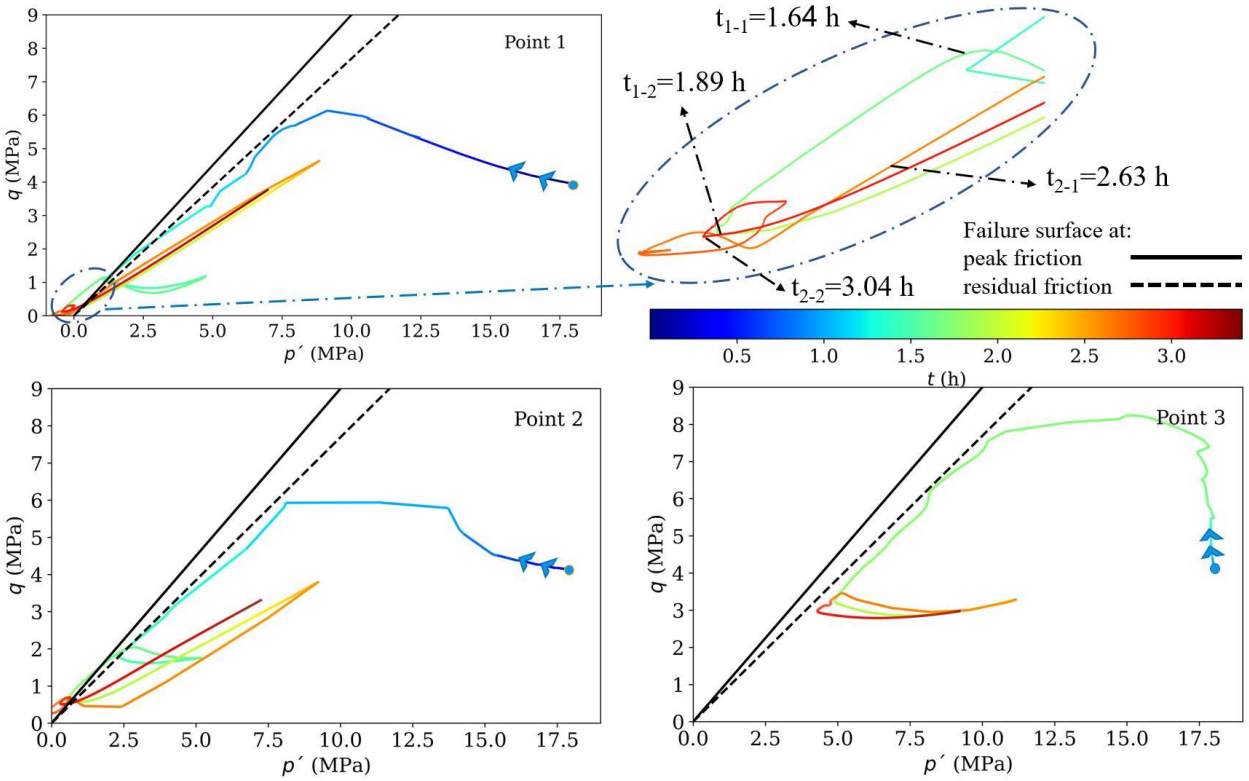

Figure 5.7 Effective stress path in the q-p' plane for the viscoplastic model (VE) and Mohr-Coulomb failure surfaces for points 1 to 3 located along the fracture (see Figure 5.6 for their location). The initial yield point indicates the onset of plastic deformation. A zoomed view for stress trajectories at point 1 is provided with time stamps for the change of the stress path. Note that the depicted timestamps correspond to those of begin and arrest of induced microseismicity, as monitored in the field (see Figure 5.3b).

5.3.3 Response at nearby fractures

Pressurization of the stimulated fracture causes a poromechanical response of the rock matrix (Figure 5.8a) inducing changes in shear stresses that affect nearby fractures (Figure 5.8c). Initially, under low injection pressures, the induced shear stresses are reversible and would even vanish shortly after an eventual shut-in. However, once the stimulated fracture is reactivated, an irreversible shear stress drop (Goertz-Allmann et al., 2011; Kim et al., 2022; Yoo et al., 2021) occurs within the slipped fracture patch and the bulbs of positive shear stress are displaced towards its tips. As slip accumulates, the region with shear stress changes extends (see points I and J, at 20 m and 1 m from the stimulated fracture), affecting nearby fractures. Thus, the stimulation of a single fracture may modify also the stability of nearby fractures (De Simone et al., 2013).

Figure 5.8c displays the stress path at eight points located in four nearby fractures. For comparison purposes, all the axes have the same range of values. The failure surface is not plotted because it is placed far away to the left of the displayed paths, i.e., all points are stable during the whole stimulation. Some areas are barely affected by stimulation (points A and B, located far away from the stimulated fracture). In contrast, others experience significant stress changes (up to 3 MPa both in deviatoric and effective mean stress), e.g., points D to F, in the fractures right above and below the stimulated one. Some points approach shear failure conditions, either because of an increase in the deviatoric stress (point A), a decrease in the effective mean stress (point G), or a combination of both (point D). The trajectories are diverse, which highlights the complexity of pore pressure variations and stress changes that occur not only within the stimulated fracture, but also in its surroundings.

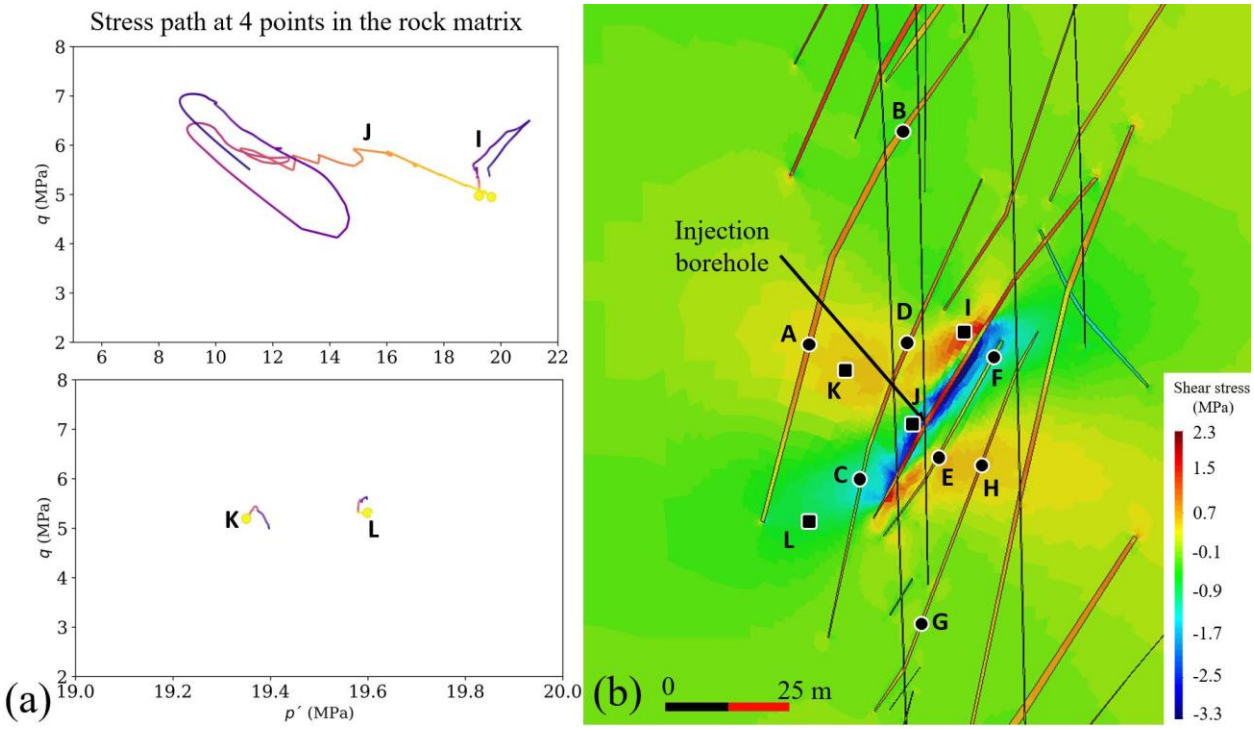

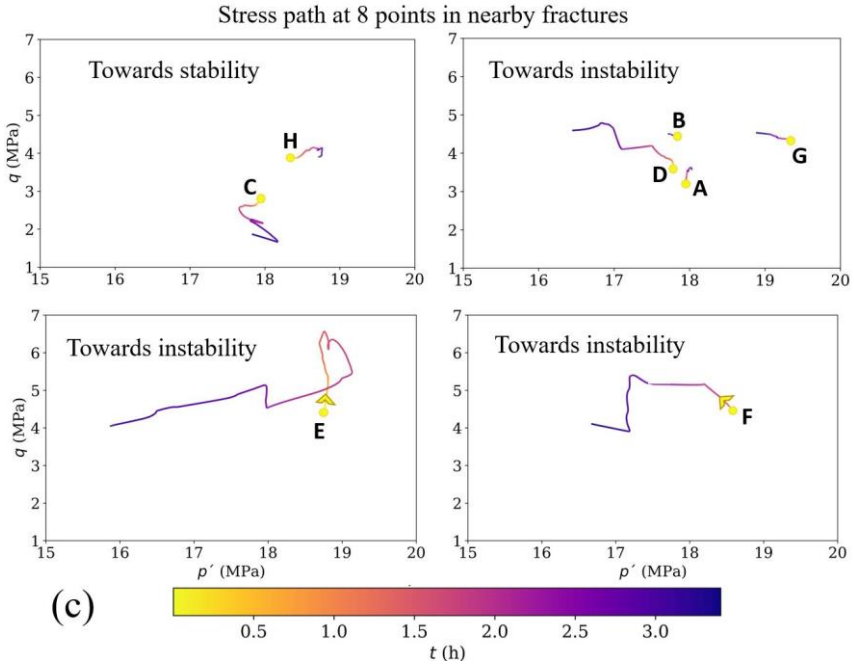

Figure 5.8 Stress paths (a) at four points in the rock matrix (I to L, depicted in panel b by squares), and (c) at eight points in nearby fractures (A to H, circles), respectively; the failure surface is located far away on the left side (all points are stable); b) Location of the selected points, with the shear stress (τ_{xy}) after 3.4 h in the background.

Shear failure conditions are also approached by a decrease in the effective mean stress and a slight decrease in the deviatoric stress (point E after 1.5 h of stimulation), which is usually the case when elastic poromechanical stress changes occur as a result of pore pressure increase (Vilarrasa et al., 2019). Yet, the trajectory at point E is more complex, showing an initial increase in deviatoric stress at constant effective mean stress, followed by a decrease in the deviatoric stress and effective mean stress, which could have been caused by shear-slip stress transfer and subsequent slip-driven pore pressure changes (Vilarrasa et al., 2021). Other sharp changes in the deviatoric stress are also induced by reactivation of the stimulated fracture (see points D and F). Other areas, affected by the stress shadow, move away from the failure surface by either increasing mean effective stress under constant deviatoric stress (point H) or by decreasing deviatoric stress under constant mean effective stress (point C).

5.3.4 Including more injection cycles in the viscoplastic model (VE)

The parameters of the model VE (Table 5.1) have been manually adjusted to render a good reproduction of the early stages of the stimulation (up to t=3.4 h, Figure 5.3a).

We validate the model by adding more injection cycles. The numerical model reproduces pore pressure evolution at the injection borehole fairly well during the validation period (from t=3.4 h to t=8 h; Figure 5.9). Thus, we conclude that the VE model reproduces the progressive hydraulic stimulation of the fracture, which enhances permeability away from the injection well as the number of injection cycles accumulates (Figure 5.10).

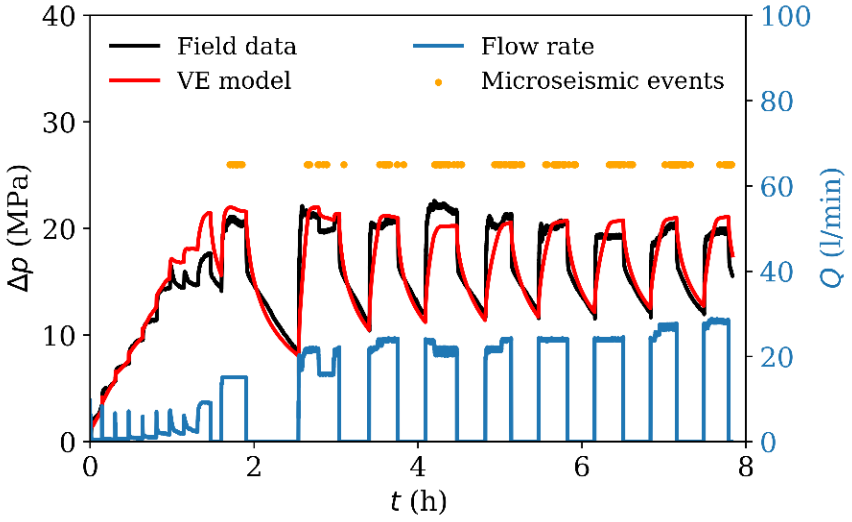

Figure 5.9 Temporal evolution of pressure and flow rate at the injection borehole for a large number of injection cycles for model VE compared to the field measurements. The timestamps of located microseismic events are indicated with orange dots.

Field measurements display a sharper pressure response at the borehole, both at the onset of injection and after shut-in, which may indicate that jacking of the fracture only occurs after exceeding a certain pressure threshold, which is not fully captured by the numerical model (Figure 5.9). It must be acknowledged, however, that compliance effects (response of packers and monitoring devices to the high and fast changes in pressure) also affect data, so we are not overly concerned by sharp responses. The relevant issue is that a number of microseismic events could be located during the field experiment. They coincide with the injection periods as the fracture undergoes shear slip. However, some occur after shut-in (Figure 5.9), as is often the case in practice (Baisch and Vörös, 2010; X. Wang et al., 2023). Microseismic events occur in every injection cycle, when permeability surpasses the previously achieved maximum value (see the permeability evolutions for 8 points located within the stimulated fracture in Figure 5.10a), a few examples are indicated with dotted arrows in Figure 5.10a and a zoom is provided in Figure 5.10b, meaning that the previously reactivated fault patch is reached and the new reactivation is accompanied by microseismic events. This observation is related to the

Kaiser effect; materials retain a "memory" of previously applied stresses (Lavrov, 2003). In the course of successive hydraulic stimulations, induced seismicity is found to be triggered solely upon surpassing the previous maximum of Coulomb stress changes (Kim and Avouac, 2023) corroborating our findings. The nucleation process is delayed if the stress decreases and it resumes only upon the return of stress to its previous peak level. In our simulation, permeability enhancement is observed 50 m away from the injection well after t~8 h of injection, coinciding with a final swarm of microseismic events (Figure 5.10a). The timestamps of microseismic events in Figure 5.10a correspond well with the times of maximum mobilized friction angle (Figure 5.10c). The continuation of the stress path at point 1 (Figure 5.7) including more injection cycles in Figure 5.11 displays a repetitive recurrence where the periodicity of the fracture reactivation shows the microseismic threshold is concomitant to plasticity.

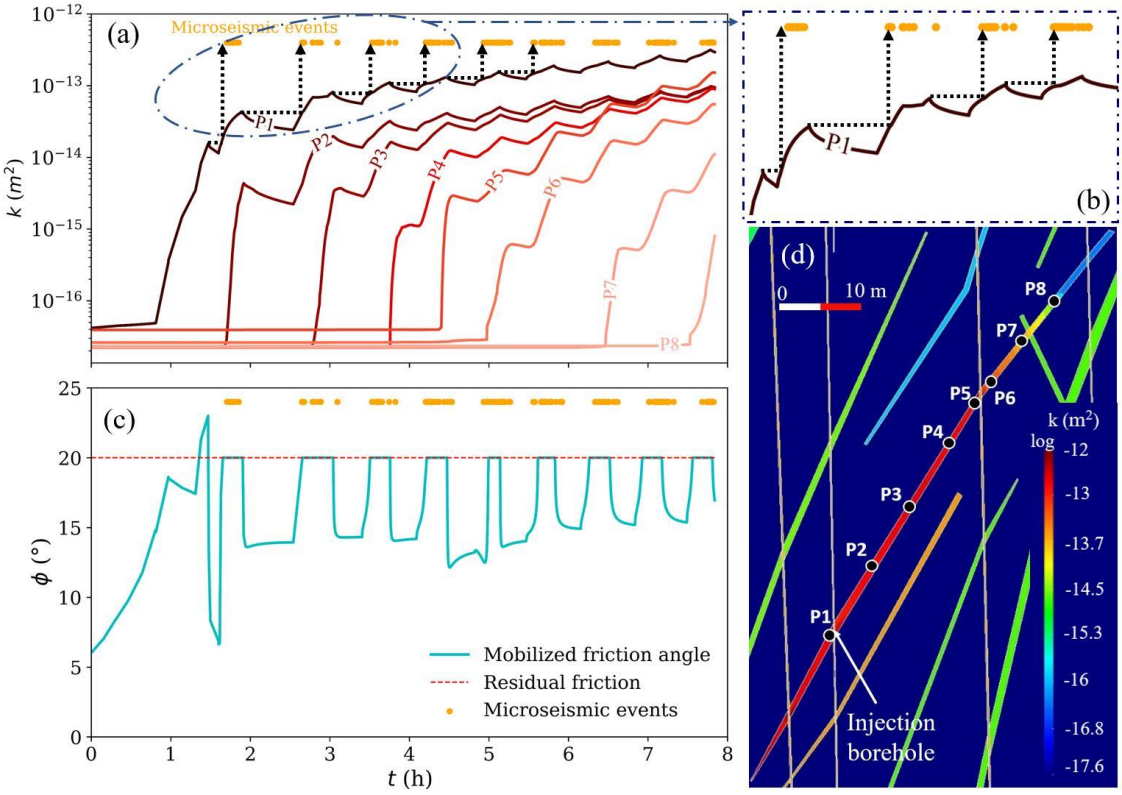

Figure 5.10 a) Temporal evolution of permeability at eight points (indicated in (d)) along the fracture together with timestamps of the microseismic events. The sharp permeability increase indicates when the pressure perturbation front reaches each point. b) Zoomed view of permeability evolution at point 1 to highlight the relation between permeability enhancement and microseismic threshold. c) Mobilized friction angle (Eq. (10)) during injection at point 1. d) Location of the 8 control points along the fracture, with the permeability contour plot after 8 hours of stimulation in the background. As a reference, point P8 is located 50 m away from the injection well.

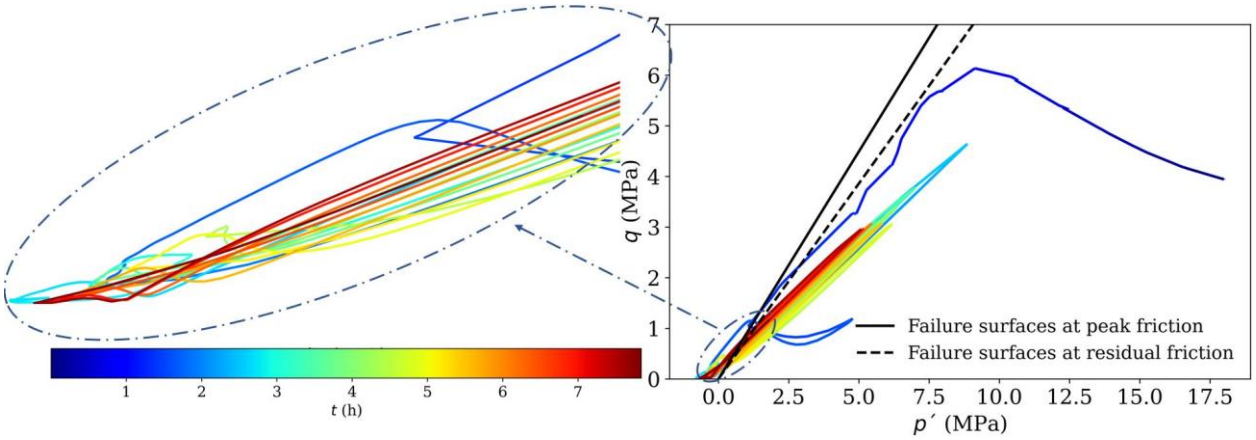

Figure 5.11 Stress path at point 1 as in Figure 5.7 for the larger number of injection cycles with a zoom in the critical area. The failure surfaces at peak and residual friction are based on Mohr-Coulomb failure criterion.

5.4 Discussion

The comparison between pore pressure evolution calculated by three models highlights that a viscoplastic model with strength weakening and dilatancy and computing fracture permeability changes as a function of volumetric strain assuming the cubic law (model VE) is needed, to reproduce field observations of hydraulic stimulation of crystalline rock. The elastic (EP and EE) models forecast significantly larger overpressures compared to the measured ones at the timestamps of microseismic events (orange dots in Figure 5.3). Thus, according to elastic models, microseismic events after shear failure should have occurred way before. This discrepancy suggests that the fracture was undergoing progressive shear slip and opening due to dilatancy, and thus permeability enhancement when the microseismic events were monitored. Furthermore, the validity of the implemented conceptual model including viscoplasticity is also confirmed by model validation, i.e., simulating further injection cycles not used for calibrating the model (Figure 5.9).

The comparison between permeability profiles along the fracture indicates a greater enhancement of permeability (Figure 5.4b) due to the larger dilatancy-induced increase of fracture opening in the viscoplastic model. The permeability enhancement of up to three orders of magnitude extends up to 40 m along the fracture towards the end of the calibration period (t~3.4 h). Figure 5.4a highlights the differences in pore pressure along the fracture for the three models once the fracture is reactivated (t>0.65 h). Simulation results show that when the permeability is manually and homogeneously adjusted in the

whole fracture (model EP), pore pressure diffuses along the whole fracture, yielding a pore pressure distribution that significantly differs from the actual one. When simulating variable permeability as a function of the injection-induced fracture aperture changes (Embedded models; EE and VE), pore pressure diffusion occurs slowly away from the stimulated fracture patch because of the low initial fracture permeability. Fracture opens up where pore pressure increases, and an additional dilation occurs in model VE when shear failure conditions are reached, yielding a progressively fracture stimulation in which permeability is enhanced (Peach and Spiers, 1996; Simpson et al., 2001; Ye and Ghassemi, 2018). The effect of the additional permeability enhancement caused by shear slip is evident when comparing the pore pressure profiles of models EE and VE, i.e., pressure build-up is lower in the viscoplastic model than in the elastic one.

Reducing the effective normal stress causes shear displacement, dilation and permeability enhancement of the natural fracture. Almost 90% of the slip displacement and dilation is estimated to occur after fracture shear failure (Xiao et al., 2019). After fracture activation, stress trajectories in the stimulated fracture follow a similar pattern in each injection cycle, i.e. decreasing both effective normal and deviatoric stress during injection and increasing again to a similar state developing fracture reactivation (Figure 5.7). This pattern would be observed in points far away the injection borehole after enough time for the reactivation front to reach distant points. These reactivation cycles are matched with the timestamps of seismic events.

When stimulating a fracture, the perturbation is not restricted to the fracture itself because (1) pore pressure diffuses, mainly through fractures, (2) induced poromechanical strain-stress changes extend further away than the stimulated fracture, and (3) shear stress transfer modifies the state of stress around the slipped patch of the fracture (Figure 5.8c), which may either promote shear failure of nearby fractures or inhibit it (stress shadow) (Safari and Ghassemi, 2016). When shear slip occurs along a fracture, the stress drop is right-lateral (blue colors in Figure 5.8c). The induced right-lateral shear stress is not restricted to the slipped patch and forms two lobes at the tips of the slipped area that affect portions of nearby fractures, creating the so-called stress shadow (Taghichian et al., 2014), which inhibits shear slip of these regions. The phenomenon of stress shadow refers to the development of a localized area exhibiting high compressive stresses that are oriented perpendicular to the fracture face in the vicinity of the fracture center. This results in the reorientation of the direction of maximum stress within the region of the stress shadow (Waters et al., 2009). Thus, if subsequent hydraulic stimulations are

performed in nearby fractures, the portions affected by the stress shadow may not be reactivated and permeability enhancement would be limited. On the contrary, the areas affected by the yellow-reddish colors in Figure 5.8c experience left-lateral shear stress that favors subsequent fracture reactivation if these fractures are stimulated. Note that the fractures placed close to the stimulated fracture contain both areas where shear slip is either promoted or inhibited.

The primary mechanism behind the manifestation of microseismic events is explicable by means of hydroshearing of pre-existing natural fractures that reach failure conditions (Yoon et al., 2017). Induced microseismicity is a phenomenon naturally accompanying plastic, i.e, irreversible, deformations. The involved hydromechanical processes including pressure increase, fracture dilation, permeability enhancement, and consequent microseismicity are well captured by our fully coupled viscoplastic model. The similar timestamps of plastic dilation (and pertinent permeability enhancement) and microseismic events (Figure 5.10) further support the model. (Minakov and Yarushina, 2021) have developed a poro-elastoplastic model to clarify the connection between the components of the seismic moment tensor and the failure process through the analysis of the acoustic emission during rock deformation. The model connects the localized failure pattern, plastic dilation ($\sin\psi$), and corresponding seismic response. Plasticity can explain induced microseismic source mechanisms. Further studies should focus on finding correlations between the spatiotemporal development of microseismicity (subject to the accuracy of the monitoring network) and the extent of the zone suffering from viscoplastic instability.

In induced seismicity, a hysteresis phenomenon known as the Kaiser effect (Lavrov, 2003), is frequently observed (Baisch et al., 2010; Dempsey and Riffault, 2019). This effect is characterized by the gradual failure of a material subjected to a series of increasing amplitude loading cycles, wherein subsequent failures typically occur at stress levels exceeding those reached in prior cycles. This effect elucidates the observation that acoustic emissions during rock failure cease when stress levels decrease and only resume once the medium is reloaded to its previous maximum (Minakov and Yarushina, 2021). It is anticipated that the Kaiser effect exhibits significant impact within a singular injection stage but displays lesser relevance between successive stages (Multi-stage injection).

Modeling hydraulic stimulation presents challenges due to the involvement of complex physical processes, such as rock deformation, fluid flow, and fracture initiation and propagation (Chen et al., 2022; Wu et al., 2022). The complexity of hydraulic stimulation arises from several factors, such as the coupling of fluid flow inside fractures with rock

and fracture deformation; the involvement of multiscale and multi-physics processes like the interaction between natural and hydraulic fractures, leak-off, and rock heterogeneity; and the difficulty in accurately modeling geological and operational conditions due to limited data availability and high costs. The challenge remains in scaling up numerical simulation capabilities from single fracture stimulation in a laboratory setting to multiple fractures at the field scale in industrial projects. This upscaling necessitates the development of more efficient numerical methods that can effectively manage the increased demand for computational resources. In order to make the study of hydraulic stimulation more tractable, some aspects of the problem need to be simplified or ignored in numerical simulations, leading to the development of multiple modeling approaches with varying applicability and limitations. We show that a viscoplastic model that accounts for strength weakening, dilatancy, and fracture permeability evolution as a function of volumetric strain enables numerical models to accurately reproduce hydraulic stimulation in crystalline rocks, thereby enhancing the understanding of the underlying processes and improving the capability to forecast hydraulic stimulation outcomes.

5.5 Conclusion

We have modeled one of the hydraulic stimulations performed at the BULGG using three different approaches. Despite reproducing a well-fitted pressure evolution curve, the model with manually calibrated permeability lacks the ability to capture the pore pressure distribution along the fracture, and consequently the poromechanical response at the rock matrix and nearby fractures, because permeability is assumed homogeneous along the fracture. Considering the embedded model to simulate permeability enhancement following the cubic law as a function of the volumetric strain improves the estimation of the spatio-temporal distribution of pressure. Yet, pressure is overestimated after the onset of fracture slips when assuming elastic behavior. To satisfactorily reproduce field measurements, an additional permeability enhancement is required in the post-failure stage, which is achieved with a viscoplastic model with strain weakening and dilatancy. This viscoplastic model, whose parameters have been manually adjusted to render a good fit of the early stages of stimulation, has been validated by extending the simulation to further injection cycles. Microseismic events in each cycle occur once plastic strain and, thus, permeability surpass the maximum value achieved in previous injection cycles. Furthermore, post-injection microseismicity becomes more perceptible as injection cycles accumulate. The timestamps of monitored microseismic events are well predicted by the viscoplastic model, which predicts unstable conditions at the time of the seismic clouds

showing that the induced microseismic threshold is concomitant to plasticity. The correlation between plasticity and induced microseismic events is illustrated by stress trajectories, which show that the timestamps of monitored microseismicity at the field laboratory coincide with the periods at which the fracture undergoes shear failure conditions. Furthermore, the viscoplastic model reproduces the coupled processes in a natural way, thus avoiding the tedious, subjective and prone-to-error manual calibration of the spatio-temporal evolution of permeability.

In summary, the proposed VE model accounts for fracture reactivation and dilatancy and allows good reproduction of observed pressure evolution, three orders of magnitude irreversible increases in permeability and the timing of microseismic events. We conclude that the insights yielded by this model are supported by observations. We conjecture that they can be extended beyond the processes and extent of the hydraulic stimulation, into a comprehensive understanding of the hydromechanical response of the subsurface to fluid injection and associated (micro) seismicity.

6

Concluding remarks

This thesis advances the understanding of the hydro-mechanical response of fractured rocks to fluid injection, with direct implications for geo-engineering and geo-energy applications, such as hydraulic stimulation of low-permeability fractured rock, geologic carbon storage, and hydraulic fracturing operations. A comprehensive exploration of coupled HM processes influencing seismicity during the stimulation and injection operations of EGS has been undertaken. The main conclusions of the Thesis are summarized below.

The investigation of the hydraulic response to water injection into a fracture surrounded by low-permeability rock has unveiled important insights. Notably, the analysis of pressure evolution has highlighted the non-negligible impact on fluid flow of leakage despite the low-permeability rock matrix. It is revealed that fractures exhibit a leaky nature, challenging the conventional assumption of impermeable matrix in certain modeling approaches (it is usually done when dealing with low-permeability media in approaches like DFN, DEM, and SFM). The short transition time to leakage-dominated flow, coupled with the potential for a prolonged leakage-dominated regime, underscores the significance of accounting for leakage in interpreting injection tests and modeling fractured media. Neglecting leakage has been shown to result in an overestimation of fracture transmissivity by a factor of two and the pressure perturbation front by a few orders of magnitude.

A novel approach involving the derivation of equivalent HM properties for an equivalent-continuum layer, significantly thicker than the represented fracture, has been

proposed. The method has demonstrated the ability to achieve identical simulation results for equivalent fracture layers with centimeter-scale thickness as the actual fracture aperture at the micrometer scale. This upscaling approach enhances the tractability of fracture discretization while preserving accuracy, presenting a useful method for modeling geo-energy and geo-engineering applications in fractured media across varying scales.

Furthermore, the modeling of hydraulic stimulations at the BULGG using different approaches has yielded valuable insights. The limitations of a manually calibrated permeability model have been identified, emphasizing the need for a more nuanced representation of permeability enhancement. An elastic poromechanical fracture representation accounting for permeability changes proportional to the cube of fracture aperture, i.e., cubic law, is capable of reproducing the observed pressure evolution in the field until the fracture is reactivated. Subsequently, a viscoplastic model, incorporating strain weakening and dilatancy, has proven instrumental in reproducing observed pressure evolution, irreversible increases in permeability, and the timing of microseismic events. The model ability to predict stress trajectories and illustrate the correlation between plasticity and induced microseismic events offers a natural and comprehensive understanding of coupled processes, mitigating the need for subjective and error-prone manual calibration. The proposed viscoplastic model, with its capacity to account for fracture reactivation and dilatancy, aligns well with observed phenomena and provides a robust foundation for extending insights beyond hydraulic stimulation processes. The findings not only contribute to the understanding of (micro)seismicity in EGS, but also offer broader implications for comprehending the HM response of the subsurface to fluid injection across various applications. This thesis, through its multifaceted exploration, marks a considerable contribution to the academic and professional discourse in the field.

7

Publications and conference presentations

Articles in the process of publications

I. Vaezi, V. Vilarrasa, F. Parisio, and K. Yoshioka. *On the leaky nature of fractures in low-permeability rock*. submitted.

I. Vaezi, A. Alcolea, P. Meier, F. Parisio, J. Carrera, and V. Vilarrasa. *Numerical modeling of hydraulic stimulation of fractured crystalline rock at the Bedretto Underground Laboratory for Geosciences and Geoenergies*. submitted.

I. Vaezi, F. Parisio, K. Yoshioka, A. Alcolea, P. Meier, J. Carrera, S. Olivella, and V. Vilarrasa. *Implicit hydro-mechanical representation of fractures using continuum approach*. submitted.

S. K. Tangirala, F. Parisio, I. Vaezi, and V. Vilarrasa. *Effectiveness of injection protocols for hydraulic stimulation in Enhanced Geothermal Systems*. submitted

I. Vaezi, K. Yoshioka, S. De Simone, B. Gómez, A. Paluszny, M. R. Jalali, I. Berre, S. Olivella, J. Rutqvist, K. Min, Q. Lei, R. Y. Makhnenko, C. Tsang, and V. Vilarrasa, *A review on thermo-hydro-mechanical modeling of coupled processes in fractured rocks: A continuum to discontinuum perspective*. Under revision by co-authors.

Presentations in conferences

I. Vaezi, A. Alcolea, P. Meier, F. Parisio, J. Carrera, and V. Vilarrasa, May 2023, *Numerical simulation of hydroshearing in fractured crystalline rock at the Bedretto Underground Laboratory (Switzerland)*, InterPore2023, Edinburgh, Scotland.

I. Vaezi, V. Vilarrasa, F. Parisio, and K. Yoshioka, Nov. 2022, *Implicit representation of a single fracture with a continuum equivalent layer to simulate coupled processes*, 3rd International Conference on Coupled Processes in Fractured Geological Media (CouFrac2022), California, USA.

I. Vaezi, V. Vilarrasa, F. Parisio, and K. Yoshioka, Apr. 2021, *Numerical simulation of coupled processes in a single fracture employing a continuum approach*, European Geosciences Union General Assembly 2021 (EGU21), Vienna, Austria.

I. Vaezi, V. Vilarrasa, F. Parisio, and K. Yoshioka, Nov. 2020, *Modeling coupled processes in fractured media using a continuum approach*, 2nd International Conference on Coupled Processes in Fractured Geological Media (CouFrac2020) Seoul, S. Korea.

8

Bibliography

Abdassah, D., Ershaghi, I., 1986. Triple-Porosity Systems for Representing Naturally Fractured Reservoirs. SPE Formation Evaluation 1, 113–127. https://doi.org/10.2118/13409-PA

Abedi, R., Clarke, P.L., 2019. A computational approach to model dynamic contact and fracture mode transitions in rock. Computers and Geotechnics 109, 248–271. https://doi.org/10.1016/j.compgeo.2019.01.010

Abushaikha, A.S.A., Gosselin, O.R., 2008. Matrix-Fracture Transfer Function in Dual-Medium Flow Simulation: Review, Comparison, and Validation. Presented at the Europec/EAGE Conference and Exhibition, OnePetro. https://doi.org/10.2118/113890-MS

Achtziger-Zupančič, P., Loew, S., Mariéthoz, G., 2017. A new global database to improve predictions of permeability distribution in crystalline rocks at site scale. Journal of Geophysical Research: Solid Earth 122, 3513–3539. https://doi.org/10.1002/2017JB014106

Adler, P.M., Thovert, J.-F., Mourzenko, V.V., 2013. Fractured Porous Media. OUP Oxford.

Afshari Moein, M.J., Somogyvári, M., Valley, B., Jalali, M., Loew, S., Bayer, P., 2018. Fracture Network Characterization Using Stress-Based Tomography. Journal of Geophysical Research: Solid Earth 123, 9324–9340. https://doi.org/10.1029/2018JB016438

Agard, P., Augier, R., Monié, P., 2011. Shear band formation and strain localization on a regional scale: Evidence from anisotropic rocks below a major detachment (Betic

Cordilleras, Spain). Journal of Structural Geology 33, 114–131. https://doi.org/10.1016/j.jsg.2010.11.011

Agheshlui, H., Sedaghat, M.H., Matthai, S., 2018. Stress Influence on Fracture Aperture and Permeability of Fragmented Rocks. Journal of Geophysical Research: Solid Earth 123, 3578–3592. https://doi.org/10.1029/2017JB015365

Aghili, J., Brenner, K., Hennicker, J., Masson, R., Trenty, L., 2019. Two-phase Discrete Fracture Matrix models with linear and nonlinear transmission conditions. Int J Geomath 10, 1. https://doi.org/10.1007/s13137-019-0118-6

Aguilar-López, J.P., Bogaard, T., Gerke, H.H., 2020. Dual-Permeability Model Improvements for Representation of Preferential Flow in Fractured Clays. Water Resources Research 56, e2020WR027304. https://doi.org/10.1029/2020WR027304

Ahmed, R., Edwards, M.G., Lamine, S., Huisman, B.A.H., Pal, M., 2017. CVD-MPFA full pressure support, coupled unstructured discrete fracture–matrix Darcy-flux approximations. Journal of Computational Physics 349, 265–299. https://doi.org/10.1016/j.jcp.2017.07.041

Alcolea, A., Kuhlmann, U., Marschall, P., Lisjak, A., Grasselli, G., Mahabadi, O., de La Vaissiere, R., Leung, H., Shao, H., 2016. A pragmatic approach to abstract the EDZ around tunnels of a geological radioactive waste repository—Application to the HG-A experiment in Mont Terri. Geological Society, London, Special Publications 443. https://doi.org/10.1144/SP443.8

Almani, T., Kumar, K., Dogru, A., Singh, G., Wheeler, M.F., 2016. Convergence analysis of multirate fixed-stress split iterative schemes for coupling flow with geomechanics. Computer Methods in Applied Mechanics and Engineering 311, 180–207. https://doi.org/10.1016/j.cma.2016.07.036

Almani, T., Kumar, K., Wheeler, M.F., 2023. Convergence analysis of single rate and multirate fixed stress split iterative coupling schemes in heterogeneous poroelastic media. Numerical Methods for Partial Differential Equations 39, 3170–3194. https://doi.org/10.1002/num.23004

Amadei, B., Saeb, S., 1990. Constitutive models of rock joints, in: International Symposium on Rock Joints. pp. 581–594.

Amann, F., Gischig, V., Evans, K., Doetsch, J., Jalali, R., Valley, B., Krietsch, H., Dutler, N., Villiger, L., Brixel, B., Klepikova, M., Kittilä, A., Madonna, C., Wiemer, S., Saar, M.O., Loew, S., Driesner, T., Maurer, H., Giardini, D., 2018a. The seismo-hydromechanical behavior during deep geothermal reservoir stimulations: open

questions tackled in a decameter-scale in situ stimulation experiment. Solid Earth 9, 115–137. https://doi.org/10.5194/se-9-115-2018

Amann, F., Wild, K.M., Loew, S., Yong, S., Thoeny, R., Frank, E., 2018b. Geomechanical behaviour of Opalinus Clay at multiple scales: results from Mont Terri rock laboratory (Switzerland), in: Bossart, P., Milnes, A.G. (Eds.), Mont Terri Rock Laboratory, 20 Years: Two Decades of Research and Experimentation on Claystones for Geological Disposal of Radioactive Waste, Swiss Journal of Geosciences Supplement. Springer International Publishing, Cham, pp. 153–173. https://doi.org/10.1007/978-3-319-70458-6_8

Anders, M.H., Laubach, S.E., Scholz, C.H., 2014. Microfractures: A review. Journal of Structural Geology, Fluids and Structures in Fold and Thrust Belts with Recognition of the Work of David V. Wiltschko 69, 377–394. https://doi.org/10.1016/j.jsg.2014.05.011

Ando, K., Kostner, A., Neuman, S.P., 2003. Stochastic continuum modeling of flow and transport in a crystalline rock mass: Fanay-Augères, France, revisited. Hydrogeology Journal 11, 521–535. https://doi.org/10.1007/s10040-003-0286-0

Andrés, S., Dentz, M., Cueto-Felgueroso, L., 2021. Multirate Mass Transfer Approach for Double-Porosity Poroelasticity in Fractured Media. Water Resources Research 57, e2021WR029804. https://doi.org/10.1029/2021WR029804

Andrews, D.J., 2005. Rupture dynamics with energy loss outside the slip zone. Journal of Geophysical Research: Solid Earth 110. https://doi.org/10.1029/2004JB003191

Andrews, D.J., 2004. Rupture Models with Dynamically Determined Breakdown Displacement. Bulletin of the Seismological Society of America 94, 769–775. https://doi.org/10.1785/0120030142

Andrews, D.J., 1985. Dynamic plane-strain shear rupture with a slip-weakening friction law calculated by a boundary integral method. Bulletin of the Seismological Society of America 75, 1–21. https://doi.org/10.1785/BSSA0750010001

Arbogast, T., 1992. The Existence of Weak Solutions to Single Porosity and Simple Dual-Porosity Models of Two-Phase Incompressible Flow.

Asadollahi, P., Tonon, F., 2010. Constitutive model for rock fractures: Revisiting Barton's empirical model. Engineering Geology 113, 11–32. https://doi.org/10.1016/j.enggeo.2010.01.007

Atkinson, B.K., 1984. Subcritical crack growth in geological materials. Journal of Geophysical Research: Solid Earth 89, 4077–4114. https://doi.org/10.1029/JB089iB06p04077

Babanouri, N., Fattahi, H., 2018. Constitutive modeling of rock fractures by improved support vector regression. Environ Earth Sci 77, 243. https://doi.org/10.1007/s12665-018-7421-7

Baca, R.G., Arnett, R.C., Langford, D.W., 1984. Modelling fluid flow in fractured-porous rock masses by finite-element techniques. International Journal for Numerical Methods in Fluids 4, 337–348.

Baghbanan, A., Jing, L., 2008. Stress effects on permeability in a fractured rock mass with correlated fracture length and aperture. International Journal of Rock Mechanics and Mining Sciences 45, 1320–1334. https://doi.org/10.1016/j.ijrmms.2008.01.015

Bahrami, B., Mohsenpour, S., Miri, M.A., Mirhaseli, R., 2017. Quantitative comparison of fifteen rock failure criteria constrained by polyaxial test data. Journal of Petroleum Science and Engineering 159, 564–580. https://doi.org/10.1016/j.petrol.2017.09.065

Bai, M., Elsworth, D., Roegiers, J.-C., 1993. Multiporosity/multipermeability approach to the simulation of naturally fractured reservoirs. Water Resources Research 29, 1621–1633. https://doi.org/10.1029/92WR02746

Bai, M., Roegiers, J.-C., 1994. Fluid flow and heat flow in deformable fractured porous media. International Journal of Engineering Science 32, 1615–1633. https://doi.org/10.1016/0020-7225(94)90169-4

Baisch, S., Vörös, R., 2010. Reservoir induced seismicity: Where, when, why and how strong, in: Proceedings World Geothermal Congress.

Baisch, S., Vörös, R., Rothert, E., Stang, H., Jung, R., Schellschmidt, R., 2010. A numerical model for fluid injection induced seismicity at Soultz-sous-Forêts. International Journal of Rock Mechanics and Mining Sciences 47, 405–413. https://doi.org/10.1016/j.ijrmms.2009.10.001

Bandis, S.C., Lumsden, A.C., Barton, N.R., 1983. Fundamentals of rock joint deformation. International Journal of Rock Mechanics and Mining Sciences & Geomechanics Abstracts 20, 249–268. https://doi.org/10.1016/0148-9062(83)90595-8

Barenblatt, G.I., 1962. The Mathematical Theory of Equilibrium Cracks in Brittle Fracture, in: Dryden, H.L., von Kármán, Th., Kuerti, G., van den Dungen, F.H.,

Howarth, L. (Eds.), Advances in Applied Mechanics. Elsevier, pp. 55–129. https://doi.org/10.1016/S0065-2156(08)70121-2

Barenblatt, G.I., Zheltov, I.P., Kochina, I.N., 1960. Basic concepts in the theory of seepage of homogeneous liquids in fissured rocks [strata]. Journal of applied mathematics and mechanics 24, 1286–1303.

Baria, R., Baumgärtner, J., Rummel, F., Pine, R.J., Sato, Y., 1999. HDR/HWR reservoirs: concepts, understanding and creation. Geothermics 28, 533–552. https://doi.org/10.1016/S0375-6505(99)00045-0

Barker, J.A., 1988. A generalized radial flow model for hydraulic tests in fractured rock. Water Resources Research 24, 1796–1804. https://doi.org/10.1029/WR024i010p01796

Barton, N., Bandis, S., Bakhtar, K., 1985. Strength, deformation and conductivity coupling of rock joints. International Journal of Rock Mechanics and Mining Sciences & Geomechanics Abstracts 22, 121–140. https://doi.org/10.1016/0148-9062(85)93227-9

Bayer, P., Attard, G., Blum, P., Menberg, K., 2019. The geothermal potential of cities. Renewable and Sustainable Energy Reviews 106, 17–30. https://doi.org/10.1016/j.rser.2019.02.019

Bear, J., 1972. Dynamics of Fluids in Porous Media. Courier Corporation.

Beauheim, R.L., Roberts, R.M., Avis, J.D., 2004. Well testing in fractured media: flow dimensions and diagnostic plots. Journal of Hydraulic Research 42, 69–76. https://doi.org/10.1080/00221680409500049

Bedoya-Gonzalez, D., Kessler, T., Rinder, T., Hilberg, S., Szabó-Krausz, Z., Schafmeister, M.-T., 2023. A Multiple Interactive Continua Model (MINC) to Simulate Reactive Mass Transport in a Post-Mining Coal Zone: A Case Study of the Ibbenbüren Westfield. Mine Water Environ 42, 266–292. https://doi.org/10.1007/s10230-023-00938-2

Ben-Zion, Y., Rice, J.R., 1993. Earthquake failure sequences along a cellular fault zone in a three-dimensional elastic solid containing asperity and nonasperity regions. Journal of Geophysical Research: Solid Earth 98, 14109–14131. https://doi.org/10.1029/93JB01096

Berkowitz, B., 2002. Characterizing flow and transport in fractured geological media: A review. Advances in Water Resources 25, 861–884. https://doi.org/10.1016/S0309-1708(02)00042-8

Berre, I., Boon, W.M., Flemisch, B., Fumagalli, A., Gläser, D., Keilegavlen, E., Scotti, A., Stefansson, I., Tatomir, A., Brenner, K., Burbulla, S., Devloo, P., Duran, O., Favino, M., Hennicker, J., Lee, I.-H., Lipnikov, K., Masson, R., Mosthaf, K., Nestola, M.G.C., Ni, C.-F., Nikitin, K., Schädle, P., Svyatskiy, D., Yanbarisov, R., Zulian, P., 2021. Verification benchmarks for single-phase flow in three-dimensional fractured porous media. Advances in Water Resources 147, 103759. https://doi.org/10.1016/j.advwatres.2020.103759

Berre, I., Doster, F., Keilegavlen, E., 2019. Flow in Fractured Porous Media: A Review of Conceptual Models and Discretization Approaches. Transp Porous Med 130, 215–236. https://doi.org/10.1007/s11242-018-1171-6

Berrone, S., Hyman, J.D., Pieraccini, S., 2020. Multilevel Monte Carlo Predictions of First Passage Times in Three-Dimensional Discrete Fracture Networks: A Graph-Based Approach. Water Resources Research 56, e2019WR026493. https://doi.org/10.1029/2019WR026493

Berrone, S., Pieraccini, S., Scialò, S., 2017. Flow simulations in porous media with immersed intersecting fractures. Journal of Computational Physics 345, 768–791. https://doi.org/10.1016/j.jcp.2017.05.049

Berrone, S., Pieraccini, S., Scialò, S., 2013. A PDE-Constrained Optimization Formulation for Discrete Fracture Network Flows. SIAM J. Sci. Comput. 35, B487–B510. https://doi.org/10.1137/120865884

Biot, 1941. General Theory of Three-Dimensional Consolidation. Journal of Applied Physics 12, 155–164. https://doi.org/10.1063/1.1712886

Biot, M.A., 1962. Mechanics of deformation and acoustic propagation in porous media. Journal of applied physics 33, 1482–1498.

Biot, M.A., 1956. Thermoelasticity and Irreversible Thermodynamics. Journal of Applied Physics 27, 240–253. https://doi.org/10.1063/1.1722351

Birkholzer, J.T., Tsang, C.-F., Bond, A.E., Hudson, J.A., Jing, L., Stephansson, O., 2019. 25 years of DECOVALEX - Scientific advances and lessons learned from an international research collaboration in coupled subsurface processes. International Journal of Rock Mechanics and Mining Sciences 122, 103995. https://doi.org/10.1016/j.ijrmms.2019.03.015

Birkholzer, J.T., Zhou, Q., Tsang, C.-F., 2009. Large-scale impact of CO2 storage in deep saline aquifers: A sensitivity study on pressure response in stratified systems. International Journal of Greenhouse Gas Control 3, 181–194. https://doi.org/10.1016/j.ijggc.2008.08.002

Bissell, R.C., Vasco, D.W., Atbi, M., Hamdani, M., Okwelegbe, M., Goldwater, M.H., 2011. A full field simulation of the in Salah gas production and CO2 storage project using a coupled geo-mechanical and thermal fluid flow simulator. Energy Procedia, 10th International Conference on Greenhouse Gas Control Technologies 4, 3290–3297. https://doi.org/10.1016/j.egypro.2011.02.249

Bizzarri, A., 2012. Modeling Repeated Slip Failures on Faults Governed by Slip-Weakening Friction. Bulletin of the Seismological Society of America 102, 812–821. https://doi.org/10.1785/0120110141

Black, J.H., Barker, J.A., 2018. An alternative approach to understanding groundwater flow in sparse channel networks supported by evidence from 'background' fractured crystalline rocks. Hydrogeol J 26, 2707–2723. https://doi.org/10.1007/s10040-018-1823-1

Black, J.H., Woodman, N.D., Barker, J.A., 2017. Groundwater flow into underground openings in fractured crystalline rocks: an interpretation based on long channels. Hydrogeol J 25, 445–463. https://doi.org/10.1007/s10040-016-1511-y

Bogdanov, I.I., Mourzenko, V.V., Thovert, J.-F., Adler, P.M., 2003. Effective permeability of fractured porous media in steady state flow. Water Resources Research 39. https://doi.org/10.1029/2001WR000756

Bonnet, E., Bour, O., Odling, N.E., Davy, P., Main, I., Cowie, P., Berkowitz, B., 2001. Scaling of fracture systems in geological media. Reviews of Geophysics 39, 347–383. https://doi.org/10.1029/1999RG000074

Boon, W.M., Nordbotten, J.M., Yotov, I., 2018. Robust Discretization of Flow in Fractured Porous Media. SIAM J. Numer. Anal. 56, 2203–2233. https://doi.org/10.1137/17M1139102

Borja, R.I., Foster, C.D., 2007. Continuum mathematical modeling of slip weakening in geological systems. Journal of Geophysical Research: Solid Earth 112. https://doi.org/10.1029/2005JB004056

Borja, R.I., Yin, Q., Zhao, Y., 2020. Cam-Clay plasticity. Part IX: On the anisotropy, heterogeneity, and viscoplasticity of shale. Computer Methods in Applied

Mechanics and Engineering 360, 112695. https://doi.org/10.1016/j.cma.2019.112695

Botros, F.E., Hassan, A.E., Reeves, D.M., Pohll, G., 2008. On mapping fracture networks onto continuum. Water Resources Research 44. https://doi.org/10.1029/2007WR006092

Bour, O., Davy, P., Darcel, C., Odling, N., 2002. A statistical scaling model for fracture network geometry, with validation on a multiscale mapping of a joint network (Hornelen Basin, Norway). Journal of Geophysical Research: Solid Earth 107, ETG 4-1-ETG 4-12. https://doi.org/10.1029/2001JB000176

Bourdet, D., Ayoub, J.A., Plrard, Y.M., 1989. Use of Pressure Derivative in Well-Test Interpretation. SPE Formation Evaluation 4, 293–302. https://doi.org/10.2118/12777-PA

Bourdet, D., Whittle, T.M., Douglas, A.A., Pirard, Y.M., 1983. A new set of type curves simplifies well test analysis. World oil 196, 95–106.

Bourdin, B., Chukwudozie, C., Yoshioka, K., 2012. A Variational Approach to the Numerical Simulation of Hydraulic Fracturing. Presented at the SPE Annual Technical Conference and Exhibition, OnePetro. https://doi.org/10.2118/159154-MS

Boyet, A., De Simone, S., Ge, S., Vilarrasa, V., 2023. Poroelastic stress relaxation, slip stress transfer and friction weakening controlled post-injection seismicity at the Basel Enhanced Geothermal System. Commun Earth Environ 4, 1–13. https://doi.org/10.1038/s43247-023-00764-y

Brace, W.F., Paulding Jr., B.W., Scholz, C., 1966. Dilatancy in the fracture of crystalline rocks. Journal of Geophysical Research (1896-1977) 71, 3939–3953. https://doi.org/10.1029/JZ071i016p03939

Bredehoeft, J.D., Wolff, R.G., Keys, W.S., Shuter, E., 1976. Hydraulic fracturing to determine the regional in situ stress field, Piceance Basin, Colorado. Geological Society of America Bulletin 87, 250–258.

Breede, K., Dzebisashvili, K., Liu, X., Falcone, G., 2013. A systematic review of enhanced (or engineered) geothermal systems: past, present and future. Geotherm Energy 1, 4. https://doi.org/10.1186/2195-9706-1-4

Bröker, K., Ma, X., 2022. Estimating the Least Principal Stress in a Granitic Rock Mass: Systematic Mini-Frac Tests and Elaborated Pressure Transient Analysis. Rock Mech Rock Eng 55, 1931–1954. https://doi.org/10.1007/s00603-021-02743-1

Brooks, Z., 2013. Fracture process zone: Microstructure and nanomechanics in quasi-brittle materials. Massachusetts Institute of Technology.

Brown, D.W., Duchane, D.V., Heiken, G., Hriscu, V.T., 2012. Mining the Earth's Heat: Hot Dry Rock Geothermal Energy. Springer Science & Business Media.

Brown, S., Caprihan, A., Hardy, R., 1998. Experimental observation of fluid flow channels in a single fracture. Journal of Geophysical Research: Solid Earth 103, 5125–5132. https://doi.org/10.1029/97JB03542

Bruel, D., 2007. Using the migration of the induced seismicity as a constraint for fractured Hot Dry Rock reservoir modelling. International Journal of Rock Mechanics and Mining Sciences 44, 1106–1117. https://doi.org/10.1016/j.ijrmms.2007.07.001

Brush, D.J., Thomson, N.R., 2003. Fluid flow in synthetic rough-walled fractures: Navier-Stokes, Stokes, and local cubic law simulations. Water Resources Research 39. https://doi.org/10.1029/2002WR001346

Bunger, A.P., McLennan, J., Jeffrey, R., 2013. Effective and sustainable hydraulic fracturing. InTech.

Byerlee, J.D., 1968. Brittle-ductile transition in rocks. Journal of Geophysical Research (1896-1977) 73, 4741–4750. https://doi.org/10.1029/JB073i014p04741

Cacas, M.C., Ledoux, E., de Marsily, G., Tillie, B., Barbreau, A., Durand, E., Feuga, B., Peaudecerf, P., 1990. Modeling fracture flow with a stochastic discrete fracture network: calibration and validation: 1. The flow model. Water Resources Research 26, 479–489. https://doi.org/10.1029/WR026i003p00479

Cao, C., Xu, Z., Chai, J., Li, Y., 2019. Radial fluid flow regime in a single fracture under high hydraulic pressure during shear process. Journal of Hydrology 579, 124142. https://doi.org/10.1016/j.jhydrol.2019.124142

Carrera, J., Martinez-Landa, L., 2000. Mixed discrete-continuum models: a summary of experiences in test interpretation and model prediction. GEOPHYSICAL MONOGRAPH-AMERICAN GEOPHYSICAL UNION 122, 251–266.

Carrier, B., Granet, S., 2012. Numerical modeling of hydraulic fracture problem in permeable medium using cohesive zone model. Engineering Fracture Mechanics 79, 312–328. https://doi.org/10.1016/j.engfracmech.2011.11.012

Castelletto, N., Klevtsov, S., Hajibeygi, H., Tchelepi, H.A., 2019. Multiscale two-stage solver for Biot's poroelasticity equations in subsurface media. Comput Geosci 23, 207–224. https://doi.org/10.1007/s10596-018-9791-z

Castelletto, N., White, J.A., Tchelepi, H.A., 2015. Accuracy and convergence properties of the fixed-stress iterative solution of two-way coupled poromechanics. International Journal for Numerical and Analytical Methods in Geomechanics 39, 1593–1618. https://doi.org/10.1002/nag.2400

Celia, M.A., Nordbotten, J.M., Court, B., Dobossy, M., Bachu, S., 2011. Field-scale application of a semi-analytical model for estimation of CO2 and brine leakage along old wells. International Journal of Greenhouse Gas Control 5, 257–269. https://doi.org/10.1016/j.ijggc.2010.10.005

Chen, B., Barboza, B.R., Sun, Y., Bai, J., Thomas, H.R., Dutko, M., Cottrell, M., Li, C., 2022. A Review of Hydraulic Fracturing Simulation. Arch Computat Methods Eng 29, 1–58. https://doi.org/10.1007/s11831-021-09653-z

Chen, H.-Y., Teufel, L.W., 1997. Coupling Fluid-Flow and Geomechanics in Dual-Porosity Modeling of Naturally Fractured Reservoirs. Presented at the SPE Annual Technical Conference and Exhibition, OnePetro. https://doi.org/10.2118/38884-MS

Chen, S., Qiao, C., 2018. Composite damage constitutive model of jointed rock mass considering crack propagation length and joint friction effect. Arab J Geosci 11, 283. https://doi.org/10.1007/s12517-018-3643-y

Chen, T., Clauser, C., Marquart, G., Willbrand, K., Hiller, T., 2018. Upscaling permeability for three-dimensional fractured porous rocks with the multiple boundary method. Hydrogeol J 26, 1903–1916. https://doi.org/10.1007/s10040-018-1744-z

Chen, Y., Lin, H., Wang, Y., Zhao, Y., 2020. Damage Statistical Empirical Model for Fractured Rock under Freezing-Thawing Cycle and Loading. Geofluids 2020, e8842471. https://doi.org/10.1155/2020/8842471

Chen, Y., Lin, H., Xie, S., Cao, R., Sun, S., Zha, W., Wang, Y., Zhao, Y., Hu, H., 2023. Fracture Closure Empirical Model and Theoretical Damage Model of Rock under Compression. Materials 16, 589. https://doi.org/10.3390/ma16020589

Chen, Y., Ma, G., Wang, H., Li, T., 2018. Evaluation of geothermal development in fractured hot dry rock based on three dimensional unified pipe-network method. Applied Thermal Engineering 136, 219–228. https://doi.org/10.1016/j.applthermaleng.2018.03.008

Cheng, A.H.-D., Morohunfola, O.K., 1993. Multilayered leaky aquifer systems: 1. Pumping well solutions. Water Resources Research 29, 2787–2800. https://doi.org/10.1029/93WR00768

Chow, V.T., 1952. On the determination of transmissibility and storage coefficients from pumping test data. Eos, Transactions American Geophysical Union 33, 397–404.

Christensen, J.L., Hain, D.S., 2017. Knowing where to go: The knowledge foundation for investments in renewable energy. Energy Research & Social Science 25, 124–133.

Cihan, A., Zhou, Q., Birkholzer, J.T., 2011. Analytical solutions for pressure perturbation and fluid leakage through aquitards and wells in multilayered-aquifer systems. Water Resources Research 47. https://doi.org/10.1029/2011WR010721

Cinco Ley, H., Samaniego V., F., Dominguez A., N., 1978. Transient Pressure Behavior for a Well With a Finite-Conductivity Vertical Fracture. Society of Petroleum Engineers Journal 18, 253–264. https://doi.org/10.2118/6014-PA

Cinco-Ley, H., Meng, H.-Z., 1988. Pressure Transient Analysis of Wells With Finite Conductivity Vertical Fractures in Double Porosity Reservoirs. Presented at the SPE Annual Technical Conference and Exhibition, OnePetro. https://doi.org/10.2118/18172-MS

CMG, 2003. Computer Modeling Group Ltd. Calgary, AB, Canada.

Cooper, H.W., Simmons, G., 1977. The effect of cracks on the thermal expansion of rocks. Earth and Planetary Science Letters 36, 404–412. https://doi.org/10.1016/0012-821X(77)90065-6

Cooper Jr, H.H., Jacob, C.E., 1946. A generalized graphical method for evaluating formation constants and summarizing well-field history. Eos, Transactions American Geophysical Union 27, 526–534.

Coussy, O., 2004. Poromechanics. John Wiley & Sons.

Cueto-Felgueroso, L., Santillán, D., Mosquera, J.C., 2017. Stick-slip dynamics of flow-induced seismicity on rate and state faults. Geophysical Research Letters 44, 4098–4106. https://doi.org/10.1002/2016GL072045

Cvetkovic, V., Selroos, J.O., Cheng, H., 1999. Transport of reactive tracers in rock fractures. Journal of Fluid Mechanics 378, 335–356. https://doi.org/10.1017/S0022112098003450

Dadvand, P., Rossi, R., Oñate, E., 2010. An Object-oriented Environment for Developing Finite Element Codes for Multi-disciplinary Applications. Arch Computat Methods Eng 17, 253–297. https://doi.org/10.1007/s11831-010-9045-2

Darcel, C., Bour, O., Davy, P., de Dreuzy, J.R., 2003. Connectivity properties of two-dimensional fracture networks with stochastic fractal correlation. Water Resources Research 39. https://doi.org/10.1029/2002WR001628

Das, S.K., Basudhar, P.K., 2009. Comparison of intact rock failure criteria using various statistical methods. Acta Geotech. 4, 223–231. https://doi.org/10.1007/s11440-009-0088-1

Daub, E.G., Carlson, J.M., 2010. Friction, Fracture, and Earthquakes. Annual Review of Condensed Matter Physics 1, 397–418. https://doi.org/10.1146/annurev-conmatphys-070909-104025

David, C., Nejati, M., Geremia, D., 2020. On petrophysical and geomechanical properties of Bedretto Granite. ETH Zurich.

David, C., Wassermann, J., Amann, F., Klaver, J., Davy, C., Sarout, J., Esteban, L., Rutter, E.H., Hu, Q., Louis, L., Delage, P., Lockner, D.A., Selvadurai, A.P.S., Vanorio, T., Amann Hildenbrand, A., Meredith, P.G., Browning, J., Mitchell, T.M., Madonna, C., Billiotte, J., Reuschlé, T., Lasseux, D., Fortin, J., Lenormand, R., Loggia, D., Nono, F., Boitnott, G., Jahns, E., Fleury, M., Berthe, G., Braun, P., Grégoire, D., Perrier, L., Polito, P., Jannot, Y., Sommier, A., Krooss, B., Fink, R., Clark, A., 2018a. KG^{2}B, a collaborative benchmarking exercise for estimating the permeability of the Grimsel granodiorite—Part 2: modelling, microstructures and complementary data. Geophysical Journal International 215, 825–843. https://doi.org/10.1093/gji/ggy305

David, C., Wassermann, J., Amann, F., Lockner, D.A., Rutter, E.H., Vanorio, T., Amann Hildenbrand, A., Billiotte, J., Reuschlé, T., Lasseux, D., Fortin, J., Lenormand, R., Selvadurai, A.P.S., Meredith, P.G., Browning, J., Mitchell, T.M., Loggia, D., Nono, F., Sarout, J., Esteban, L., Davy, C., Louis, L., Boitnott, G., Madonna, C., Jahns, E., Fleury, M., Berthe, G., Delage, P., Braun, P., Grégoire, D., Perrier, L., Polito, P., Jannot, Y., Sommier, A., Krooss, B., Fink, R., Hu, Q., Klaver, J., Clark, A., 2018b. KG^{2}B, a collaborative benchmarking exercise for estimating the permeability of the Grimsel granodiorite – Part 1: measurements,

pressure dependence and pore-fluid effects. Geophysical Journal International 215, 799–824. https://doi.org/10.1093/gji/ggy304

Davy, P., Darcel, C., Le Goc, R., Mas Ivars, D., 2018. Elastic Properties of Fractured Rock Masses With Frictional Properties and Power Law Fracture Size Distributions. Journal of Geophysical Research: Solid Earth 123, 6521–6539. https://doi.org/10.1029/2017JB015329

de Borst, R., 2002. Fracture in quasi-brittle materials: a review of continuum damage-based approaches. Engineering Fracture Mechanics 69, 95–112. https://doi.org/10.1016/S0013-7944(01)00082-0

de Borst, R., Duretz, T., 2020. On viscoplastic regularisation of strain-softening rocks and soils. International Journal for Numerical and Analytical Methods in Geomechanics 44, 890–903. https://doi.org/10.1002/nag.3046

de Dreuzy, J.-R., Méheust, Y., Pichot, G., 2012. Influence of fracture scale heterogeneity on the flow properties of three-dimensional discrete fracture networks (DFN). Journal of Geophysical Research: Solid Earth 117. https://doi.org/10.1029/2012JB009461

De Simone, S., Bour, O., Davy, P., 2023a. Impact of Matrix Diffusion on Heat Transport Through Heterogeneous Fractured Aquifers. Water Resources Research 59, e2022WR033910. https://doi.org/10.1029/2022WR033910

De Simone, S., Carrera, J., 2017. Analytical Solutions to Coupled HM Problems to Highlight the Nonlocal Nature of Aquifer Storage. Water Resources Research 53, 9580–9599. https://doi.org/10.1002/2017WR020824

De Simone, S., Carrera, J., Vilarrasa, V., 2017. Superposition approach to understand triggering mechanisms of post-injection induced seismicity. Geothermics 70, 85–97. https://doi.org/10.1016/j.geothermics.2017.05.011

De Simone, S., Darcel, C., Kasani, H.A., Mas Ivars, D., Davy, P., 2023b. Equivalent Biot and Skempton Poroelastic Coefficients for a Fractured Rock Mass from a DFN Approach. Rock Mech Rock Eng. https://doi.org/10.1007/s00603-023-03515-9

De Simone, S., Pinier, B., Bour, O., Davy, P., 2021. A particle-tracking formulation of advective–diffusive heat transport in deformable fracture networks. Journal of Hydrology 603, 127157. https://doi.org/10.1016/j.jhydrol.2021.127157

De Simone, S., Vilarrasa, V., Carrera, J., Alcolea, A., Meier, P., 2013. Thermal coupling may control mechanical stability of geothermal reservoirs during cold water

injection. Physics and Chemistry of the Earth, Parts A/B/C, Coupled Physical and Chemical Transformations Affecting the Performance of GeoSystems 64, 117–126. https://doi.org/10.1016/j.pce.2013.01.001

De Smedt, F., 2022. Analytical Solution for Fractional Well Flow in a Double-Porosity Aquifer with Fractional Transient Exchange between Matrix and Fractures. Water 14, 456. https://doi.org/10.3390/w14030456

De Smedt, F., 2011. Analytical Solution for Constant-Rate Pumping Test in Fissured Porous Media with Double-Porosity Behaviour. Transp Porous Med 88, 479–489. https://doi.org/10.1007/s11242-011-9750-9

De Smedt, F., Zijl, W., El-Rawy, M., 2018. Double Constraint Method for Pumping Test Analysis. Journal of Hydrologic Engineering 23, 06018003. https://doi.org/10.1061/(ASCE)HE.1943-5584.0001677

Dean, R.H., Gai, X., Stone, C.M., Minkoff, S.E., 2006. A Comparison of Techniques for Coupling Porous Flow and Geomechanics. SPE Journal 11, 132–140. https://doi.org/10.2118/79709-PA

Delay, F., Kaczmaryk, A., Ackerer, P., 2007. Inversion of interference hydraulic pumping tests in both homogeneous and fractal dual media. Advances in Water Resources 30, 314–334. https://doi.org/10.1016/j.advwatres.2006.06.008

Dempsey, D., Riffault, J., 2019. Response of Induced Seismicity to Injection Rate Reduction: Models of Delay, Decay, Quiescence, Recovery, and Oklahoma. Water Resources Research 55, 656–681. https://doi.org/10.1029/2018WR023587

Desai, C.S., Fishman, K.L., 1991. Plasticity-based constitutive model with associated testing for joints. International Journal of Rock Mechanics and Mining Sciences & Geomechanics Abstracts 28, 15–26. https://doi.org/10.1016/0148-9062(91)93229-Y

Desai, C.S., Salami, M.R., 1987. Constitutive Model for Rocks. Journal of Geotechnical Engineering 113, 407–423. https://doi.org/10.1061/(ASCE)0733-9410(1987)113:5(407)

Desroches, J., Detournay, E., Lenoach, B., Papanastasiou, P., Pearson, J.R.A., Thiercelin, M., Cheng, A., 1994. The crack tip region in hydraulic fracturing. Proceedings of the Royal Society of London. Series A: Mathematical and Physical Sciences 447, 39–48.

Dessirier, B., Sharma, K.M., Pedersen, J., Tsang, C.-F., Niemi, A., 2023. Channel Network Modeling of Flow and Transport in Fractured Rock at the Äspö HRL: Data-Worth Analysis for Model Development, Calibration and Prediction. Water Resources Research 59, e2022WR033816. https://doi.org/10.1029/2022WR033816

Dessirier, B., Tsang, C.-F., Niemi, A., 2018. A new scripting library for modeling flow and transport in fractured rock with channel networks. Computers & Geosciences 111, 181–189. https://doi.org/10.1016/j.cageo.2017.11.013

Detournay, E., 2016. Mechanics of hydraulic fractures. Annual review of fluid mechanics 48, 311–339.

Detournay, E., 2004. Propagation Regimes of Fluid-Driven Fractures in Impermeable Rocks. International Journal of Geomechanics 4, 35–45. https://doi.org/10.1061/(ASCE)1532-3641(2004)4:1(35)

Dewandel, B., Aunay, B., Maréchal, J.C., Roques, C., Bour, O., Mougin, B., Aquilina, L., 2014. Analytical solutions for analysing pumping tests in a sub-vertical and anisotropic fault zone draining shallow aquifers. Journal of Hydrology 509, 115–131. https://doi.org/10.1016/j.jhydrol.2013.11.014

Dewandel, B., Lanini, S., Lachassagne, P., Maréchal, J.-C., 2018. A Generic analytical solution for modelling pumping tests in wells intersecting fractures. Journal of Hydrology 559, 89–99. https://doi.org/10.1016/j.jhydrol.2018.02.013

Dieterich, J.H., 1979. Modeling of rock friction: 1. Experimental results and constitutive equations. Journal of Geophysical Research: Solid Earth 84, 2161–2168. https://doi.org/10.1029/JB084iB05p02161

Dieterich, J.H., 1978. Time-Dependent Friction and the Mechanics of Stick-Slip, in: Byerlee, J.D., Wyss, M. (Eds.), Rock Friction and Earthquake Prediction, Contributions to Current Research in Geophysics (CCRG). Birkhäuser, Basel, pp. 790–806. https://doi.org/10.1007/978-3-0348-7182-2_15

Dippenaar, M.A., Van Rooy, J.L., 2016. On the cubic law and variably saturated flow through discrete open rough-walled discontinuities. International Journal of Rock Mechanics and Mining Sciences 89, 200–211. https://doi.org/10.1016/j.ijrmms.2016.09.011

Doolaeghe, D., Davy, P., Hyman, J.D., Darcel, C., 2020. Graph-based flow modeling approach adapted to multiscale discrete-fracture-network models. Phys. Rev. E 102, 053312. https://doi.org/10.1103/PhysRevE.102.053312

Doolin, D.M., Mauldon, M., 2001. Fracture permeability normal to bedding in layered rock masses. International Journal of Rock Mechanics and Mining Sciences 38, 199–210. https://doi.org/10.1016/S1365-1609(00)00056-3

Du, Q., Wang, C., Zhao, G., Jia, H., 2015. Development of constitutive model of fractured rock mass based on strain softening effect and its application. Journal of Yangtze River Scientific Research Institute 32, 82.

Dugdale, D.S., 1960. Yielding of steel sheets containing slits. Journal of the Mechanics and Physics of Solids 8, 100–104. https://doi.org/10.1016/0022-5096(60)90013-2

Durlofsky, L.J., 1991. Numerical calculation of equivalent grid block permeability tensors for heterogeneous porous media. Water Resources Research 27, 699–708. https://doi.org/10.1029/91WR00107

Dutler, N., Nejati, M., Valley, B., Amann, F., Molinari, G., 2018. On the link between fracture toughness, tensile strength, and fracture process zone in anisotropic rocks. Engineering Fracture Mechanics 201, 56–79. https://doi.org/10.1016/j.engfracmech.2018.08.017

Dykhuizen, R.C., 1987. Transport of solutes through unsaturated fractured media. Water Research 21, 1531–1539. https://doi.org/10.1016/0043-1354(87)90138-2

Ellsworth, W.L., 2013. Injection-Induced Earthquakes. Science 341, 1225942. https://doi.org/10.1126/science.1225942

Erdogan, F., Sih, G.C., 1963. On the Crack Extension in Plates Under Plane Loading and Transverse Shear. Journal of Basic Engineering 85, 519–525. https://doi.org/10.1115/1.3656897

Esposito, C., Martino, S., Mugnozza, G.S., 2007. Mountain slope deformations along thrust fronts in jointed limestone: An equivalent continuum modelling approach. Geomorphology 90, 55–72. https://doi.org/10.1016/j.geomorph.2007.01.017

Evans, B., Fredrich, J.T., Wong, T.-F., 1990. The Brittle-Ductile Transition in Rocks: Recent Experimental and Theoretical Progress, in: The Brittle-Ductile Transition in Rocks. American Geophysical Union (AGU), pp. 1–20. https://doi.org/10.1029/GM056p0001

Evans, K.F., Genter, A., Sausse, J., 2005. Permeability creation and damage due to massive fluid injections into granite at 3.5 km at Soultz: 1. Borehole observations. Journal of Geophysical Research: Solid Earth 110. https://doi.org/10.1029/2004JB003168

Fadakar Alghalandis, Y., 2017. ADFNE: Open source software for discrete fracture network engineering, two and three dimensional applications. Computers & Geosciences 102, 1–11. https://doi.org/10.1016/j.cageo.2017.02.002

Farhat, F., Shen, W.Q., Shao, J.F., 2017. A micro-mechanics based viscoplastic model for clayey rocks. Computers and Geotechnics 89, 92–102. https://doi.org/10.1016/j.compgeo.2017.04.014

Farmer, C.L., 2002. Upscaling: a review. International Journal for Numerical Methods in Fluids 40, 63–78. https://doi.org/10.1002/fld.267

Faybishenko, B., Benson, S.M., Gale, J.E., 2015. Fluid Dynamics in Complex Fractured-Porous Systems. John Wiley & Sons.

Fernández, L.E., Ayala, G., 2004. Constitutive modeling of discontinuities by means of discrete and continuum approximations and damage models. International Journal of Solids and Structures 41, 1453–1471. https://doi.org/10.1016/j.ijsolstr.2003.10.010

Fernández-Pato, J., García-Navarro, P., 2014. A Pipe Network Simulation Model with Dynamic Transition between Free Surface and Pressurized Flow. Procedia Engineering, 12th International Conference on Computing and Control for the Water Industry, CCWI2013 70, 641–650. https://doi.org/10.1016/j.proeng.2014.02.070

Figueiredo, B., Tsang, C.-F., Niemi, A., Lindgren, G., 2016. Review: The state-of-art of sparse channel models and their applicability to performance assessment of radioactive waste repositories in fractured crystalline formations. Hydrogeol J 24, 1607–1622. https://doi.org/10.1007/s10040-016-1415-x

Flemisch, B., Berre, I., Boon, W., Fumagalli, A., Schwenck, N., Scotti, A., Stefansson, I., Tatomir, A., 2018. Benchmarks for single-phase flow in fractured porous media. Advances in Water Resources 111, 239–258. https://doi.org/10.1016/j.advwatres.2017.10.036

Flemisch, B., Darcis, M., Erbertseder, K., Faigle, B., Lauser, A., Mosthaf, K., Müthing, S., Nuske, P., Tatomir, A., Wolff, M., Helmig, R., 2011. DuMux: DUNE for multi-{phase,component,scale,physics,...} flow and transport in porous media. Advances in Water Resources, New Computational Methods and Software Tools 34, 1102–1112. https://doi.org/10.1016/j.advwatres.2011.03.007

Flemisch, B., Fumagalli, A., Scotti, A., 2016. A Review of the XFEM-Based Approximation of Flow in Fractured Porous Media, in: Ventura, G., Benvenuti, E.

(Eds.), Advances in Discretization Methods: Discontinuities, Virtual Elements, Fictitious Domain Methods, SEMA SIMAI Springer Series. Springer International Publishing, Cham, pp. 47–76. https://doi.org/10.1007/978-3-319-41246-7_3

Fossen, H., Schultz, R.A., Shipton, Z.K., Mair, K., 2007. Deformation bands in sandstone: a review. Journal of the Geological Society 164, 755–769. https://doi.org/10.1144/0016-76492006-036

Fossum, A.F., Brannon, R.M., 2006. On a viscoplastic model for rocks with mechanism-dependent characteristic times. Acta Geotech. 1, 89–106. https://doi.org/10.1007/s11440-006-0010-z

Fumagalli, A., Keilegavlen, E., Scialò, S., 2019. Conforming, non-conforming and non-matching discretization couplings in discrete fracture network simulations. Journal of Computational Physics 376, 694–712. https://doi.org/10.1016/j.jcp.2018.09.048

Gai, X., Sun, S., Wheeler, M.F., Klie, H., 2005. A Timestepping Scheme for Coupled Reservoir Flow and Geomechanics on Nonmatching Grids. Presented at the SPE Annual Technical Conference and Exhibition, OnePetro. https://doi.org/10.2118/97054-MS

Gan, Q., Elsworth, D., 2014. Analysis of fluid injection-induced fault reactivation and seismic slip in geothermal reservoirs. Journal of Geophysical Research: Solid Earth 119, 3340–3353. https://doi.org/10.1002/2013JB010679

Gardner, R., Piazolo, S., Evans, L., Daczko, N., 2017. Patterns of strain localization in heterogeneous, polycrystalline rocks – a numerical perspective. Earth and Planetary Science Letters 463, 253–265. https://doi.org/10.1016/j.epsl.2017.01.039

Garipov, T.T., Hui, M.H., 2019. Discrete Fracture Modeling approach for simulating coupled thermo-hydro-mechanical effects in fractured reservoirs. International Journal of Rock Mechanics and Mining Sciences 122, 104075. https://doi.org/10.1016/j.ijrmms.2019.104075

Garipov, T.T., Karimi-Fard, M., Tchelepi, H.A., 2016. Discrete fracture model for coupled flow and geomechanics. Comput Geosci 20, 149–160. https://doi.org/10.1007/s10596-015-9554-z

Gaston, D., Newman, C., Hansen, G., Lebrun-Grandié, D., 2009. MOOSE: A parallel computational framework for coupled systems of nonlinear equations. Nuclear Engineering and Design 239, 1768–1778. https://doi.org/10.1016/j.nucengdes.2009.05.021

Geertsma, J., Haafkens, R., 1979. A Comparison of the Theories for Predicting Width and Extent of Vertical Hydraulically Induced Fractures. Journal of Energy Resources Technology 101, 8–19. https://doi.org/10.1115/1.3446866

Geiger, S.., Dentz, M.., Neuweiler, I.., 2013. A Novel Multirate Dual-Porosity Model for Improved Simulation of Fractured and Multiporosity Reservoirs. SPE Journal 18, 670–684. https://doi.org/10.2118/148130-PA

Gelet, R., Loret, B., Khalili, N., 2012. A thermo-hydro-mechanical coupled model in local thermal non-equilibrium for fractured HDR reservoir with double porosity. Journal of Geophysical Research: Solid Earth 117. https://doi.org/10.1029/2012JB009161

Gerke, H.H., 2006. Preferential flow descriptions for structured soils. Journal of Plant Nutrition and Soil Science 169, 382–400. https://doi.org/10.1002/jpln.200521955

Gerritsen, M.G., Durlofsky, L.J., 2005. Modeling Fluid Flow in Oil Reservoirs. Annual Review of Fluid Mechanics 37, 211–238. https://doi.org/10.1146/annurev.fluid.37.061903.175748

Gischig, V.S., Giardini, D., Amann, F., Hertrich, M., Krietsch, H., Loew, S., Maurer, H., Villiger, L., Wiemer, S., Bethmann, F., Brixel, B., Doetsch, J., Doonechaly, N.G., Driesner, T., Dutler, N., Evans, K.F., Jalali, M., Jordan, D., Kittilä, A., Ma, X., Meier, P., Nejati, M., Obermann, A., Plenkers, K., Saar, M.O., Shakas, A., Valley, B., 2020. Hydraulic stimulation and fluid circulation experiments in underground laboratories: Stepping up the scale towards engineered geothermal systems. Geomechanics for Energy and the Environment, Physical behavior of Fluid-Induced earthquake 24, 100175. https://doi.org/10.1016/j.gete.2019.100175

Goertz-Allmann, B.P., Goertz, A., Wiemer, S., 2011. Stress drop variations of induced earthquakes at the Basel geothermal site. Geophysical Research Letters 38. https://doi.org/10.1029/2011GL047498

González Nicieza, C., Álvarez Fernández, M.I., Menéndez Díaz, A., Álvarez Vigil, A.E., 2006. Modification of rock failure criteria considering the RMR caused by joints. Computers and Geotechnics 33, 419–431. https://doi.org/10.1016/j.compgeo.2006.08.004

Goodman, R.E., Taylor, R.L., Brekke, T.L., 1968. A Model for the Mechanics of Jointed Rock. Journal of the Soil Mechanics and Foundations Division 94, 637–659. https://doi.org/10.1061/JSFEAQ.0001133

Goto, R., Watanabe, N., Sakaguchi, K., Miura, T., Chen, Y., Ishibashi, T., Pramudyo, E., Parisio, F., Yoshioka, K., Nakamura, K., Komai, T., Tsuchiya, N., 2021.

Creating Cloud-Fracture Network by Flow-induced Microfracturing in Superhot Geothermal Environments. Rock Mech Rock Eng 54, 2959–2974. https://doi.org/10.1007/s00603-021-02416-z

Gottron, D., Henk, A., 2021. Upscaling of fractured rock mass properties – An example comparing Discrete Fracture Network (DFN) modeling and empirical relations based on engineering rock mass classifications. Engineering Geology 294, 106382. https://doi.org/10.1016/j.enggeo.2021.106382

Grasselli, G., Egger, P., 2003. Constitutive law for the shear strength of rock joints based on three-dimensional surface parameters. International Journal of Rock Mechanics and Mining Sciences 40, 25–40. https://doi.org/10.1016/S1365-1609(02)00101-6

Griffith, A.A., 1921. VI. The phenomena of rupture and flow in solids. Philosophical transactions of the royal society of london. Series A, containing papers of a mathematical or physical character 221, 163–198.

Grigoli, F., Cesca, S., Priolo, E., Rinaldi, A.P., Clinton, J.F., Stabile, T.A., Dost, B., Fernandez, M.G., Wiemer, S., Dahm, T., 2017. Current challenges in monitoring, discrimination, and management of induced seismicity related to underground industrial activities: A European perspective. Reviews of Geophysics 55, 310–340. https://doi.org/10.1002/2016RG000542

Gringarten, A.C., Ramey, H.J., Jr., Raghavan, R., 1974. Unsteady-State Pressure Distributions Created by a Well With a Single Infinite-Conductivity Vertical Fracture. Society of Petroleum Engineers Journal 14, 347–360. https://doi.org/10.2118/4051-PA

Gross, D., Seelig, T., 2017. Fracture mechanics: with an introduction to micromechanics. Springer.

Guglielmi, Y., Cappa, F., Avouac, J.-P., Henry, P., Elsworth, D., 2015a. Seismicity triggered by fluid injection–induced aseismic slip. Science 348, 1224–1226. https://doi.org/10.1126/science.aab0476

Guglielmi, Y., Elsworth, D., Cappa, F., Henry, P., Gout, C., Dick, P., Durand, J., 2015b. In situ observations on the coupling between hydraulic diffusivity and displacements during fault reactivation in shales. Journal of Geophysical Research: Solid Earth 120, 7729–7748. https://doi.org/10.1002/2015JB012158

Guimerà, J., Carrera, J., 2000. A comparison of hydraulic and transport parameters measured in low-permeability fractured media. Journal of Contaminant Hydrology 41, 261–281. https://doi.org/10.1016/S0169-7722(99)00080-7

Gylling, B., Moreno, L., Neretnieks, I., 1999. The Channel Network Model—A Tool for Transport Simulations in Fractured Media. Groundwater 37, 367–375. https://doi.org/10.1111/j.1745-6584.1999.tb01113.x

Hadgu, T., Karra, S., Kalinina, E., Makedonska, N., Hyman, J.D., Klise, K., Viswanathan, H.S., Wang, Y., 2017. A comparative study of discrete fracture network and equivalent continuum models for simulating flow and transport in the far field of a hypothetical nuclear waste repository in crystalline host rock. Journal of Hydrology 553, 59–70. https://doi.org/10.1016/j.jhydrol.2017.07.046

Hægland, H., Assteerawatt, A., Dahle, H.K., Eigestad, G.T., Helmig, R., 2009. Comparison of cell- and vertex-centered discretization methods for flow in a two-dimensional discrete-fracture–matrix system. Advances in Water Resources 32, 1740–1755. https://doi.org/10.1016/j.advwatres.2009.09.006

Hamm, S.-Y., Bidaux, P., 1996. Dual-Porosity Fractal Models for Transient Flow Analysis in Fissured Rocks. Water Resources Research 32, 2733–2745. https://doi.org/10.1029/96WR01464

Hanano, M., 2004. Contribution of fractures to formation and production of geothermal resources. Renewable and Sustainable Energy Reviews 8, 223–236. https://doi.org/10.1016/j.rser.2003.10.007

Hantush, M.S., 1960. Modification of the theory of leaky aquifers. Journal of Geophysical Research (1896-1977) 65, 3713–3725. https://doi.org/10.1029/JZ065i011p03713

Hantush, M.S., 1956. Analysis of data from pumping tests in leaky aquifers. Eos, Transactions American Geophysical Union 37, 702–714.

Hantush, M.S., Jacob, C.E., 1955. Non-steady radial flow in an infinite leaky aquifer. Eos, Transactions American Geophysical Union 36, 95–100. https://doi.org/10.1029/TR036i001p00095

Häring, M.O., Schanz, U., Ladner, F., Dyer, B.C., 2008. Characterisation of the Basel 1 enhanced geothermal system. Geothermics 37, 469–495. https://doi.org/10.1016/j.geothermics.2008.06.002

Hatano, T., 2009. Scaling of the critical slip distance in granular layers. Geophysical Research Letters 36. https://doi.org/10.1029/2009GL039665

Hoek, E., 1983. Strength of jointed rock masses. Géotechnique 33, 187–223. https://doi.org/10.1680/geot.1983.33.3.187

Hoek, E., Brown, E.T., 1997. Practical estimates of rock mass strength. International Journal of Rock Mechanics and Mining Sciences 34, 1165–1186. https://doi.org/10.1016/S1365-1609(97)80069-X

Hoek, E., Martin, C.D., 2014. Fracture initiation and propagation in intact rock – A review. Journal of Rock Mechanics and Geotechnical Engineering 6, 287–300. https://doi.org/10.1016/j.jrmge.2014.06.001

Hosking, L.J., Chen, M., Thomas, H.R., 2020. Numerical analysis of dual porosity coupled thermo-hydro-mechanical behaviour during CO2 sequestration in coal. International Journal of Rock Mechanics and Mining Sciences 135, 104473. https://doi.org/10.1016/j.ijrmms.2020.104473

Hosking, L.J., Thomas, H.R., Sedighi, M., 2018. A dual porosity model of high-pressure gas flow for geoenergy applications. Can. Geotech. J. 55, 839–851. https://doi.org/10.1139/cgj-2016-0532

Hou, W., Pan, P.-Z., Wang, Z., 2023. Modeling of rock multiple fractures system with a new contact algorithm and a novel approach for complex topology construction. Theoretical and Applied Fracture Mechanics 124, 103778. https://doi.org/10.1016/j.tafmec.2023.103778

Hu, F., Huang, H., Chen, X., 2017. Effect of the time-weakening friction law during the nucleation process. Earthq Sci 30, 91–96. https://doi.org/10.1007/s11589-017-0183-6

Huang, W., Cao, W., Jiang, F., 2017. Heat extraction performance of EGS with heterogeneous reservoir: A numerical evaluation. International Journal of Heat and Mass Transfer 108, 645–657. https://doi.org/10.1016/j.ijheatmasstransfer.2016.12.037

Hubbert, M.K., Rubey, W.W., 1959. Mechanics of fluid-filled porous solids and its application to overthrust faulting. Geological Society of America Bulletin 70, 115–166.

Huber, M.L., Perkins, R.A., Friend, D.G., Sengers, J.V., Assael, M.J., Metaxa, I.N., Miyagawa, K., Hellmann, R., Vogel, E., 2012. New International Formulation for the Thermal Conductivity of H2O. Journal of Physical and Chemical Reference Data 41, 033102. https://doi.org/10.1063/1.4738955

Huber, M.L., Perkins, R.A., Laesecke, A., Friend, D.G., Sengers, J.V., Assael, M.J., Metaxa, I.N., Vogel, E., Mareš, R., Miyagawa, K., 2009. New International

Formulation for the Viscosity of H2O. Journal of Physical and Chemical Reference Data 38, 101–125. https://doi.org/10.1063/1.3088050

Hui, M.-H. (Robin), Karimi-Fard, M., Mallison, B., Durlofsky, L.J., 2018. A General Modeling Framework for Simulating Complex Recovery Processes in Fractured Reservoirs at Different Resolutions. SPE Journal 23, 598–613. https://doi.org/10.2118/182621-PA

Huitt, J.L., 1956. Fluid flow in simulated fractures. AIChE Journal 2, 259–264. https://doi.org/10.1002/aic.690020224

Hyman, J.D., Aldrich, G., Viswanathan, H., Makedonska, N., Karra, S., 2016. Fracture size and transmissivity correlations: Implications for transport simulations in sparse three-dimensional discrete fracture networks following a truncated power law distribution of fracture size. Water Resources Research 52, 6472–6489. https://doi.org/10.1002/2016WR018806

Hyman, J.D., Gable, C.W., Painter, S.L., Makedonska, N., 2014. Conforming Delaunay Triangulation of Stochastically Generated Three Dimensional Discrete Fracture Networks: A Feature Rejection Algorithm for Meshing Strategy. SIAM J. Sci. Comput. 36, A1871–A1894. https://doi.org/10.1137/130942541

Hyman, J.D., Hagberg, A., Osthus, D., Srinivasan, S., Viswanathan, H., Srinivasan, G., 2018. Identifying Backbones in Three-Dimensional Discrete Fracture Networks: A Bipartite Graph-Based Approach. Multiscale Model. Simul. 16, 1948–1968. https://doi.org/10.1137/18M1180207

Hyman, J.D., Karra, S., Makedonska, N., Gable, C.W., Painter, S.L., Viswanathan, H.S., 2015. dfnWorks: A discrete fracture network framework for modeling subsurface flow and transport. Computers & Geosciences 84, 10–19. https://doi.org/10.1016/j.cageo.2015.08.001

Hyman, J.D., Rajaram, H., Srinivasan, S., Makedonska, N., Karra, S., Viswanathan, H., Srinivasan, G., 2019. Matrix Diffusion in Fractured Media: New Insights Into Power Law Scaling of Breakthrough Curves. Geophysical Research Letters 46, 13785–13795. https://doi.org/10.1029/2019GL085454

Hyman, J.D., Sweeney, M.R., Gable, C.W., Svyatsky, D., Lipnikov, K., David Moulton, J., 2022. Flow and transport in three-dimensional discrete fracture matrix models using mimetic finite difference on a conforming multi-dimensional mesh. Journal of Computational Physics 466, 111396. https://doi.org/10.1016/j.jcp.2022.111396

Ikari, M.J., Marone, C., Saffer, D.M., Kopf, A.J., 2013. Slip weakening as a mechanism for slow earthquakes. Nature Geosci 6, 468–472. https://doi.org/10.1038/ngeo1818

Illman, W.A., Liu, X., Takeuchi, S., Yeh, T.-C.J., Ando, K., Saegusa, H., 2009. Hydraulic tomography in fractured granite: Mizunami Underground Research site, Japan. Water Resources Research 45. https://doi.org/10.1029/2007WR006715

Ingebritsen, S.E., Manning, C.E., 2010. Permeability of the continental crust: dynamic variations inferred from seismicity and metamorphism. Geofluids 10, 193–205. https://doi.org/10.1111/j.1468-8123.2010.00278.x

IPCC, Climate Change (Synthesis Report), 2023. , Contribution of Working Groups I, II and III to the Sixth Assessment Report of the Intergovernmental Panel on Climate Change.

Irwin, G.R., 1957. Analysis of Stresses and Strains Near the End of a Crack Traversing a Plate. Journal of Applied Mechanics 24, 361–364. https://doi.org/10.1115/1.4011547

Jackson, C.P., Hoch, A.R., Todman, S., 2000. Self-consistency of a heterogeneous continuum porous medium representation of a fractured medium. Water Resources Research 36, 189–202. https://doi.org/10.1029/1999WR900249

Jacob, C.E., 1947. Drawdown Test to Determine Effective Radius of Artesian Well. Transactions of the American Society of Civil Engineers 112, 1047–1064. https://doi.org/10.1061/TACEAT.0006033

Jacob, C.E., 1940. On the flow of water in an elastic artesian aquifer. Eos, Transactions American Geophysical Union 21, 574–586. https://doi.org/10.1029/TR021I002P00574

Jacob, C.E., Lohman, S.W., 1952. Nonsteady flow to a well of constant drawdown in an extensive aquifer. Eos, Transactions American Geophysical Union 33, 559–569. https://doi.org/10.1029/TR033i004p00559

Jaeger, J.C., Cook, N.G., Zimmerman, R., 2009. Fundamentals of rock mechanics. John Wiley & Sons.

Jaiswal, A., Shrivastva, B.K., 2012. A generalized three-dimensional failure criterion for rock masses. Journal of Rock Mechanics and Geotechnical Engineering 4, 333–343. https://doi.org/10.3724/SP.J.1235.2012.00333

Jalali, M.R., Dusseault, M.B., 2012. Coupling geomechanics and transport in naturally fractured reservoirs. International Journal of Mining and Geo-Engineering 46, 105–131.

Jeanne, P., Rutqvist, J., Dobson, P.F., Walters, M., Hartline, C., Garcia, J., 2014. The impacts of mechanical stress transfers caused by hydromechanical and thermal processes on fault stability during hydraulic stimulation in a deep geothermal reservoir. International Journal of Rock Mechanics and Mining Sciences 72, 149–163. https://doi.org/10.1016/j.ijrmms.2014.09.005

Jha, B., Juanes, R., 2014. Coupled multiphase flow and poromechanics: A computational model of pore pressure effects on fault slip and earthquake triggering. Water Resources Research 50, 3776–3808. https://doi.org/10.1002/2013WR015175

Ji, S.-H., Park, K.W., Lim, D.-H., Kim, C., Kim, K.S., Dershowitz, W., 2012. A hybrid modeling approach to evaluate the groundwater flow system at the low- and intermediate-level radioactive waste disposal site in Gyeong-Ju, Korea. Hydrogeol J 20, 1341–1353. https://doi.org/10.1007/s10040-012-0875-x

Jiang, F., Luo, L., Chen, J., 2013. A novel three-dimensional transient model for subsurface heat exchange in enhanced geothermal systems. International Communications in Heat and Mass Transfer 41, 57–62. https://doi.org/10.1016/j.icheatmasstransfer.2012.11.003

Jiang, J., Younis, R.M., 2017. An improved projection-based embedded discrete fracture model (pEDFM) for multiphase flow in fractured reservoirs. Advances in Water Resources 109, 267–289. https://doi.org/10.1016/j.advwatres.2017.09.017

Jiang, J., Younis, R.M., 2016. Hybrid Coupled Discrete-Fracture/Matrix and Multicontinuum Models for Unconventional-Reservoir Simulation. SPE Journal 21, 1009–1027. https://doi.org/10.2118/178430-PA

Jiang, J., Younis, R.M., 2015. Numerical study of complex fracture geometries for unconventional gas reservoirs using a discrete fracture-matrix model. Journal of Natural Gas Science and Engineering 26, 1174–1186. https://doi.org/10.1016/j.jngse.2015.08.013

Jin, L., Zoback, M.D., 2017. Fully Coupled Nonlinear Fluid Flow and Poroelasticity in Arbitrarily Fractured Porous Media: A Hybrid-Dimensional Computational Model. Journal of Geophysical Research: Solid Earth 122, 7626–7658. https://doi.org/10.1002/2017JB014892

Jing, L., 2003. A review of techniques, advances and outstanding issues in numerical modelling for rock mechanics and rock engineering. International Journal of Rock Mechanics and Mining Sciences 40, 283–353. https://doi.org/10.1016/S1365-1609(03)00013-3

Jing, L., Hudson, J.A., 2002. Numerical methods in rock mechanics. International Journal of Rock Mechanics and Mining Sciences, Numerical Methods in Rock Mechanics 39, 409–427. https://doi.org/10.1016/S1365-1609(02)00065-5

Jing, L., Stephansson, O., 2007a. 10 - Discrete Fracture Network (DFN) Method, in: Jing, L., Stephansson, O. (Eds.), Developments in Geotechnical Engineering, Fundamentals of Discrete Element Methods for Rock Engineering. Elsevier, pp. 365–398. https://doi.org/10.1016/S0165-1250(07)85010-3

Jing, L., Stephansson, O., 2007b. Fundamentals of Discrete Element Methods for Rock Engineering: Theory and Applications. Elsevier.

Jing, L., Stephansson, O., 2007c. 3 - Constitutive Models of Rock Fractures and Rock Masses – The Basics, in: Jing, L., Stephansson, O. (Eds.), Developments in Geotechnical Engineering, Fundamentals of Discrete Element Methods for Rock Engineering. Elsevier, pp. 47–109. https://doi.org/10.1016/S0165-1250(07)85003-6

Jones, R.E., Papadopoulos, P., 2000. A yield-limited Lagrange multiplier formulation for frictional contact. International Journal for Numerical Methods in Engineering 48, 1127–1149. https://doi.org/10.1002/(SICI)1097-0207(20000720)48:8<1127::AID-NME937>3.0.CO;2-C

Jourde, H., Cornaton, F., Pistre, S., Bidaux, P., 2002. Flow behavior in a dual fracture network. Journal of Hydrology 266, 99–119. https://doi.org/10.1016/S0022-1694(02)00120-8

Joyce, S., Hartley, L., Applegate, D., Hoek, J., Jackson, P., 2014. Multi-scale groundwater flow modeling during temperate climate conditions for the safety assessment of the proposed high-level nuclear waste repository site at Forsmark, Sweden. Hydrogeol J 22, 1233–1249. https://doi.org/10.1007/s10040-014-1165-6

Junqi, W., Ziyan, W., Xiaoting, W., 2022. The Seepage Tensor of the Multiparameter Model of Pipe Element in Fractured Rock Mass. Frontiers in Built Environment 8.

Kachanov, L.M., 1958. Time of rupture process under deep conditions. Izv. Akad. Nauk SSSR 8, 26.

Karimi-Fard, M., Durlofsky, L.J., 2016. A general gridding, discretization, and coarsening methodology for modeling flow in porous formations with discrete geological features. Advances in Water Resources 96, 354–372. https://doi.org/10.1016/j.advwatres.2016.07.019

Karimi-Fard, M., Durlofsky, L.J., Aziz, K., 2004. An Efficient Discrete-Fracture Model Applicable for General-Purpose Reservoir Simulators. SPE Journal 9, 227–236. https://doi.org/10.2118/88812-PA

Katsuki, D., Gutierrez, M., Almrabat, A., 2019. Stress-dependent shear wave splitting and permeability in fractured porous rock. Journal of Rock Mechanics and Geotechnical Engineering 11, 1–11. https://doi.org/10.1016/j.jrmge.2018.08.004

Kazemi, H., 1969. Pressure Transient Analysis of Naturally Fractured Reservoirs with Uniform Fracture Distribution. Society of Petroleum Engineers Journal 9, 451–462. https://doi.org/10.2118/2156-A

Kc, B., Ghazanfari, E., 2021. Geothermal reservoir stimulation through hydro-shearing: an experimental study under conditions close to enhanced geothermal systems. Geothermics 96, 102200. https://doi.org/10.1016/j.geothermics.2021.102200

Keilegavlen, E., Berge, R., Fumagalli, A., Starnoni, M., Stefansson, I., Varela, J., Berre, I., 2021a. PorePy: an open-source software for simulation of multiphysics processes in fractured porous media. Comput Geosci 25, 243–265. https://doi.org/10.1007/s10596-020-10002-5

Keilegavlen, E., Duboeuf, L., Dichiarante, A.M., Halldórsdóttir, S., Stefansson, I., Naumann, M., Guðnason, E.Á., Ágústsson, K., Eggertsson, G.H., Oye, V., Berre, I., 2021b. Hydro-mechanical simulation and analysis of induced seismicity for a hydraulic stimulation test at the Reykjanes geothermal field, Iceland. Geothermics 97, 102223. https://doi.org/10.1016/j.geothermics.2021.102223

Khademi, B., Moreno, L., Neretnieks, I., 1999. The Channel Network Model and Field Applications. MRS Online Proceedings Library 556, 721. https://doi.org/10.1557/PROC-556-721

Khalili, N., Selvadurai, A.P.S., 2003. A fully coupled constitutive model for thermo-hydro-mechanical analysis in elastic media with double porosity. Geophysical Research Letters 30. https://doi.org/10.1029/2003GL018838

Kim, J.., Tchelepi, H.A.. A., Juanes, R.., 2011. Stability, Accuracy, and Efficiency of Sequential Methods for Coupled Flow and Geomechanics. SPE Journal 16, 249–262. https://doi.org/10.2118/119084-PA

Kim, K., Makhnenko, R.Y., 2020. Coupling Between Poromechanical Behavior and Fluid Flow in Tight Rock. Transp Porous Med 135, 487–512. https://doi.org/10.1007/s11242-020-01484-z

Kim, K.-I., Yoo, H., Park, S., Yim, J., Xie, L., Min, K.-B., Rutqvist, J., 2022. Induced and triggered seismicity by immediate stress transfer and delayed fluid migration in a fractured geothermal reservoir at Pohang, South Korea. International Journal of Rock Mechanics and Mining Sciences 153, 105098. https://doi.org/10.1016/j.ijrmms.2022.105098

Kim, T., Avouac, J.-P., 2023. Stress-Based and Convolutional Forecasting of Injection-Induced Seismicity: Application to the Otaniemi Geothermal Reservoir Stimulation. Journal of Geophysical Research: Solid Earth 128, e2022JB024960. https://doi.org/10.1029/2022JB024960

Kim, W.-Y., 2013. Induced seismicity associated with fluid injection into a deep well in Youngstown, Ohio. Journal of Geophysical Research: Solid Earth 118, 3506–3518. https://doi.org/10.1002/jgrb.50247

Kivi, I.R., Pujades, E., Rutqvist, J., Vilarrasa, V., 2022. Cooling-induced reactivation of distant faults during long-term geothermal energy production in hot sedimentary aquifers. Sci Rep 12, 2065. https://doi.org/10.1038/s41598-022-06067-0

Klaas, D.K.S.Y., Imteaz, M., Sudiayem, I., Klaas, E.M.E., Klaas, E.C.M., 2019. Parameterisation of physical models to configure subsurface characteristics of groundwater basins. Groundwater for Sustainable Development 9, 100255. https://doi.org/10.1016/j.gsd.2019.100255

Ko, T.Y., Kemeny, J., 2013. Determination of the subcritical crack growth parameters in rocks using the constant stress-rate test. International Journal of Rock Mechanics and Mining Sciences 59, 166–178. https://doi.org/10.1016/j.ijrmms.2012.11.006

Ko, T.Y., Kemeny, J., 2011. Subcritical crack growth in rocks under shear loading. Journal of Geophysical Research: Solid Earth 116. https://doi.org/10.1029/2010JB000846

Konzuk, J.S., Kueper, B.H., 2004. Evaluation of cubic law based models describing single-phase flow through a rough-walled fracture. Water Resources Research 40. https://doi.org/10.1029/2003WR002356

Koudina, N., Gonzalez Garcia, R., Thovert, J.-F., Adler, P.M., 1998. Permeability of three-dimensional fracture networks. Phys. Rev. E 57, 4466–4479. https://doi.org/10.1103/PhysRevE.57.4466

Kraft, T., Mai, P.M., Wiemer, S., Deichmann, N., Ripperger, J., Kästli, P., Bachmann, C., Fäh, D., Wössner, J., Giardini, D., 2009. Enhanced Geothermal Systems: Mitigating Risk in Urban Areas. Eos, Transactions American Geophysical Union 90, 273–274. https://doi.org/10.1029/2009EO320001

Krevor, S., de Coninck, H., Gasda, S.E., Ghaleigh, N.S., de Gooyert, V., Hajibeygi, H., Juanes, R., Neufeld, J., Roberts, J.J., Swennenhuis, F., 2023. Subsurface carbon dioxide and hydrogen storage for a sustainable energy future. Nat Rev Earth Environ 4, 102–118. https://doi.org/10.1038/s43017-022-00376-8

Kruseman, G.P., De Ridder, N.A., 1994. Analysis and evaluation of pumping test data. Publication 47. Intern. Inst. for Land Reclamation and Improvement, Wageningen, The Netherlands, 370p.

Kumari, W.G.P., Ranjith, P.G., 2019. Sustainable development of enhanced geothermal systems based on geotechnical research – A review. Earth-Science Reviews 199, 102955. https://doi.org/10.1016/j.earscirev.2019.102955

Labuz, J.F., Zeng, F., Makhnenko, R., Li, Y., 2018. Brittle failure of rock: A review and general linear criterion. Journal of Structural Geology 112, 7–28. https://doi.org/10.1016/j.jsg.2018.04.007

Ladner, F., Häring, M.O., 2009. Hydraulic characteristics of the basel 1 enhanced geothermal system. GRC Transactions 33, 199–203.

Lang, P.S., Paluszny, A., Zimmerman, R.W., 2014. Permeability tensor of three-dimensional fractured porous rock and a comparison to trace map predictions. Journal of Geophysical Research: Solid Earth 119, 6288–6307. https://doi.org/10.1002/2014JB011027

Larsson, M., Niemi, A., Tsang, C.-F., 2012. A study of flow-wetted surface area in a single fracture as a function of its hydraulic conductivity distribution. Water Resources Research 48. https://doi.org/10.1029/2011WR010686

Lavrov, A., 2003. The Kaiser effect in rocks: principles and stress estimation techniques. International Journal of Rock Mechanics and Mining Sciences 40, 151–171. https://doi.org/10.1016/S1365-1609(02)00138-7

Le Guennec, Y., Cottereau, R., Clouteau, D., Soize, C., 2014. A coupling method for stochastic continuum models at different scales. Probabilistic Engineering Mechanics 37, 138–147. https://doi.org/10.1016/j.probengmech.2013.10.005

Lecampion, B., Desroches, J., 2015. Simultaneous initiation and growth of multiple radial hydraulic fractures from a horizontal wellbore. Journal of the Mechanics and Physics of Solids 82, 235–258. https://doi.org/10.1016/j.jmps.2015.05.010

Lecampion, B., Desroches, J., Weng, X., Burghardt, J., Brown, J.E., 2015. Can we engineer better multistage horizontal completions? Evidence of the importance of near-wellbore fracture geometry from theory, lab and field experiments, in: SPE Hydraulic Fracturing Technology Conference. OnePetro.

Lee, C.-H., Deng, B.-W., Chang, J.-L., 1995. A continuum approach for estimating permeability in naturally fractured rocks. Engineering Geology 39, 71–85. https://doi.org/10.1016/0013-7952(94)00064-9

Lee, H.S., Cho, T.F., 2002. Hydraulic Characteristics of Rough Fractures in Linear Flow under Normal and Shear Load. Rock Mech Rock Engng 35, 299–318. https://doi.org/10.1007/s00603-002-0028-y

Lee, J., Min, K.B., Rutqvist, J., 2015. Tough-UDEC Simulator for the Coupled Multiphase Fluid Flow, Heat Transfer, and Deformation in Fractured Porous Media. Presented at the 13th ISRM International Congress of Rock Mechanics, OnePetro.

Lee, S.H., Lough, M.F., Jensen, C.L., 2001. Hierarchical modeling of flow in naturally fractured formations with multiple length scales. Water Resources Research 37, 443–455. https://doi.org/10.1029/2000WR900340

Lee, Y.-K., Pietruszczak, S., Choi, B.-H., 2012. Failure criteria for rocks based on smooth approximations to Mohr–Coulomb and Hoek–Brown failure functions. International Journal of Rock Mechanics and Mining Sciences 56, 146–160. https://doi.org/10.1016/j.ijrmms.2012.07.032

Lei, Q., Barton, N., 2022. On the selection of joint constitutive models for geomechanics simulation of fractured rocks. Computers and Geotechnics 145, 104707. https://doi.org/10.1016/j.compgeo.2022.104707

Lei, Q., Gao, K., 2018. Correlation Between Fracture Network Properties and Stress Variability in Geological Media. Geophysical Research Letters 45, 3994–4006. https://doi.org/10.1002/2018GL077548

Lei, Q., Gholizadeh Doonechaly, N., Tsang, C.-F., 2021. Modelling fluid injection-induced fracture activation, damage growth, seismicity occurrence and connectivity change in naturally fractured rocks. International Journal of Rock Mechanics and Mining Sciences 138, 104598. https://doi.org/10.1016/j.ijrmms.2020.104598

Lei, Q., Latham, J.-P., Tsang, C.-F., 2017. The use of discrete fracture networks for modelling coupled geomechanical and hydrological behaviour of fractured rocks. Computers and Geotechnics 85, 151–176. https://doi.org/10.1016/j.compgeo.2016.12.024

Lei, Q., Latham, J.-P., Xiang, J., 2016. Implementation of an Empirical Joint Constitutive Model into Finite-Discrete Element Analysis of the Geomechanical Behaviour of Fractured Rocks. Rock Mech Rock Eng 49, 4799–4816. https://doi.org/10.1007/s00603-016-1064-3

Lei, Q., Wang, X., 2016. Tectonic interpretation of the connectivity of a multiscale fracture system in limestone. Geophysical Research Letters 43, 1551–1558. https://doi.org/10.1002/2015GL067277

Lei, Q., Wang, X., Min, K.-B., Rutqvist, J., 2020. Interactive roles of geometrical distribution and geomechanical deformation of fracture networks in fluid flow through fractured geological media. Journal of Rock Mechanics and Geotechnical Engineering 12, 780–792. https://doi.org/10.1016/j.jrmge.2019.12.014

Leij, F.J., Toride, N., Field, M.S., Sciortino, A., 2012. Solute transport in dual-permeability porous media. Water Resources Research 48. https://doi.org/10.1029/2011WR011502

Lemonnier, P., Bourbiaux, B., 2010. Simulation of Naturally Fractured Reservoirs. State of the Art - Part 2 – Matrix-Fracture Transfers and Typical Features of Numerical Studies. Oil Gas Sci. Technol. – Rev. IFP 65, 263–286. https://doi.org/10.2516/ogst/2009067

Lepillier, B., Yoshioka, K., Parisio, F., Bakker, R., Bruhn, D., 2020. Variational Phase-Field Modeling of Hydraulic Fracture Interaction With Natural Fractures and Application to Enhanced Geothermal Systems. Journal of Geophysical Research: Solid Earth 125, e2020JB019856. https://doi.org/10.1029/2020JB019856

Li, L., Lee, S.H., 2008. Efficient Field-Scale Simulation of Black Oil in a Naturally Fractured Reservoir Through Discrete Fracture Networks and Homogenized Media. SPE Reservoir Evaluation & Engineering 11, 750–758. https://doi.org/10.2118/103901-PA

Li, S.C., Xu, Z.H., Ma, G.W., 2014. A Graph-theoretic Pipe Network Method for water flow simulation in discrete fracture networks: GPNM. Tunnelling and Underground Space Technology 42, 247–263. https://doi.org/10.1016/j.tust.2014.03.012

Li, X., Li, D., Xu, Y., Feng, X., 2020. A DFN based 3D numerical approach for modeling coupled groundwater flow and solute transport in fractured rock mass. International Journal of Heat and Mass Transfer 149, 119179. https://doi.org/10.1016/j.ijheatmasstransfer.2019.119179

Li, Y., Hu, W., Zhang, Zhihong, Zhang, Zhaobin, Shang, Y., Han, L., Wei, S., 2021. Numerical simulation of hydraulic fracturing process in a naturally fractured reservoir based on a discrete fracture network model. Journal of Structural Geology 147, 104331. https://doi.org/10.1016/j.jsg.2021.104331

Lin, H., Xie, S., Yong, R., Chen, Y., Du, S., 2019. An empirical statistical constitutive relationship for rock joint shearing considering scale effect. Comptes Rendus Mécanique 347, 561–575. https://doi.org/10.1016/j.crme.2019.08.001

Lin, Y.-C., Yeh, H.-D., 2021. An Analytical Model With a Generalized Nonlinear Water Transfer Term for the Flow in Dual-Porosity Media Induced by Constant-Rate Pumping in a Leaky Fractured Aquifer. Water Resources Research 57, e2020WR029186. https://doi.org/10.1029/2020WR029186

Liu, G., Pu, H., Zhao, Z., Liu, Y., 2019. Coupled thermo-hydro-mechanical modeling on well pairs in heterogeneous porous geothermal reservoirs. Energy 171, 631–653. https://doi.org/10.1016/j.energy.2019.01.022

Liu, H., Yuan, X., 2015. A damage constitutive model for rock mass with persistent joints considering joint shear strength. Can. Geotech. J. 52, 1136–1143. https://doi.org/10.1139/cgj-2014-0252

Liu, H., Zhang, L., 2015. A Damage Constitutive Model for Rock Mass with Nonpersistently Closed Joints Under Uniaxial Compression. Arab J Sci Eng 40, 3107–3117. https://doi.org/10.1007/s13369-015-1777-8

Liu, H.-H., Rutqvist, J., 2013. Coupled Hydro-mechanical Processes Associated with Multiphase Flow in a Dual-continuum System: Formulations and an Application. Rock Mech Rock Eng 46, 1103–1112. https://doi.org/10.1007/s00603-012-0313-3

Liu, H.Y., Lv, S.R., Zhang, L.M., Yuan, X.P., 2015. A dynamic damage constitutive model for a rock mass with persistent joints. International Journal of Rock Mechanics and Mining Sciences 75, 132–139. https://doi.org/10.1016/j.ijrmms.2015.01.013

Liu, J., Zhou, Y., Chen, J., 2021. A Two-Dimensional Partitioning of Fracture–Matrix Flow in Fractured Reservoir Rock Using a Dual-Porosity Percolation Model. Energies 14, 2209. https://doi.org/10.3390/en14082209

Liu, L., Neretnieks, I., Shahkarami, P., Meng, S., Moreno, L., 2018. Solute transport along a single fracture in a porous rock: a simple analytical solution and its extension for modeling velocity dispersion. Hydrogeol J 26, 297–320. https://doi.org/10.1007/s10040-017-1627-8

Liu, R., Li, B., Jiang, Y., Huang, N., 2016. Review: Mathematical expressions for estimating equivalent permeability of rock fracture networks. Hydrogeol J 24, 1623–1649. https://doi.org/10.1007/s10040-016-1441-8

Lockner, D.A., 1995. Rock failure. Rock physics and phase relations: A handbook of physical constants 3, 127–147.

Lockner, D.A., Byerlee, J.D., Kuksenko, V., Ponomarev, A., Sidorin, A., 1991. Quasi-static fault growth and shear fracture energy in granite. Nature 350, 39–42. https://doi.org/10.1038/350039a0

Long, J.C.S., Remer, J.S., Wilson, C.R., Witherspoon, P.A., 1982. Porous media equivalents for networks of discontinuous fractures. Water Resources Research 18, 645–658. https://doi.org/10.1029/WR018i003p00645

Ma, L., Han, D., Qian, J., Gao, D., Ma, H., Deng, Y., Hou, X., 2023. Numerical evaluation of the suitability of the equivalent porous medium model for characterizing the two-dimensional flow field in a fractured geologic medium. Hydrogeol J 31, 913–930. https://doi.org/10.1007/s10040-023-02627-4

Ma, X., Doonechaly, N.G., Hertrich, M., Gischig, V., Klee, G., 2019. Preliminary in situ stress and fracture characterization in the bedretto underground laboratory, Swiss Alps: implications on hydraulic stimulation, in: Rock Mechanics for Natural Resources and Infrastructure Development. CRC Press, pp. 1559–1567.

Ma, X., Hertrich, M., Amann, F., Bröker, K., Gholizadeh Doonechaly, N., Gischig, V., Hochreutener, R., Kästli, P., Krietsch, H., Marti, M., Nägeli, B., Nejati, M., Obermann, A., Plenkers, K., Rinaldi, A.P., Shakas, A., Villiger, L., Wenning, Q., Zappone, A., Bethmann, F., Castilla, R., Seberto, F., Meier, P., Driesner, T., Loew, S., Maurer, H., Saar, M.O., Wiemer, S., Giardini, D., 2022. Multi-disciplinary characterizations of the BedrettoLab – a new underground geoscience research facility. Solid Earth 13, 301–322. https://doi.org/10.5194/se-13-301-2022

Mahabadi, O.K., Lisjak, A., He, L., Tatone, B.S.A., Kaifosh, P., Grasselli, G., 2016. Development of a New Fully-Parallel Finite-Discrete Element Code: Irazu. Presented at the 50th U.S. Rock Mechanics/Geomechanics Symposium, OnePetro.

Mahmoudzadeh, B., Liu, L., Moreno, L., Neretnieks, I., 2013. Solute transport in fractured rocks with stagnant water zone and rock matrix composed of different geological layers—Model development and simulations. Water Resources Research 49, 1709–1727. https://doi.org/10.1002/wrcr.20132

Majer, E.L., Baria, R., Stark, M., Oates, S., Bommer, J., Smith, B., Asanuma, H., 2007. Induced seismicity associated with Enhanced Geothermal Systems. Geothermics 36, 185–222. https://doi.org/10.1016/j.geothermics.2007.03.003

Makedonska, N., Painter, S.L., Bui, Q.M., Gable, C.W., Karra, S., 2015. Particle tracking approach for transport in three-dimensional discrete fracture networks. Comput Geosci 19, 1123–1137. https://doi.org/10.1007/s10596-015-9525-4

Mallikamas, W., Rajaram, H., 2005. On the anisotropy of the aperture correlation and effective transmissivity in fractures generated by sliding between identical self-affine surfaces. Geophysical Research Letters 32. https://doi.org/10.1029/2005GL022859

Manga, M., Beresnev, I., Brodsky, E.E., Elkhoury, J.E., Elsworth, D., Ingebritsen, S.E., Mays, D.C., Wang, C.-Y., 2012. Changes in permeability caused by transient stresses: Field observations, experiments, and mechanisms. Reviews of Geophysics 50. https://doi.org/10.1029/2011RG000382

Maranini, E., Yamaguchi, T., 2001. A non-associated viscoplastic model for the behaviour of granite in triaxial compression. Mechanics of Materials 33, 283–293. https://doi.org/10.1016/S0167-6636(01)00052-7

March, R., Doster, F., Geiger, S., 2018. Assessment of CO2 Storage Potential in Naturally Fractured Reservoirs With Dual-Porosity Models. Water Resources Research 54, 1650–1668. https://doi.org/10.1002/2017WR022159

Martinez-Landa, L., Carrera, J., 2006. A methodology to interpret cross-hole tests in a granite block. Journal of Hydrology 325, 222–240. https://doi.org/10.1016/j.jhydrol.2005.10.017

Masters, I., Pao, W.K.S., Lewis, R.W., 2000. Coupling temperature to a double-porosity model of deformable porous media. International Journal for Numerical Methods in Engineering 49, 421–438. https://doi.org/10.1002/1097-0207(20000930)49:3<421::AID-NME48>3.0.CO;2-6

Mathias, S.A., González Martínez de Miguel, G.J., Thatcher, K.E., Zimmerman, R.W., 2011. Pressure Buildup During CO2 Injection into a Closed Brine Aquifer. Transp Porous Med 89, 383–397. https://doi.org/10.1007/s11242-011-9776-z

Matthäi, S.K., Belayneh, M., 2004. Fluid flow partitioning between fractures and a permeable rock matrix. Geophysical Research Letters 31. https://doi.org/10.1029/2003GL019027

Matthäi, S.K., Geiger, S., Roberts, S.G., Paluszny, A., Belayneh, M., Burri, A., Mezentsev, A., Lu, H., Coumou, D., Driesner, T., Heinrich, C.A., 2007. Numerical simulation of multi-phase fluid flow in structurally complex reservoirs. Geological Society, London, Special Publications 292, 405–429. https://doi.org/10.1144/SP292.22

McClure, M., Fowler, G., Hewson, C., Kang, C., 2022. The A to Z Guide to Accelerating Continuous Improvement with ResFrac. arXiv preprint arXiv:2205.14820.

McClure, M.W., Horne, R.N., 2014. An investigation of stimulation mechanisms in Enhanced Geothermal Systems. International Journal of Rock Mechanics and Mining Sciences 72, 242–260. https://doi.org/10.1016/j.ijrmms.2014.07.011

McClure, M.W., Horne, R.N., 2011. Investigation of injection-induced seismicity using a coupled fluid flow and rate/state friction model. GEOPHYSICS 76, WC181–WC198. https://doi.org/10.1190/geo2011-0064.1

McDermott, C.I., Randriamanjatosoa, A.R.L., Tenzer, H., Kolditz, O., 2006. Simulation of heat extraction from crystalline rocks: The influence of coupled processes on differential reservoir cooling. Geothermics 35, 321–344. https://doi.org/10.1016/j.geothermics.2006.05.002

McLennan, J., Tran, D., Zhao, N., Thakur, S., Deo, M., Gil, I., Damjanac, B., 2010. Modeling Fluid Invasion and Hydraulic Fracture Propagation in Naturally Fractured Rock: A Three-Dimensional Approach. Presented at the SPE International Symposium and Exhibition on Formation Damage Control, OnePetro. https://doi.org/10.2118/127888-MS

McTigue, D.F., 1986. Thermoelastic response of fluid-saturated porous rock. Journal of Geophysical Research: Solid Earth 91, 9533–9542. https://doi.org/10.1029/JB091iB09p09533

Meier, P., Guinot, F., Bethmann, F., Faschingbauer, R., Alcolea, A., Liautaud, F., Thanourey, J., Schott, T., Carrera, J., Vilarrasa, V., 2020. ZoDrEx an European Endeavour for Optimising Zonal Isolation, Drilling and Exploitation of EGS Projects, in: Proceedings World Geothermal Congress. p. 1.

Meier, P.M., Serbeto, F., Christe, F., Alcolea, A., Castilla, R., Bethmann, F., Dyer, B., 2022. Results from Benchmark Testing of Zonal Isolation Borehole Completions for

Multi-Stage EGS Stimulation in the Bedretto Underground Rock Laboratory in Switzerland. Presented at the 56th U.S. Rock Mechanics/Geomechanics Symposium, OnePetro. https://doi.org/10.56952/ARMA-2022-0292

Meng, M., Frash, L.P., Li, W., Welch, N.J., Carey, J.W., Morris, J., Neupane, G., Ulrich, C., Kneafsey, T., 2022. Hydro-Mechanical Measurements of Sheared Crystalline Rock Fractures With Applications for EGS Collab Experiments 1 and 2. Journal of Geophysical Research: Solid Earth 127, e2021JB023000. https://doi.org/10.1029/2021JB023000

Min, K.-B., Rutqvist, J., Tsang, C.-F., Jing, L., 2004. Stress-dependent permeability of fractured rock masses: a numerical study. International Journal of Rock Mechanics and Mining Sciences 41, 1191–1210. https://doi.org/10.1016/j.ijrmms.2004.05.005

Minakov, A., Yarushina, V., 2021. Elastoplastic source model for microseismicity and acoustic emission. Geophysical Journal International 227, 33–53. https://doi.org/10.1093/gji/ggab207

Moench, A.F., 1985. Transient Flow to a Large-Diameter Well in an Aquifer With Storative Semiconfining Layers. Water Resources Research 21, 1121–1131. https://doi.org/10.1029/WR021i008p01121

Moench, A.F., 1984. Double-Porosity Models for a Fissured Groundwater Reservoir With Fracture Skin. Water Resources Research 20, 831–846. https://doi.org/10.1029/WR020i007p00831

Mohammadnejad, M., Liu, H., Chan, A., Dehkhoda, S., Fukuda, D., 2021. An overview on advances in computational fracture mechanics of rock. Geosystem Engineering 24, 206–229. https://doi.org/10.1080/12269328.2018.1448006

Moinfar, A., Narr, W., Hui, M.-H., Mallison, B., Lee, S.H., 2011. Comparison of Discrete-Fracture and Dual-Permeability Models for Multiphase Flow in Naturally Fractured Reservoirs. Presented at the SPE Reservoir Simulation Symposium, OnePetro. https://doi.org/10.2118/142295-MS

Monteagudo, J.E.P., Firoozabadi, A., 2004. Control-volume method for numerical simulation of two-phase immiscible flow in two- and three-dimensional discrete-fractured media. Water Resources Research 40. https://doi.org/10.1029/2003WR002996

Moreno, L., Neretnieks, I., 1993. Fluid flow and solute transport in a network of channels. Journal of Contaminant Hydrology 14, 163–192. https://doi.org/10.1016/0169-7722(93)90023-L

Mourzenko, V.V., Thovert, J.-F., Adler, P.M., 2004. Macroscopic permeability of three-dimensional fracture networks with power-law size distribution. Phys. Rev. E 69, 066307. https://doi.org/10.1103/PhysRevE.69.066307

Moya, D., Aldás, C., Kaparaju, P., 2018. Geothermal energy: Power plant technology and direct heat applications. Renewable and Sustainable Energy Reviews 94, 889–901. https://doi.org/10.1016/j.rser.2018.06.047

Murakami, H., Hegemier, G.A., 1989. Development of a nonlinear continuum model for wave propagation in joined media: theory for single joint set. Mechanics of Materials 8, 199–218. https://doi.org/10.1016/0167-6636(89)90012-4

Muskat, M., 1938. The Flow of Homogeneous Fluids Through Porous Media. Soil Science 46, 169.

Nara, Y., Yamanaka, H., Oe, Y., Kaneko, K., 2013. Influence of temperature and water on subcritical crack growth parameters and long-term strength for igneous rocks. Geophysical Journal International 193, 47–60. https://doi.org/10.1093/gji/ggs116

National Academies of Sciences, E., 2015. Characterization, Modeling, Monitoring, and Remediation of Fractured Rock. https://doi.org/10.17226/21742

Neretnieks, I., 2006. Channeling with diffusion into stagnant water and into a matrix in series. Water Resources Research 42. https://doi.org/10.1029/2005WR004448

Neuman, S.P., 2005. Trends, prospects and challenges in quantifying flow and transport through fractured rocks. Hydrogeol J 13, 124–147. https://doi.org/10.1007/s10040-004-0397-2

Neuman, S.P., 1990. Universal scaling of hydraulic conductivities and dispersivities in geologic media. Water Resources Research 26, 1749–1758. https://doi.org/10.1029/WR026i008p01749

Neuman, S.P., 1988. A proposed conceptual framework and methodology for investigating flow and transport in Swedish crystalline rocks. SKB Arbestrapport 88–37.

Neuman, S.P., 1987. Stochastic Continuum Representation Of Fractured Rock Permeability As An Alternative To The Rev And Fracture Network Concepts. Presented at the The 28th U.S. Symposium on Rock Mechanics (USRMS), OnePetro.

Neuman, S.P., Witherspoon, P.A., 1969. Theory of Flow in a Confined Two Aquifer System. Water Resources Research 5, 803–816. https://doi.org/10.1029/WR005i004p00803

Neuzil, C.E., Tracy, J.V., 1981. Flow through fractures. Water Resources Research 17, 191–199. https://doi.org/10.1029/WR017i001p00191

Nguyen, B.N., Hou, Z., Stewart, M.L., Murray, C.J., Bonneville, A., 2016. Thermal impact of CO2 injection on geomechanical response at the FutureGen 2.0 Site: A three-dimensional thermo-geomechanical approach. International Journal of Greenhouse Gas Control 54, 29–49. https://doi.org/10.1016/j.ijggc.2016.08.026

Nguyen, T.S., Selvadurai, A.P.S., 1998. A model for coupled mechanical and hydraulic behaviour of a rock joint. International Journal for Numerical and Analytical Methods in Geomechanics 22, 29–48. https://doi.org/10.1002/(SICI)1096-9853(199801)22:1<29::AID-NAG907>3.0.CO;2-N

Nguyen, V.P., Lian, H., Rabczuk, T., Bordas, S., 2017. Modelling hydraulic fractures in porous media using flow cohesive interface elements. Engineering Geology, Special Issue: Characterisation of Fractures in Rock: from Theory to Practice (ROCKFRAC) 225, 68–82. https://doi.org/10.1016/j.enggeo.2017.04.010

Nick, H.M., Matthäi, S.K., 2011. Comparison of Three FE-FV Numerical Schemes for Single- and Two-Phase Flow Simulation of Fractured Porous Media. Transp Porous Med 90, 421–444. https://doi.org/10.1007/s11242-011-9793-y

Nield, D.A., Bejan, A., 2017. Convection in Porous Media. Springer International Publishing, Cham. https://doi.org/10.1007/978-3-319-49562-0

Nielsen, K.A., 2007. Fractured Aquifiers: Formation Evaluation by Well Testing. Trafford Publishing.

Niemi, A., Edlmann, K., Ramírez, J., Juhlin, C., Tatomir, A., Ghergut, I., Sauter, M., Bensabat, J., Fagerlund, F., Cornet, F., Vilarrasa, V., McDermott, C., 2017. Site Characterization. pp. 309–380. https://doi.org/10.1007/978-94-024-0996-3_7

Nikolić, M., Roje-Bonacci, T., Ibrahimbegović, A., 2016. Overview of the numerical methods for the modelling of rock mechanics problems. Tehnički vjesnik 23, 627–637.

Noorian Bidgoli, M., Jing, L., 2014. Anisotropy of strength and deformability of fractured rocks. Journal of Rock Mechanics and Geotechnical Engineering 6, 156–164. https://doi.org/10.1016/j.jrmge.2014.01.009

Noorishad, J., Mehran, M., 1982. An upstream finite element method for solution of transient transport equation in fractured porous media. Water Resources Research 18, 588–596. https://doi.org/10.1029/WR018i003p00588

Noorishad, J., Tsang, C.-F., 1996. Coupled thermohydroelasticity phenomena in variably saturated fractured porous rocks -- formulation and numerical solution, in: Stephansson, O., Jing, L., Tsang, C.-F. (Eds.), Developments in Geotechnical Engineering, Coupled Thermo-Hydro-Mechanical Processes of Fractured Media. Elsevier, pp. 93–134. https://doi.org/10.1016/S0165-1250(96)80023-X

Oda, M., 1985. Permeability tensor for discontinuous rock masses. Géotechnique 35, 483–495. https://doi.org/10.1680/geot.1985.35.4.483

Öhman, J., Niemi, A., 2003. Upscaling of fracture hydraulics by means of an oriented correlated stochastic continuum model. Water Resources Research 39. https://doi.org/10.1029/2002WR001776

Olasolo, P., Juárez, M.C., Morales, M.P., D´Amico, S., Liarte, I.A., 2016. Enhanced geothermal systems (EGS): A review. Renewable and Sustainable Energy Reviews 56, 133–144. https://doi.org/10.1016/j.rser.2015.11.031

Oliveira, D.V., Lourenço, P.B., 2004. Implementation and validation of a constitutive model for the cyclic behaviour of interface elements. Computers & Structures, Computational Mechanics in Portugal 82, 1451–1461. https://doi.org/10.1016/j.compstruc.2004.03.041

Olivella, S., Alonso, E.E., 2008. Gas flow through clay barriers. Géotechnique 58, 157–176. https://doi.org/10.1680/geot.2008.58.3.157

Olivella, S., Carrera, J., Gens, A., Alonso, E.E., 1994. Nonisothermal multiphase flow of brine and gas through saline media. Transp Porous Med 15, 271–293. https://doi.org/10.1007/BF00613282

Olivella, S., Gens, A., 2005. Double structure THM analyses of a heating test in a fractured tuff incorporating intrinsic permeability variations. International Journal of Rock Mechanics and Mining Sciences, Research results from the Decovalex III & Benchpar projects 42, 667–679. https://doi.org/10.1016/j.ijrmms.2005.03.007

Olivella, S., Gens, A., Carrera, J., Alonso, E.E., 1996. Numerical formulation for a simulator (CODE_BRIGHT) for the coupled analysis of saline media. Engineering Computations 13, 87–112. https://doi.org/10.1108/02644409610151575

Oliver, J., 2000. On the discrete constitutive models induced by strong discontinuity kinematics and continuum constitutive equations. International Journal of Solids and Structures 37, 7207–7229. https://doi.org/10.1016/S0020-7683(00)00196-7

Oliver, J., Huespe, A.E., Pulido, M.D.G., Chaves, E., 2002. From continuum mechanics to fracture mechanics: the strong discontinuity approach. Engineering Fracture Mechanics 69, 113–136. https://doi.org/10.1016/S0013-7944(01)00060-1

Olsen-Kettle, L., Sarout, J., 2022. Assessment of Tensorial and Scalar Damage Models for an Isotropic Thermally Cracked Rock Under Confining Pressure Using Experimental Data: Continuum Damage Mechanics Versus Effective Medium Theory. Rock Mech Rock Eng 55, 505–519. https://doi.org/10.1007/s00603-021-02693-8

Olsson, R., Barton, N., 2001. An improved model for hydromechanical coupling during shearing of rock joints. International Journal of Rock Mechanics and Mining Sciences 38, 317–329. https://doi.org/10.1016/S1365-1609(00)00079-4

Orlecka-Sikora, B., Cielesta, S., 2020. Evidence for subcritical rupture of injection-induced earthquakes. Sci Rep 10, 4016. https://doi.org/10.1038/s41598-020-60928-0

Oron, A.P., Berkowitz, B., 1998. Flow in rock fractures: The local cubic law assumption reexamined. Water Resources Research 34, 2811–2825. https://doi.org/10.1029/98WR02285

Ortiz, M., 1988. Microcrack coalescence and macroscopic crack growth initiation in brittle solids. International Journal of Solids and Structures 24, 231–250.

Osthus, D., Hyman, J.D., Karra, S., Panda, N., Srinivasan, G., 2020. A Probabilistic Clustering Approach for Identifying Primary Subnetworks of Discrete Fracture Networks with Quantified Uncertainty. SIAM/ASA J. Uncertainty Quantification 8, 573–600. https://doi.org/10.1137/19M1279265

Ostoja-Starzewski, M., 2002. Towards Stochastic Continuum Thermodynamics 27, 335–348. https://doi.org/10.1515/JNETDY.2002.020

Ouellet, A., Bérard, T., Desroches, J., Frykman, P., Welsh, P., Minton, J., Pamukcu, Y., Hurter, S., Schmidt-Hattenberger, C., 2011. Reservoir geomechanics for assessing containment in CO2 storage: A case study at Ketzin, Germany. Energy Procedia, 10th International Conference on Greenhouse Gas Control Technologies 4, 3298–3305. https://doi.org/10.1016/j.egypro.2011.02.250

Painter, S., Cvetkovic, V., Selroos, J.-O., 2002. Power-law velocity distributions in fracture networks: Numerical evidence and implications for tracer transport. Geophysical Research Letters 29, 20-1-20–4. https://doi.org/10.1029/2002GL014960

Pandey, S.N., Chaudhuri, A., Kelkar, S., 2017. A coupled thermo-hydro-mechanical modeling of fracture aperture alteration and reservoir deformation during heat extraction from a geothermal reservoir. Geothermics 65, 17–31. https://doi.org/10.1016/j.geothermics.2016.08.006

Pardoen, B., Seyedi, D.M., Collin, F., 2015. Shear banding modelling in cross-anisotropic rocks. International Journal of Solids and Structures 72, 63–87. https://doi.org/10.1016/j.ijsolstr.2015.07.012

Parisio, F., Vilarrasa, V., Laloui, L., 2018. Hydro-mechanical Modeling of Tunnel Excavation in Anisotropic Shale with Coupled Damage-Plasticity and Micro-dilatant Regularization. Rock Mech Rock Eng 51, 3819–3833. https://doi.org/10.1007/s00603-018-1569-z

Parisio, F., Vilarrasa, V., Wang, W., Kolditz, O., Nagel, T., 2019. The risks of long-term re-injection in supercritical geothermal systems. Nature Communications 10, 1–11.

Parisio, F., Yoshioka, K., 2020. Modeling Fluid Reinjection Into an Enhanced Geothermal System. Geophysical Research Letters 47, e2020GL089886. https://doi.org/10.1029/2020GL089886

Peach, C.J., Spiers, C.J., 1996. Influence of crystal plastic deformation on dilatancy and permeability development in synthetic salt rock. Tectonophysics 256, 101–128. https://doi.org/10.1016/0040-1951(95)00170-0

Pearson, C., 1981. The relationship between microseismicity and high pore pressures during hydraulic stimulation experiments in low permeability granitic rocks. Journal of Geophysical Research: Solid Earth 86, 7855–7864. https://doi.org/10.1029/JB086iB09p07855

Phillips, P.J., Wheeler, M.F., 2007. A coupling of mixed and continuous Galerkin finite element methods for poroelasticity I: the continuous in time case. Computational Geosciences 11. https://doi.org/10.1007/s10596-007-9045-y

Pine, R.J., Batchelor, A.S., 1984. Downward migration of shearing in jointed rock during hydraulic injections. International Journal of Rock Mechanics and Mining Sciences & Geomechanics Abstracts 21, 249–263. https://doi.org/10.1016/0148-9062(84)92681-0

Plesha, M.E., 1987. Constitutive models for rock discontinuities with dilatancy and surface degradation. International Journal for Numerical and Analytical Methods in Geomechanics 11, 345–362. https://doi.org/10.1002/nag.1610110404

Preisig, M., Prévost, J.H., 2011. Coupled multi-phase thermo-poromechanical effects. Case study: CO2 injection at In Salah, Algeria. International Journal of Greenhouse Gas Control 5, 1055–1064. https://doi.org/10.1016/j.ijggc.2010.12.006

Prevost, J.H., 1993. DYNAFLOW: A nonlinear transient finite element analysis program. Dept. Civ. Engng. and Op. Research.

Pruess, K., 2006. Enhanced geothermal systems (EGS) using CO2 as working fluid—A novel approach for generating renewable energy with simultaneous sequestration of carbon. Geothermics 35, 351–367. https://doi.org/10.1016/j.geothermics.2006.08.002

Pruess, K., 1992. Brief guide to the MINC-method for modeling flow and transport in fractured media (No. LBL-32195). Lawrence Berkeley National Lab. (LBNL), Berkeley, CA (United States). https://doi.org/10.2172/6951290

Pruess, K., 1983. GMINC: a mesh generator for flow simulations in fractured reservoirs (No. LBL-15227). Lawrence Berkeley National Lab. (LBNL), Berkeley, CA (United States). https://doi.org/10.2172/6065621

Pruess, K., Narasimhan, T.N., 1985. A Practical Method for Modeling Fluid and Heat Flow in Fractured Porous Media. Society of Petroleum Engineers Journal 25, 14–26. https://doi.org/10.2118/10509-PA

Puig Damians, I., Olivella Pastallé, S., Bathurst, R., Lloret Morancho, A., Josa Garcia-Tornel, A., 2022. Modeling soil-facing interface interaction with continuum element methodology. Frontiers in built environment 8, 842495–1.

Pyrak-Nolte, L.J., Cook, N.G.W., Nolte, D.D., 1988. Fluid percolation through single fractures. Geophysical Research Letters 15, 1247–1250. https://doi.org/10.1029/GL015i011p01247

Qin, C., Chen, G., Li, T., Hu, K., Zhang, G., 2023. Shear behaviors of rock masses containing nonpersistent joints affected by normal stress rebound under excavations and river incisions. Bull Eng Geol Environ 82, 171. https://doi.org/10.1007/s10064-023-03209-0

Rafiei Renani, H., Cai, M., 2022. Forty-Year Review of the Hoek–Brown Failure Criterion for Jointed Rock Masses. Rock Mech Rock Eng 55, 439–461. https://doi.org/10.1007/s00603-021-02661-2

Rahman, M.K., Hossain, M.M., Rahman, S.S., 2002. A shear-dilation-based model for evaluation of hydraulically stimulated naturally fractured reservoirs. International Journal for Numerical and Analytical Methods in Geomechanics 26, 469–497. https://doi.org/10.1002/nag.208

Rahman, M.K., Hossain, M.M., Rahman, S.S., 2000. An analytical method for mixed-mode propagation of pressurized fractures in remotely compressed rocks. International Journal of Fracture 103, 243–258. https://doi.org/10.1023/A:1007624315096

Raleigh, C.B., Healy, J.H., Bredehoeft, J.D., 1976. An Experiment in Earthquake Control at Rangely, Colorado. Science 191, 1230–1237. https://doi.org/10.1126/science.191.4233.1230

Ramakrishnan, T.S., Kuchuk, F.J., 1993. Pressure transients during injection: Constant rate and convolution solutions. Transp Porous Med 10, 103–136. https://doi.org/10.1007/BF00617004

Ramos, G., Carrera, J., Gómez, S., Minutti, C., Camacho, R., 2017. A stable computation of log-derivatives from noisy drawdown data. Water Resources Research 53, 7904–7916. https://doi.org/10.1002/2017WR020811

Randolph, J.B., Saar, M.O., 2011. Combining geothermal energy capture with geologic carbon dioxide sequestration. Geophysical Research Letters 38. https://doi.org/10.1029/2011GL047265

Rattez, H., Stefanou, I., Sulem, J., Veveakis, M., Poulet, T., 2018. Numerical Analysis of Strain Localization in Rocks with Thermo-hydro-mechanical Couplings Using Cosserat Continuum. Rock Mech Rock Eng 51, 3295–3311. https://doi.org/10.1007/s00603-018-1529-7

Read, H.E., Hegemier, G.A., 1984. Strain softening of rock, soil and concrete — a review article. Mechanics of Materials 3, 271–294. https://doi.org/10.1016/0167-6636(84)90028-0

Renard, P., Ababou, R., 2022. Equivalent Permeability Tensor of Heterogeneous Media: Upscaling Methods and Criteria (Review and Analyses). Geosciences 12, 269. https://doi.org/10.3390/geosciences12070269

Renard, P., Glenz, D., Mejias, M., 2009. Understanding diagnostic plots for well-test interpretation. Hydrogeol J 17, 589–600. https://doi.org/10.1007/s10040-008-0392-0

Riahi, A., Damjanac, B., 2013. Numerical study of hydro-shearing in geothermal reservoirs with a pre-existing discrete fracture network, in: Proceedings of the 38th Workshop on Geothermal Reservoir Engineering, Stanford, CA. pp. 11–13.

Rice, J.R., 1993. Spatio-temporal complexity of slip on a fault. Journal of Geophysical Research: Solid Earth 98, 9885–9907. https://doi.org/10.1029/93JB00191

Rinaldi, A.P., Rutqvist, J., 2019. Joint opening or hydroshearing? Analyzing a fracture zone stimulation at Fenton Hill. Geothermics 77, 83–98. https://doi.org/10.1016/j.geothermics.2018.08.006

Rinaldi, Antonio P., Rutqvist, J., Cappa, F., 2014. Geomechanical effects on CO2 leakage through fault zones during large-scale underground injection. International Journal of Greenhouse Gas Control 20, 117–131. https://doi.org/10.1016/j.ijggc.2013.11.001

Rinaldi, A. P., Rutqvist, J., Finsterle, S., Liu, H.H., 2014. Forward and Inverse Modeling of Ground Surface Uplift at In Salah, Algeria. Presented at the 48th U.S. Rock Mechanics/Geomechanics Symposium, OnePetro.

Ringel, L.M., Jalali, M., Bayer, P., 2022. Characterization of the highly fractured zone at the Grimsel Test Site based on hydraulic tomography. Hydrology and Earth System Sciences 26, 6443–6455. https://doi.org/10.5194/hess-26-6443-2022

Ringel, L.M., Somogyvári, M., Jalali, M., Bayer, P., 2019. Comparison of Hydraulic and Tracer Tomography for Discrete Fracture Network Inversion. Geosciences 9, 274. https://doi.org/10.3390/geosciences9060274

Rogers, S., Enachescu, C., Trice, R., Buer, K., 2007. Integrating discrete fracture network models and pressure transient data for testing conceptual fracture models of the Valhall chalk reservoir, Norwegian North Sea. Geological Society, London, Special Publications 270, 193–204. https://doi.org/10.1144/GSL.SP.2007.270.01.13

Romano, V., Bigi, S., Carnevale, F., De'Haven Hyman, J., Karra, S., Valocchi, A.J., Tartarello, M.C., Battaglia, M., 2020. Hydraulic characterization of a fault zone from fracture distribution. Journal of Structural Geology 135, 104036. https://doi.org/10.1016/j.jsg.2020.104036

Roubinet, D., de Dreuzy, J.-R., Davy, P., 2010. Connectivity-consistent mapping method for 2-D discrete fracture networks. Water Resources Research 46. https://doi.org/10.1029/2009WR008302

Rudnicki, J.W., 2011. Eshelby's Technique for Analyzing Inhomogeneities in Geomechanics, in: Leroy, Y.M., Lehner, F.K. (Eds.), Mechanics of Crustal Rocks, CISM Courses and Lectures. Springer, Vienna, pp. 43–72. https://doi.org/10.1007/978-3-7091-0939-7_2

Ruina, A., 1983. Slip instability and state variable friction laws. Journal of Geophysical Research: Solid Earth 88, 10359–10370. https://doi.org/10.1029/JB088iB12p10359

Russell, D.G., Truitt, N.E., 1964. Transient Pressure Behavior in Vertically Fractured Reservoirs. Journal of Petroleum Technology 16, 1159–1170. https://doi.org/10.2118/967-PA

Rutqvist, J., 2017. An overview of TOUGH-based geomechanics models. Computers & Geosciences, TOUGH Symposium 2015: recent enhancements to the TOUGH family of codes and coupled flow and geomechanics processes modeling 108, 56–63. https://doi.org/10.1016/j.cageo.2016.09.007

Rutqvist, J., 2015. Fractured rock stress-permeability relationships from in situ data and effects of temperature and chemical-mechanical couplings. Geofluids 15, 48–66. https://doi.org/10.1111/gfl.12089

Rutqvist, J., Birkholzer, J., Cappa, F., Tsang, C.-F., 2007. Estimating maximum sustainable injection pressure during geological sequestration of CO2 using coupled fluid flow and geomechanical fault-slip analysis. Energy Conversion and Management, Geologic Carbon Sequestration and Methane Hydrates Research from the TOUGH Symposium 2006 48, 1798–1807. https://doi.org/10.1016/j.enconman.2007.01.021

Rutqvist, J., Leung, C., Hoch, A., Wang, Y., Wang, Z., 2013. Linked multicontinuum and crack tensor approach for modeling of coupled geomechanics, fluid flow and transport in fractured rock. Journal of Rock Mechanics and Geotechnical Engineering 5, 18–31. https://doi.org/10.1016/j.jrmge.2012.08.001

Rutqvist, J., Stephansson, O., 2003. The role of hydromechanical coupling in fractured rock engineering. Hydrogeology Journal 11, 7–40. https://doi.org/10.1007/s10040-002-0241-5

Rutqvist, J., Wu, Y.-S., Tsang, C.-F., Bodvarsson, G., 2002. A modeling approach for analysis of coupled multiphase fluid flow, heat transfer, and deformation in

fractured porous rock. International Journal of Rock Mechanics and Mining Sciences, Numerical Methods in Rock Mechanics 39, 429–442. https://doi.org/10.1016/S1365-1609(02)00022-9

Sævik, P.N., Berre, I., Jakobsen, M., Lien, M., 2013. A 3D Computational Study of Effective Medium Methods Applied to Fractured Media. Transp Porous Med 100, 115–142. https://doi.org/10.1007/s11242-013-0208-0

Sævik, P.N., Jakobsen, M., Lien, M., Berre, I., 2014. Anisotropic effective conductivity in fractured rocks by explicit effective medium methods. Geophysical Prospecting 62, 1297–1314. https://doi.org/10.1111/1365-2478.12173

Safari, R., Ghassemi, A., 2016. Three-dimensional poroelastic modeling of injection induced permeability enhancement and microseismicity. International Journal of Rock Mechanics and Mining Sciences 84, 47–58. https://doi.org/10.1016/j.ijrmms.2015.12.007

Safari, R., Ghassemi, A., 2015. 3D thermo-poroelastic analysis of fracture network deformation and induced micro-seismicity in enhanced geothermal systems. Geothermics 58, 1–14. https://doi.org/10.1016/j.geothermics.2015.06.010

Saksala, T., Brancherie, D., Harari, I., Ibrahimbegovic, A., 2015. Combined continuum damage-embedded discontinuity model for explicit dynamic fracture analyses of quasi-brittle materials. International Journal for Numerical Methods in Engineering 101, 230–250. https://doi.org/10.1002/nme.4814

Salimzadeh, S., Paluszny, A., Nick, H.M., Zimmerman, R.W., 2018. A three-dimensional coupled thermo-hydro-mechanical model for deformable fractured geothermal systems. Geothermics 71, 212–224. https://doi.org/10.1016/j.geothermics.2017.09.012

Salimzadeh, S., Paluszny, A., Zimmerman, R.W., 2017. Three-dimensional poroelastic effects during hydraulic fracturing in permeable rocks. International Journal of Solids and Structures 108, 153–163. https://doi.org/10.1016/j.ijsolstr.2016.12.008

Sánchez-Vila, X., Girardi, J.P., Carrera, J., 1995. A Synthesis of Approaches to Upscaling of Hydraulic Conductivities. Water Resources Research 31, 867–882. https://doi.org/10.1029/94WR02754

Sandve, T.H., Berre, I., Nordbotten, J.M., 2012. An efficient multi-point flux approximation method for Discrete Fracture–Matrix simulations. Journal of Computational Physics 231, 3784–3800. https://doi.org/10.1016/j.jcp.2012.01.023

Sarris, E., Papanastasiou, P., 2011. The influence of the cohesive process zone in hydraulic fracturing modelling. Int J Fract 167, 33–45. https://doi.org/10.1007/s10704-010-9515-4

Scanlon, B.R., Mace, R.E., Barrett, M.E., Smith, B., 2003. Can we simulate regional groundwater flow in a karst system using equivalent porous media models? Case study, Barton Springs Edwards aquifer, USA. Journal of Hydrology 276, 137–158. https://doi.org/10.1016/S0022-1694(03)00064-7

Scholz, C.H., 1998. Earthquakes and friction laws. Nature 391, 37–42. https://doi.org/10.1038/34097

Schultz, R.A., 2000. Growth of geologic fractures into large-strain populations: review of nomenclature, subcritical crack growth, and some implications for rock engineering. International Journal of Rock Mechanics and Mining Sciences 37, 403–411. https://doi.org/10.1016/S1365-1609(99)00115-X

Schwenck, N., Flemisch, B., Helmig, R., Wohlmuth, B.I., 2015. Dimensionally reduced flow models in fractured porous media: crossings and boundaries. Comput Geosci 19, 1219–1230. https://doi.org/10.1007/s10596-015-9536-1

Secchi, S., Schrefler, B.A., 2012. A method for 3-D hydraulic fracturing simulation. Int J Fract 178, 245–258. https://doi.org/10.1007/s10704-012-9742-y

Segall, P., 2010. Earthquake and volcano deformation, in: Earthquake and Volcano Deformation. Princeton University Press.

Settari, A., Walters, D.A., 2001. Advances in Coupled Geomechanical and Reservoir Modeling With Applications to Reservoir Compaction. SPE Journal 6, 334–342. https://doi.org/10.2118/74142-PA

Shahbazi, A., Saeidi, A., Chesnaux, R., 2020. A review of existing methods used to evaluate the hydraulic conductivity of a fractured rock mass. Engineering Geology 265, 105438. https://doi.org/10.1016/j.enggeo.2019.105438

Shahkarami, P., Liu, L., Moreno, L., Neretnieks, I., 2016. The effect of stagnant water zones on retarding radionuclide transport in fractured rocks: An extension to the Channel Network Model. Journal of Hydrology 540, 1122–1135. https://doi.org/10.1016/j.jhydrol.2016.07.031

Shahkarami, P., Neretnieks, I., Moreno, L., Liu, L., 2019. Channel network concept: an integrated approach to visualize solute transport in fractured rocks. Hydrogeol J 27, 101–119. https://doi.org/10.1007/s10040-018-1855-6

Shakas, A., Maurer, H., Giertzuch, P.-L., Hertrich, M., Giardini, D., Serbeto, F., Meier, P., 2020. Permeability Enhancement From a Hydraulic Stimulation Imaged With Ground Penetrating Radar. Geophysical Research Letters 47, e2020GL088783. https://doi.org/10.1029/2020GL088783

Sharma, K.M., Dessirier, B., Tsang, C.-F., Niemi, A., 2023. Apparent flow-dimension approach to the study of heterogeneous fracture network systems. Hydrogeol J 31, 873–891. https://doi.org/10.1007/s10040-023-02622-9

Shen, B., Stephansson, O., 1994. Modification of the G-criterion for crack propagation subjected to compression. Engineering Fracture Mechanics 47, 177–189. https://doi.org/10.1016/0013-7944(94)90219-4

Shen, P., Tang, H., Ning, Y., Xia, D., 2019. A damage mechanics based on the constitutive model for strain-softening rocks. Engineering Fracture Mechanics 216, 106521. https://doi.org/10.1016/j.engfracmech.2019.106521

Shortall, R., Davidsdottir, B., Axelsson, G., 2015. Geothermal energy for sustainable development: A review of sustainability impacts and assessment frameworks. Renewable and Sustainable Energy Reviews 44, 391–406. https://doi.org/10.1016/j.rser.2014.12.020

Sih, G.C., 1974. Strain-energy-density factor applied to mixed mode crack problems. Int J Fract 10, 305–321. https://doi.org/10.1007/BF00035493

Simpson, G., Guéguen, Y., Schneider, F., 2001. Permeability enhancement due to microcrack dilatancy in the damage regime. Journal of Geophysical Research: Solid Earth 106, 3999–4016. https://doi.org/10.1029/2000JB900194

Šimůnek, J., Jarvis, N.J., van Genuchten, M.Th., Gärdenäs, A., 2003. Review and comparison of models for describing non-equilibrium and preferential flow and transport in the vadose zone. Journal of Hydrology, Soil Hydrological Properties and Processes and their Variability in Space and Time 272, 14–35. https://doi.org/10.1016/S0022-1694(02)00252-4

Singh, M., 2000. Applicability of a Constitutive Model to Jointed Block Mass. Rock Mech Rock Engng 33, 141–147. https://doi.org/10.1007/s006030050039

Singhal, B.B.S., Gupta, R.P., 2010. Applied hydrogeology of fractured rocks. Springer Science & Business Media.

Siripatrachai, N., Ertekin, T., Johns, R., 2016. Compositional Simulation of Discrete Fractures Incorporating the Effect of Capillary Pressure on Phase Behavior.

Presented at the SPE Improved Oil Recovery Conference, OnePetro. https://doi.org/10.2118/179660-MS

Snow, D.T., 1969. Anisotropie Permeability of Fractured Media. Water Resources Research 5, 1273–1289. https://doi.org/10.1029/WR005i006p01273

Snow, D.T., 1965. A parallel plate model of fractured permeable media (Ph. D. thesis). University of California, Berkeley.

Soltanzadeh, H., Hawkes, C.D., 2009. Assessing fault reactivation tendency within and surrounding porous reservoirs during fluid production or injection. International Journal of Rock Mechanics and Mining Sciences 46, 1–7. https://doi.org/10.1016/j.ijrmms.2008.03.008

Somogyvári, M., Jalali, M., Jimenez Parras, S., Bayer, P., 2017. Synthetic fracture network characterization with transdimensional inversion. Water Resources Research 53, 5104–5123. https://doi.org/10.1002/2016WR020293

Song, J., Dong, M., Koltuk, S., Hu, H., Zhang, L., Azzam, R., 2018. Hydro-mechanically coupled finite-element analysis of the stability of a fractured-rock slope using the equivalent continuum approach: a case study of planned reservoir banks in Blaubeuren, Germany. Hydrogeol J 26, 803–817. https://doi.org/10.1007/s10040-017-1694-x

Souley, M., Armand, G., Su, K., Ghoreychi, M., 2011. Modeling the viscoplastic and damage behavior in deep argillaceous rocks. Physics and Chemistry of the Earth, Parts A/B/C, Clays in Natural & Engineered Barriers for Radioactive Waste Confinement 36, 1949–1959. https://doi.org/10.1016/j.pce.2011.10.012

Souley, M., Homand, F., Amadei, B., 1995. An extension to the Saeb and Amadei constitutive model for rock joints to include cyclic loading paths. International Journal of Rock Mechanics and Mining Sciences & Geomechanics Abstracts 32, 101–109. https://doi.org/10.1016/0148-9062(94)00039-6

Stacey, R.W., Williams, M.J., 2017. Validation of ECLIPSE reservoir simulator for geothermal problems. GRC Transactions 41, 2095–2109.

Stefansson, I., Berre, I., Keilegavlen, E., 2021. A fully coupled numerical model of thermo-hydro-mechanical processes and fracture contact mechanics in porous media. Computer Methods in Applied Mechanics and Engineering 386, 114122. https://doi.org/10.1016/j.cma.2021.114122

Stephansson, O., Jing, L., Tsang, C.F., 1997. Coupled Thermohydroelasticity Phenomena in Variably Saturated. Coupled Thermo-Hydro-Mechanical Processes of Fractured Media: Mathematical and Experimental Studies 79, 93.

Su, T., Zhou, H., Zhao, J., Liu, Z., Deng, H., 2022. A modeling approach to stress-dependent porosity and permeability decays of rocks. Journal of Natural Gas Science and Engineering 106, 104765. https://doi.org/10.1016/j.jngse.2022.104765

Suzuki, T., Yamashita, T., 2008. Nonlinear effects of temperature, fluid pressure, and inelastic porosity on dynamic fault slip and fault tip propagation: Emergence of slip strengthening and pulse-like fault slip. Journal of Geophysical Research: Solid Earth 113. https://doi.org/10.1029/2008JB005581

Suzuki, T., Yamashita, T., 2007. Understanding of slip-weakening and -strengthening in a single framework of modeling and its seismological implications. Geophysical Research Letters 34. https://doi.org/10.1029/2007GL030260

Svensson, U., 2001. A continuum representation of fracture networks. Part I: Method and basic test cases. Journal of Hydrology 250, 170–186. https://doi.org/10.1016/S0022-1694(01)00435-8

Sweeney, M.R., Gable, C.W., Karra, S., Stauffer, P.H., Pawar, R.J., Hyman, J.D., 2020. Upscaled discrete fracture matrix model (UDFM): an octree-refined continuum representation of fractured porous media. Comput Geosci 24, 293–310. https://doi.org/10.1007/s10596-019-09921-9

Taghichian, A., Zaman, M., Devegowda, D., 2014. Stress shadow size and aperture of hydraulic fractures in unconventional shales. Journal of Petroleum Science and Engineering 124, 209–221. https://doi.org/10.1016/j.petrol.2014.09.034

Tangirala, S.K., Vilarrasa, V., Parisio, F., 2023. Hydraulic stimulation of tight geothermal reservoirs, in: Enhanced Geothermal Systems (EGS). CRC Press, pp. 151–164.

Tao, Q., Ghassemi, A., Ehlig-Economides, C.A., 2011. A fully coupled method to model fracture permeability change in naturally fractured reservoirs. International Journal of Rock Mechanics and Mining Sciences 48, 259–268. https://doi.org/10.1016/j.ijrmms.2010.11.012

Taron, J., Elsworth, D., 2009. Thermal–hydrologic–mechanical–chemical processes in the evolution of engineered geothermal reservoirs. International Journal of Rock Mechanics and Mining Sciences 46, 855–864. https://doi.org/10.1016/j.ijrmms.2009.01.007

Tatomir, A.B., Szymkiewicz, A., Class, H., Helmig, R., 2011. Modeling two phase flow in large scale fractured porous media with an extended multiple interacting continua method. Computer Modeling in Engineering and Sciences 77, 81.

Taylor, W.L., Pollard, D.D., Aydin, A., 1999. Fluid flow in discrete joint sets: Field observations and numerical simulations. Journal of Geophysical Research: Solid Earth 104, 28983–29006. https://doi.org/10.1029/1999JB900179

Tejchman, J., Bobiński, J., 2012. Continuous and discontinuous modelling of fracture in concrete using FEM. Springer Science & Business Media.

Terzaghi, K., 1925. Erdbaumechanik auf bodenphysikalischer Grundlage. F. Deuticke.

Theis, C.V., 1935. The relation between the lowering of the Piezometric surface and the rate and duration of discharge of a well using ground-water storage. Eos, Transactions American Geophysical Union 16, 519–524. https://doi.org/10.1029/TR016i002p00519

Thomas, R.N., Paluszny, A., Zimmerman, R.W., 2020. Permeability of Three-Dimensional Numerically Grown Geomechanical Discrete Fracture Networks With Evolving Geometry and Mechanical Apertures. Journal of Geophysical Research: Solid Earth 125, e2019JB018899. https://doi.org/10.1029/2019JB018899

Tiab, D., 2005. Analysis of pressure derivative data of hydraulically fractured wells by the Tiab's Direct Synthesis technique. Journal of Petroleum Science and Engineering 49, 1–21. https://doi.org/10.1016/j.petrol.2005.07.001

Tomac, I., Sauter, M., 2018. A review on challenges in the assessment of geomechanical rock performance for deep geothermal reservoir development. Renewable and Sustainable Energy Reviews 82, 3972–3980. https://doi.org/10.1016/j.rser.2017.10.076

Townend, J., Zoback, M.D., 2000. How faulting keeps the crust strong. Geology 28, 399–402.

Tran, D., Nghiem, L., Buchanan, L., 2005. An overview of iterative coupling between geomechanical deformation and reservoir flow, in: SPE International Thermal Operations and Heavy Oil Symposium. OnePetro.

Trautwein, U., 2002. Permeability changes as a function of pore pressure in sandstones: laboratory experiments under uniaxial strain boundary conditions, in: Poromechanics II. CRC Press.

Trimmer, D., Bonner, B., Heard, H.C., Duba, A., 1980. Effect of pressure and stress on water transport in intact and fractured gabbro and granite. Journal of Geophysical Research: Solid Earth 85, 7059–7071. https://doi.org/10.1029/JB085iB12p07059

Tsang, C.-F., 1999. Linking Thermal, Hydrological, and Mechanical Processes in Fractured Rocks. Annual Review of Earth and Planetary Sciences 27, 359–384. https://doi.org/10.1146/annurev.earth.27.1.359

Tsang, C.-F., 1991. Coupled hydromechanical-thermochemical processes in rock fractures. Reviews of Geophysics 29, 537–551. https://doi.org/10.1029/91RG01832

Tsang, C.-F., 1987. Coupled processes associated with nuclear waste repositories. Elsevier.

Tsang, C.-F., Neretnieks, I., 1998. Flow channeling in heterogeneous fractured rocks. Reviews of Geophysics 36, 275–298. https://doi.org/10.1029/97RG03319

Tsang, Y.W., 1992. Usage of "Equivalent apertures" for rock fractures as derived from hydraulic and tracer tests. Water Resources Research 28, 1451–1455. https://doi.org/10.1029/92WR00361

Tsang, Y.W., Tsang, C.F., 1987. Channel model of flow through fractured media. Water Resources Research 23, 467–479. https://doi.org/10.1029/WR023i003p00467

Tsang, Y.W., Tsang, C.F., Hale, F.V., Dverstorp, B., 1996. Tracer transport in a stochastic continuum model of fractured media. Water Resources Research 32, 3077–3092. https://doi.org/10.1029/96WR01397

Tsang, Y.W., Tsang, C.F., Neretnieks, I., Moreno, L., 1988. Flow and tracer transport in fractured media: A variable aperture channel model and its properties. Water Resources Research 24, 2049–2060. https://doi.org/10.1029/WR024i012p02049

Ujiie, K., Tsutsumi, A., Fialko, Y., Yamaguchi, H., 2009. Experimental investigation of frictional melting of argillite at high slip rates: Implications for seismic slip in subduction-accretion complexes. Journal of Geophysical Research: Solid Earth 114. https://doi.org/10.1029/2008JB006165

Valkó, P., Economides, M.J., 1995. Hydraulic fracture mechanics. Wiley Chichester.

Vanderborght, J., Kasteel, R., Vereecken, H., 2006. Stochastic Continuum Transport Equations for Field-Scale Solute Transport: Overview of Theoretical and Experimental Results. Vadose Zone Journal 5, 184–203. https://doi.org/10.2136/vzj2005.0024

Veling, E.J.M., Maas, C., 2010. Hantush Well Function revisited. Journal of Hydrology 393, 381–388. https://doi.org/10.1016/j.jhydrol.2010.08.033

Vermilye, J.M., Scholz, C.H., 1998. The process zone: A microstructural view of fault growth. Journal of Geophysical Research: Solid Earth 103, 12223–12237. https://doi.org/10.1029/98JB00957

Verruijt, A., 1969. Elastic storage of aquifers. Flow through porous media 1, 331–376.

Vilarrasa, V., Bolster, D., Olivella, S., Carrera, J., 2010. Coupled hydromechanical modeling of CO2 sequestration in deep saline aquifers. International Journal of Greenhouse Gas Control, CO2 Storage at the EGU General Assembly 2009 4, 910–919. https://doi.org/10.1016/j.ijggc.2010.06.006

Vilarrasa, V., Bustarret, G., Laloui, L., Zeidouni, M., 2017a. A methodology to detect and locate low-permeability faults to reduce the risk of inducing seismicity of fluid injection operations in deep saline formations. International Journal of Greenhouse Gas Control 59, 110–122. https://doi.org/10.1016/j.ijggc.2017.02.010

Vilarrasa, V., Carrera, J., Olivella, S., 2013a. Hydromechanical characterization of CO2 injection sites. International Journal of Greenhouse Gas Control 19, 665–677. https://doi.org/10.1016/j.ijggc.2012.11.014

Vilarrasa, V., Carrera, J., Olivella, S., Rutqvist, J., Laloui, L., 2019. Induced seismicity in geologic carbon storage. Solid Earth 10, 871–892. https://doi.org/10.5194/se-10-871-2019

Vilarrasa, V., De Simone, S., Carrera, J., Villaseñor, A., 2022. Multiple induced seismicity mechanisms at Castor underground gas storage illustrate the need for thorough monitoring. Nat Commun 13, 3447. https://doi.org/10.1038/s41467-022-30903-6

Vilarrasa, V., De Simone, S., Carrera, J., Villaseñor, A., 2021. Unraveling the Causes of the Seismicity Induced by Underground Gas Storage at Castor, Spain. Geophysical Research Letters 48, e2020GL092038. https://doi.org/10.1029/2020GL092038

Vilarrasa, V., Koyama, T., Neretnieks, I., Jing, L., 2011. Shear-Induced Flow Channels in a Single Rock Fracture and Their Effect on Solute Transport. Transp Porous Med 87, 503–523. https://doi.org/10.1007/s11242-010-9698-1

Vilarrasa, V., Olivella, S., Carrera, J., Rutqvist, J., 2014. Long term impacts of cold CO2 injection on the caprock integrity. International Journal of Greenhouse Gas Control 24, 1–13. https://doi.org/10.1016/j.ijggc.2014.02.016

Vilarrasa, V., Rinaldi, A.P., Rutqvist, J., 2017b. Long-term thermal effects on injectivity evolution during CO2 storage. International Journal of Greenhouse Gas Control 64, 314–322. https://doi.org/10.1016/j.ijggc.2017.07.019

Vilarrasa, V., Silva, O., Carrera, J., Olivella, S., 2013b. Liquid CO2 injection for geological storage in deep saline aquifers. International Journal of Greenhouse Gas Control 14, 84–96. https://doi.org/10.1016/j.ijggc.2013.01.015

Viswanathan, H.S., Ajo-Franklin, J., Birkholzer, J.T., Carey, J.W., Guglielmi, Y., Hyman, J.D., Karra, S., Pyrak-Nolte, L.J., Rajaram, H., Srinivasan, G., Tartakovsky, D.M., 2022. From Fluid Flow to Coupled Processes in Fractured Rock: Recent Advances and New Frontiers. Reviews of Geophysics 60, e2021RG000744. https://doi.org/10.1029/2021RG000744

Vogel, T., Gerke, H.H., Zhang, R., Van Genuchten, M.Th., 2000. Modeling flow and transport in a two-dimensional dual-permeability system with spatially variable hydraulic properties. Journal of Hydrology 238, 78–89. https://doi.org/10.1016/S0022-1694(00)00327-9

Walsh, J.B., 1981. Effect of pore pressure and confining pressure on fracture permeability. International Journal of Rock Mechanics and Mining Sciences & Geomechanics Abstracts 18, 429–435. https://doi.org/10.1016/0148-9062(81)90006-1

Walton, G., 2021. A New Perspective on the Brittle–Ductile Transition of Rocks. Rock Mech Rock Eng 54, 5993–6006. https://doi.org/10.1007/s00603-021-02595-9

Walton, W.C., 2006. Aquifer Test Modeling. CRC Press, Boca Raton. https://doi.org/10.1201/9781420042931

Wang, G., 2005. A triple-continuum numerical model for simulating multiphase flow in vuggy fractured reservoirs. Citeseer.

Wang, J., Liu, W., Shen, J., 2021. Investigation on the Fracturing Permeability Characteristics of Cracked Specimens and the Formation Mechanism of Inrush Channel from Floor. Shock and Vibration 2021, e8858733. https://doi.org/10.1155/2021/8858733

Wang, K., Liu, H., Luo, J., Wu, K., Chen, Z., 2017. A Comprehensive Model Coupling Embedded Discrete Fractures, Multiple Interacting Continua, and Geomechanics in Shale Gas Reservoirs with Multiscale Fractures. Energy Fuels 31, 7758–7776. https://doi.org/10.1021/acs.energyfuels.7b00394

Wang, K., Zhou, J., Ma, Y., Ding, A., Chen, X., 2023. Constitutive and numerical modeling for the coupled thermal-hydro-mechanical processes in dual-porosity geothermal reservoir. Applied Thermal Engineering 223, 120027. https://doi.org/10.1016/j.applthermaleng.2023.120027

Wang, L., Lei, Q., 2023. Modelling the pre- and post-failure behaviour of faulted rock slopes based on the particle finite element method with a damage mechanics model. Computers and Geotechnics 153, 105057. https://doi.org/10.1016/j.compgeo.2022.105057

Wang, L., Lei, Q., 2021. A dual-scale fracture network model for computing hydro-mechanical properties of fractured rock. Computers and Geotechnics 138, 104357. https://doi.org/10.1016/j.compgeo.2021.104357

Wang, L., Wang, Y., Vuik, C., Hajibeygi, H., 2022. Accurate modeling and simulation of seepage in 3D heterogeneous fractured porous media with complex structures. Computers and Geotechnics 150, 104923. https://doi.org/10.1016/j.compgeo.2022.104923

Wang, S., Zhao, W., Fu, X., Zhang, Z., Wang, T., Ge, J., 2020. A universal method for quantitatively evaluating rock brittle-ductile transition behaviors. Journal of Petroleum Science and Engineering 195, 107774. https://doi.org/10.1016/j.petrol.2020.107774

Wang, W., Kolditz, O., 2007. Object-oriented finite element analysis of thermo-hydro-mechanical (THM) problems in porous media. International Journal for Numerical Methods in Engineering 69, 162–201. https://doi.org/10.1002/nme.1770

Wang, X., Liu, D., Li, X., Gao, Q., 2023. Mechanism and implications of shut-in induced earthquakes. Alexandria Engineering Journal 65, 837–846. https://doi.org/10.1016/j.aej.2022.09.042

Wang, Y., 2017. On subsurface fracture opening and closure. Journal of Petroleum Science and Engineering, Energy Frontier Research Centers for Investigating Carbon Sequestration 155, 46–53. https://doi.org/10.1016/j.petrol.2016.10.051

Wang, Z., Rutqvist, J., Wang, Y., Leung, C., Hoch, A., Dai, Y., 2014. The Effect of Stress on Flow and Transport in Fractured Rock Masses Using an Extended Multiple Interacting Continua Method with Crack Tensor Theory. Nuclear Technology 187, 158–168. https://doi.org/10.13182/NT13-76

Warren, J.E., Root, P.J., 1963. The Behavior of Naturally Fractured Reservoirs. Society of Petroleum Engineers Journal 3, 245–255. https://doi.org/10.2118/426-PA

Watanabe, N., Wang, W., Taron, J., Görke, U.J., Kolditz, O., 2012. Lower-dimensional interface elements with local enrichment: application to coupled hydro-mechanical problems in discretely fractured porous media. International Journal for Numerical Methods in Engineering 90, 1010–1034. https://doi.org/10.1002/nme.3353

Waters, G., Dean, B., Downie, R., Kerrihard, K., Austbo, L., McPherson, B., 2009. Simultaneous Hydraulic Fracturing of Adjacent Horizontal Wells in the Woodford Shale. Presented at the SPE Hydraulic Fracturing Technology Conference, OnePetro. https://doi.org/10.2118/119635-MS

Willis-Richards, J., Watanabe, K., Takahashi, H., 1996. Progress toward a stochastic rock mechanics model of engineered geothermal systems. Journal of Geophysical Research: Solid Earth 101, 17481–17496. https://doi.org/10.1029/96JB00882

Winhausen, L., Khaledi, K., Jalali, M., Urai, J.L., Amann, F., 2022. Failure mode transition in Opalinus Clay: a hydro-mechanical and microstructural perspective. Solid Earth 13, 901–915. https://doi.org/10.5194/se-13-901-2022

Witherspoon, P.A., Wang, J.S.Y., Iwai, K., Gale, J.E., 1980. Validity of Cubic Law for fluid flow in a deformable rock fracture. Water Resources Research 16, 1016–1024. https://doi.org/10.1029/WR016i006p01016

Wong, D.L.Y., Doster, F., Geiger, S., Kamp, A., 2020. Partitioning Thresholds in Hybrid Implicit-Explicit Representations of Naturally Fractured Reservoirs. Water Resources Research 56, e2019WR025774. https://doi.org/10.1029/2019WR025774

Wong, T., Baud, P., 2012. The brittle-ductile transition in porous rock: A review. Journal of Structural Geology 44, 25–53. https://doi.org/10.1016/j.jsg.2012.07.010

Wu, F., Wang, S., 2001. A stress–strain relation for jointed rock masses. International Journal of Rock Mechanics and Mining Sciences 38, 591–598. https://doi.org/10.1016/S1365-1609(01)00027-2

Wu, H., Vilarrasa, V., De Simone, S., Saaltink, M., Parisio, F., 2021. Analytical Solution to Assess the Induced Seismicity Potential of Faults in Pressurized and Depleted Reservoirs. Journal of Geophysical Research: Solid Earth 126, e2020JB020436. https://doi.org/10.1029/2020JB020436

Wu, Y.-S., 2016. Chapter 9 - Multiphase Flow in Fractured Porous Media, in: Wu, Y.-S. (Ed.), Multiphase Fluid Flow in Porous and Fractured Reservoirs. Gulf Professional Publishing, Boston, pp. 207–250. https://doi.org/10.1016/B978-0-12-803848-2.00009-X

Wu, Y.-S., Liu, H.H., Bodvarsson, G.S., 2004. A triple-continuum approach for modeling flow and transport processes in fractured rock. Journal of Contaminant Hydrology 73, 145–179. https://doi.org/10.1016/j.jconhyd.2004.01.002

Wu, Y.-S., Pruess, K., 1988. A Multiple-Porosity Method for Simulation of Naturally Fractured Petroleum Reservoirs. SPE Reservoir Engineering 3, 327–336. https://doi.org/10.2118/15129-PA

Wu, Z., Cui, C., Jia, P., Wang, Z., Sui, Y., 2022. Advances and challenges in hydraulic fracturing of tight reservoirs: A critical review. Energy Geoscience, SI: Tight Reservoirs 3, 427–435. https://doi.org/10.1016/j.engeos.2021.08.002

Xiao, Y., Guo, J., Wang, H., Lu, L., Chen, M., 2019. Elastoplastic constitutive model for hydraulic aperture analysis of hydro-shearing in geothermal energy development. SIMULATION 95, 861–872. https://doi.org/10.1177/0037549718793216

Xie, L., Min, K.-B., 2016. Initiation and propagation of fracture shearing during hydraulic stimulation in enhanced geothermal system. Geothermics 59, 107–120. https://doi.org/10.1016/j.geothermics.2015.10.012

Xie, S., Han, Z., Hu, H., Lin, H., 2022a. Application of a novel constitutive model to evaluate the shear deformation of discontinuity. Engineering Geology 304, 106693. https://doi.org/10.1016/j.enggeo.2022.106693

Xie, S., Lin, H., Chen, Y., 2022b. New constitutive model based on disturbed state concept for shear deformation of rock joints. Archiv.Civ.Mech.Eng 23, 26. https://doi.org/10.1007/s43452-022-00560-z

Xie, S., Lin, H., Chen, Y., Yong, R., Xiong, W., Du, S., 2020a. A damage constitutive model for shear behavior of joints based on determination of the yield point. International Journal of Rock Mechanics and Mining Sciences 128, 104269. https://doi.org/10.1016/j.ijrmms.2020.104269

Xie, S., Lin, H., Wang, Y., Cao, R., Yong, R., Du, S., Li, J., 2020b. Nonlinear shear constitutive model for peak shear-type joints based on improved Harris damage function. Archiv.Civ.Mech.Eng 20, 95. https://doi.org/10.1007/s43452-020-00097-z

Xiong, X., Li, B., Jiang, Y., Koyama, T., Zhang, C., 2011. Experimental and numerical study of the geometrical and hydraulic characteristics of a single rock fracture during shear. International Journal of Rock Mechanics and Mining Sciences 48, 1292–1302. https://doi.org/10.1016/j.ijrmms.2011.09.009

Xu, C., Dowd, P., 2010. A new computer code for discrete fracture network modelling. Computers & Geosciences 36, 292–301. https://doi.org/10.1016/j.cageo.2009.05.012

Xu, H., Rutqvist, J., Birkholzer, J., 2020. A study of thermal pressurization and potential for hydro-fracturing associated with nuclear waste disposal in argillaceous claystone. International Journal of Rock Mechanics and Mining Sciences 136, 104536. https://doi.org/10.1016/j.ijrmms.2020.104536

Xue, Y., Teng, T., Dang, F., Ma, Z., Wang, S., Xue, H., 2020. Productivity analysis of fractured wells in reservoir of hydrogen and carbon based on dual-porosity medium model. International Journal of Hydrogen Energy, The 7th International Conference on Energy, Engineering and Environmental Engineering 45, 20240–20249. https://doi.org/10.1016/j.ijhydene.2019.11.146

Yan, B., Wang, P., Ren, F., Guo, Q., Cai, M., 2020. A review of mechanical properties and constitutive theory of rock mass anisotropy. Arab J Geosci 13, 487. https://doi.org/10.1007/s12517-020-05536-y

Yan, B., Wang, Y., Killough, J.E., 2016. Beyond dual-porosity modeling for the simulation of complex flow mechanisms in shale reservoirs. Comput Geosci 20, 69–91. https://doi.org/10.1007/s10596-015-9548-x

Yang, T.H., Jia, P., Shi, W.H., Wang, P.T., Liu, H.L., Yu, Q.L., 2014. Seepage–stress coupled analysis on anisotropic characteristics of the fractured rock mass around roadway. Tunnelling and Underground Space Technology 43, 11–19. https://doi.org/10.1016/j.tust.2014.03.005

Ye, Z., Ghassemi, A., 2018. Injection-Induced Shear Slip and Permeability Enhancement in Granite Fractures. Journal of Geophysical Research: Solid Earth 123, 9009–9032. https://doi.org/10.1029/2018JB016045

Yeo, I.W., de Freitas, M.H., Zimmerman, R.W., 1998. Effect of shear displacement on the aperture and permeability of a rock fracture. International Journal of Rock Mechanics and Mining Sciences 35, 1051–1070. https://doi.org/10.1016/S0148-9062(98)00165-X

Yoo, H., Park, S., Xie, L., Kim, K.-I., Min, K.-B., Rutqvist, J., Rinaldi, A.P., 2021. Hydro-mechanical modeling of the first and second hydraulic stimulations in a fractured geothermal reservoir in Pohang, South Korea. Geothermics 89, 101982. https://doi.org/10.1016/j.geothermics.2020.101982

Yoon, J.S., Zang, A., Stephansson, O., Hofmann, H., Zimmermann, G., 2017. Discrete Element Modelling of Hydraulic Fracture Propagation and Dynamic Interaction with Natural Fractures in Hard Rock. Procedia Engineering, ISRM European Rock Mechanics Symposium EUROCK 2017 191, 1023–1031. https://doi.org/10.1016/j.proeng.2017.05.275

Yoshioka, K., Bourdin, B., 2016. A variational hydraulic fracturing model coupled to a reservoir simulator. International Journal of Rock Mechanics and Mining Sciences 88, 137–150. https://doi.org/10.1016/j.ijrmms.2016.07.020

Yoshioka, K., Naumov, D., Kolditz, O., 2020. On crack opening computation in variational phase-field models for fracture. Computer Methods in Applied Mechanics and Engineering 369, 113210. https://doi.org/10.1016/j.cma.2020.113210

Yoshioka, K., Parisio, F., Naumov, D., Lu, R., Kolditz, O., Nagel, T., 2019. Comparative verification of discrete and smeared numerical approaches for the simulation of hydraulic fracturing. Int J Geomath 10, 13. https://doi.org/10.1007/s13137-019-0126-6

Youssef, A.A., Alnuaim, S., 2017. IPR of Triple Continuum Reservoirs, Analytical Approach. Presented at the SPE Kingdom of Saudi Arabia Annual Technical Symposium and Exhibition, OnePetro. https://doi.org/10.2118/187973-MS

Yu, Y., Damians, I.P., Bathurst, R.J., 2015. Influence of choice of FLAC and PLAXIS interface models on reinforced soil–structure interactions. Computers and Geotechnics 65, 164–174. https://doi.org/10.1016/j.compgeo.2014.12.009

Yuan, F., Prakash, V., 2012. Laboratory observations of transient frictional slip in rock–analog materials at co-seismic slip rates and rapid changes in normal stress. Tectonophysics 558–559, 58–69. https://doi.org/10.1016/j.tecto.2012.06.026

Zareidarmiyan, A., Parisio, F., Makhnenko, R.Y., Salarirad, H., Vilarrasa, V., 2021. How Equivalent Are Equivalent Porous Media? Geophysical Research Letters 48, e2020GL089163. https://doi.org/10.1029/2020GL089163

Zareidarmiyan, A., Salarirad, H., Vilarrasa, V., De Simone, S., Olivella, S., 2018. Geomechanical Response of Fractured Reservoirs. Fluids 3, 70. https://doi.org/10.3390/fluids3040070

Zareidarmiyan, A., Salarirad, H., Vilarrasa, V., Kim, K.-I., Lee, J., Min, K.-B., 2020. Comparison of numerical codes for coupled thermo-hydro-mechanical simulations

of fractured media. Journal of Rock Mechanics and Geotechnical Engineering 12, 850–865. https://doi.org/10.1016/j.jrmge.2019.12.016

Zhang, G.Q., Cui, B., 2011. The study of Thermal-Hydrologic-Mechanical (THM) coupled process in dual-porosity rock. Rock Mechanics: Achievements and Ambitions 413.

Zhang, H., Huang, G., Song, H., Kang, Y., 2013. Experimental characterization of strain localization in rock. Geophysical Journal International 194, 1554–1558. https://doi.org/10.1093/gji/ggt201

Zhang, J., Yao, B., Ao, Y., Jin, C., Sun, C., 2021. Analysis and numerical calculation of a coupled creep and strain-softening model for soft rock tunnels. PLOS ONE 16, e0256243. https://doi.org/10.1371/journal.pone.0256243

Zhang, M., Yao, J., Sun, H., Zhao, J., Fan, D., Huang, Z., Wang, Y., 2015. Triple-continuum modeling of shale gas reservoirs considering the effect of kerogen. Journal of Natural Gas Science and Engineering 24, 252–263. https://doi.org/10.1016/j.jngse.2015.03.032

Zhang, T., Li, Z., Adenutsi, C.D., Lai, F., 2017. A new model for calculating permeability of natural fractures in dual-porosity reservoir. Advances in Geo-Energy Research 1, 86–92.

Zhang, W., Diab, W., Hajibeygi, H., Al Kobaisi, M., 2020. A Computational Workflow for Flow and Transport in Fractured Porous Media Based on a Hierarchical Nonlinear Discrete Fracture Modeling Approach. Energies 13, 6667. https://doi.org/10.3390/en13246667

Zhang, Z., Nemcik, J., 2013. Fluid flow regimes and nonlinear flow characteristics in deformable rock fractures. Journal of Hydrology 477, 139–151. https://doi.org/10.1016/j.jhydrol.2012.11.024

Zhao, G., Shi, G.-H., Zhao, J., 2011. Manifold and advanced numerical techniques for discontinuous dynamic computations. Advances in rock dynamics and applications 321–344.

Zhao, Y., Chen, M., 2006. Fully coupled dual-porosity model for anisotropic formations. International Journal of Rock Mechanics and Mining Sciences 43, 1128–1133. https://doi.org/10.1016/j.ijrmms.2006.03.001

Zhao, Y., Liu, Q., Zhang, C., Liao, J., Lin, H., Wang, Y., 2021. Coupled seepage-damage effect in fractured rock masses: model development and a case study. International

Journal of Rock Mechanics and Mining Sciences 144, 104822. https://doi.org/10.1016/j.ijrmms.2021.104822

Zheng, Z., Su, H., Mei, G., Wang, W., Liu, H., Zhang, Q., Wang, Y., 2023. A thermodynamic damage model for 3D stress-induced mechanical characteristics and brittle–ductile transition of rock. International Journal of Damage Mechanics 32, 623–648. https://doi.org/10.1177/10567895231160813

Zhong, Z., Ding, J., Hu, Y., 2022. Size effect on the hydraulic behavior of fluid flow through rough-walled fractures: a case of radial flow. Hydrogeol J 30, 97–109. https://doi.org/10.1007/s10040-021-02415-y

Zhou, C.B., Sharma, R.S., Chen, Y.F., Rong, G., 2008. Flow–stress coupled permeability tensor for fractured rock masses. International Journal for Numerical and Analytical Methods in Geomechanics 32, 1289–1309. https://doi.org/10.1002/nag.668

Zhou, H., Jia, Y., Shao, J.F., 2008. A unified elastic–plastic and viscoplastic damage model for quasi-brittle rocks. International Journal of Rock Mechanics and Mining Sciences 45, 1237–1251. https://doi.org/10.1016/j.ijrmms.2008.01.004

Zhou, J., Zhang, L., Li, X., Pan, Z., 2019. Experimental and modeling study of the stress-dependent permeability of a single fracture in shale under high effective stress. Fuel 257, 116078. https://doi.org/10.1016/j.fuel.2019.116078

Zhou, Q., Birkholzer, J.T., Tsang, C.-F., 2009. A Semi-Analytical Solution for Large-Scale Injection-Induced Pressure Perturbation and Leakage in a Laterally Bounded Aquifer–Aquitard System. Transp Porous Med 78, 127–148. https://doi.org/10.1007/s11242-008-9290-0

Zhou, Q., Birkholzer, J.T., Tsang, C.-F., Rutqvist, J., 2008. A method for quick assessment of CO2 storage capacity in closed and semi-closed saline formations. International Journal of Greenhouse Gas Control, TCCS-4: The 4th Trondheim Conference on CO2 Capture, Transport and Storage 2, 626–639. https://doi.org/10.1016/j.ijggc.2008.02.004

Zhou, Q., Oldenburg, C.M., Rutqvist, J., Birkholzer, J.T., 2017. Revisiting the Fundamental Analytical Solutions of Heat and Mass Transfer: The Kernel of Multirate and Multidimensional Diffusion. Water Resources Research 53, 9960–9979. https://doi.org/10.1002/2017WR021040

Zhou, X., Aydin, A., Liu, F., Pollard, D.D., 2010. Numerical modeling of secondary thermal fractures in hot dry geothermal reservoirs. Proceedings in Thirty-Fifth

Work-shop on Geothermal Reservoir Engineering Stanford University, Stanford, California.

Zienkiewicz, O.C., Mroz, Z., 1984. Generalized plasticity formulation and applications to geomechanics. Mechanics of engineering materials 44, 655–680.

Zienkiewicz, O.C., Paul, D.K., Chan, A.H.C., 1988. Unconditionally stable staggered solution procedure for soil-pore fluid interaction problems. International Journal for Numerical Methods in Engineering 26, 1039–1055. https://doi.org/10.1002/nme.1620260504

Zimmerman, R.W., 2000. Coupling in poroelasticity and thermoelasticity. International Journal of Rock Mechanics and Mining Sciences 37, 79–87. https://doi.org/10.1016/S1365-1609(99)00094-5

Zimmerman, R.W., Bodvarsson, G.S., 1996. Hydraulic conductivity of rock fractures. Transp Porous Med 23, 1–30. https://doi.org/10.1007/BF00145263

Zimmerman, R.W., Chen, G., Hadgu, T., Bodvarsson, G.S., 1993. A numerical dual-porosity model with semianalytical treatment of fracture/matrix flow. Water Resources Research 29, 2127–2137. https://doi.org/10.1029/93WR00749

Zimmerman, R.W., Yeo, I.-W., 2000. Fluid flow in rock fractures: From the Navier-Stokes equations to the cubic law. Geophysical Monograph-American Geophysical Union 122, 213–224.

Zoorabadi, M., Saydam, S., Timms, W., Hebblewhite, B., 2022. Analytical methods to estimate the hydraulic conductivity of jointed rocks. Hydrogeol J 30, 111–119. https://doi.org/10.1007/s10040-021-02413-0

Zou, L., Jing, L., Cvetkovic, V., 2015. Roughness decomposition and nonlinear fluid flow in a single rock fracture. International Journal of Rock Mechanics and Mining Sciences 75, 102–118. https://doi.org/10.1016/j.ijrmms.2015.01.016